Regulation of Crystallization Dynamic Rendering Highly Efficient Narrow-Bandgap Perovskite Solar Cells

by

GUOCONG CHEN

A thesis submitted to the University of Birmingham for the degree of

DOCTOR OF PHILOSOPHY

School of Chemistry

University of Birmingham

January 2024

Abstract

Perovskite solar cells (PSCs) have attracted increasing interest during the last decade due to their great potential to make full use of solar energy at low cost. Among all kinds of PSCs, narrow-bandgap perovskite solar cells are theoretically able to achieve efficiency approaching the S-Q efficiency limit. However, the uncontrolled crystallization process becomes one of the significant obstacles to realizing high-quality narrow-bandgap perovskite films and achieving highly efficient PSCs. In this thesis, I present my study on regulating crystallization dynamics of narrow-bandgap perovskites, including pure α-$FAPbI_3$ perovskite and mixed tin-lead perovskites (TLPs), to produce perovskite films with improved crystallinity and suppressed defect density and, therefore, realize impressive improvements in the efficiency of PSCs. I first developed a coordinator replenishment strategy by utilizing tetramethylurea (TMU) as a coordinating agent to facilitate the pre-nucleation of α-$FAPbI_3$ perovskite crystals and, thus, regulate the crystallization dynamic of the α-$FAPbI_3$ perovskite film in an air atmosphere. This led to the remarkable improvement in crystallinity, orientation, defect density, and lattice strain of the α-$FAPbI_3$ perovskite films. As a result, the PSCs based on such perovskite films have achieved the highest efficiency of 23.2%, along with enhanced long-term stability. Then, I investigated strategies to improve the film quality of TLPs. We introduced 3,4-dihydroxybenzylamine hydrobromide (DHBABr) as an additive, which was demonstrated to preferentially coordinate with SnI_2 in the precursor. Consequently, the DHBABr additive balanced the crystallization rate of both Sn- and Pb-based perovskite components during their anti-solvent

treatment and annealing processes, realizing TLP films with homogeneous Sn/Pb distribution, higher crystallinity, and lower defect density. The PSCs based on such TLP films finally achieved enhanced efficiency of 22.44% and improved long-term stability. Lastly, I have also explored a templated-growth approach for the regulation of the crystallization dynamic of TLPs by utilizing 2-phosphonoethan-1-aminium iodide (2PEAI) as an additive. The 2PEAI additive was determined to selectively coordinate with SnF_2 and form a SnF_2-2PEA adduct, which regulates the crystallization by templated-anchoring the perovskite components. As a result, TLP films with higher crystallinity and lower defect density were obtained. Benefiting from the improved TLP film quality, the corresponding PSCs achieved the highest PCE of 21.95%. In all these research works, the mechanisms of the regulation of crystallization dynamics were comprehensively studied and discussed.

Acknowledgements

The achievements showcased in this thesis owe their success to the invaluable assistance and encouragement I received from the universities, my supervisors, exceptional group members, and other scientists with whom I had the privilege to collaborate. I sincerely extend my gratitude for their invaluable support, contributions to my research outcomes, and guidance on this thesis.

Firstly, I express my heartfelt appreciation to the University of Birmingham for granting me the opportunity and funding to pursue my PhD degree. This esteemed institution offers an excellent learning and research environment. I am also grateful to the Southern University of Science and Technology, where I conducted the primary research for this thesis.

Secondly, I would like to convey my sincere thanks to my esteemed supervisors: Prof. Peter R. Slater, Prof. Zhubing He, and Paul Anderson. Their visionary guidance and unwavering support have been instrumental in steering my research in the right direction. I especially want to acknowledge Prof. Peter R. Slater for his patient assistance throughout this thesis, including giving comments on writing and checking in language, spelling and grammar.

My profound gratitude also goes to Dr. Wei Chen, who took me under his wing as a young scientist with no prior experience in the field of perovskite solar cells. His vision and passion have been a

lifelong source of inspiration. I am deeply saddened by his passing due to cancer and will forever cherish the positive experiences I had with him.

I am deeply thankful for the extensive assistance provided by both current and former group members who aided in characterizing my research work and engaged in enlightening scientific discussions. I wish to acknowledge their contributions and name them as follows: Dr. Bo Dong, Dr. Elizebeth Driscoll, Dr. Jingwei Xiu, Dr. Binbin Yu, Dr. Zheng Do, Dr. Zhaoning Li, Dr. Qin Tan, Xusheng Zhang, Gangsen Su, Qiang Sun, Han Gao, Kaiyuan Liu, Hao Li, Jiafeng Wang, Dong He, Guoqiang Ma, Zeyu Niu, and Tianle Cheng.

Last but certainly not least, I extend my gratitude to my parents for their unwavering love and support throughout my life, especially during my PhD studies. Their encouragement has been an invaluable pillar of strength for me.

Table of Contents

1 INTRODUCTION 1

2 THEORIES AND BACKGROUND 8

2.1 Energy dilemma and renewable energy sources 9

2.2 Solar energy and solar cells 10

2.3 Perovskite solar cells (PSCs) 11

2.4 Perovskite crystals: structure, composition, properties, and preparation methods 22

2.5 Sustainability of PSCs 38

3 EXPERIMENTAL METHODS AND CHARACTERIZATIONS 46

3.1 Materials 47

3.2 Fabrication of perovskite solar cells 48

3.3 Materials characterizations 49

3.4 Optical characterizations of perovskite films 61

3.5 Device physics characterizations 64

3.6 Device performance and stability characterizations 69

4 COORDINATOR REPLENISHMENT STRATEGY IMPROVING PERFORMANCE OF $FAPBI_3$-BASED PSCS 73

4.1 Introduction 74

4.2 Experimental details 77

4.3 Interaction between coordinator and perovskite components 82

4.4 Study of crystallization dynamic of perovskite films 87

4.5 Film quality investigation 96

4.6 Amelioration of energy band alignment 104

4.7 Performance of PSCs 108

4.8 Device physics 110

4.9 Stability of PSCs 113

4.10 Conclusions 115

5 PREFERENTIAL COORDINATING SN IONS TO BALANCE THE CRYSTALLIZATION OF MIXED SN-PB PSCS 116

5.1 Introduction 117

5.2 Experimental details 120

5.3 Film quality analysis 123

5.4 Schottky contact at the top and bottom interface of TLP films 128

5.5 Performance and stability of PSCs 132

5.6 Device physics 137

5.7 Mechanism study of the suppression of the composition segregation 139

5.8 The primary reasons behind the improved stability 152

5.9 Conclusions 158

6 TEMPLATED-GROWTH PROCESS OF MIXED TIN-LEAD PEROVSKITE INDUCED BY SNF_2-2PEA ADDUCT 160

6.1 Introduction 161

6.2 Experimental details 164

6.3 Mechanism study: interaction modes and templated anchoring 167

6.4 Study of the film quality 173

6.5 Schottky contact 176

6.6 Performance of PSCs 179

6.7 Device physics 181

6.8 Conclusions 184

7 CONCLUSIONS AND FUTURE PROSPECTIVES 185

7.1 Conclusions 186

7.2 Future perspectives 188

LIST OF REFERENCES 192

List of Abbreviations

2AEPA ····· 2-(Aminoethyl)phosphonic acid
2PACz ····· [2-(9H-Carbazol-9-yl)ethyl]phosphonic acid
2PEAI ····· 2-phosphonoethan-1-aminium iodide
AFM ····· Atomic force microscopy
AFM-IR ····· Atomic force microscopy-infrared spectroscopy
AN ····· Acceptor number
BCP ····· Bathocuproine
CB ····· Chlorobenzene
CBM ····· Conduction band minimum
CR ····· Coordinator replenishment
DE ····· Diethyl ether
DHBABr ····· 3,4-Dihydroxybenzylamine hydrobromide
DMF ····· N, N-dimethylformamide
DMSO ····· Dimethyl sulfoxide
DN ····· Donor number
DSC ····· Differential scanning calorimetry
EA····· Ethyl acetate
EIS ····· Electrochemical impedance spectroscopy
EQE ····· External quantum efficiency
ETL ····· Electron-transporting layer
ETM ····· Electron-transporting materials
FA ····· Formamidinium ion, $CH(NH_2)_2^+$
FF ····· Fill factor
FTIR ····· Fourier transform infrared
FWHM ····· Full width at half maximum
GBs ····· Grain boundaries
GIWAXS ····· Grazing-incidence wide-angle X-ray scattering
HBA ····· Hydrogen bond accepting ability
HTL ····· Hole-transporting layer
HTM ····· Hole-transporting materials
ICP-MS ····· Inductively coupled plasma-mass spectrometer
IPA ····· Isopropanol
IR ····· Infrared
ITO ····· Indium doped tin oxide
KPFM ····· Kelvin probe force microscopy
LED ····· Light-emitting diode

List of Abbreviations

MA ····· Methylammonium ion, $CH_3NH_3^+$
MPP ····· Maximum power point
MPPT ····· Maximum power point tracking
MS ····· Mott-Schottky
NMR ····· Nuclear magnetic resonance
PB ····· Photobleaching
PCBM ····· Phenyl-C61-butyric acid methyl ester
PCE ····· Power conversion efficiency
PEA ····· Phenethylammonium
PEDOT:PSS····· Poly(3,4-ethylenedioxythiophene):polystyrenesulfonate
PL ····· Photoluminescence
PSCs ····· Perovskite solar cells
PV ····· Photovoltaics
SAMs ····· Self-assembled monolayers
SCLC ····· Space charge limited currents
SEM ····· Scanning electron microscopy
Spiro-OMeTAD ··· 2,2',7,7'-Tetrakis[N,N-di(4-methoxyphenyl)amino]-9,9'-spirobifluorene
SPO ····· Stabilized power output
S-Q limit····· Shockley-Queisser detailed-balance efficiency limit
TA ····· Transient absorption
TAS ····· Transient absorption spectroscopy
TCO ····· Transparent conductive oxide
TEL ····· Trap filling limit
TEM-EDS ····· Transmission electron microscopy-energy dispersive spectrometer
TGA ····· Thermogravimetry analysis
TLP ····· Mixed tin-lead perovskite
TLPSC ····· Mixed tin-lead perovskite solar cell
TMU ····· Tetramethylurea
TPC ····· Transient photocurrent
TPV ····· Transient photovoltage
TRPL ····· Time-resolved photoluminescence
UPS ····· Ultraviolet photoelectron spectroscopy
UV-vis ····· Ultraviolet-visible
VBM ····· Valence band maximum
WF ····· Work function
WH ····· Williamson–Hall
XPS ····· X-ray photoelectron spectroscopy
XRD ····· X-ray diffraction

List of Figures

Figure 2.1. Best Research-Cell Efficiency Chart maintained by National Renewable Energy Laboratory (NREL), presented with permission.[1] 13
Figure 2.2. Three types of structures of PSCs: a) n–i–p mesoscopic, b) n–i–p planar, and c) p–i–n planar structure. 14
Figure 2.3. Band theory of solid. Band structure of a) insulators, b) conductors, and c) semiconductors. 19
Figure 2.4. Band structures of a) intrinsic, b) n-type, and c) p-type semiconductors. 20
Figure 2.5. Energy band alignment of a p-i-n structured PSC and its working principle. 22
Figure 2.6. Crystal structure of cubic perovskites. Reproduced with permission.[46] Copyright 2014, Springer Nature. 23
Figure 2.7. a) Origination of S-Q limit. b) bandgap dependent S-Q limit (black line) and 75% and 50% of the S-Q limit (gray lines). Some representative PCE for some photovoltaic materials with various bandgaps are presented. Reproduced with permission,[13] copyright 2016 AAAS. 26
Figure 2.8. Bandgap of TLPs with various contents of Sn. Reproduced with permission.[12] Copyright 2017, American Chemical Society. 30
Figure 2.9. a) Perfect lattice and various types of intrinsic defects, including atomic vacancies, interstitials, and anti-site substitution defects.[71] Copyright 2021, John Wiley and Sons. b) Diagram of defect energy levels. Reproduced with permission.[72] Copyright 2020, the Royal Society of Chemistry. 32
Figure 2.10. Schematics of perovskite film preparation methods. a) One-step solution spin-coating method. b) Sequential two-step solution spin-coating method. c) Vapor deposition method. Reproduced with permission,[84] Copyright 2013, Springer Nature. 38
Figure 2.11. Proposed cyclic degradation mechanism of a tin iodide perovskite under ambient air exposure. Reproduced with permission.[93] Copyright 2021, Springer Nature. 42
Figure 3.1. Device structure of a) pure α-$FAPbI_3$ PSCs and b) TLPSCs. 49
Figure 3.2. Schematic of X-ray diffraction. 53
Figure 3.3. Fitting curves and standard deviations of the ICP-MS results of Pb and Sn standard solution. The point of 600 ppb with a large deviation was eliminated from fitting in both Pb and Sn standard solution. 60
Figure 3.4. Example equivalent circuit model for fitting of Nyquist plots. 66
Figure 4.1. (a) Chemical structure of DMSO and TMU. (b) Proposed interaction modes for FAI·PbI_2·DMSO and FAI·PbI_2·TMU adducts. 83
Figure 4.2. a) FTIR spectra of DMSO and its complexes with FAI and PbI_2. b) FTIR spectra of TMU and its adducts with FAI and PbI_2. c) FTIR spectra of FAI and its adducts with DMSO and TMU coordinator. d) FTIR spectra of FAI and its complex with various components, to real the effect of adding PbI_2 to FAI's adducts in b) and c). e) FTIR spectra of FAI and its mixtures with PbI_2, DMSO,

and both. f) FTIR spectra of FAI and its mixtures with PbI_2, TMU, and both. 84
Figure 4.3. a, b) TG analysis of a) the FAI·PbI_2·DMSO and b) the FAI·PbI_2·TMU adducts. c, d) DSC study of c) the FAI·PbI_2·DMSO and d) the FAI·PbI_2·TMU adducts. 86
Figure 4.4. Photographs of perovskite films fabricated using a) regular anti-solvent processing and b) coordinator replenishment strategy, both fabricated from the precursor with TMU as coordinator. 87
Figure 4.5. Study of crystallization dynamic of perovskite films based on different solvent coordinators. a) Schematics to illustrate the spin-coating process of perovskite films. b) Schematic of coordinator replenishment process. c) Schematic of the composition of adducts films. d) Schematic of the annealing process and energy barrier between adduct films and α-$FAPbI_3$. 88
Figure 4.6. SEM surface scanning of the a, b) perovskite films fabricated from precursors with a) DMSO and b) TMU as coordinator using diethyl ether as anti-solvent, and c, d) the perovskite films fabricated from the same precursors but with a certain amount of Lewis base adding into the anti-solvent (fabrication conditions were listed in **Table 4.2**). Photographs of the relative films were embedded. 90
Figure 4.7. Study of crystallization dynamic of perovskite films based on different solvent coordinators. a) Photographs of the as prepared adduct films aging for various time at room temperature. b) XRD patterns of the perovskite films of $FAPbI_3$ before and after annealing, and $MAPbI_3$. c) XRD patterns of adduct films aging for 30 min at RT. 92
Figure 4.8. Study of crystallization dynamic of perovskite films based on different solvent coordinators. a, b) In-situ GIWAXS patterns of d) control and e) TMU-CR perovskites. c-h) Representative 2D GIWAXS patterns of c-e) control and f-h) TMU-CR perovskite films during the annealing process. 93
Figure 4.9. a, b) 1D GIWAXS patterns derived from 2D GIWAXS patterns of intermediate adduct films at the beginning of annealing. c, d) 1D GIWAXS patterns derived from 2D GIWAXS patterns of intermediate adduct films at various time of annealing. 94
Figure 4.10. a, b) Top-view SEM images of the a) control and b) TMU-CR perovskite. c-d) Cross-sectional SEM images of the c) control and d) TMU-CR perovskite. AFM images of e) control and f) TMU-CR perovskite films. 97
Figure 4.11. a) UV-vis absorption (left axis) and PL (right axis) patterns of as prepared perovskite films. b) TRPL patterns of perovskite films. The fitting of the spectra was based on **Equation 3.2** and the average lifetimes were calculated through **Equation 3.3** as depicted in **Section 3.4.3**. 98
Figure 4.12. a, b) Ultra-fast TA analysis of the a) control and b) TMU-CR perovskite films deposited on quartz glass. The scale bar is the intensity of diffraction. c, d) 1D transient TA spectra at various decay time derived from the 2D Ultra-fast TA spectra of c) control and d) TMU-CR perovskite films. e) Normalized TA decays at 785 nm of 2D TA spectra, and their fitting curves. ΔA is the signal derectly obtained from the measurements, and it was the difference between the probe absorption $A(\lambda)$ obtained by irradiating the sample with the probe light minus the probe absorption $A_0(\lambda)$ obtained by directly exciting the sample with the probe light. 99
Figure 4.13. a) XRD patterns of as prepared perovskite films. b, c) 2D GIWAXS maps of the b) control and c) TMU-CR perovskite films. The scale bar is the intensity of diffraction. d, e) Azimuthal

angular intensity of the (100) plane integrated from the 2D GIWAXS patterns of d) control and e) TMU-CR perovskite films. f, g) Integral patterns of 2D GIWAXS patterns of f) control and g) TMU-CR perovskite films. 101
Figure 4.14. WH plots of the perovskite films. β_{hkl} is the value of FWHM of the relevant XRD peak. 103
Figure 4.15. Normalized 1D GIWAX patterns of the control and TMU-CR perovskite films in a) out-of-plane and b) in-plane directions. c) Tauc-plots of perovskite films. 104
Figure 4.16. UPS spectra of the a) perovskite films. b) NiOx and NiOx:2PACz as well as c) PCBM. d) Tauc-plot of PCBM derived from UV-vis absorption. 105
Figure 4.17. Energy band alignment at top and bottom interface of perovskite films in their PSCs. 106
Figure 4.18. a, b) KPFM images of the a) control and b) TMU-CR perovskite films. c) Line scans derived from the KPFM images at the axis of y = 2.0 μm. 107
Figure 4.19. a) Schematic of the structure of as prepared PSCs. b) J-V curves in reverse (solid line) and forward (dashed line) scans of champion PSCs under illumination (AM 1.5 G, 100 $mW \cdot cm^{-2}$). c) EQE (left) and their integral J_{sc} (right) patterns of the champion PSCs. d) SPO current density (left) and PCE (right) of unencapsulated PSCs at the voltage of maximum power point (MPP). e) Performance distribution for 30 devices of each set of devices. 109
Figure 4.20. a) Mott-Schottky plots of as prepared PSCs. b) Nyquist plots of PSCs measured at a voltage of 0.95 V near their MPP voltage. The equivalent circuit model for fitting was embedded. c) Plots of V_{oc}-Light intensity and their fitting curves, measured by scanning J-V curves under various light intensity (100 $mW \cdot cm^{-2}$ - 0.1 $mW \cdot cm^{-2}$). d) Dark J-V curves PSCs. e, f) SCLC patterns of e) eletron-only device and f) hole-only devices. g, h) TPV (g) and TPC (h) of PSCs.....111
Figure 4.21. a) PCE tracking of PSCs. The devices were unencapuslted and stored in dry box with humidity of ~20%. b) Normalized MPPT of encapsulated PSCs under continuous white LED light illumination at room temperature with a humidity of around 50%. The PSCs were encapsulated with glass and UV curing adhesive..... 114
Figure 5.1. Chemical structure of DHBABr and its electrostatic potential. 124
Figure 5.2. b-d) Top-view SEM images and e-g) surface AFM images, and g-i) cross-sectional SEM images of as prepared TLP films. 125
Figure 5.3. XPS F1s spectra of as prepared TLP films. 125
Figure 5.4. a) XRD patterns, b) UV–vis absorption spectra and c) Tauc-plot of the three TLP films. d) Steady-state and time-resolved PL (e) of the three TLP films exited from the top side. f) TRPL of control and DHBA-dop TLP films exited from the bottom side. The fitting of the spectra was based on **Equation 3.2** and the average lifetimes were calculated through **Equation 3.3** as depicted in Section 3.4.3. 127
Figure 5.5. UPS spectra of a) perovskites and b) PEDOT:PSS measured under a bias of -10V. ... 129
Figure 5.6. Device energy level diagram for the three TLPs. 130
Figure 5.7. Schematics of energy band bending at interfaces between ETL and c) Control, d) DHBA-dop and e) DHBA-dop+pas. All TLP films were fabricated on ITO/PEDOT:PSS substrates. 131
Figure 5.8. a) UPS spectra of the bottom surface of perovskite measured under a bias of -10 V. b-c)

Schematics of energy band bending at interfaces between HTL and a) control perovskite and b) DHBA-dop perovskite. 132
Figure 5.9. Inverted planar structure of as prepared TLPSCs with DHBABr passivation. 132
Figure 5.10. Photovoltaic performance and long-term stability of as prepared PSCs. a) J–V curves in reverse scans of champion PSCs under AM 1.5 G illumination (100 $mW \cdot cm^{-2}$). b) Performance distribution for 18 devices of each set of devices. c-e). J-V curves of thec) control, d) DHBA-dop, and e) DHBA-dop+pas devices in both forward (dashed line) and reverse (solid line) scaning. f) External quantum efficiency (EQE) of the champion device. g) SPO of an unencapsulated DHBA-dop+pas device at the voltage of maximum power point (MPP). h) Reverse-scan J–V curves of champion devices with active area of 1 cm^2, table of detailed parameters was embedded. 133
Figure 5.11. a). Average PCE tracking of six devices in each condition. The devices were unencapuslted, stored in glowbox with N_2 atmosphere, and scaned J-V curves in air atmorsphere. The error bars are sample standard deviations (n = 6). b) Normalized MPPT of devices (encapsulated) under continuous white LED light illumination at room temperature with a humidity of around 50%. The PSCs were encapsulated with glass and UV curing adhesive. The device was tracked after approaching its highest efficiency. 136
Figure 5.12. **Study of device physics**. a) Dark J-V curves of devices with an active area of ~0.15 cm^2. b) Plots of Light intensity dependent V_{oc} and their fitting curves. c) TPV of devices. d) SCLC of hole-only devices with a structure of ITO/PEDOT:PSS/TLP/Spiro-OMeTAD/Au, tested in dark. e) Mott-Schottky plots of devices. f) Nyquist plots of devices, with the equivalent circuit model inset. 137
Figure 5.13. a) Full-range and b) magnified FTIR spectra of DHBABr and TLP films with and without DHBABr deposited on KBr wafer. Content of DHBABr in perovskite was increased to 10% relative to A-site cation to pronounce the shift of peaks. 140
Figure 5.14. Study of the interactions between DHBABr and TLP components through a FTIR technique. a) magnified FTIR spectra of FAI, DHBABr and their mixture, deposited on KBr wafer. b) Magnified FTIR spectra of FAI, DHBABr, and their mixture in a molar ratio of 1:1, deposited on KBr wafer.c) magnified FTIR spectra of DHBABr, and its mixture with PbI_2 and SnI_2 in a molar ratio of 1:1, deposited on KBr wafer. 141
Figure 5.15. Study of the Interactions between DHBABr and TLP components through NMR techniques. a)^{1}H NMR spectra of DHBABr and its mixture with FAI, PbI_2, and SnI_2 in a molar ratio of 1:1, dissoved in DMSO d6. b) ^{1}H NMR spectra of DHBABr and its mixture with $PbBr_2$ and PbI_2 in a molar ratio of 1:1, dissolved in DMSO d6. c) ^{13}C NMR spectra of DHBABr and its mixture with FAI, PbI_2, and SnI_2 in a molar ratio of 1:1, dissolved in DMSO d6. 143
Figure 5.16. XPS spectra of a) Pb4f, b) Sn3d, and c) I3d of TLP films with and without DHBABr doping. 144
Figure 5.17. XRD patterns of a) $FAPbI_3$ without and with DHBABr doping and b) $FASnI_3$ without and with DHBABr doping, annealed for various time. c, d) XRD patterns of c) $FAPbI_3$ without and with DHBABr doping and d) $FASnI_3$ without and with DHBABr doping, eliminated from anti-solvent treatment and annealing. DHBABr doping was enlarged to 2% to magnify the phenomena. 146
Figure 5.18. Sn atomic proportion of B-site metal in 10 pieces of the control and DHBA-dop TLP

films, measured using ICP-MS. 147
Figure 5.19. a) Schematic of 12 regions divided for ICP-MS measurement. b) Distribution of Sn proportion in 36 areas in the Control and DHBA-dop films, tested witha ICP-MS instrument. c, d) Distribution of Sn proportion in the center, middle, and outer areas of c) Control and d) DHBABr-dop films, respectively. These data were measuredwith a ICP-MS instrument. 148
Figure 5.20. Depth dependent Sn/Pb ratio obtained from XPS depth profiles of a) the control and b) the DHBA-dop TLP films. Both were performed at a 500 μm spot within the position for device fabrication (Ag electrode deposition).The right y-axis refer to peak areas of In3d. The appearance of In3d signals means it was etched into the bottom of the TLP films. 150
Figure 5.21. TEM-EDS images of dispersed perovskite particles scraped from a) control and b) DHBA-dop TLP films. The particles are randomly selected. 152
Figure 5.22. AFM-IR images of the three TLP films surfaces, recorded with a feature absorption peak of DHBABr. 153
Figure 5.23. Schematic illustration of the distribution of $DHBA^+$ and its coordination with perovskite. 154
Figure 5.24. a) Photographs of PSCs aged in air in various time. b) XPS spectra of I3d scanned on the surface of electrodes in PSCs aging for 10 days. 155
Figure 5.25. Photographs of TLP films aged in air for various time. 156
Figure 5.26. a) Surface and cross-sectional SEM images of TLP films aged in air for 3days, with humidity at ~20%. b) UV-vis absorption spectra of fresh TLP films (dashed lines) and those aged for 3 days (solid lines). 157
Figure 5.27. XPS spectra of Sn 3d of a) Control, b) DHBA-dop, and c) DHBA-dop+pas films exposed to air for 2 h, respectively. 158
Figure 6.1. Chemical equation of the synthesis of 2PEAI. 165
Figure 6.2. Study of chemical interaction between 2PEAI and perovskite components using NMR techniques. a) ^1H NMR spectra of 2PEAI and its mixture with FAI, PbI_2, SnI_2, and SnF_2. b) ^{31}P NMR spectra of 2PEAI and its mixture with FAI, PbI_2, SnI_2, and SnF_2. c) ^{19}F NMR spectra of 2PEAI and its mixture with SnF_2. The mixtures were all prepared by dissolving 2PEAI and each perovskite component in a molar ratio of 1:1, with DMSO-d6 as solvent and its chemical shift as reference. 168
Figure 6.3. The proposed interaction modes between 2PEAI and perovskite components. 170
Figure 6.4. Study of chemical interaction between 2PEAI and perovskite components using XPS techniques. a) Pb4f XPS spectra of PbI_2 and its mixture with 2PEAI. b) Sn3d XPS spectra of SnI_2 and its mixture with 2PEAI. c) Sn3d XPS spectra of SnF_2 and its mixture with 2PEAI. d) F1s XPS spectra of SnF_2 and its mixture with 2PEAI. 172
Figure 6.5. Photographs recording the immediate color change from white to orange after adding 2PEAI powder to the incompletely dissolved SnF_2 solution. 173
Figure 6.6. a-f) Top-view SEM images of the a, c, e) control and b, d, f) target TLP films in various scales. g, h) Cross-sectional SEM images of the g) control and h) target TLP films in various scales. 174
Figure 6.7. AFM images of the control and the target TLP films. 175

Figure 6.8. a) XRD patterns, steady-state PL, and UV-vis absorption spectra of the control and target TLP films. 176
Figure 6.9. KPFM images of the a) control and b) target TLP films. c) Line scans derived from the KPFM images at the axis of y=1.5 μm..... 177
Figure 6.10. a) UPS spectra of the TLP films. b) Energy band alignment at top and bottom interface of TLP films in their TLPSCs. 178
Figure 6.11. J-V curves of the control and target TLPSCs. 180
Figure 6.12. **Study of device physics**. a) Dark J-V curves of devices with an active area of ~0.15 cm^2. b) Mott-Schottky plots of devices, recorded from 0V to 0.8 V, with a step size of 0.01 V. c) Nyquist plots of devices, measured in a bias of 0.5 V, with a frequency range of 1 Hz - 1×10^6 Hz. The equivalent circuit model was embedded. d) SCLC of electron-only devices with a structure of ITO/SnO_2/perovskite/PCBM:C_{60}/Ag, tested in a dark enviroment. e) TPV of devices. f) TPC of devices. 182

List of Tables

Table 2.1. Summary of compositions of perovskite and their corresponding bandgap. 27
Table 2.2. Summary of bandgaps ranges corresponding to Pb-based, Sn-based, and mixed Sn-Pb perovskite. 31
Table 4.1. Donor number (*DN*), acceptor number (*AN*) and hydrogen bond accepting ability (*HBA, β*) of DMSO and TMU. 83
Table 4.2. Fabrication conditions of the perovskite films in **Figure 4.6**. 90
Table 4.3. Fitting parameters of TRPL patterns of control and TMU-CR perovskite films. The TRPL spectra were fitted through **Equation 3.2** and the average lifetimes (τ_{ave}) of perovskite films were calculated via **Equation 3.3** based on the fitting fast-decay-time constant (τ_1) and slow-decay-time constant (τ_2). 98
Table 4.4. Fitting parameters of TA decays in **Figure 4.12e**. The TA spectra were fitted through **Equation 3.2** and the average lifetimes (τ_{ave}) of perovskite films were calculated via **Equation 3.3** based on the fitting fast-decay-time constant (τ_1) and slow-decay-time constant (τ_2). 100
Table 4.5. Average and standard derivation of photovoltaic parameters for 30 pieces of PSCs prepared from each method. The parameter η refers to PCE. 110
Table 4.6. The fitting parameters of the Nyquist plots according to the equivalent circuit model employed in **Figure 4.20b**. R_s, R_{rec}, and C refer to series resistance, recombination resistance, and capacitance, respectively. 112
Table 4.7. Fitting lifetimes from TPV and TPC of PSCs. τ_{TPV} and τ_{TPC} refer to average TPV lifetime and TPC lifetime, respectively. 113
Table 5.1. The ratios of F element on surface of TLP films comparing to Pb, Sn, and I elements integrated via XPS spectra of as prepared TLP films. 126
Table 5.2. Fitting parameters of TRPL that were stimulated from the front side. The TRPL spectra were fitted through **Equation 3.2** and the average lifetimes (τ_{ave}) of perovskite films were calculated via **Equation 3.3** based on the fitting fast-decay-time constant (τ_1) and slow-decay-time constant (τ_2). 128
Table 5.3. Fitting parameters of TRPL that were stimulated from the back side. The TRPL spectra were fitted through **Equation 3.2** and the average lifetimes (τ_{ave}) of perovskite films were calculated via **Equation 3.3** based on the fitting fast-decay-time constant (τ_1) and slow-decay-time constant (τ_2). 128
Table 5.4. Average and standard derivation of photovoltaic parameters. The parameter η refers to PCE. 134
Table 5.5. Fitting lifetimes from TPV of TLPSCs. τ_{TPV} refers to average TPV lifetime. 138
Table 5.6. The fitting parameters of the EIS plots according to the equivalent circuit model employed in **Figure 5.12f**. R_s, R_{rec}, and C refer to series resistance, recombination resistance, and capacitance, respectively. 139

Table 5.7. FWHM of static-state PL obtained by Gaussian fitting from patterns of **Figure 5.4d**.. 148
Table 5.8. The Sn proportion (%) in 10 individual perovskite particles of the Control and DHBA-dop TLP films. 151
Table 6.1. Detailed parameters of J-V curves in **Figure 6.11**. The parameter η refers to PCE. 181
Table 6.2. The fitting parameters of the EIS plots according to the equivalent circuit model employed in **Figure 6.12b**. R_s, R_{rec}, and C refer to series resistance, recombination resistance, and capacitance, respectively. 182
Table 6.3. Fitting lifetimes from TPV and TPC of the TLPSCs. τ_{TPV} and τ_{TPC} refer to average TPV lifetime and TPC lifetime, respectively. 184

Chapter 1

INTRODUCTION

This chapter will briefly introduce the framework of this thesis, presenting what content will be included in each chapter.

1. Introduction

It is predicted that electric consumption in the near future will grow exponentially.[2] However, the primary source of electricity generation presently relies heavily on non-renewable fossil fuels.[3] This escalating demand for electricity threatens to exacerbate the energy crisis, compounded by the associated environmental consequences such as increased CO_2 emissions, intensified greenhouse effects, and ecological disruptions. To combat these impending environmental challenges and the looming energy dilemma, a critical shift from fossil fuels to carbon-neutral renewable energy sources is imperative.

Inexhaustible solar energy has the potential to meet global energy demands.[4] The conversion of solar energy to electricity can be done by solar photovoltaic technology. In the last 50 years, research on solar photovoltaic technology has focused on silicon solar cells. Though silicon solar cells have achieved satisfactory power conversion efficiency (PCE), and the cost of their manufacture has been cut down by an order of magnitude in the last decade, they still suffer from several shortages. Firstly, the manufacturing process is complex, leading to relatively high costs.[5] Secondly, the manufacturing process involves environmentally harmful byproducts.[6] Finally, silicon solar cell panels are inflexible, limiting their application in a wide range of scenarios.

Third-generation solution-processing solar cells, like organic solar cells, dye-sensitized solar cells, and perovskite solar cells, exhibit great potential to address these issues.[7, 8] Their manufacture is pretty simple and cost-effective. Moreover, flexible solar cells can be produced easily through these

solution-processing techniques. However, most of these techniques face challenges in commercial application due to their relatively lower efficiency and operating stability. Among all these third-generation solar cells, the advanced perovskite solar cells (PSCs) in the last decade have demonstrated their great potential in commercial applications. Since PSCs were first produced in 2009,[9] their PCEs have experienced huge growth from 3.8% in 2009 to 26.1% in 2023, comparable to silicon solar cells.[1] Moreover, a lot of companies like Renshing Solar have begun building production lines and started trial production in 2023. These facts all suggest that PSCs are the most promising candidates for commercial applications in the near future. However, we cannot deny that PSCs are still facing some challenges that limit their up-scaling production, especially the lower PCE in large-scale devices and the degradation problem in air exposure.[10, 11] In this thesis, I aim to address some of the issues contributing to the PSCs community.

One of the merits of PSCs is that their optical bandgaps are tunable when their composition is regulated.[12] According to the theoretical Shockley-Queisser detailed-balance efficiency limit (S-Q limit), PSCs with a bandgap lower than 1.5 eV, which are called narrow-bandgap PSCs, are promising candidates to achieve high PCE approaching 32.7%.[13, 14] Pb-based PSCs presently are the most popular kind of PSCs that have achieved the certified record efficiency and exhibited the best long-term durability.[15] α-$FAPbI_3$ perovskite has a bandgap of around 1.5 eV, which is the narrowest bandgap among all Pb-based perovskites.[16] Therefore, it can be classified as a narrow-band perovskite and is one of the most promising candidates for fabricating PSCs to reach the S-Q efficiency limit. In

addition, mixed Sn-Pb perovskite (TLP) materials with a bandgap at around 1.25 eV are another kind of narrow-bandgap perovskites that have attracted increasing interest in recent years. Theoretically, perovskites with bandgap between 1.1-1.4 eV can absorb the most visible light and thus their PSCs become the most promising candidate to overcome the S-Q limit.[13, 14] Therefore, I have focused on narrow-bandgap α-$FAPbI_3$ based PSCs and mixed Sn-Pb PSCs in my experimental research, aiming to address parts of the problems suffered by these kinds of PSCs and achieve high-efficiency narrow-bandgap PSCs with superior long-term stability. Moreover, as high-quality perovskite films are the guarantee for PSCs to achieve high efficiency and long-term stability, while the crystallization dynamic of perovskite is the most critical factor that influences the quality of perovskite films, I aim to improve the film quality of a-$FAPbI_3$ and TLP by regulating their crystallization dynamics.

In Chapter 2, I will first introduce the background knowledge of PSCs and the theories that are essential for understanding the development of PSCs. I will begin by introducing solar energy and the utilization of clean energy. Subsequently, I will delve into metal halide PSCs, covering aspects such as their definition, historical context, architectural design, and operational principles. The chapter will also explore various theories related to perovskite crystals, encompassing discussions on crystal structure, relative tolerance factors, the impact of crystal composition on perovskite bandgaps, defects, and their connection to charge recombination. Additionally, I will examine the electrical properties of perovskites, including carrier mobility, lifetime, and charge diffusion length, with accompanying explanations. To enhance understanding, I will provide visual representations of

commonly used methods for preparing perovskite materials. Finally, I will address sustainability concerns, such as perovskite degradation, the toxicity associated with PbI_2, and the potential for toxic PbI_2 leakage.

Chapter 3 will provide an introduction to the experimental methods and characterization techniques employed in my research. These experimental methods encompass the origins or synthetic pathways of the materials utilized in my experiments, as well as the structure and manufacturing process of PSCs. Furthermore, I will delve into various characterization techniques, including materials analysis, optical properties assessment, device physics investigation, and device performance and stability evaluation. These techniques were used to explore aspects such as the quality, optical and electronic properties of perovskite films, semiconductor physics, the performance and stability of PSCs, and the mechanisms that explain the enhanced performance and stability of these solar cells.

In Chapter 4, I focus on preparing high-quality pure α-$FAPbI_3$ inverted PSCs. I propose an innovative coordinator replenishment approach by utilizing tetramethylurea (TMU) as a coordinating agent to optimize the nucleation and crystallization of α-$FAPbI_3$ perovskite. This technique effectively reduces the energy barrier for formation of α-$FAPbI_3$ crystals, resulting in improved film crystallinity, orientation, and photovoltaic performance. Consequently, the resulting PSCs exhibit a substantially increased PCE of 23.2%, accompanied with noteworthy enhancements in both open-circuit voltage (V_{oc}) and fill factor (FF). Besides, both encapsulated and unencapsulated devices demonstrate

enhanced long-term stability. The encapsulated device displays significantly improved operational stability, with a T_{80} lifetimes (the time when a solar cell decay from its initial PCE to 80% of its initial PCE) of 1000 hours under continuous 1-sun standard illumination. Additionally, the unencapsulated TMU-coordinated device retains 85.6% of its initial power conversion efficiency after being exposed to air for over 1500 hours. This advancement represents a significant stride towards achieving more efficient and stable inverted PSCs based on pure α-$FAPbI_3$.

In Chapter 5, my primary focus is on achieving a balanced crystallization rate of both Sn- and Pb-based components in mixed Sn-Pb perovskites (TLPs) during their anti-solvent treatment and annealing processes. This aims to address issues related to the segregation of their compositions and to create high-quality TLP films with a uniform distribution of Sn and Pb. I present a novel approach in which 3,4-dihydroxybenzylamine hydrobromide (DHBABr) is introduced into the TLP precursor solution. This strategy successfully resolves the critical challenges mentioned above. DHBABr is shown to form a stable amorphous intermediate complex involving FAI (formamidinium iodide), DHBABr, and SnI_2. This complex effectively slows down the crystallization rate of Sn-based perovskite, thereby achieving a balanced crystallization rate between Sn- and Pb-based perovskites. Consequently, the spatial distribution of Sn and Pb becomes more uniform across the entire TLP film, which is advantageous for scaling up the manufacturing process. The average Sn/Pb ratio is found to be 47.6:52.4, compared to the divergent control film with a ratio of 46.7:53.3, although it still falls slightly below the intended 50:50 ratio. By implementing this strategy, I achieved an exceptional PCE

of 22.44% in the champion device, with a V_{oc} of 0.853 V and FF of 80.0%. Additionally, the long-term operating stability of the devices was significantly improved. This enhancement in stability can be attributed to the strong coordination ability and reducibility of DHBABr, which inhibits iodide migration and the oxidation of Sn^{2+}, respectively. These factors contribute to the overall enhanced stability of the devices.

In Chapter 6, I continue to explore strategies to improve the crystallinity of the TLP films. I have introduced a more rational templated-growth anchoring approach to control the crystallization throughout the entire film. This approach involved the use of 2-phosphonoethan-1-aminium iodide (2PEAI) as an additive in a TLP precursor. It was observed that the 2PEAI additive primarily interacts with SnF_2, forming SnF_2-2PEA adducts, which optimizes the crystallization process by securely anchoring the perovskite components in the precursor through the amine and phosphate groups. As a result, I am able to produce TLP films with significantly improved crystallinity, better morphology, appropriate energy band alignment, and reduced defect density. The PSCs fabricated using this templated-growth process achieved a remarkable highest PCE of 21.95%, along with a V_{oc} of 0.84 V, J_{sc} of 33.18 $mA \cdot cm^{-2}$, and FF of 78.8%.

Lastly, in Chapter 7, I will summarize the primary conclusions of this thesis and propose potential avenues for future research.

Chapter 2

THEORIES AND BACKGROUND

This chapter will briefly introduce the theory and background of PSCs. This chapter will first introduce solar energy and the usage of clean solar energy. It will then introduce metal halide PSCs, including the definition, history, architecture, and working principles. Theories on perovskites, including crystal structure and relative tolerance factor, effects of crystal composition in the bandgap of perovskites, and defects and their relationship with charge recombination, will be introduced. The electrical properties of perovskites, including carrier mobility, lifetime, and charge diffusion length, will also be discussed. Widely used methods for perovskite preparation will be illustrated with schematics. Lastly, sustainability issues, such as degradation of the perovskite, toxicity of PbI_2, and leakage of toxic PbI_2, will be discussed.

2.1 Energy dilemma and renewable energy sources

According to the International Energy Agency's (IEA) "Net Zero by 2050" report in 2021, global electricity consumption is expected to exceed 50 trillion kilowatt-hours by 2050, which is 2.5 times the current consumption.[2] At present, a majority of the world's electrical energy is generated through the burning of oil, coal, and natural gas.[3] Therefore, the growing demand for electricity would lead to increasing consumption of these non-renewable fossil fuels, which ultimately leads to a severe energy crisis for humanity. Such a crisis is further exacerbated by environmental ramifications linked to fossil fuel overutilization, including heightened CO_2 emissions, amplified greenhouse effects, and subsequent ecological imbalances. To address the upcoming environmental issues and energy dilemma, it is urgent to convert fossil fuel energy sources for electricity generation to CO_2-neutral renewable energy sources.

CO_2-neutral renewable energy sources are comprised of wind energy, solar energy, hydroelectric energy, biomass energy, geothermal energy, ocean energy, and hydrogen energy. With growing efforts on the utilization of renewable energy sources, the proportion of renewable energy sources for global electricity generation reached 39% of the total worldwide electricity in 2022.[17] However, these mainly come from hydroelectric energy, which has limited capacity for growth. Therefore, it is necessary to further develop other promising renewable energy to replace the usage of fossil fuels.

2.2 Solar energy and solar cells

Among all renewable energy resources, solar energy, derived from the radiant light and heat of sun, is inexhaustible and the most available renewable energy source on Earth. It was estimated that the solar energy reaching the Earth daily is enough to meet the global population's energy needs for 27 years.[4] Therefore, solar energy is believed to be a pivotal solution in our quest for sustainable energy. According to the "Global Electricity Review 2023" reported by EMBER, solar energy occupied only 4.5% share of the total worldwide electricity generation in 2022, which means there is still plenty of room for growth in the utilization of solar energy sources.[17]

The conversion of solar energy into electricity is achieved by solar photovoltaic technology, namely solar cells. The first practical solar cell was developed in 1953 at Bell Labs[5] based on the principle of the photovoltaic effect discovered in 1839-1841.[18] Briefly, when exposed to light, the semiconductor in a solar cell absorbs the light energy (photons) and excites the electrons. The excited electrons are then collected by a n-type semiconductor, while the holes generated simultaneously are collected by a p-type semiconductor. The photocurrent is generated after the electrons and holes move forward to the electrodes and form a circuit.

Since the first invention of practical silicon solar cells,[5] solar cells have experienced over 70 years of development. A variety of types of solar cells were produced during this period. Generally, solar cells were categorized into three distinct generations based on their primary materials. The first-generation

solar cells are silicon solar cells which are produced since 1953. They consist of single-crystal, monocrystalline silicon (c-Si), and poly or multi-crystalline silicon (p-Si) solar cells, which own the merits of high-PCE and longevity. The silicon solar cells are the most mature technology and dominate the photovoltaic market so far. However, the production of silicon solar cells is expensive and involves environmentally harmful byproducts such as $SiCl_4$, $AsCl_3$, $AsCl_5$, and etc.[6] The second-generation solar cells are primarily composed of cadmium telluride (CdTe), gallium arsenide (GaAs), and copper indium gallium selenide (CIGS) thin-film solar cells. These types of solar cells are noted for their high PCEs and stable performance. Yet, their key materials contain toxic and/or rare elements, which limits their practical applications.[7, 8] The third-generation solar cells include PSCs and organic solar cells, which have attracted tremendous interest during the past decade due to their simple and low-cost manufacturing processes as well as their potential for PCEs approaching S-Q limits.[19-22]

2.3 Perovskite solar cells (PSCs)

2.3.1 Definition and history of PSCs

PSCs are a kind of thin-film photovoltaic (PV) or solar cell technology that utilizes perovskite materials to convert sunlight into electricity. PSCs are classified as the third generation of solar cells and have attracted increasing interest since this technology was first reported. This is attributed to their excellent light-absorption properties, long carrier lifetimes, facile tunability of their electronic bandgap, low-cost manufacturing procedures, and great potential for scale-up fabrication, making them ideal candidates for commercial solar cell applications.[23] Benefiting from these merits, PSCs

have become a groundbreaking innovation in the field of photovoltaics after only 14 years of development, offering a promising avenue for the development of highly efficient and cost-effective technologies for solar energy conversion.

Though the research on metal halide perovskite materials that are now applied as light absorbers can be dated back to a century ago, these materials were not recognized to be light-absorbing materials for photovoltaics until 2009, when Tsutomu Miyasaka and coworkers introduced methylammonium lead iodide ($CH_3NH_3PbI_3$) as the light-absorbing perovskite material and fabricated the first practical perovskite solar cell.[9] Although the PCE achieved in this first PSC was relatively low (approximately 3.8%), it was a remarkable leap forward compared to earlier attempts. Besides, this breakthrough marked a significant turning point in the history of PSCs.

Since then, the research field of PSCs has experienced exponential growth, with more and more researchers entering this field. Since the PCE of the first PCS is relatively low compared to other types of solar cells, like silicon solar cells, researchers have explored various strategies to improve the photovoltaic performance of PSCs. In 2011, Park and coworkers raised the PCE to 6.5% by depositing $CH_3NH_3PbI_3$ perovskite nanocrystals on crystalline TiO_2.[24] Later, they further improved the PCE to 9.7% by using spiro-MeOTAD as a hole transporting material and fabricated an the all-solid-state PSCs.[25] This was the first report of all-solid-state configuration of PSCs. This optimized configuration significantly improved the performance of PSCs and suppressed the degradation of the

perovskite absorber caused by the liquid electrolyte. By achieving PSCs with high efficiency and enhanced stability, this work set a foundation on future development for PSCs and significantly broadened the field.

Future progress on the performance of PSCs was achieved by exploring various hole and electron transporting materials, regulating the compositions and configurations of perovskite materials, and treatment on the interface of perovskite, etc.[26] Recently, a certified PCEs of 26.1% was achieved in the laboratory setting, as shown in Best Research-Cell Efficiency Chart (**Figure 2.1**) reported by National Renewable Energy Laboratory (NREL).[1] Throughout the years, researchers have also addressed challenges related to perovskite solar cell stability, toxicity relative to Pb-based perovskite, and scaling up production processes.[16, 27, 28]

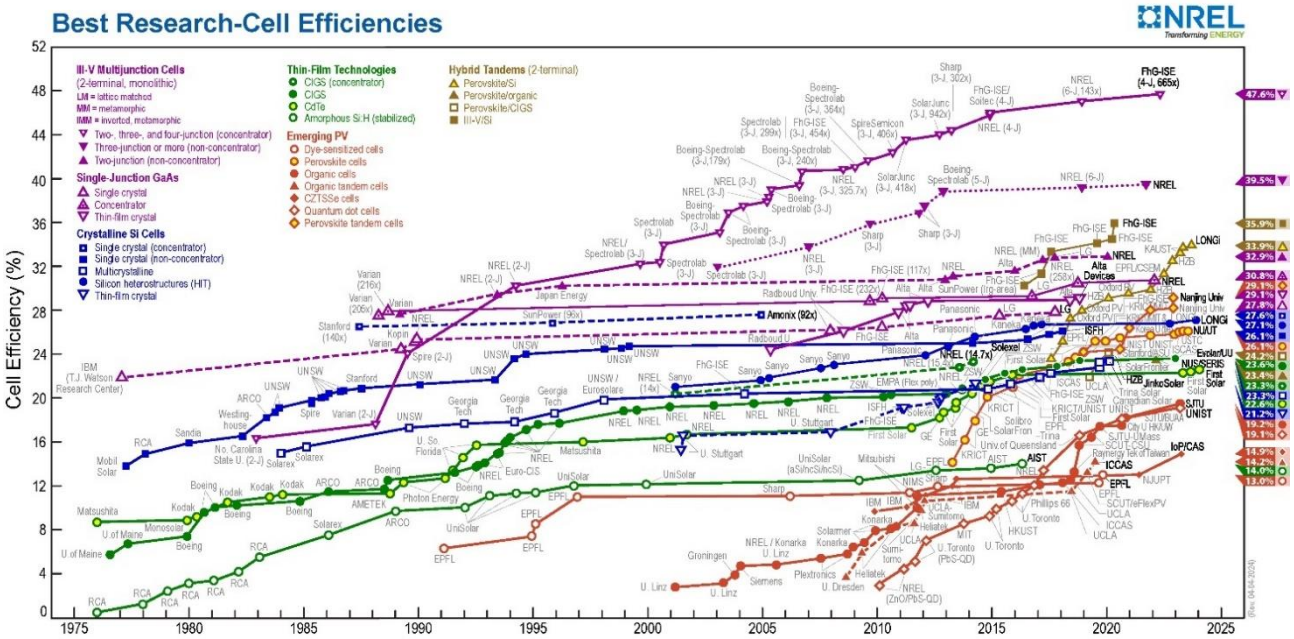

Figure 2.1. Best Research-Cell Efficiency Chart maintained by National Renewable Energy Laboratory (NREL), presented with permission.[1]

2.3.2 The architectures of PSCs

The architectures of PSCs can be categorized into two groups: regular n-i-p and inverted p-i-n structures, depending on the side location of hole-transporting layer (HTL) and electron-transporting layer (ETL) relative to the perovskite film. Moreover, the regular n-i-p structured PSCs can be categorized into mesoporous and planar structures according to the microscopic morphology of their ETL. Regular n-i-p PSCs with a mesoporous ETL were classified as n-i-p mesoporous structures, while those with a planar ETL were categorized as n-i-p planar structures. The inverted p-i-n PSCs, on the other hand, are usually in planar structures.[29]

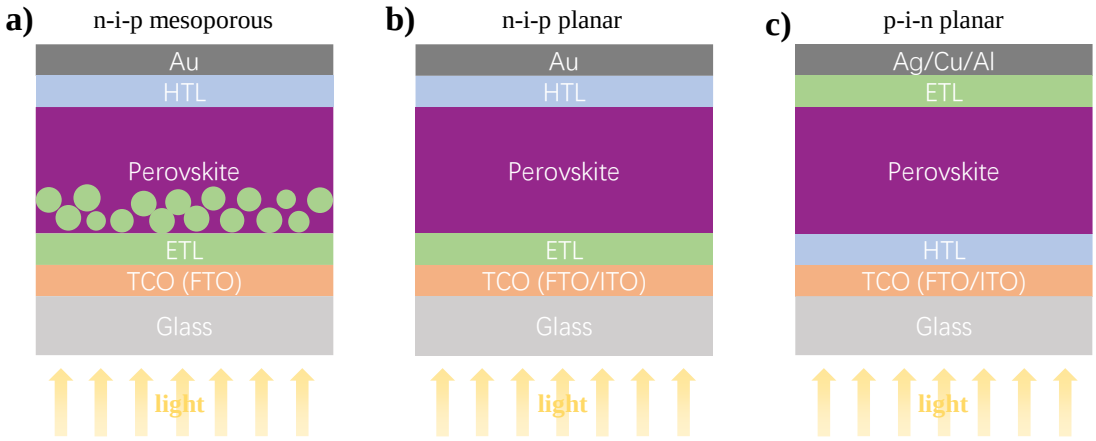

Figure 2.2. Three types of structures of PSCs: a) n–i–p mesoscopic, b) n–i–p planar, and c) p–i–n planar structure.

Specifically, in a regular n-i-p mesoporous PSC, a compact layer of titanium dioxide (c-TiO_2) was used as an ETL and was first deposited on the transparent conductive oxide (TCO) electrode. The assembly is followed by depositing of mesoporous TiO_2 (m-TiO_2), perovskite, HTL, and metal electrode (**Figure 2.2a**). This architecture originates from the production of the first particle PSC and

dominated the field in the early years of development due to superior charge extraction efficiency in such mesoporous structure.[9, 30, 31] However, processing such TiO_2 materials in PSCs requires high annealing temperature (~500°C), which is economically unfriendly. The n-i-p mesoporous structure fell in status after the discovery of highly efficient tin dioxide (SnO_2) as a planar ETL, which can be processed at a low temperature (<200°C).[32] m-TiO_2 was eliminated from the n-i-p architecture of PSCs after using SnO_2 as ETL (**Figure 2.2b**). Though planar n-i-p structured PSCs using SnO_2 as ETL showed more *J-V* hysteresis in the beginning of their use due to the inferior charge extraction at a planar interface, it has achieved considerable photovoltaic performance after years of optimization.[33-35]

In contrast to the regular n-i-p planar PSCs, the inverted p-i-n planar PSCs have an architecture with the HTL deposited on the bottom TCO substrate and with the ETL deposited on the top surface of perovskite, contacting with the top metal electrode (**Figure 2.2c**). As the investment of inverted p-i-n planar PSCs was much later than that of regular n-i-p PSCs, the progress on inverted PSCs has lagged behind that of regular PSCs prior to 2022.[27, 36] During this period, high-performance PSCs with PCE over 25% were primarily achieved by devices employing the n-i-p structure.[33, 37-39] Nevertheless, these devices faced a notable challenge in terms of stability due to factors such as degradation triggered by dopants in the HTL.[38] In addition, n-i-p structured PSCs necessitate expensive Au electrodes, which further limits their commercial application. On the contrary, inverted p-i-n structured PSCs demonstrate more advantages, including remarkable long-term stability, better

repeatability, negligible hysteresis, use of low-cost fabrication materials, suitability for use on flexible substrate, and, more importantly, suitability for integrating with p-type silicon bottom solar cells to form perovskite-Si tandem solar cells, which overcome the efficiency of S-Q limit.[1, 29] Considerable effort has been carried on inverted PSCs, and it is noteworthy that the progress of inverted PSCs has experienced a breakthrough in 2023, when the photovoltaic performance of inverted PSCs exceeded that achieved in regular n-i-p PSCs.[1, 40, 41]

2.3.3 Working principle of PSCs

The operation of PSCs is based on the formation of excitons and their transfer between the energy bands of each layer of semiconductors in a PSC. Before illustrating the working process, basic concepts on excitons, energy band theory, optical bandgaps, and light absorption phenomenon in a semiconductor will be introduced.

Excitons

An exciton is a bound state that forms when an electron and a positively charged hole are attracted to each other by the Coulomb force. As an electrically neutral quasiparticle, the excitons can travel through the lattice without any net transfer of charge. The excitons can form when an electron is excited from its usual energy state (valanced band) to a higher one (conduction band), leaving behind a positively charged hole in its original position. This phenomenon commonly occurs in insulators and semiconductors like halide perovskites when they absorb photons or other forms of energy,

leading to the creation of excitons.[42]

Based on the radius of the exciton and the magnitude of the coulomb force between the excited electron and the hole, excitons in solids can be divided into Frenkel excitons and Wannier-Mott excitons.[43] Frenkel excitons usually exist in materials with a relatively small dielectric constant, such as ionic crystals and aromatic molecules, which makes their electron and hole tightly bound together and difficult to separate. Such excitons have a typical binding energy of 0.1-1 eV. Wannier-Mott excitons exist in semiconductors with large dielectric constant. Such excitons have a relatively large radius compared to the lattice spacing, meaning the electron and hole are not tightly bound and can move over a large distance within the crystal lattice. The binding energy of Wannier-Mott excitons is usually much less than that of a hydrogen atom, typically on the order of 0.01 eV. As semiconductors, metal halide perovskites can produce Wannier-Mott excitons when absorbing photons, contributing to their excellent optoelectronic properties, making these materials highly promising for applications in solar cells, LEDs, and other devices.

Energy band theory and optical bandgap (E_g)[44]

Energy band theory is a fundamental concept in solid-state physics, which provides a theoretical framework for understanding the behavior of electrons in a crystalline solid, particularly in metals, semiconductors, and insulators. The principle of orbital conservation dictates that when two atoms form molecular orbitals, every interacting pair of atomic orbitals generates two molecular orbitals

(bonding orbital and anti-bonding orbital). In solid materials, including amorphous and crystalline solid, there's a large quantity of atoms, resulting in a correspondingly vast number of orbitals and closely clustered energy levels. This leads to the formation of an energy band comprising orbitals with similar energy levels that are continuous throughout the solid, different to the distinct energy levels observed in small molecules. These energy bands consist of valence bands and conduction bands. The valence band (VB) represents the highest energy levels that electrons can occupy at absolute zero temperature (0 K), whilst the conduction band (CB) refers to energy levels where electrons are free to move and participate in electrical conduction (**Figure 2.3**). Valence band maximum (VBM) and conduction band minimum (CBM), which are the highest energy level of valence band and the lowest energy level of conduction band, are crucial in the study of electron behavior in semiconductors. The energy different between the VBM and the CBM is so called a bandgap (E_g), representing the energy that an electron required to move from the VBM to the CBM. For amorphous solid materials, due to the lack of long-range periodicity, they do not have a well-defined bandgap, but possess a form of band structure characterized by broadened bands and a significant presence of localized states. For crystalline solid materials, they can be classified as insulator, conductor, and semiconductor according to the electron filling state of the bands (**Figure 2.3**). In materials with filled VBs and a great E_g, the electrons are hindered from movement and therefore, the material acts as an insulator with electrons are typically not delocalized (**Figure 2.3a**). In materials with partially filled orbitals, the boundary between the VBs and CBs becomes indistinct, and minimal energy is needed to elevate certain electrons to higher energy states within the band.

These materials are conductors, whose electrons are highly delocalized (**Figure 2.3b**). Some materials have bands that are entirely filled or completely empty, yet they differ from insulators in that their bands are very closely aligned in energy. These materials are semiconductors, which are the crucial materials in my research. Their electrons in VBs can be excited to CBs at higher temperatures or under photo illumination, and hence is delocalized, though less than that of conductors (**Figure 2.3c**).

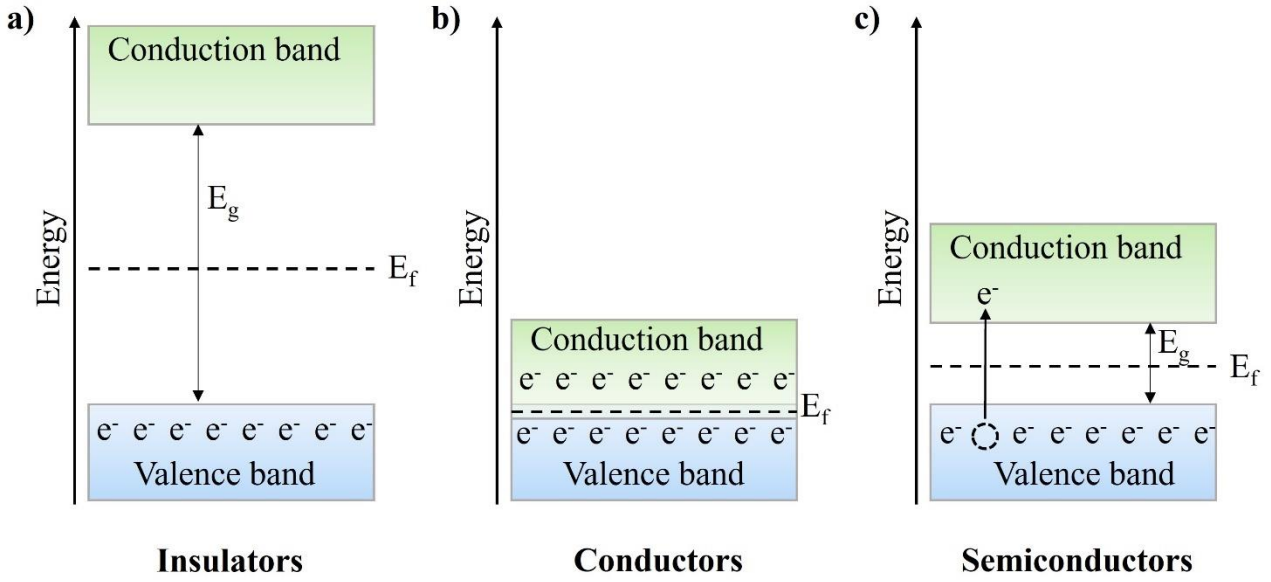

Figure 2.3. Band theory of solid. Band structure of a) insulators, b) conductors, and c) semiconductors.

Besides VBM, CBM and E_g, Fermi level (E_f) is another typically used concepts in the study of semiconductors. In a semiconductor, the E_f is between the VBM and CBM, and it is the energy level where an electron has an equal probability of being in either of the VBs and CBs (**Figure 2.3c**). The position of the Fermi level relative to the VBM and CBM determines the electrical and thermal properties of the material. For an intrinsic semiconductor, like perovskite, the E_f is in the center of

the E_g (**Figure 2.4a**). E_f in an n-type semiconductor is beyond the center of the E_g (**Figure 2.4a**), while that in a p-type semiconductor is below the center (**Figure 2.4a**). According to these theories, an n-type semiconductor is suitable for electron conduction and therefore, plays as an electron-transporting materials (ETM) in PSCs, whilst a p-type semiconductor is suitable for hole conduction and thus acts as a hole-transporting materials (HTM) in PSCs.

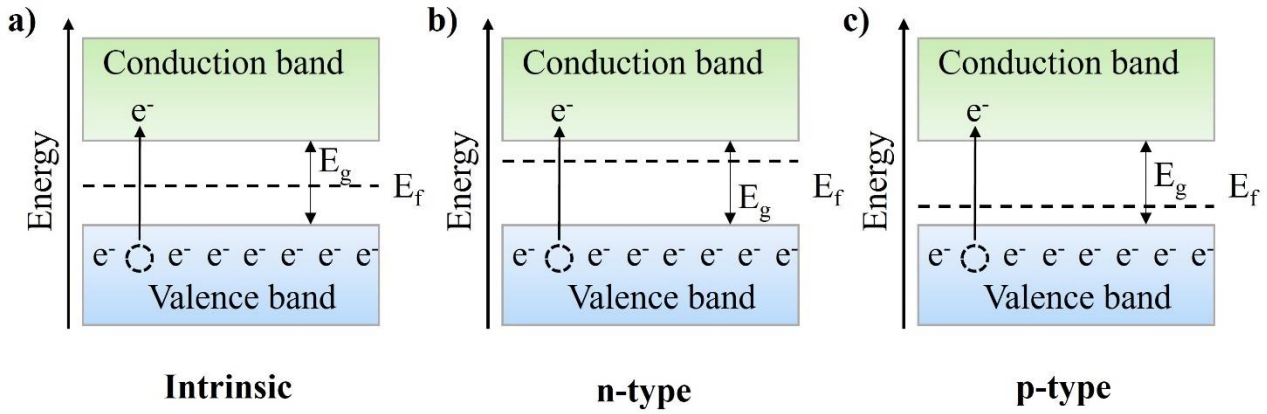

Figure 2.4. Band structures of a) intrinsic, b) n-type, and c) p-type semiconductors.

Absorption

The absorption of light is a fundamental process in semiconductors. In ideal semiconductors, the absorption occurs only when the energy of light exceeds their bandgaps. However, in real semiconductor, optical excitations are possible below the optical gap due to the existence of sub-bandgap states caused by defects, and other factors such as phonon-assisted transitions, interband transitions, and excitonic effects etc. Benefited from their narrow bandgap, semiconductors are able to absorb ultraviolet and visible light. In an absorption process, the electrons in the valence band are

excited to the higher-energy conduction band, leaving holes in the valence band. These exciton pairs can be transferred by charge-transporting materials, which is the key nature of perovskite materials. Alternatively, the exciton pairs can also recombine and result in light emission, which is so-called "photoluminescence".

Working principle

An inverted p-i-n structured PSC will be taken as an example here to illustrate the working mechanism of a PSC. **Figure 2.5** shows the energy band alignment of an inverted PSC, which helps to show the working process. Initially, the perovskite absorber is excited by the incident light (photons) to form exciton pairs at the top and bottom interface of the perovskite electron bands. The resulting electrons would be at the CBM energy level, while the hole would exist at the VBM energy level. Then, electrons at CBM would be detached with the holes and extracted from the perovskite surface to the ETL, forced by the electric field from the ETL to the perovskite surface. On the other side, holes at VBM would be captured by the HTL, forced by the electric field from the perovskite surface to the HTL. Lastly, the electrons and holes would be further transferred to the metal electrode and TCO eletrode respectively, which further forms a circuit to generate current.[45]

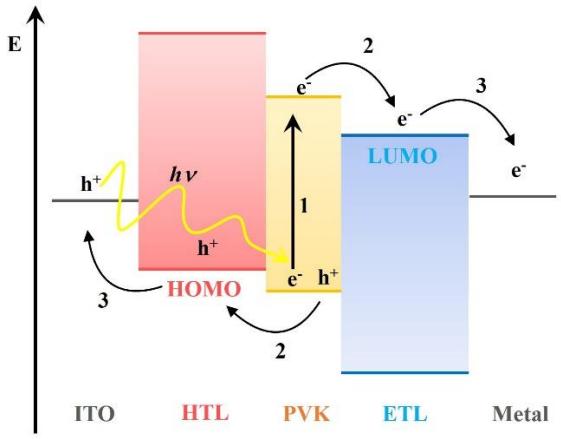

Figure 2.5. Energy band alignment of a p-i-n structured PSC and its working principle.

2.4 Perovskite crystals: structure, composition, properties, and preparation methods

2.4.1 Crystal structure and tolerance factor of perovskite materials

"Perovskite" is a term that was first used to describe the crystal structure of $CaTiO_3$. Later, with more and more compounds in the same crystal structure discovered, perovskite was used to describe various compounds with the same crystal structure as $CaTiO_3$. The absorber used in PSCs was determined to show such structure and, therefore, was called a "perovskite."

The chemical formula of perovskite materials used in PSCs can be shown as ABX_3, where A is a monovalent cation or divalent cation, typically an alkali metal or organic cation (e.g., Cs+, Formamidinium (FA^+), and methylammonium (MA^+)). B represents a divalent metal cation, typically a transition metal from group IV-A (e.g., Pb^{2+}, Sn^{2+}, Bi^{3+} and Ge^{2+}). X refers to a monovalent anion, typically a halide anion (e.g., I^-, Br^-, and Cl^-). As presented in the perovskite crystal structure shown in **Figure 2.6**, an ideal perovskite structure is cubic, where the A cation is located at the center of the

cubic unit cell, while BX_6 octahedra occupy the corners of the unit cell. In the BX_6 corner-sharing octahedron, the B-site metal cation occupies the center of the octahedra, while X halide anions are located at the corners, surrounding the B-site metal cation.

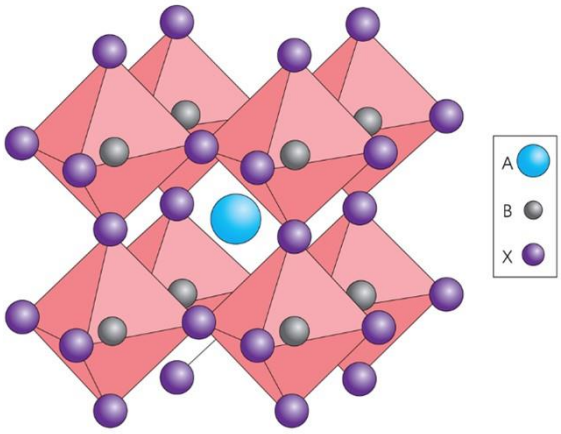

Figure 2.6. Crystal structure of cubic perovskites. Reproduced with permission.[46] Copyright 2014, Springer Nature.

Ideally, perovskites are in a cubic structure with a space group Pm-3m,[47] but in reality, they exhibit a pseudo-cubic or distorted cubic configuration.[46] The relative sizes of A, B, and X atoms have a significant effect on the configuration of perovskite. Ion size incompatibility of each site can lead to structure distortion and instability. Goldschmidt's tolerance factor, a dimensionless number that is determined by the ionic radii of all A-, B-, and X-site ions, is proposed as an indicator to determine the compatibility of a specific crystal structure.[48, 49] The Goldschmidt's tolerance factor follows the equation $t = \frac{(R_A+R_X)}{\sqrt{2}(R_B+R_X)}$, where R_A, R_B, and R_X refer to the ionic radii of A, B, and X, respectively. A stable perovskite structure is expected to have a tolerance factor from 0.8 to 1.0.[50, 51]

The crystal structure of perovskites is variable under different temperatures. Take $FAPbI_3$ provskite, which is the main perovskite materials studied in Chapter 3, as an example, it crystallizes into a yellow non-perovskite crystalline structure at room temperature (δ-phase), adopting a hexagonal lattice within the space group $P6_3mc$.[47] When crystallized at high temperatures, typically over 150°C, $FAPbI_3$ transforms into a black phase (α-phase) with cubic structure in the group space Pm-3m. However, this phase is thermally unstable and will gradually transit into α-phase under thermal, environmental, and light stressors.[52]

2.4.2 Compositions and tunable bandgap of perovskite materials

The $MAPbI_3$ and $MAPbBr_3$ perovskite were first used in PSCs.[9] However, perovskites with such compositions show poor stability and crystallinity due to the thermal instability of MA^+ and ion migration of I^-, leading to poor photovoltaic performance and stability of the PSCs. In addition, the toxicity of the Pb^{2+} metal ion also hinders the commercial application of PSCs. To address these issues, researchers have tried to partially or completely substitute the thermal unstable MA^+ with FA^+, Cs^+, etc.[53-56] The substitution of halide ions was also widely explored.[57, 58] All these efforts attempted to improve the crystallinity and structural stability of perovskite during the fabrication process, which, therefore, enhanced the performance and stability of PSCs. To deal with the environmentally unfriendly Pb^{2+} metal ion，researchers have tried substituting it with $Sn^{2+}$and Bi^{3+}, forming lead-free tin-based, mixed tin-lead, and bismuth-based perovskite.[59-61]

Besides the targets of improving crystallinity and stability as well as reducing the toxicity of perovskite materials, regulation in compositions of perovskite materials also has significant effects on the optical and electrical properties, especially the optical bandgap (E_g) of perovskite materials, which is a critical factor that directly affects the theoretical PCE that a PSC can achieve, according to S-Q limit.[13, 14] The S-Q limit is the highest theoretical efficiency of a solar cell utilizing a single p-n junction for power collection, calculated based on a series of assumptions and factors. These include that the solar cells are illuminated under standard solar spectrum without concentration, only one electron-hole pair is produced by one photon, the cell is in thermal equilibrium, the solar cell absorbs all photons with energy greater than the bandgap energy and none below it, and the only recombination mechanism is radiative recombination, etc. Taking these considerations into account, the S-Q limit was attributed to several parts of energy loss (**Figure 2.7a**). Firstly, light (photons) with energies lower than the bandgap of the absorber cannot be absorbed, leading to the waste of a lot of photons. Secondly, when light (photons) with energies higher than the bandgap is absorbed, the excitons proceed a quick relaxation to the band edge due to the high density-of-states near the band edges driven by the interaction with phonons. The excitons, therefore, lose excess kinetic energy by emitting phonons (knowns as thermalization) on a timescale of picoseconds. The above two parts are the main energy loss in a solar cell. Other energy losses include blackbody radiation and the loss caused by the lower the maximum-power-point voltage than the bandgap based on the diode principle. Taking these factors into account, absorbers with an E_g ranging from 1.1 to 1.4 eV were able to achieve the highest PCE (~33.7%) theoretically **(Figure 2.7b)**. In reality, however, energy may loss

due to the refection of light, non-radiative recombination, therefore, the PCE achieved in a sing-junction solar is impossible to reach the S-Q limit under normal sunlight intensity. Nevertheless, because the S-Q limit was proposed under the assumptions of single p-n junction and standard solar spectrum, this limit can be overcome by fabricating tandem solar cells and operating in a concentrated sunlight.

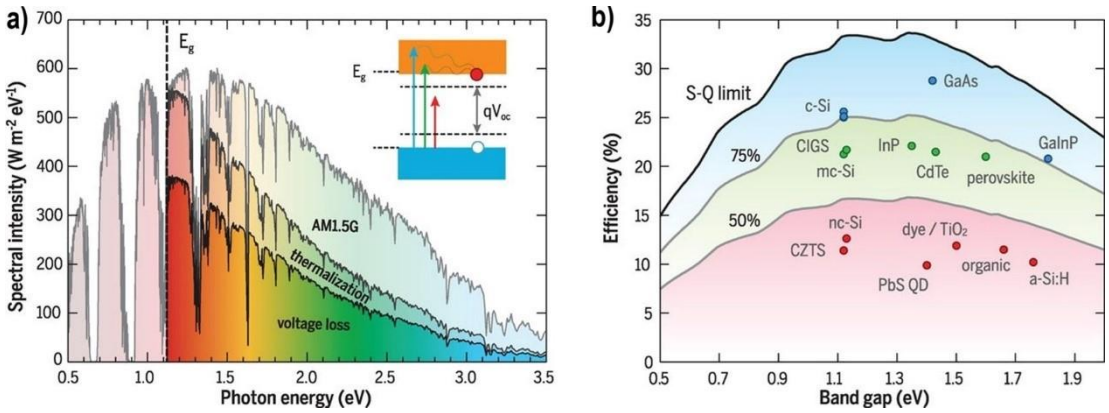

Figure 2.7. a) Origination of S-Q limit. b) bandgap dependent S-Q limit (black line) and 75% and 50% of the S-Q limit (gray lines). Some representative PCE for some photovoltaic materials with various bandgaps are presented. Reproduced with permission,[13] copyright 2016 AAAS.

To elucidate the relationship between the compositions and E_g of perovskite materials, herein, I classify the perovskite materials into three types, which are Pb-based perovskite, Sn-based perovskite, and mixed Sn-Pb perovskite, according to the variety of B-site metal cations in perovskite materials. As the first perovskite applied in PSCs is Pb-based $MAPbI_3$ perovskite, the Pb-based perovskite have attracted more attention and have been investigated for a more extended period compared to the other types of perovskite materials. Therefore, Pb-based perovskites are first taken as examples to clarify the effects of A-site and X-site modulation of perovskite materials on their E_g. The effects of B-site

regulation will also be discussed afterwards. The E_g of the examples discussed below are summarized in **Table 2.1**.

Table 2.1. Summary of compositions of perovskite and their corresponding bandgap.

Compositions	Bandgap (eV)	Ref.
$MAPbI_3$	1.57	16
$FAPbI_3$	1.48	16
$CsPbI_3$	1.73	62
$MAPbBr_3$	2.30	63
$MAPbCl_3$	2.90	64
$FASnI_3$	1.41	65
$FA_{0.7}MA_{0.3}Sn_{0.5}Pb_{0.5}I_3$	1.25	66

As mentioned before, the E_g of perovskite originates from the difference between the CBM and VBM of the perovskite materials, which are determined by their crystal symmetry.[46] Previous reports have demonstrated that the CBM is mainly determined by the Pb 6p orbitals, while the VBM affected by the strong antibonding character between the Pb 6s and X p orbitals.[67] Composition changes in each site of the perovskite crystal will alter the character of the atomic orbitals and thus affect the energy level of CBM and VBM, leading to the change of E_g.

A-site regulation

Taking $MAPbI_3$ perovskite as the initial sample, the A-site MA^+ can be partially or completely substituted with FA^+, Cs^+ and other cations. To simplify the discussion, only the situation in which MA^+ is entirely substituted with FA^+ and Cs^+ is considered. According to the above discussion, A-site cations do not directly impact both the CBM and VBM of perovskite materials. Yet, the change in size of A-site cations would vary the lattice spacing and the electron cloud overlapping of B-X orbitals and thus affect the band structure of the perovskite crystals. As the FA^+ cation is larger than the MA^+ cation, introducing the FA^+ cation into the A-site of the ABX_3 lattice would unquestionably result in a larger volume of the lattice and a longer B-X bond length. This, therefore, decreases the electron clouds overlapping of B-X orbitals and results in a lower E_g of 1.48 eV compared to 1.57 eV of $MAPbI_3$.[16] In contrast, substituting MA^+ with a smaller Cs^+ to form a $CsPbI_3$ crystal would lead to a higher E_g of 1.73 eV.[62]

X-site regulation

Substitution of the X-site I^- anion with Br^- and Cl^- anion would influence both the CBM and VBM of perovskite crystal significantly. As the CBM is predominantly affected by the Pb 6p orbitals, when the I^- anion is substituted with Br^- and Cl^- anions, the distance between Pb cations and X anions decreases due to the smaller radius of Br^- and Cl^- compared to I^-. This results in increased electron cloud density around the Pb atom and thus elevates the CBM of perovskite crystals. On the other hand, the VBM shifts downwards significantly because of the increased electronegativity and strength

of Pb-X hybridization. Consequently, the E_g significantly increases as a result of the upshift of the CBM and downshift of the VBM when X-site halide anions are substituted with the smaller-size Br^- and Cl^- anions. This is consistent with the significant increased E_g of 2.3 eV and 2.90 eV for $MAPbBr_3$ and $MAPbCl_3$ respectively, compared to 1.57 eV of $MAPbI_3$.[63, 64]

B-site regulation

As both the CBM and VBM are substantially influenced by the orbitals of the B-site metal cation, the E_g of perovskite crystals is significantly decreased when substituting Pb^{2+} with Sn^{2+}. The decrease of E_g is attributed to the different electronic structure of Sn^{2+}, specifically, the smaller electronegativity. Both VBM and CBM upshift, according to previous reports, but the upshift of VBM is larger than that of the CBM.[68] Consequently，the E_g decreases from 1.48 eV to 1.41 eV when Pb^{2+} in $FAPbI_3$ was substituted with Sn^{2+} to form $FASnI_3$. [16, 65] It is worth noting that the E_g of perovskite crystals can be continuously regulated by substituting Pb^{2+} with various contents of Sn^{2+} to form TLP compounds.[69, 70] As shown in **Figure 2.8**, the E_g of TLP is tunable between 1.2eV and 1.55eV.[12] By regulating the Sn proportion to the range of 20-90%, the E_g can be matched with the ideal E_g range of 1.1-1.4 eV according to the S-Q limit, which indicates great potential for TLPSCs to approach the efficiency of S-Q limit. However, it is worth noting that the bandgap of TLPs is non-linear to the ratio of Sn/Pb element and thus obey the Vegard's law, which is so called the "bowing effect". There are several hypotheses put forth in the literature. Kanatzidis et al. attributed this effect to competition between bandgap reduction as a result of spin–orbit coupling and bandwidth decrease due to the

lattice distortion.[69] However, Stevanovic's group disagreed with this hypothesis and they primarily ascribed the bowing effect to chemical effect like the energy mismatch of *s* orbital in Sn and *p* orbital in Pb, which determine the band edges of the TLP. Specifically, due to weak interaction between orbitals of Sn and that of Pb, the VBM was determined by Sn component while the CBM was acquired by the Pb component. This results in the decrease of the TLP's bandgap, making it smaller than that of either of the Sn and Pb-based perovskite.[70]

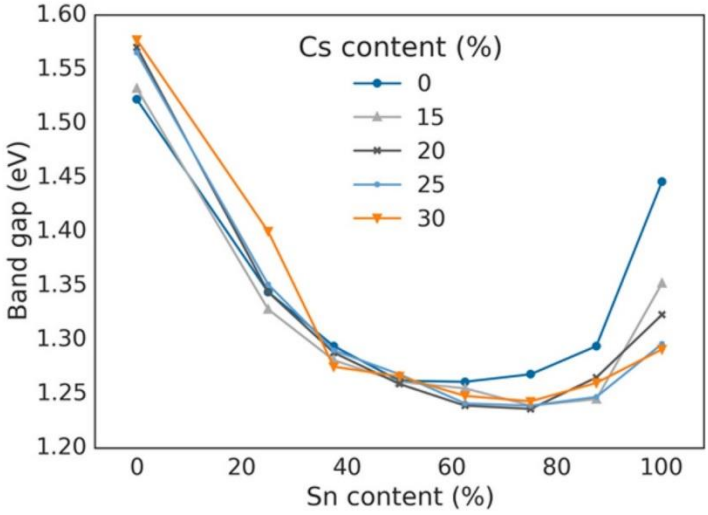

Figure 2.8. Bandgap of TLPs with various contents of Sn. Reproduced with permission.[12] Copyright 2017, American Chemical Society.

In summary, regulating perovskite composition will change the bandgaps of perovskites in various ranges, depending on the types of perovskites (**Table 2.2**). For Pb-based perovskites, the bandgaps vary in a range of 1.5-3.0 eV. For Sn-based perovskite, this range changes between 1.2 eV to 1.4 eV after regulating the A-site and X-site of the perovskite crystals. Regarding TLP, the bandgaps, ranging from 1.2 eV to 1.6 eV, are mainly dependent on the Sn/Pb ratios in perovskite crystal.

Table 2.2. Summary of bandgaps ranges corresponding to Pb-based, Sn-based, and mixed Sn-Pb perovskite.

Types of perovskites	Bandgap (eV)
Pb-based	1.5-3.0
Sn-based	1.2-1.4
Mixed Sn-Pb	1.2-1.6

2.4.3 Defects and charge recombination

The formation of defects is inevitable during the fabrication process of perovskite films owing to the fast crystallization and growth of the perovskite.[71] The defects in perovskite films can be classified as intrinsic defects and extrinsic defects.

Intrinsic defects are located in the bulk of perovskite, originating from atomic vacancies, interstitials, and anti-site substitutions, as illustrated in **Figure 2.9a**.[71] These intrinsic defects will results in the formation of a transition energy level within the bandgap area. As shown in **Figure 2.9b**, when the transition energy level is positioned close to the VBM or CBM, it refers to a shallow trap state, which will hinder the transfer of carriers. On the other hand, if such a transition energy level is located at the center of the bandgap, it is named a deep-level trap state. Deep-level trap states can act as recombination centers, leading to fast recombination in the perovskite films, which, therefore, reduce carriers' lifetime and decrease the photovoltaic performance of PSCs. [72]

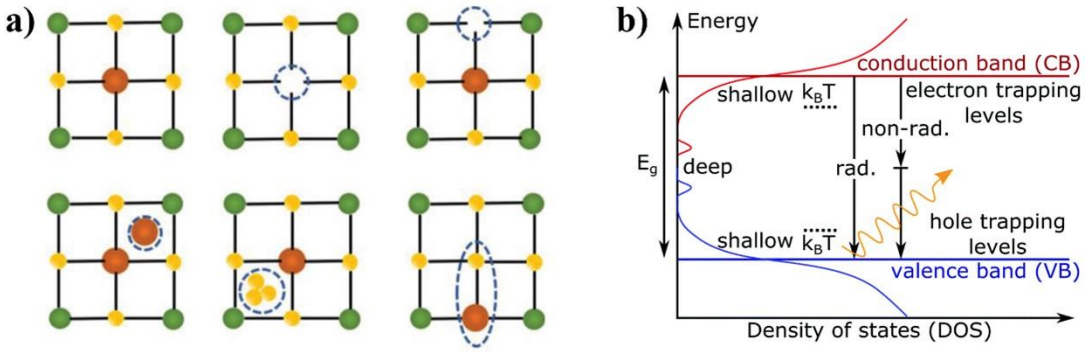

Figure 2.9. a) Perfect lattice and various types of intrinsic defects, including atomic vacancies, interstitials, and anti-site substitution defects.[71] Copyright 2021, John Wiley and Sons. b) Diagram of defect energy levels. Reproduced with permission.[72] Copyright 2020, the Royal Society of Chemistry.

The formation of extrinsic defects may be attributed to impurities in the starting materials and unintentional contamination of the solution used for film fabrication, etc. The extrinsic defects prefer to gather along the grain boundaries (GBs) and interfaces of perovskite films because of the presence of abundant dangling bonds and unfulfilled stoichiometry. The influence of extrinsic defects at GBs on the performance of PSCs is controversial. First principle calculation has suggested that trap states at GBs are benign, as they are unveiled to be low-level defect states.[73] This clarification was also supported by experiments, where the authors demonstrated that photovoltage along the GBs is higher than that at grain interior under illumination.[74] However, these conclusions were challenged by Ginger's group.[75] They demonstrated that perovskites with defects at GBs exhibit inferior photoluminescence intensity and lifetime decay, suggesting more serious non-radiative recombination.[75]

Different from defects at GBs, defects at the interface are undoubtedly harmful to the photovoltaic

performance of PSCs. As the interface is known as a bridge between the perovskite and the charge transporting materials, a good interface is vital for carrier extraction, transport, and to eliminate trapping. It was reported that defects-induced non-radiative charge recombination at the interface is 1-2 orders of magnitude to that in bulk and at GBs.[76] High densities of defects at the interface may cause significant non-radiative recombination, leading to loss of V_{oc} in PSCs and thus energy loss.[77] Additionally, defects at the interface will change the bandgap on the surface, leading to mismatch energy band alignment and, therefore, hindering the charge transfer.[71]

Besides negative effects on the photovoltaic performance of PSCs, both intrinsic and extrinsic defects in the bulk and at the surface of perovskite films facilitate the degradation of perovskite in the practical working environment. For example, the formation of Pb vacancy defects results in a MAI-terminal group, which was demonstrated to be highly hydrophilic and thus tends to be solvated by water molecules.[78]

2.4.4 Mobility, carrier lifetime, and diffusion length

The electrical properties of semiconductors, such as mobility, carrier lifetime, and diffusion length, are crucial parameters that reflect the quality of perovskite crystals and have an evident influence on the photovoltaic performance of PSCs. The electrical mobility, denoted as μ, characterizes the ease with which charge carriers (electrons and holes) move through a semiconductor material under the force of an electric field. It is typically expressed as $cm^2 \cdot V^{-1} \cdot s^{-1}$ and quantifies the speed of charge

carriers' response to an applied electric field. The carrier lifetime (τ) signifies the average duration a charge carrier remains in an excited state before recombination occurs. It plays a pivotal role in determining the overall charge transport and recombination dynamics in semiconductor materials. The diffusion length (L) represents the average distance that a charge carrier (electron L_e, hole, L_h) can travel before recombining with its counterpart (electron-hole recombination). It is a critical parameter determining the efficiency of charge collection in semiconductor devices.

The mobility, carrier lifetime, and diffusion length in perovskite films are highly dependent on crystal quality. Higher film quality and lower defect density lead to higher mobility, longer carrier lifetime, and longer diffusion length. In the early years, the quality of perovskite films was limited by the fabrication techniques and, therefore, exhibited inferior electrical performance. Over the decade, all mobility, carrier lifetime, and diffusion length of perovskite have been significantly enhanced along with the improvement of perovskite film crystallinity and morphology, benefiting from the boost of advanced deposition techniques.

The carrier mobility is mainly dependent on the morphology of perovskite films and does not show an evident relationship with the composition of the perovskite. In polycrystalline perovskite films, carrier mobility is usually below 40 $cm^2 V^{-1} s^{-1}$, while that in a single crystal perovskite was measured over 100 $cm^2 V^{-1} s^{-1}$.[79] This suggests that mobility is relative to the density of GBs or grain size of perovskite films.

2. Theories and Background

The carrier lifetime, which is characterized by time-resolved photoluminescence (TRPL), is the most commonly characterized parameter to estimate the quality of perovskite films. The carrier lifetime is substantially influenced by the non-radiative recombination process. Therefore, it is dependent on the defect density in the bulk and especially at the interface of perovskite films, which is the key factor that leads to non-radiative recombination. The carrier lifetime of perovskite films has been improved from hundreds of nanoseconds to several microseconds over the years.[15, 16, 80]

The diffusion length of a perovskite film determines the ability of carriers to transfer over the films in a vertical direction perpendicular to the substrate. Perovskite films with thickness over the diffusion length will suffer from serious recombination, as holes or electrons cannot transfer over the films and be captured by the hole-transporting materials or electron-transporting materials. Therefore, rationally designing film thickness based on the diffusion length of the perovskite is critical to achieving efficient PSCs. However, a thicker perovskite film results in a higher absorption of light, leading to increased current density of a PSC. Therefore, strategies should be proposed to improve the crystallinity of perovskite, suppress defect density in perovskite, and thus enhance the diffusion length of carriers. In this way, the thickness of perovskite films can be increased to improve light absorption without limiting the diffusion ability of carriers. The diffusion length of mixed Sn-Pb perovskite was improved to exceed 5 μm in recent years, which has allowed the authors to fabricate a perovskite film with a thickness of over 1.2 μm.[81]

In summary, the carrier mobility, lifetime, and diffusion length of perovskite are critical factors that affect the performance of PSCs. Therefore, when preparing a perovskite, the parameters should be rationally measured to estimate the film quality and then help improve the deposition techniques.

2.4.5 Perovskite films preparation

The preparation of high-quality perovskite films is essential for achieving optimal device performance. There are several methods for preparing perovskite films, and the selection of method relies on the particular application and desired film properties. These methods include solution processing methods and vapor deposition methods. The solution processing methods can be further categorized into spin-coating methods, spray-coating methods, and blade-coating methods.

Among all preparation methods, solution processing methods, in which the precursors are in the solution state, are widely used due to their low cost and easy processing properties. Solution processing spin-coating methods can be further divided into two categories, which are the one-step spin-coating method and the two-step spin-coating method. Snaith et al. first introduced the one-step spin-coating method to fabricate a $MAPbI_{3-x}Cl_x$ perovskite film in a regular structured PSC in 2012.[82] In this method, a perovskite precursor solution was first prepared by dissolving the lead halide salts and organic halides into a solvent (DMF and DMSO). The solution was then deposited onto a substrate using a spin coater. The substrate was then spun at high speeds accompanied by an anti-solvent dripping process to achieve uniform and thin perovskite films. The film is subsequently

annealed at a specific temperature to promote crystallization. The process is illustrated in **Figure 2.10a**. The one-step spin-coating method has the advantage of simple processing but requires an anti-solvent process, which is sometimes difficult to control. In 2013, Grätzel's group first fabricated $MAPbI_3$ perovskite through a two-step spin-coating method.[83] In a two-step spin-coating method, PbI_2 was first deposited on the substrate through a spin-coating process. After that, MAI was further deposited on the PbI_2 film. MAI will diffuse into the PbI_2 film during the annealing process. This process is illustrated in **Figure 2.10b**. The sequential two-step spin-coating method necessitates a reduced annealing time and is typically utilized in the production of solar cells with mesoporous structures because it encounters detachment issues when employed on planar PSCs.

These solution-based methods are cost-effective and only require a simple spin-coater. However, crystallization of perovskite in a solution processing method is difficult to control. In addition, the solution processing method shows limitations in up-scaling fabrication. As a consequence, vapor deposition methods have been proposed. In 2013, Snaith's group first reported a vapor deposition method to fabricate $MAPbI_3$ perovskite by evaporating PbI_2 and MAI to the substrate simultaneously (**Figure 2.10c**).[84]

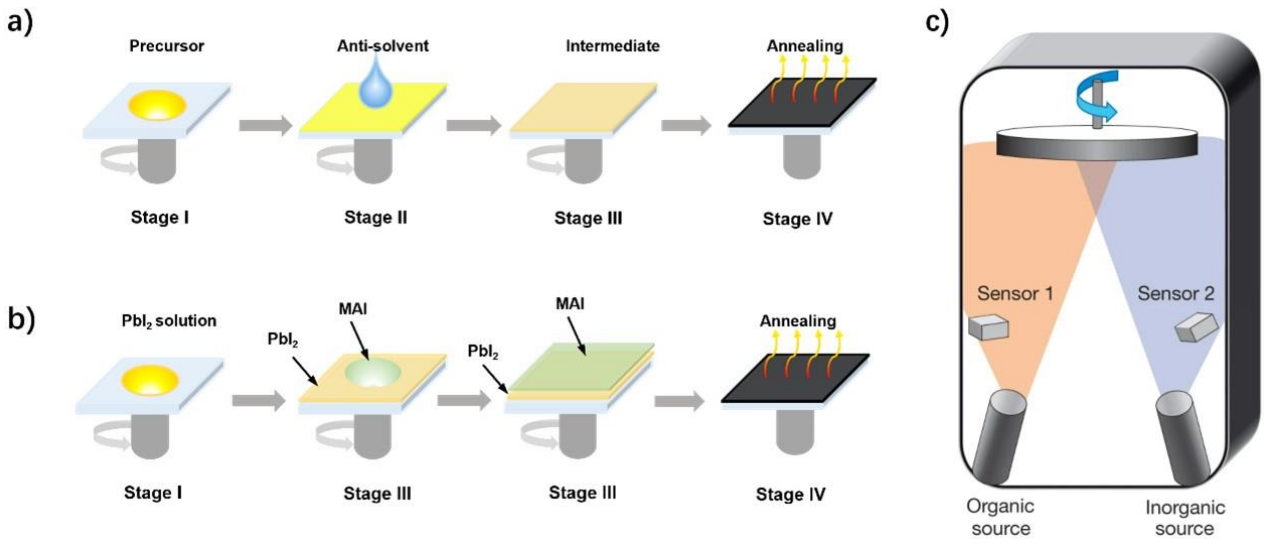

Figure 2.10. Schematics of perovskite film preparation methods. a) One-step solution spin-coating method. b) Sequential two-step solution spin-coating method. c) Vapor deposition method. Reproduced with permission,[84] Copyright 2013, Springer Nature.

2.5 Sustainability of PSCs

Recently, highly efficient PSCs with PCE over 26% have been produced in a laboratory.[1] However, there are still a lot of problems, especially the degradation of perovskite materials, toxicity and leakage of perovskite materials, and up-scaling fabrication, which are required by researchers to address when aiming to realize the commercial application of PSCs.

2.5.1 Degradation of perovskite materials

Based on the intrinsic nature of perovskite materials, PSCs are prone to stability concerns, which encompass ion migration, phase transition, component decomposition, and material evaporation. These issues can result in the degradation of perovskite materials, particularly when operating in conditions characterized by high humidity, high temperatures, and exposure to ultraviolet radiation.

For Sn-included perovskite, the high potential for oxidation of Sn^{2+} is another key factor that facilitates the degradation of Sn-based and TLP. The degradation mechanism of perovskites under each environmental condition will be discussed below:

High humidity

Moisture instability is derived from the sensitivity of A-site organic cations to moisture. Due to the hydrophilic properties of MA^+ and FA^+, these cations would dramatically interact with water molecules intruding into the interface or grain boundaries of perovskite, leading to a rapid reaction between A-site cations and H_2O and, thus, degradation of perovskite. Herein, $MAPbI_3$ perovskite is taken as an example to illustrate the fragmentation process of perovskite under high humidity. The fragmentation process is summarized as equations shown below.[85]

$$CH_3NH_3PbI_3(s) \leftrightarrow PbI_2(s) + CH_3NH_3I(aq) \quad (2.1)$$

$$PbI_2 \leftrightarrow Pb(g)+I_2(s) \quad (2.2)$$

$$CH_3NH_3I(aq) \leftrightarrow CH_3NH_2(g) + HI(aq) \quad (2.3)$$

$$4HI(aq) + O_2(g) \leftrightarrow 2I_2(s/l/g) +2H_2O(I) \quad (2.4)$$

$$2HI(aq) \leftrightarrow H_2(g) + I_2(s/l/g) \quad (2.5)$$

Firstly, water molecules from the surrounding environment are absorbed by perovskites due to their hygroscopic nature, which becomes the initiation of perovskite decomposition. The bond between

Pb^{2+} and MA^{+}, which is the key to maintaining the crystal structure of perovskite,[86] would then be easily destroyed by the high-polarity water molecules, leading to the decomposition of $MAPbI_3$ to PbI_2 and MAI (**Equation 2.1**). Then, PbI_2 and MAI further decompose under other environmental conditions, like heating (**Equation 2.2, 2.3**). The resulting methylamine will escape from the system by evaporation, while the remaining HI further decomposes into iodide and hydrogen gas (**Equation 2.4, 2.5**).

High temperature

PSCs are required to work under continuous strong sunlight illumination, which results in high-temperature exposure of the PSCs. So far, it is unavoidable for most of the high-performance PSCs to use MA^{+} as a part of the perovskite components to improve the quality of perovskite films,[15, 34, 40] but this leads the thermal decomposition of the perovskite. Bakulin and co-workers reported that at higher temperatures, A-site MA^{+} possesses the ability to rotate freely within the PbI_6 octahedral cages., indicating weak interaction between MA^{+} and PbI_6 cages.[87] The MA^{+} cations, therefore, suffer from decomposition and evaporation out from the perovskite crystal. Two decomposition pathways were proposed as shown in the below equations:[88, 89]

$$CH_3NH_3PbX_3(s) \leftrightarrow PbX_2\ (s) + CH_3NH_2\ (g) + HX\ (g) \qquad (2.6)$$

$$CH_3NH_3PbX_3(s) \leftrightarrow PbX_2\ (s) + CH_3X\ (g) + NH_3\ (g) \qquad (2.7)$$

Ultraviolet radiation

Exposure of PSCs to high-intensity ultraviolet radiation will also significantly accelerate the degradation of their performance. In the $MAPbI_3$ perovskite system, $MAPbI_3$ crystals or films will rapidly break down into methylamine, PbI_2, and I_2 when they are exposed to ultraviolet radiation, even in a dry environment at room temperature.[90] Decomposition induced by ultraviolet radiation is reported to be a photocatalytic process. Possible reactions in the decomposition process are presented in **Equation 2.8-2.15**.[91] Rappich et al. also reported that ultraviolet radiation-induced fragmentation of MA^+ would occur even without air exposure, though the reaction rate is relatively slower.[92]

$$2I^- \leftrightarrow I_2 + 2e^- \quad (2.8)$$

$$I^- + I_2 \leftrightarrow I_3^- \quad (2.9)$$

$$CH_3NH_3^+ + I_3^- \leftrightarrow CH_3NH_2 + I_2 + HI \quad (2.10)$$

$$O_2 + e^- \leftrightarrow O_2^- \quad (2.11)$$

$$CO_2 + e^- \leftrightarrow CO_2^- \quad (2.12)$$

$$O_2^- + 4CH_3NH_3^+ + 3e^- \leftrightarrow 4CH_3NH_2 + 2H_2O \quad (2.14)$$

$$CO_2^- + CH_3NH_3^+ \leftrightarrow CH_3NH_2 + HCO_2 \quad (2.15)$$

Oxygen exposure

For tin-containing perovskites, including Sn-based perovskite and mixed Sn-Pb perovskite, in addition to the above high humidity, high temperature, and ultraviolet radiation, oxygen in the air will

also have a significant impact on the degradation of these perovskites. The instability of tin-containing perovskite is attributed to the Sn^{2+} metal cation in the perovskite, which is easily oxidized to Sn^{4+}. As a result, the degradation of tin-containing perovskite initializes from the oxidation of Sn^{2+}, as shown in chemical **equation 2.16**. Once the SnI_4 forms after oxidation of Sn^{2+}, it facilitates the further decomposition of perovskite. A cyclic degradation mechanism of tin-containing perovskite is illustrated in **Figure 2.11**. Triggered by the oxidation product (SnI_4), the perovskite rapidly degrades into SnO_2, I_2, H_2O, and A_2SnI_6, which is a non-photoactive phase.[93] This severe oxygen exposure-induced degradation problem has produced a great barrier to the commercial applications of tin-containing perovskites.

$$2ASnI_3 + O_2 \rightarrow SnI_4 + SnO_2 + 2AI \qquad (2.16)$$

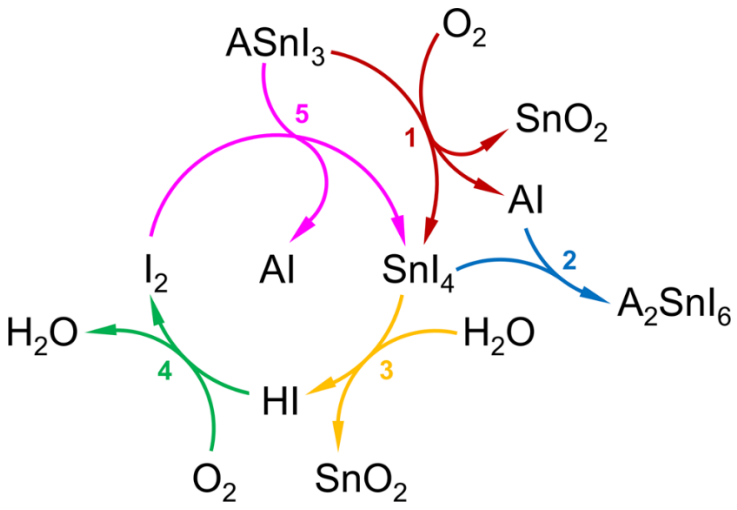

Figure 2.11. Proposed cyclic degradation mechanism of a tin iodide perovskite under ambient air exposure. Reproduced with permission.[93] Copyright 2021, Springer Nature.

2.5.2 Toxicity and leakage of perovskite materials

At present, Pb-based perovskite materials play an enormous role in achieving high-performance PSCs. However, once decomposed, the degradation products, including the organic cation, halide anion, and lead compound, will inevitably leak into the environment if no protection measures are taken, causing water and soil contamination. These leaked toxic Pb compounds could finally get into the human body through various ways, resulting in lead poisoning.[94]

Toxicity of Pb compounds

The toxicity of Pb elements and Pb compounds has been widely investigated. Upon entry into the body, lead initially enters the bloodstream and coordinates with blood cells, leading to an elevated lead concentration in the blood.[95] Diagnostic criteria for lead poisoning were established by the World Congress of Pediatrics in 1994. When a child's blood lead level surpasses 100 $\mu g \cdot L^{-1}$, it is classified as lead poisoning in children. For adults, a blood lead level exceeding 200 $\mu g \cdot L^{-1}$ is categorized as moderate lead poisoning.[96] In serious cases, lead poisoning will cause cancer. Lead toxicity arises due to its resemblance to essential biological ions like Ca^{2+}, Fe^{2+}, and Zn^{2+}. Consequently, Pb^{2+} can engage in competition with these vital cations for binding sites, disrupting their regular physiological functions and affecting numerous biochemical processes, including the inhibition of calcium and interaction with proteins.[97]

Strategies to prevent Pb leakage

During the decade, researchers have explored numberous strategies to address the toxicity issues of PSCs. These include methods avoiding or reducing the use of lead components in PSCs and encapsulation of PSCs.

Undoubtedly, the most efficient way to prevent Pb leakage is to avoid using Pb elements in PSCs. Therefore, researchers have widely explored alternatives to replace Pb^{2+} metal cations in perovskite crystals in the early years of the research on PSCs. These alternatives include tin (Sn^{2+}), germanium (Ge^{2+}), and bismuth (Bi^{3+}).[28] Among these alternatives, Sn^{2+} was determined to be the most promising one. Sn-based perovskites were first explored in 2012 when Kanatzidis and Shum's groups clarified that $CsSnI_3$ can be alternatively used as a light-sensitive absorber for dye-sensitized solar cells.[98] Later, they reported the first Sn-based PSCs in 2014, achieving a PCE of 5.73%.[99] In recent years, a highest PCE of 14.8% was achieved in a Sn-based PSC.[65] Partially substituting Pb^{2+} to give mixed Sn-Pb PSCs was also explored, which achieved a certified PCE of 23.8% in 2023.[100] However, These lead-free and lead-lean PSCs suffer from serious oxidation and degradation problems, resulting in poorer photovoltaic performance and long-term durability of the devices.[28]

Other methods have focused on the encapsulation of PSCs, preventing Pb from leaking out of the solar cell panels. The most direct encapsulation method is to cover the whole PSC panel with glass and resin, which is also a regular commercial method.[101] However, this method is not completely safe.

If the panels are broken, Pb leakage can still occur under various conditions like rain. To compensate for such deficiency, lead-absorbing encapsulation materials were investigated to replace the glass for encapsulation. These materials can effectively absorb Pb^{2+} ions through chemical coordination and thus suppress Pb leakage even if the panels are broken.[102-105] All these methods were demonstrated to suppress leakage effectively. However, none of them can guarantee 100% protection from leakage, and even a slight leakage is dangerous. Thus, the commercial application of PSCs still necessitates more effective strategies to prevent Pb leakage.

Chapter 3

EXPERIMENTAL METHODS AND CHARACTERIZATIONS

This chapter will first introduce the sources of chemicals and other materials that are used in my experiments. Then, the structure and fabrication process of PSCs, including a-$FAPbI_3$ PSCs in Chapter 4 and TLPSCs in Chapter 5 and Chapter 6, will be introduced. Lastly, this chapter will present the characterization methods, including materials characterization, optical characterization, device physics characterization, and device performance and stability characterization for characterizing materials, thin films, and PSCs. These characterization methods involve the study of the quality of perovskite films, optical and electronic properties of perovskite films, physics of semiconductors, especially the charge transporting nature in perovskite films as well as at the interface, photovoltaic performance and long-term stability of PSCs, and mechanism interpretation of the improved performance and stability of PSCs.

3. Experimental Methods and Characterizations

3.1 Materials

3.1.1 Purchased materials

Most of the chemicals and other materials used for PSC fabrication were purchased from suppliers. Unless otherwise stated, all purchased materials were used as received. The purchased chemicals include N, N-dimethylformamide (DMF), dimethyl sulfoxide (DMSO), and isopropanol (IPA), 1,1,3,3-tetramethylurea (TMU), diethyl ether (DE), poly(3,4-ethylenedioxythiophene):polystyrenesulfonate (PEDOT:PSS, AI4083, 1.3-1.7 wt.%), [2-(9H-Carbazol-9-yl)ethyl]phosphonic acid (2PACz), lead iodide (PbI_2), tin (II) iodide (SnI_2), tin fluoride (SnF_2), formamidinium iodide (FAI), methylammonium iodide (MAI), methylammonium chloride (MACl), phenethylammonium bromide (PEABr, 99.5%), 3,4-dihydroxybenzylamine hydrobromide (DHBABr), formamidinesulfinic acid (FSA), (2-Aminoethyl)phosphonic acid (2AEPA), bathocuproine (BCP), and phenyl-C61-butyric acid methyl ester (PCBM), and chlorobenzene (CB), hydroiodic acid (HI), nickel nitrate hexahydrate ($Ni(NO_3)_2{\cdot}6H_2O$), sodium hydroxide (NaOH), and dimethyl sulfoxide-d6 (DMSO-d6) etc. The chemicals used in the experimental works in Chapters 4-6 are slightly different. Detailed information is provided in each chapter.

Other materials include indium doped tin oxide (ITO) glass as a substrate for PSCs and ultraviolet curing adhesive for encapsulation of PSCs. Detailed information is provided in each relative chapter.

3.1.2 Self-synthesized materials

NiO_x nanoparticles were self-synthesized, according to previous report.[106] A detailed synthesis process is given in Chapter 4. 2-Phosphonoethan-1-aminium iodide (2PEAI) was synthesized from (2-aminoethyl)phosphonic acid (2EAPA) and hydroiodic acid. A detailed synthesis process is given in Chapter 6.

3.2 Fabrication of perovskite solar cells

In my experiments, both pure α-$FAPbI_3$ PSCs and TLPSCs were fabricated in an invert-structure (p-i-n) with the solution-processed method.[16, 66] For pure α-$FAPbI_3$ PSCs, the devices were fabricated to a structure of ITO/NiO_x/2PACz/Perovskite(α-$FAPbI_3$)/PEABr/PCBM/BCP/Ag (**Figure 3.1a**). For TLPSCs, the devices' structure is ITO/PEDOT:PSS/Perovskite(Sn-Pb)/DHBABr/PCBM/C60/BCP/Ag (**Figure 3.1b**). The perovskite layer is a photoactive layer, which produces excitons when illuminated under light. PEABr and DHBABr are passivation layers that passivate the defects on the surface of perovskite. The HTL (NiOx, 2PACz, and PEDOT:PSS) is responsible for hole extraction from the perovskite layer. The ETL (PCBM and C60) is responsible for electron extraction from the perovskite layer. BCP is a buffer layer that prevent damage of the ETL layer during the deposition process of metal electrode (Ag). It regulates the band alignment between ETL and metal electrode as well. ITO and Ag are electrodes on each side of the devices, which conduct the holes and electrons in each side to the circuit. The HTL, perovskite layer, perovskite passivation layer, and PCBM of the devices were deposited successively onto the substrate

with a spin coating method, while the C_{60} electron-transporting layer, BCP, and Ag electrode layer were deposited through a thermal evaporation method. The fabrication procedures of specific PSCs were varied in detail and thus are presented in the experimental section of each results chapter (Chapters 4-6).

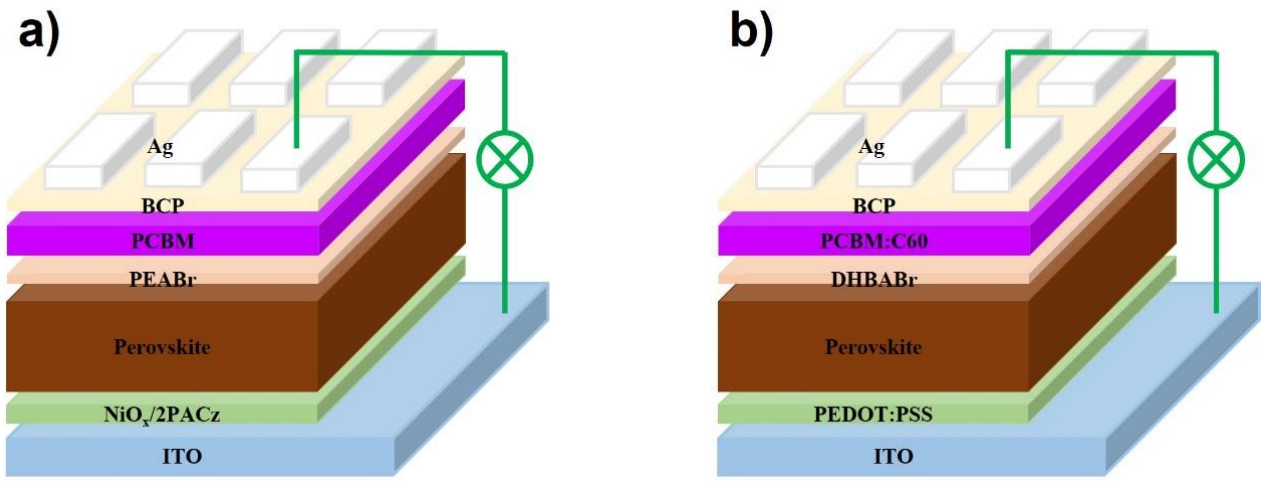

Figure 3.1. Device structure of a) pure α-$FAPbI_3$ PSCs and b) TLPSCs.

3.3 Materials characterizations

In this section, materials characterizations for morphology, crystal structure, composition, electronic structure, and crystallization dynamic study of perovskite films and their relative materials will be introduced. These characterization methods include scanning electron microscopy (SEM), atomic force microscopy (AFM), Kelvin probe force microscopy (KPFM), atomic force microscopy-infrared spectroscopy (AFM-IR), transmission electron microscopy-energy dispersive spectrometer (TEM-EDS), X-ray diffraction (XRD), grazing-incidence wide-angle X-ray scattering (GIWAXS), Fourier transform infrared (FTIR) spectroscopy, nuclear magnetic resonance (NMR), thermogravimetry

analysis (TGA), differential scanning calorimetry (DSC), X-ray photoelectron spectroscopy (XPS), ultraviolet photoelectron spectroscopy (UPS), inductively coupled plasma-mass spectrometer (ICP-MS), and Hall coefficient. Unless otherwise stated, the characterizations were performed by myself.

3.3.1 Scanning electron microscopy (SEM)

A SEM is an generally used imaging technique in material science that scan and produce microscopic images of sample surfaces in a high vacuum through utilizing a focused electron beam.[107] In my research works, SEM was used to scan both the top surface and cross-section of perovskite films and obtain microscopic images, which were critical for analyzing the surface and cross-sectional morphology of perovskite films. In my work, SEM images were measured using a HITACHI SU8230 instrument in a secondary electron mode. Electron beams with 3-5 kV accelerated voltage were used, accompanied by an in-lens detector.

3.3.2 Atomic force microscopy (AFM)

An AFM is an imaging technique that maps the surface of a material at the atomic level by sensing the force between the surface and a precise probe. This technology enables the detailed study of physical characteristics, including surface morphology at the nanoscale under atmospheric and even liquid environments.[108] In my research works, AFM was used as a tool to acquire the surface morphology and roughness of as prepared perovskite films, which is important for the analysis of the contact between perovskite film and electron transporting layer. In each experimental chapter, AFM

images with a 5*5 μm scope at a resolution of 256*256 data points were scanned using a MFP-3D-Stand Alone instrument (Asylum Research Abingdon-on-Thames, UK) under contact mode. The assessment of surface roughness was conducted by calculating the root-mean-squared roughness across the scanned area. The KPFM measurements were performed by Jiafeng Wang.

3.3.3 Kelvin probe force microscopy (KPFM)

A KPFM is a specialized form of AFM that measures the surface potential difference between a sample and a probe.[109] The Work function (WF) on the surface of the samples can, therefore, be calculated from the WF of the probe, which is usually Au, and the difference that was measured. This technique is widely used to analyze the electrical properties of surfaces at the nanoscale, providing insights into charge distribution and variations. In my works, KPFM was used as a method to analyze the homogeneity of electrical potential on the surface of perovskite films and as a supplementary technique to confirm the variation of WF between control and target perovskite films. The same instrument as AFM (MFP-3D-Stand Alone, Asylum Research Abingdon-on-Thames, UK) was used to scan KPFM images with a 5 *5 μm scale at a resolution of 256×256 data points. The KPFM measurements were performed by Jiafeng Wang.

3.3.4 Atomic force microscopy-infrared spectroscopy (AFM-IR)

An AFM-IR is a hybrid technique that combines AFM and infrared nanospectroscopy. This technique merges the nanoscale-resolution mapping power of AFM and the benefits of molecular-level analysis

of infrared spectroscopy. Therefore, it enables precise identification and mapping of organic chemical composition and distribution on a microscopic scale.[110, 111] In Chapter 5, AFM-IR was used to scan the surface of the TLP films and identify the distribution of DHBABr dopant on the surface of the TLP films. AFM-IR images in Chapter 5 were scanned with a nanoIR2 system (Anasys Instruments, Inc., Santa Barbara, CA, USA) in contact mode at ambient atmosphere. The IR images were recorded by detecting the characteristic stretching vibration of C=C in $DHBA^+$ at 1525 cm^{-1}. The AFM-IR characterization was performed by Xusheng Zhang.

3.3.5 Transmission electron microscopy-energy dispersive spectrometer (TEM-EDS)

A TEM is a powerful imaging technique that uses a high-energy electron beam that is transmitted through a specimen to examine thin samples (usually less than 100 nm thick), providing detailed internal structural and compositional information at the atomic or molecular level.[111] An EDS is a sophisticated analytical tool used in conjunction with electron microscopes, designed to analyze the elemental composition of samples by detecting X-rays emitted during electron beam interactions.[112] A TEM-ESD is a technique that combines TEM and EDS to analyze the elemental composition of samples at the nanoscale and produce images of elemental distribution. In Chapter 5, we scraped down perovskite films and dispersed the resulting perovskite powder into chlorobenzene to obtain nanoscale perovskite particles according to the method previously reported.[113] Then TEM-EDS was performed to analyze their elemental composition and reveal the homogeneity of Sn/Pb elemental distribution in mixed Sn-Pb perovskite films. TEM-EDS was performed using a Titan Themis G2 by

3.3.6 X-ray Diffraction (XRD)

XRD measurement is a powerful and widely used technique for characterizing the crystal structure of materials. It operates based on the diffraction phenomenon of light. Specifically, when a beam of X-rays strikes a crystalline material, it is diffracted in specific directions. This occurs because the layers of atoms in the crystal act like a diffraction grating, scattering the incoming X-rays in various directions. The X-ray scattering follows Bragg's law,[114] as shown in **Equation 3.1** and **Figure 3.2**:

$$sin\theta = \frac{n\lambda}{2d} \qquad (3.1)$$

where θ is the angle of diffraction, n is the order of diffraction, λ is the wavelength added, and d is the distance between atomic planes.

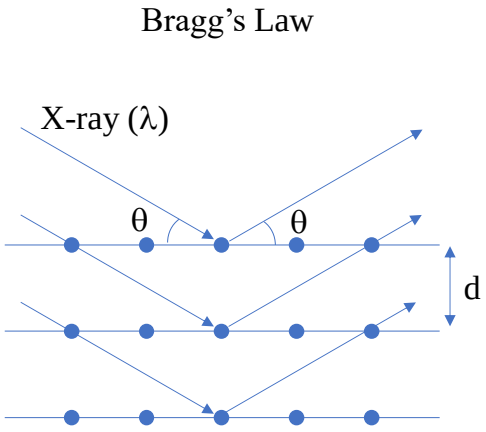

Figure 3.2. Schematic of X-ray diffraction.

By measuring the angles and intensities of these diffracted beams, XRD can provide a wealth of information about the crystal's structure, including the spacing of crystal layers, the size, crystallinity, and orientation of the crystallites, and imperfections or impurities in the crystal structure. In my research works, XRD measurements were performed to identify the impurities, crystallinity, and orientation of the perovskite films. In Chapter 4, XRD data were also used for the analysis of lattice strain in α-$FAPbI_3$ perovskite films according to the Williamson-Hall method.[115] In Chapter 4, XRD measurements were performed using a Bruker D8 Advance ECO diffractometer with Cu $K\alpha_{1,2}$ radiation (λ = 1.541 Å, 1kW). Diffraction patterns were measured within an angular range of $5° < 2\theta < 45°$ with a step size of $\Delta\theta = 0.02°$. In Chapters 5-6, XRD data were measured using a Rigaku Smartlab diffractometer with Cu $K\alpha_{1,2}$ radiation (λ = 1.541 Å, 9kW). The data were acquired from $10° < 2\theta < 40°$ with $\Delta\theta$=0.02°.

3.3.7 Grazing-incidence wide-angle X-ray scattering (GIWAXS)

GIWAXS is an advanced X-ray diffraction technique specifically designed for thin films and surface layers.[116] By directing X-rays to the sample at a very shallow angle, GIWAXS can analyze the crystalline structure and orientation of materials at or near the surface. Because the data acquisition of a GIWAXS technique is very fast (completed in seconds or even milliseconds per sample), GIWAXS measurements were widely used for in-situ monitoring of the crystal growth of perovskite films. In Chapter 4, GIWAXS measurements were performed to determine the crystallinity and orientation of as prepared perovskite films. Moreover, in-situ GIWAXS measurements during thermal

annealing were conducted to analyze the crystal growth dynamics of α-$FAPbI_3$ perovskite films. GIWAXS and in-situ GIWAXS experiments were performed at the BL14B1 beamline of Shanghai Synchrotron Radiation Facility (SSRF), Shanghai, China. The measurement was conducted using a Mar 225 detector under a beam energy of 10 keV (λ = 1.24 Å). The grazing-incidence angles were 0.5° for both GIWAXS and in-situ GIWAXS measurement.

3.3.8 Fourier transform infrared (FTIR) spectroscopy

FTIR spectroscopy is a qualitative technique used to acquire the infrared transmission spectrum of a material. This method works by applying a broad spectrum of infrared light to a sample and measuring the intensity of the light that is absorbed at different wavelengths. FTIR spectroscopy is highly effective for identifying organic materials by analyzing their chemical fingerprints.[117] In my works, FTIR spectroscopy was performed to study the interaction between additive and perovskite components by comparing the chemical shifts of infrared peaks of specific chemical groups before and after the mixing of the components. In all my works, FTIR spectra were measured using a Bruker Vertex v70 with transmission mode. The measurement was carried out at a range of 400 nm - 4000 nm^{-1}, with a wavenumber length size of 4 nm^{-1}.

3.3.9 Nuclear magnetic resonance (NMR)

NMR is an analytical technique used primarily in chemistry and biology to explore the chemical structure of organic molecules and inorganic compounds. NMR measurements are based on the

magnetic characteristics of certain atomic nuclei. When exposed to a specific frequency of radio waves in a magnetic field, these nuclei resonate and emit detectable radio signals. Information such as molecular structure, chemical environment of the molecule, and intramolecular and intermolecular interaction can be obtained by analyzing these signals.[118] As the chemical shift of a peak in the NMR spectrum of a molecule is influenced by the chemical environment, an NMR measurement can be used to identify the coordination mode of two or more molecules. By comparing the chemical shift of certain atomic nuclei in a single molecule and its mixture with other compounds, the interaction sites and strength of the coordinators can be identified. In Chapter 4, ^{1}H NMR measurements were performed to explore the interaction mode and the strength between the coordinators (DMSO and TMU) and perovskite components (FAI and PbI_2). In Chapter 5, ^{1}H NMR and ^{13}C NMR measurements were performed to analyze the interaction strength of DHBABr with FAI, SnI_2, and PbI_2. Solution NMR measurements with DMSO-d6 as solution and its chemical shift as reference were conducted on a Bruker Avance 400 spectrometer (400M).

3.3.10 Thermogravimetry analysis (TGA)

TGA is an analytical technique employed to track the variation in the mass of a material in relation to temperature or time under a certain atmosphere (air, O_2, N_2 or Ar gas). The data obtained from TGA can reveal information about the thermal stability, composition, decomposition temperatures, moisture content, and the amount of volatiles and fillers in the material.[119] In Chapter 4, TGA was performed to determine the evaporation temperature of DMSO from FAI-DMSO-PbI_2 mixture and

TMU from FAI-TMU-PbI_2 mixture, which can, therefore, reveal the interaction strength of DMSO and TMU with perovskite components in perovskite precursor and perovskite adduct films before annealing. TGA was performed under N_2-gas atmosphere with a TGA/DSC1 instrument (METTLER TOLEDO) at a heating rate of 2 $K \cdot min^{-1}$, beginning at 30 °C and ending at 400 °C. The measurements were performed by Xusheng Zhang and Zeyu Niu.

3.3.11 Differential scanning calorimetry (DSC)

DSC is a thermal analysis method employed to measure the heat flow absorbed or released during phase transitions or decomposition process of a material relative to the change of temperature or time. In this method, a sample and a reference are subjected to the same temperature regime while the heat need for keeping both of them at an identical temperature is monitored. Differences in heat flow can indicate phase transitions like melting, crystallization, glass transitions, and chemical reactions. In Chapter 4, DSC measurements were performed to evaluate the energy required to eliminate Lewis bases (DMSO and TMU) from their perovskite adducts by integrating the differential heat absorbed. The difference in interaction strength between DMSO and TMU and their perovskite adducts was therefore determined. DSC measurements were performed under N_2-gas atmosphere with a TGA/DSC1 instrument (METTLER TOLEDO) at a heating rate of 2 $K \cdot min^{-1}$, beginning at 30 °C and ending at 400 °C. The measurements were performed by Xusheng Zhang and Zeyu Niu.

3.3.12 X-ray photoelectron spectroscopy (XPS)

A XPS is a qualitative and quantitative technique utilized to determine the chemical state and elemental composition of a material.[120] XPS measurements rely on irradiation of a material when exposure to a beam of X-rays. Specifically, X-ray incidence will result in the release of electrons from the surface layer of a material, typically within the top 1-10 nanometers of the samples. Because the kinetic energy of an released electron reflects electron density in an atom, the XPS technique can be applied to study the role of passivators on the surface of perovskite films.[121] In addition, XPS can be used to determine the oxygen tolerance of a TLP film by analyzing the oxidation state of the Sn element. In Chapter 5, XPS measurements were conducted to reveal the interaction of the DHBABr dopant and passivator with SnI_2 and PbI_2 in TLP. Chemical states of the Sn element were also fitted from the XPS data to determine the stability of TLP films. XPS measurements were performed with a Thermo Fisher Scientific ESCALAB Xi+ with pass energy of 30 eV and a step size of 0.1 eV.

3.3.13 Ultraviolet photoelectron spectroscopy (UPS)

An UPS is a technique utilized to study the energy band structure of materials, particularly the valence band Fermi level of semiconducting materials.[122] In my research works, UPS measurements were performed to determine the work functions (Fermi level) and valence bands of each layer of semiconducting materials deposited in a perovskite solar cell. Conducting bands of the materials can be calculated from their valence band and band gap measured by Tauc-plot, which will be elucidated in 3.4.1. With the energy band structure of all layers in a PSC, we can analyze the charge transporting

barriers at the interface through analyzing the band alignment and then optimizing the semiconducting materials that were used. In all my works, UPS spectra were measured using an Thermo Fisher Scientific ESCALAB Xi+ instrument. A non-monochromated HeI α photon source (hν = 21.22 eV) was applied for measurement. Au is taken for calibration.

3.3.14 Inductively coupled plasma mass spectrometer (ICP-MS)

A ICP-MS is a highly sensitive and accurate analytical technique used to detect concentration of metals and several non-metals ions with very low detection limits.[123] In ICP-MS measurements, a high-temperature plasma source is used to ionize the sample, and then these ions are separated and detected based on their mass-to-charge ratio. In Chapter 5, ICP-MS measurements were performed to distinguish the Sn/Pb ratio in 12 positions of TLP films and thus evaluate their spatial homogeneity. ICP-MS measurements were performed using an Agilent 7700X. The perovskite solution samples were prepared as follows: First, perovskite powder was scraped down from the films and collected into a 4 ml vial. Then, the collected perovskite powder was digested with concentrated hydrochloric acid. Last, the resulting concentrated solution was diluted to around 10 ppm with 1%vol HCl solution. The standard solution of Sn and Pb was prepared to be 200 ppb, 400 ppb, 600 ppb, 800 ppb, 1000 ppb, 1500 ppb, and 2000 ppb. The standard deviation of the fitting curves of Sn and Pb standard solutions were 0.9998 and 0.9997, respectively (**Figure 3.3**).

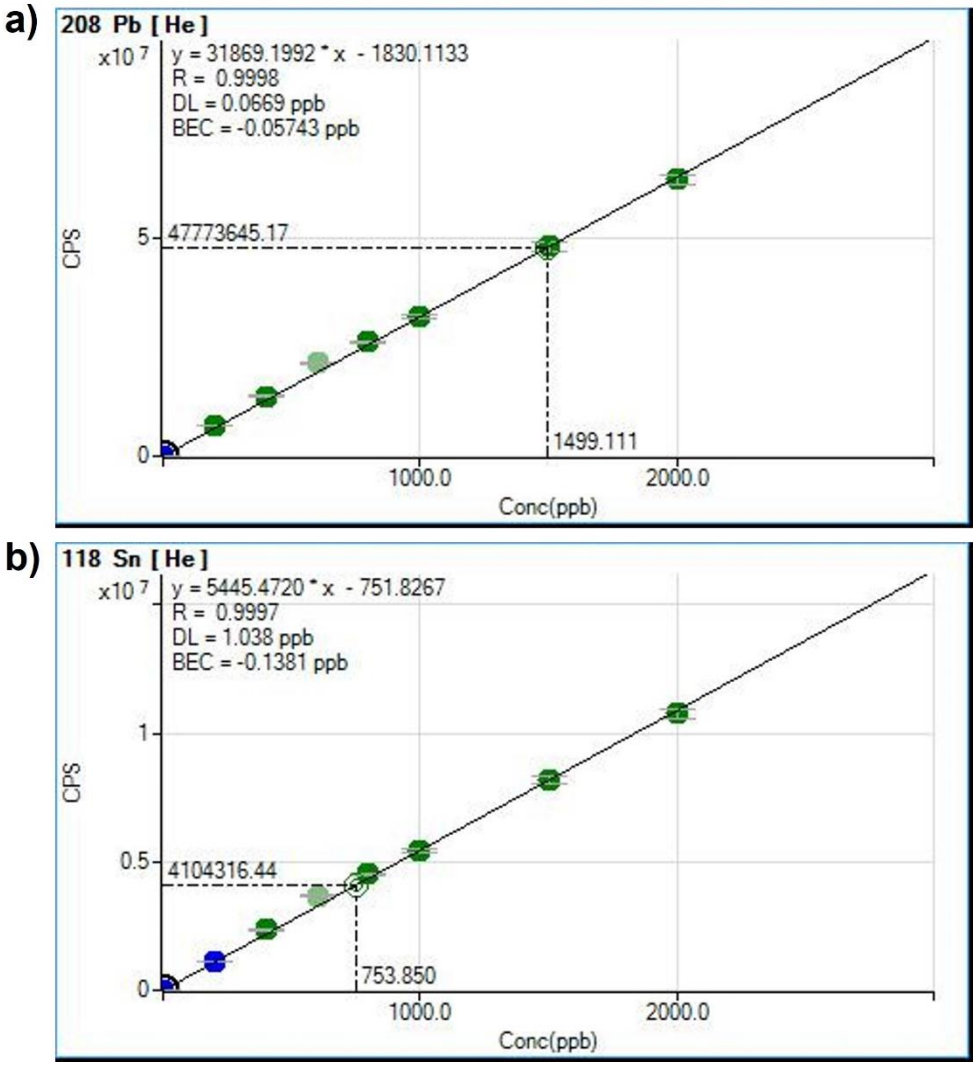

Figure 3.3. Fitting curves and standard deviations of the ICP-MS results of Pb and Sn standard solution. The point of 600 ppb with a large deviation was eliminated from fitting in both Pb and Sn standard solution.

3.3.15 Hall coefficient measurement

The Hall coefficient measurement is a method used in solid-state physics to determine the type, concentration, and mobility of charge carriers (electrons or holes) in a semiconductor or metal. This is achieved by placing a sample in a magnetic field and measuring the Hall voltage that develops perpendicular to both the current flow and magnetic field. The Hall Coefficient, derived from this

voltage, provides valuable insights into the characteristics of the material's charge carriers, helping in understanding its electrical properties and behavior under different conditions.[124] In my experiments, Hall coefficients were measured to confirm the semiconducting type of the perovskite layer that were evaluated by UPS methods in Chapter 5. Hall measurements were conducted in an ambient environment with a magnetic field strength of 0.5 Tesla, using a HL5500 instrument from Nanometrics Co. Ltd.

3.4 Optical characterizations of perovskite films

Optical characterizations were performed to study the optical and electronic properties of perovskite films. These characterizations include ultraviolet-visible (UV-vis) absorption spectroscopy, photoluminescence (PL), time-resolved photoluminescence (TRPL), and transient absorption (TA). All characterizations were performed by myself unless otherwise stated.

3.4.1 Ultraviolet-visible (UV-vis) spectroscopy

An UV-vis spectroscopy is an optical technique utilized to measure the absorbance of light in the ultraviolet and visible regions of the electromagnetic spectrum by a substance.[125] In my works, UV-vis spectroscopy was performed to evaluate the perovskite films' ability in absorbing light in both the ultraviolet and visible regions, which is a critical nature of perovskite materials in a high-performance PSC. In addition, the band gap of perovskite and other semiconducting materials can be determined by plotting Tauc-plots with the UV-vis absorption data.[126] UV-vis absorption measurements were

conducted with a Lambda 950 spectrometer, measured over a range of 1100 nm-400 nm with a step size of 1 nm.

3.4.2 Photoluminescence (PL) measurement

PL is a process in which a photoactive material is first excited to an excited state by absorbing photons, and then the excitons undergo a recombination process, resulting in light emission.[127] Steady-state PL measurement is a technique used to record the position and intensity of light emission, which can be used for analysis of the trap density in perovskite films.[128] In my works, PL measurements were performed using an FLS980 spectrofluorometer (Edinburgh instruments), with the sample excited under light wavelength at 405 nm provided by a laser.

3.4.3 Time-resolved Photoluminescence (TRPL) measurement

TRPL measurement is a technique that is widely applied to evaluate the lifetime of the excited state of a photoactive material, like perovskites.[129] The measurement is achieved by stimulating the sample with a pulsed laser and detecting the emitted light at different time intervals following the excitation. In Chapter 4, TRPL measurements were performed using an FLS980 spectrofluorometer with a standard detector, excited by a pulsed laser with a wavelength of 405 nm. In Chapter 5, the TRPL spectra were measured utilizing a FLS980E Fluorescence Spectrophotometer (United Kingdom), excited by a pulsed laser with a wavelength of 532 nm. The measurements were performed by Family of Master and Doctor Corp, China. The TRPL spectra were fitted through a biexponential function

(**Equation 3.2**) and the average lifetimes (τ_{ave}) of perovskite films were calculated via **Equation 3.3**.

$$y = y_0 + A_1\exp(-t/\tau_1) + A_2\exp(-t/\tau_2) \quad (3.2)$$

$$\tau_{ave} = (A_1\tau_1^2 + A_2\tau_2^2)/(A_1\tau_1 + A_2\tau_2) \quad (3.3)$$

where y and t represent the given value refer to intensity (y axis) and decay time (t axis), A_1 and A_2 are two fitting constants; τ_1, and τ_2 refer to the fitting fast-decay-time constant and slow-decay-time constant, respectively.

3.4.4 Transient absorption spectroscopy (TAS)

A TAS is a technique used to study the ultrafast dynamics of electronic and structural changes in molecules and materials following photoexcitation. In this method, a sample is first excited with a short pulse of light, creating an excited state. Then, a second pulse of light, typically of a different wavelength, probes the sample, then the change in absorption of this probe light is measured over time.[130] In Chapter 4, TAS measurements were conducted to measure the TA intensity and decay time, which reflect the carrier density and carrier lifetime in α-$FAPbI_3$ perovskite films. Perovskite films for TAS measurements were deposited on quartz glass. TA spectra were measured using a pump–probe spectrometer (TA-100, Time-tech spectra) and were illuminated on the top surface with a 400 nm pump. Similar to TRPL, the TA spectra were fitted through **Equation 3.2**, and the average lifetimes (τ_{ave}) of perovskite films were calculated via **Equation 3.3**.

3.5 Device physics characterizations

In this section, characterization methods for studying the physics of semiconductors, especially the charge-transporting nature in perovskite films and at the interface will be presented. These characterization methods include the dark current density-voltage (J-V) measurement, light intensity dependent open circuit voltage, electrochemical impedance spectroscopy (EIS), Mott-Schottky, Space charge limited currents (SCLC), transient photovoltage (TPV) and transient photocurrent (TPC), and external quantum efficiency (EQE). All characterizations were performed by myself, otherwise specified.

3.5.1 Dark current density-voltage (J-V) measurement

Dark J-V measurement is a technique used to measure the current that flows through a photovoltaic device under an applied voltage in the absence of light. The dark J-V curves provide valuable insights into the characteristics of the device, such as diode quality, leakage currents, and defects-dependent recombination mechanisms within the material.[131] In my works, dark J-V measurements were performed by applying a range of voltages and recording the corresponding current under a dark environment. The dark J-V curves were plotted to compare the defect density in perovskite films and at their interface. The measurements were performed using a Keithley 2400 instrument in an ambient and dark environment (~20 ºC and ~60% RH).

3.5.2 Light-dependent open-circuit voltage measurement

The V_{oc} of a solar cell varies under different light intensities. By recording the V_{oc} of PSCs exposed to different light intensities, we can plot light intensity-V_{oc} curves. Consequently, an ideality factor (n) can be calculated through the following diode equation:[132]

$$V_i = V_0 + \frac{nK_BT}{q} ln \frac{P_i}{P_0} \qquad (3.4)$$

where P_0 represents the initial light intensity (100 mW·cm^{-2}) for the J-V curve measurements, while P_i represents various light intensities lower than 100 mW·cm^{-2} for J-V curve scanning. V_0 and V_i refer to the measured V_{oc} at P_0 and P_i, respectively. n is the ideal factor that was intended to be calculated, K_B is the Boltzmann constant, T is the absolute temperature of devices when measured, and q is the elementary charge. A smaller ideal factor indicates a reduced level of trap density in the PSCs.[133] Therefore, light-dependent V_{oc} measurements are crucial for assessing the quality of the photovoltaic material and the solar cell design. In my works, light-dependent V_{oc} was measured by scanning J-V curves under various light intensity, ranging from 100 mW·cm^{-2} to 0.1 mW·cm^{-2}. The measurements were performed using a Keithley 2400 instrument in an ambient environment (~20 ºC and ~60% RH).

3.5.3 Electrochemical impedance spectroscopy (EIS)

In the study of PSCs, An EIS is a technique utilized to study the electrical properties and charge transfer processes within photovoltaic devices. By applying a small alternating current (AC) voltage

across a PSC and measuring the resultant current, EIS can analyze the impedance of the PSC at various frequencies. This provides detailed insights into recombination, charge accumulation, and transport mechanisms.[134] In my works, EIS measurements were performed to evaluate the recombination resistance (R_{rec}) and charge transfer resistance (R_s) in the PSCs by fitting the Nyquist plots derived from EIS data using the equivalent circuit model shown in **Figure 3.4**. EIS measurements were conducted using a Zahner Zennium electrochemical workstation. In Chapter 4, EIS measurements were employed under a bias of 0.9 V, scanned from 1 MHz to 1 Hz. In Chapters 5-6, EIS measurements were employed under a bias of 0.75 V, scanned from 1 MHz to 1 Hz.

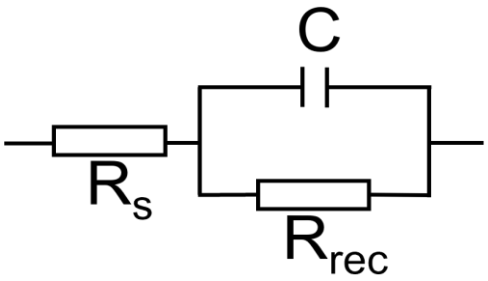

Figure 3.4. Example equivalent circuit model for fitting of Nyquist plots.

3.5.4 Mott-Schottky (MS) measurement

In perovskite solar cells, a Mott-Schottky measurement is an electrochemical technique used to analyze the semiconductor properties of the perovskite material based on Mott-Schottky theory, which relates the capacitance of a semiconductor-semiconductor junction to the applied voltage and the carrier density of the perovskite materials.[135] In a Mott-Schottky analysis, the capacitance of the perovskite solar cell is measured across a range of applied voltages. By plotting the reciprocal square

of the capacitance ($1 \cdot C^{-2}$) against the applied voltage, it is possible to determine the build-in potential (V_{bi}) and the trap density, which is helpful in studying the charge transport and recombination dynamics, which are crucial for their performance.[136] In my works, MS measurements were performed to obtain MS plots, which were then used to estimate the build-in potential (V_{bi}) of PSCs and thus trap density in perovskite films. MS measurements were conducted using a Zahner Zennium electrochemical workstation. In Chapter 4, MS plots were recorded from 0 V to 1.2 V, with a step size of 0.01 V. While in Chapters 5-6, they were recorded from 0 V to 0.9 V, with a step size of 0.01 V.

3.5.5 Space charge limited current (SCLC) measurement

SCLC measurement for perovskite solar cells is a crucial technique for investigating charge transport properties within photovoltaic devices. The SCLC method involves measuring the current flowing through a PSC under conditions where the current is not limited by the material's intrinsic conductivity but by the accumulation of space charge.[137] In practical terms, this is typically done by applying a range of voltages to the solar cell in a controlled environment (electron-only or hole-only devices) and observing the current response. In the SCLC regime, the current increases sharply within a small range of the applied voltage, agreeing with the linear increase observed in ohmic behavior. In my works, SCLC measurements were performed to acquire the voltage of the trap filling limit, and thus calculate the trap density of the perovskite films according to **Equation 3.3**:

$$N_t = \frac{2\varepsilon_0 \varepsilon V_{TFL}}{eL^2} \quad (3.5)$$

where ε_0 is the permittivity of vacuum, ε is the relative dielectric constant (typically 35 for perovskites), V_{TFL} is the onset voltage of trap filling limit (TEL), e is the elementary charge, and L is the thickness of the perovskite films. In Chapter 4, I performed SCLC measurements on both electron-only devices with a structure of ITO/SnO_2/Perovskite/PCBM/BCP/Ag and hole-only devices with a structure of ITO/NiO_x:2PACz/Perovskite/Spiro-OMeTAD/Au. In Chapter 5, SCLC measurements on hole-only devices with a structure of ITO/PEDOT:PSS/Perovskite/Spiro-OMeTAD/Au were performed. In Chapter 6, SCLCs on hole-only devices with a structure of ITO/SnO_2/Perovskite/PCBM:C60/BCP/Ag were measured. The measurements were carried out using a Keithley 2400 instrument in an ambient and dark environment (~20 ºC and ~60% RH).

3.5.6 Transient photovoltage (TPV) and transient photocurrent (TPC) measurements

TPV and TPC measurements are two important techniques that are used to measure the change in voltage and current across a photovoltaic device immediately after it is exposed to a light pulse. The decay of TPV helps in the understanding of non-radiative recombination kinetics of charge carriers. By analyzing the TPV decay profiles, the lifetime of the carrier generated in perovskite films was estimated, whilst TPC provides direct information about the generation, extraction, and transport of charge carriers within the PSCs. The rate at which the photocurrent rises and falls in response to the light pulse can reveal details about the charge carrier mobility, the traps or defects density, and the

effectiveness of the charge extraction at the interface of perovskite films.[138] In my works, TPV and TPC measurements were conducted to evaluate the carrier lifetime and charge extraction time in the PSCs. Both TPV and TPC patterns were fitted through a single exponential function. Both TPV and TPC measurements were conducted by Guoqiang Ma using a platform built by Time Tech Spectra Co. LTD.

3.5.7 External quantum efficiency (EQE) measurement

EQE is a key measurement ultilized to determine the efficiency with which a PSC converts the photons into electrons. EQE is described as the proportion of charge carriers gathered by the photovoltaic device to the quantity of photons with a given energy that are incident on a photovoltaic device. EQE is usually used to support the reliability of the current density measured by J-V measurement (introduced in section 3.6.1).[100, 139, 140] In my works, EQE measurements were conducted with an Enli-Tech (Taiwan) instrument. The light intensity for EQE measurements was calibrated using a standard single-crystal silicon solar cell. For $FAPbI_3$ based PSCs discussed in Chapter 4, the EQE scanning range from 300 nm to 900 nm, while for TLPSCs discussed in Chapter 5, the scanning range is 300 nm - 1200 nm. The light intensity for EQE measurements was calibrated using a standard single-crystal silicon solar cell.

3.6 Device performance and stability characterizations

In this section, characterization methods for determining the photovoltaic performance and long-term

stability of a PSC will be introduced. The photovoltaic performance of a PSC can be determined by current density-voltaic (J-V) measurement and stabilized power output (SPO), whilst the long-term stability of a PSC can be measured through maximum power point tracking (MPPT).

3.6.1 Current density-voltage (J-V) measurement

A J-V measurement is a fundamental technique in the evaluation of the performance of photovoltaic cells. This measurement is performed by applying various voltages to a solar cell and then measuring the resulting current density. The J-V curve, which plots the current density against the applied voltage, provides critical information about the device's performance, including the four key parameters: J_{sc}, V_{oc}, FF, and PCE. The J-V measurement is crucial in assessing the efficiency and quality of PSCs and in understanding their behavior under different operating conditions. It is a standard method for comparing different cell technologies and for identifying areas for improvement in cell design and fabrication. In my works, J-V measurements were performed with a Keithley 2400 instrument in an ambient environment (~20 ºC and ~60% RH). An Oriel Sol3A solar simulator was employed to produce 1-sun light illumination (AM 1.5G, 100 $mW \cdot cm^{-2}$), which was calibrated using a standard KG-5 Si diode. The devices for J-V measurements were covered with a shadow mask during the measurements to control the active area to be 0.08 cm^2. For measurements of large-area devices, a shadow mask with 1 cm^2 hole area was employed. The measurements were conducted with unencapsulated devices. In Chapter 4, the devices were soaked in light for around 3 min before J-V scanning. J-V curves were measured both in reverse scan (from 1.2 V to -0.2 V) and forward scan

(from -0.2 V to 1.2 V) with a step size of 0.01 V. In Chapters 5-6, the devices were prevented from light soaking before measurement. J-V curves were measured both in reverse scan (from 0.9 V to -0.2 V) and forward scan (from -0.2 V to 0.9 V) with a step size of 0.02 V.

3.6.2 Stabilized power output (SPO) measurement

Compared to J-V measurements, which are instantaneous, a SPO measurement is more reliable in determining the photovoltaic performance of a PSC as it evaluates the devices under steady-state conditions, often for a prolonged period, to mimic actual operating environments.[141] This gives a more accurate and realistic understanding of the device's performance, accounting for factors like thermal effects, light-induced degradation, and other long-term stability issues. SPO measurements were performed by tracking the current density of PSCs at the voltage of maximum power point (V_{max}) under continuous 1-sun standard illumination (AM 1.5G, 100 $mW \cdot cm^{-2}$). Consequently, an SPO was then calculated by multiplying the given V_{max} and the current density that was measured. In my works, SPO measurements were performed using a Keithley 2400 instrument in an ambient environment (~20 ºC and ~60% RH). In Chapter 5, the temperature of devices was kept below 35 ºC through N_2 gas flow, while those in Chapter 4 were not control.

3.6.3 Maximum power point tracking (MPPT)

MPPT is a technique used to estimate the long-term stability of a PSC. MPPT was measured by tracking the PCE of a PSC under continuous light illumination in an ambient environment, aiming to

simulate the realistic working environment of the PSCs. The tracking time is usually over hundreds of hours, depending on the type of perovskite materials. In Chapter 4, the α-$FAPbI_3$ PSCs were tracked for 1000 h, whilst in Chapter 5, the TLPSCs were tracked for 500 h. Both MPPT measurements in Chapter 4 and 5 were performed under continuous LED light illumination in an ambient environment (~20 ^{o}C and ~60% RH). The maximum power point (MPP) was measured every 17 s.

Chapter 4

COORDINATOR REPLENISHMENT STRATEGY IMPROVING PERFORMANCE OF $FAPBI_3$-BASED PSCS

Pure $FAPbI_3$ based perovskite with excellent thermal stability and low band gap exhibit great potential in approaching the Shockley–Queisser limit of power conversion efficiency (PCE). Despite the significant progress in $FAPbI_3$ based regular-structure perovskite solar cells (PSCs), the usage of $FAPbI_3$ as photoactive materials in inverted PSCs has been limited by the challenges in fabricating high-quality α-$FAPbI_3$ perovskite films on substrates of inverted PSCs. Herein, I introduce a novel coordinator replenishment strategy by using tetramethylurea (TMU) as a coordinator to enhance the crystallization process of α-$FAPbI_3$. This method effectively lowers the energy barrier for α-$FAPbI_3$ formation, leading to improved film crystallinity and orientation as well as photovoltaic performance. The resultant PSCs exhibit a significantly enhanced PCE of 23.2%, compared to 21.3% of the control, with notable improvements in V_{oc} and FF. Additionally, both encapsulated and unencapsulated devices exhibit improved long-term stability. An encapsulated device exhibits a highly enhanced operating stability of T_{80}>1000 h tracking under continuous 1-sun standard illumination. In addition, the unencapsulated target device retained 85.6% of its initial PCE after exposure in air for over 1500 h. This advance marks a significant step towards more efficient and stable $FAPbI_3$ based inverted PSCs.

4. Coordinator Replenishment Strategy Improving $FAPbI_3$-based PSCs

4.1 Introduction

During the last decade, PSCs have attracted increasing research interest and have achieved a dazzling certified PCE of 26.1%.[1, 9] Among numerous classes of perovskite materials, formamidinium lead triiodide ($FAPbI_3$) has gained favor due to its excellent thermal stability and low band gap (~1.5 eV) adjacent to the ideal band gap (1.1-1.4 eV) that allows their PSCs approach to the S–Q limit.[14, 16] In recent years, vast effort has been placed on $FAPbI_3$-based PSCs, which by far prompted their highest PCE to a certified value of 25.7%.[15, 33, 38, 39, 142, 143]

Fabrication of high-quality pure α-$FAPbI_3$ is challenging due to the metastability of α-$FAPbI_3$ at room temperature, which is mainly attributed to the lattice strain and structural disorder induced by the relatively large size of FA^+.[144-148] Substitution of A-site and X-site of $FAPbI_3$ with smaller cations (MA^+, Cs^+, Rb^+ etc.)[53-56, 149] and anions (Cl^-, Br^-, $HCOO^-$ etc.)[16, 30, 38, 150-152] is proven to be one of the effective ways to mitigate the lattice strain and structural disorder, which thus improves its long-term stability. However, this inevitably expands the bandgap of perovskite and causes phase segregation issues, leading to inferior light absorption and photovoltaic performance. To reserve the merits of pure $FAPbI_3$, alternative strategies that regulated the crystallization process and released micro strain within the perovskite films whist avoided compositional change have been proposed. These include organic amine salt doping,[15, 80, 151, 153] volatile additives,[30] vapor-assisted crystallization,[154] and solvent engineering.[39, 155] Though most of these approaches exhibit unparalleled effectiveness in PSCs with regular-structure (n-i-p), their success cannot be duplicated to the invert-structure (p-i-n)

4. Coordinator Replenishment Strategy Improving $FAPbI_3$-based PSCs

PSCs, which provide the merits of outstanding stability, being superior in flexible and scalable processing, and favored in tandem devices.[40, 100, 106, 156, 157] For the $FAPbI_3$-based inverted PSCs, it is therefore hard to achieve a PCE exceeding 23%,[158-160] which is far behind that in regular-structure (n-i-p) counterparts.[15, 33] This is probably due to the requirement of high annealing temperature during film fabrication process and uncontrollable crystallization rate, which leads to the formation of unfavorable δ-$FAPbI_3$ and thus results in α-$FAPbI_3$ films with poor quality. Therefore, to catch up with the pace of regular-structure PSCs, further exploration for effective strategies to improve crystallinity and carrier extraction in inverted $FAPbI_3$-based PSCs is necessary.

Though the starting application of $FAPbI_3$ in inverted PSCs happened at a similar to the regular counterparts,[36, 161-163] just a handful of research works have been conducted on $FAPbI_3$-based inverted PSCs.[53, 155, 157-161, 164-167] Volatile MACl, which was widely used to assist the crystallization of $FAPbI_3$ films in regular PSCs, is applicable for improving the quality of $FAPbI_3$ perovskite in an inverted structure.[55, 158] A buffer layer of self-assembled monolayers (SAMs) semiconductor was demonstrated to benefit the charge transporting at the NiOx/PVK interface of $FAPbI_3$-based perovskite and its long-term stability.[159, 165] Furthermore, recent studies have verified that regulation of crystal growth dynamics via ion liquid additives and vapor assisted crystallization process are reliable in fabricating $FAPbI_3$ on SAMs and PTAA substrates, which were attributed to the offset of residual strain in the perovskite lattice.[155, 160] The aforementioned studies certainly benefit the community of $FAPbI_3$-based inverted PSCs, however, most of them progressed under the shadow of

previous studies in $FAPbI_3$-based regular-structure PSCs.[30, 33, 38, 39, 154, 168] Moreover, dopant species and complicated fabrication procedures are usually necessary in such approaches, which increases the material expenditure and time cost as well. Hence, further exploration of new strategies for $FAPbI_3$-based inverted PSCs that exclude additives usage, and do not increase process and time costs are still required.

DMSO that strongly coordinated with perovskite component species is widely used as a co-solvent to form adducts to prevent fast crystallization of perovskite, which would result in rough perovskite films with incomplete coverage. However, its coordination with perovskite components may be too strong to induce the formation of α-$FAPbI_3$ nuclei and their growth on substrates for $FAPbI_3$-based invert-structure PSCs.[169] Such a high energy barrier made the intermediate adducts preferentially transfer to δ-$FAPbI_3$ before it finally transferred into α-$FAPbI_3$ under the annealing operation. This unquestionably results in poor crystallization of α-$FAPbI_3$. Herein, I replaced DMSO with a larger, weaker, and green Lewis base, TMU, and control the crystallization through a coordinator replenishment strategy. Through such approach, I had speeded up the formation of α-$FAPbI_3$ crystal seeds but avoided fast crystal growth of α-$FAPbI_3$. This was attributed to the higher energy level of the $FAI{\cdot}PbI_2{\cdot}$TMU adduct compared to the $FAI{\cdot}PbI_2{\cdot}$DMSO counterpart, which therefore lower the energy barrier between α-$FAPbI_3$ and the adduct phase. The $FAI{\cdot}PbI_2{\cdot}$TMU adduct, in this way, prefers to directly transform into α-$FAPbI_3$ with the formation of δ-$FAPbI_3$ inhibited. As a result, a highly oriented pure α-$FAPbI_3$ with significantly enhanced photovoltaic property was obtained. The

4. Coordinator Replenishment Strategy Improving $FAPbI_3$-based PSCs

$FAPbI_3$-based inverted PSCs fabricated from such perovskite films exhibited noticeable improved V_{oc} = 1.13 V, FF%=81.7%, and PCE=23.2%. Moreover, both unencapsulated and encapsulated devices shown improved long-term stability due to the mitigation of tensile strain in crystal lattice. The unencapsulated device retained 86% of its initial efficiency after storage in an ambient environment (RH: 20±5%) for 1500 h, while the encapsulated device achieved an operating stability of $T_{80} >$ 1000 h under continuous illumination.

4.2 Experimental details

4.2.1 Materials

Unless otherwise state, all materials were used as received. Anhydrous solvents including N, N-dimethylformamide (DMF, 99.8%), dimethyl sulfoxide (DMSO, 99.8%), chlorobenzene (CB, 99.8%), and isopropanol (IPA, 99.5%) were purchased from Sigma-Aldrich. 1,1,3,3-Tetramethylurea (TMU, 99%) was purchased from Shanghai Xianding Biotechnology Co., LTD. Anhydrous diethyl ether (DE) was purchase from Shenzhen chemical test technology Co., LTD. Lead iodide (PbI_2, 99.99%) and [2-(9H-carbazol-9-yl)ethyl]phosphonic acid (2PACz, >98.0%) were purchased from TCI. Formamidinium iodide (FAI, 99.99%) was purchased from Great Cell Solar. Methylammonium chloride (MACl), phenethylammonium bromide (PEABr, 99.5%), bathocuproine (BCP, >99%), and phenyl-C61-butyric acid methyl ester (PCBM, >99%) were purchased from Lumtec. ITO glass was purchased from Suzhou ShangYang Solar Technology Co. Ltd. Nickel nitrate hexahydrate ($Ni(NO_3)_2{\cdot}6H_2O$) and sodium hydroxide (NaOH) used for synthesis of nickel oxide (NiO_x)

nanoparticles were purchased from Sigma-Aldrich.

4.2.2 Synthesis of NiO_x nanoparticles

NiO_x nanoparticles were synthesized in the lab according to previous report.[106] 0.25 M of aqueous Ni $(NO_3)_2$ solution was prepared by weighing 7.26 g (25 mmol) of $Ni(NO_3)_2 \cdot 6H_2O$ and dissolving it into a 500 ml-flask following by adding 100 ml of deionized water and a stirrer. 0.5 M of NaOH solution was prepared by weighing and dissolving 2 g (50 mmol) of NaOH into a beaker following by adding 100 ml of deionized water into the beaker. After fully dissolving, the NaOH solution was transferred to a dropping funnel. This NaOH solution was slowly dripped (2-3 drops per second) into the as prepared green $Ni(NO_3)_2$ solution under vigorously stirring at room temperature. Green $Ni(OH)_2$ sol-gel was obtained during the dripping process. After this process, the mixture was stirred for additional 20 min to allow the reaction to complete. Thereafter, the resulting green $Ni(OH)_2$ sol-gel product was collected by centrifugation at 8,000 rpm for 5 min. Then, the collected $Ni(OH)_2$ sol-gel product was washed with deionized water and collected again by centrifugation. The above washing and centrifugation steps were repeated 3-5 times to make sure the pH values of the supernatants become neutral. Then, the obtained $Ni(OH)_2$ product was dried in a freeze dryer for 48 h. Finally, the dried green powders were sintered for 2 h at 285 °C in a tube furnace. The temperature of the furnace was ramped up in a rate of 3 °C·min^{-1} and ramped down in a rate of 5 °C·min^{-1} after finishing sintering. After cooling down, the NiO_x nanoparticles were stored in a dry box with humidity ≤15%. The NiO_x nanoparticles produced in such method are pretty fine and exhibit great dispersibility, therefore, were

used without further crushing.

4.2.3 Preparation of NiO_x ink

20 mg of NiO_x nanoparticle powder was weighed to a 4 ml vial follow by adding 1 ml of deionized water. The mixture was shaken until there were no particles sink at the bottom. The resulting mixture was then treated in an ultrasonic water bath (600 W, 40 kHz) for 1 h with the temperature kept below 30 °C. Then, the mixture was aged by simply standing for another 1 h before use.

4.2.4 Preparation of 1.4 M perovskite precursors

For all perovskite precursors, firstly, 14.2 mg of MACl (15% relative to A-site cation), 240.8 mg of FAI, and 645.4 mg of PbI_2 were weighed and added to a 4 ml vial successively. Then, for the control precursor, anhydrous DMF (889 ml) and DMSO (111 ml) were added to the vial. For the target (TMU-CR) precursor, DMSO was replaced by equal volume of TMU. The mixture was shaken until all the component dissolved, then was further stirred for 1 h at 60 °C. After that, the precursors were cooled down for use.

4.2.5 Fabrication of inverted α-$FAPbI_3$ PSCs

The ITO glasses were cleaned with detergent, deionized water, isopropanol, acetone, and isopropanol successively in an ultrasonic water bath (600 W, 40 kHz) with the temperature kept below 30 °C. The ITO glasses were then dried under N_2 flow and treated with UV-ozone for 30 mins to ameliorate the

infiltration performance of ITO substrate. Then well-dispersed NiO_x in (20 $mg \cdot ml^{-1}$) was spin-coated on the ITO substrate with speed of 3000 rpm for 40 s, and then was annealed for 10 min at 110 °C. After annealing, 2PACz was then deposited on the NiO_x to form a self-assembly monolayer. Specifically, 0.75 $mg \cdot ml^{-1}$ of 2PACz solution in IPA was spin-coated on the NiO_x layer with a speed of 5000 rpm for 30 s, followed by annealing for 10 min at 100 °C. Afterwards, the substrates were transferred to a dry-air glove box with humidity below 10% for fabrication of perovskite films.

The as prepared perovskite precursor was spin-coated onto the resulting NiO_x:2PACz layer with a speed of 4000 rpm for 35 s. For the control perovskite, 1 ml of DE was dripped with pipette after 10 s of spinning. For the target (TMU-CR) perovskite, 1 ml of anti-solvent (TMU:DE=1:100) was dripped after 5 s of spinning. It is worth noting that the pipette tip should be very close (~2 mm) to the films and the dripping should be completed within 1s. This is the key to obtained high-quality α-$FAPbI_3$ films. The resulting adduct films were then immediately annealed for 10 min at 150 °C. It should be noted that, in both the perovskite films, as MACl has been used in the fabrication, a small amount of MA^+ would retain in the films, though it would decompose and evaporate out from the films.[38] Solid-state NMR was well-established to present of MA^+,[38, 154] and it has been characterized through this technique that the MA^+ occupies only around 5% of the A-site cations in the $FAPbI_3$ films.[38] In films of my work, the proportion of MA^+ was expected to be lower as the amount of MACl (15 mol%) used in my work is much lower than that in the above work (35 mol%).

4. Coordinator Replenishment Strategy Improving $FAPbI_3$-based PSCs

For passivation of perovskite, 1 $mg \cdot ml^{-1}$ PEABr solution in IPA, with equal quantity of FAI with respect to PEABr and 0.5 vol% of DMF, was spin-coated onto the top of perovskite with a speed of 5000 rpm for 30 s followed by annealing for 5 min at 100 °C. The morphology and chemical interaction at such interface were well-explored through SEM, AFM, TEM, XRD, XPS, and solid-state NMR etc.[170, 171] And it has been widely reported that the post-treatment with PEABr would lead to formation of 2D/3D heterojunction on the surface of perovskite, which benefits the defect suppression, charge transporting, and stability of the perovskite films.[172, 173]

Then a layer of PCBM (20 $mg \cdot ml^{-1}$ in CB) was coated with a speed of 1500 rpm for 30 s and thereafter annealed for 10 min at 100 °C, followed by deposition of BCP (6 nm), and Ag (100 nm) via thermal evaporation. The thickness of each layer was monitored and controlled using a film thickness gauge within the thermal evaporator.

4.2.6 Solar cells characterization

The performance and stability of the PSCs were characterized through J-V, dark J-V, light dependent V_{oc}, SCLC, SPO, EQE, EIS, MS, TPV and TPC measurements, which were performed according to the methods mentioned in Chapter 3.

4.2.7 Perovskite films characterization

The quality of the $FAPbI_3$ perovskite films were characterized through SEM, AFM, UV-vis

absorption, PL, TRPL, TA, XRD, GIWAXS, in-suit GIWAXS, and UPS technology etc. Their data were collected through the methods presented in Chapter 3.

4.2.8 Characterization of chemical interaction

Chemical interaction between coordinators and perovskite components were explored through FTIR, TGA, and DSC measurements, which were performed according to the methods detailed in Chapter 3.

4.3 Interaction between coordinator and perovskite components

The chemical structures of DMSO and TMU are shown in **Figure 4.1a**, where both contain chemical groups that exhibit electron-donor nature. Compared to DMSO, TMU has a similar donor number (DN) and a lower acceptor number (AN), and thus exhibits a higher hydrogen bond accepting ability (HBA, β) (**Table 4.1**),[174] which is favorable as a Lewis base in perovskite precursor preperation.[169] TMU is thus a reasonable candidate as a Lewis base for forming adduct films during perovskite fabrication process. As the variation of crystallization dynamics of $FAPbI_3$-based perovskites originated from the different coordination nature of the intermediate adducts ($FAI{\cdot}PbI_2{\cdot}$DMSO and $FAI{\cdot}PbI_2{\cdot}$TMU), it is vital to further investigate their intrinsic interaction properties. The proposed interaction modes for both adducts are shown in **Figure 4.1b**. Benefiting from the more electron-donor centers and higher HBA, the interaction framework between TMU and perovskite components (FAI and PbI_2) is denser than that in $FAI{\cdot}PbI_2{\cdot}$DMSO adduct. However, it is unreasonable to conclude

that TMU exhibits stronger bonding with FAI and PbI_2 due to the steric effect and the influence of matching of the hardness and softness of the Lewis Acid and Base.[169]

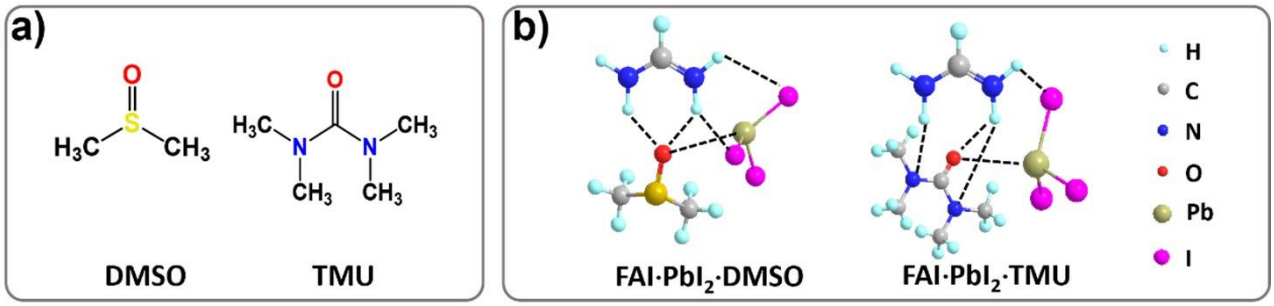

Figure 4.1. (a) Chemical structure of DMSO and TMU. (b) Proposed interaction modes for FAI·PbI_2·DMSO and FAI·PbI_2·TMU adducts.

Table 4.1. Donor number (*DN*), acceptor number (*AN*) and hydrogen bond accepting ability (*HBA, β*) of DMSO and TMU.

Solvent	**DMSO**	**TMU**
DN	29.8	29.6
AN	19.3	9.2
HBA(β)	76	80

To reveal the interaction nature of the adducts, FTIR spectroscopy was used to evaluate the interaction strength of both Lewis bases with perovskite components. Similar to the blue shift of IR peaks attributed to the S=O stretching ($\nu_{S=O}$) of DMSO after mixing with FAI and PbI_2 ($\nu_{(S=O,\ DMSO)}$= 1019 cm^{-1}, $\nu_{S=O,\ FAI\cdot DMSO}$= 1016 cm^{-1}, and $\nu_{S=O,\ PbI2\cdot DMSO}$= 1018 cm^{-1}) (**Figure 4.2a**), the peaks assigned to C=O stretching ($\nu_{C=O}$) of TMU blue-shifted from 1627 cm^{-1} for pure TMU to 1610 cm^{-1} for FAI·TMU adduct and 1620 cm^{-1} for PbI_2·TMU adduct, demonstrating strong coordination of TMU with both

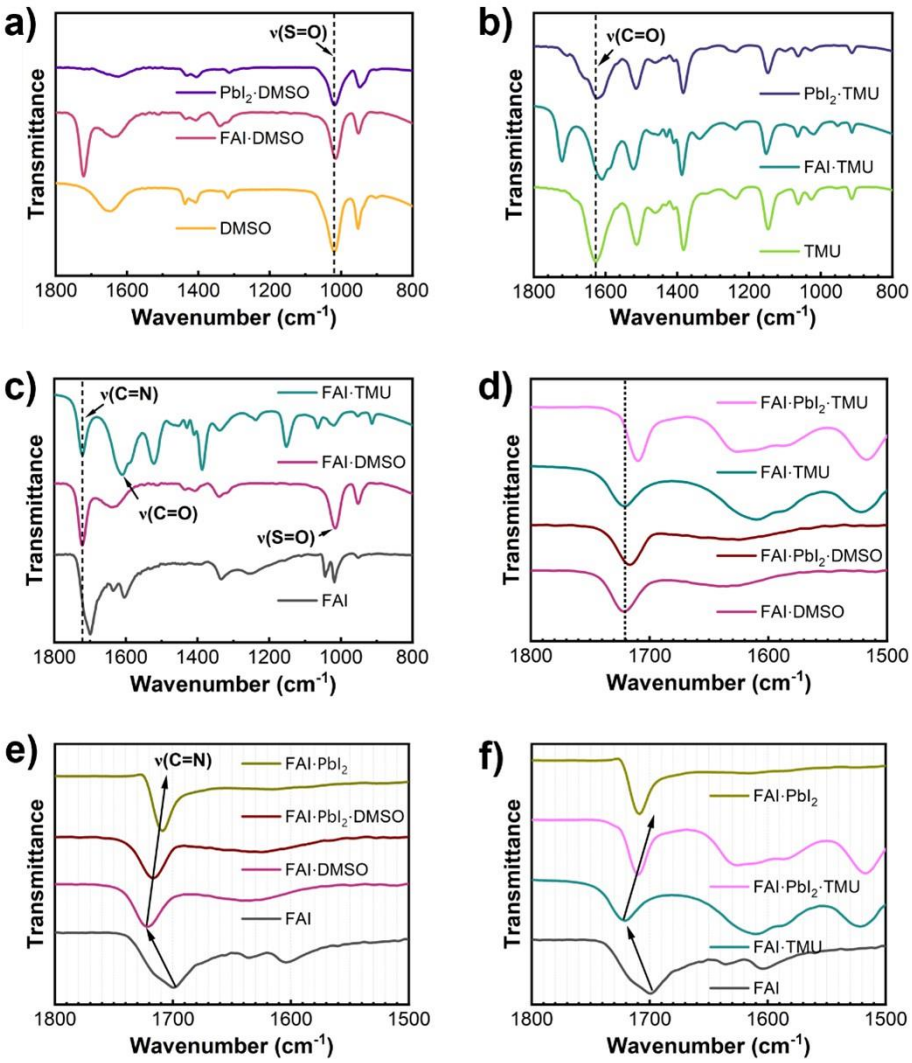

Figure 4.2. a) FTIR spectra of DMSO and its complexes with FAI and PbI_2. b) FTIR spectra of TMU and its adducts with FAI and PbI_2. c) FTIR spectra of FAI and its adducts with DMSO and TMU coordinator. d) FTIR spectra of FAI and its complex with various components, to real the effect of adding PbI_2 to FAI's adducts in b) and c). e) FTIR spectra of FAI and its mixtures with PbI_2, DMSO, and both. f) FTIR spectra of FAI and its mixtures with PbI_2, TMU, and both.

FAI and PbI_2 (**Figure 4.2b**). In addition, the IR shift of C=N stretching ($\nu_{C=N}$) in pure FAI and its mixtures with DMSO and TMU were compared in **Figure 4.2c**. It was worth-noting that $\nu_{C=N}$ of both FAI·DMSO and FAI·TMU mixtures red-shifted from 1700 cm^{-1} to 1721 cm^{-1}, indicating that the binding strength between TMU and FAI is similar to that between DMSO and FAI. When PbI_2 was

added into such mixtures and forms FAI·PbI_2·DMSO and the FAI·PbI_2·TMU adducts, $\nu_{C=N}$ of FAI blue-shifted from 1721 cm^{-1} to 1716 cm^{-1} and 1710 cm^{-1} for the DMSO adduct and TMU adduct, respectively (**Figure 4.2d-f**). This is because PbI_2 coordinated with Lewis bases attract parts of the electron density from the Lewis bases and thus reduces their interaction with FAI. A larger wavenumber-shift in the FAI·PbI_2·TMU adducts suggests that PbI_2 exhibits a stronger interaction with TMU compared to DMSO.

Besides the coordination with the single perovskite component, Lewis bases' bonding properties with FAI and PbI_2 together is more crucial to determine the crystallization dynamics during the fabrication process. TGA and DSC of the adducts powder were therefore conducted to compare the bonding strength of DMSO and TMU with perovskite components in their adducts. Regarding the TGA curves, the weight losses of FAI·PbI_2·DMSO beginning at ~70 °C and ~190 °C were attributed to the evaporation of DMSO (**Figure 4.3a**), while that of FAI·PbI_2·TMU starting at ~40 °C were due to the evaporation of TMU (**Figure 4.3b**). The lower beginning temperature of weight loss for the FAI·PbI_2·TMU adduct shows an easier escape from the adduct and a lower interaction with perovskite components, which benefits the formation of α-$FAPbI_3$. Regarding the FAI·PbI_2·DMSO adduct, the higher beginning temperature of weight loss inhibits the escape of DMSO and the transfer of adduct phase to α-$FAPbI_3$ as well. Besides, two distinct stage of weight losses was observed from the FAI·PbI_2·DMSO adduct. This indicates that the adduct is unstable, which may lead to transfer to a secondary phase like PbI_2·$DMSO_n$.[169] In addition, the high evaporation temperature (~190 °C) of

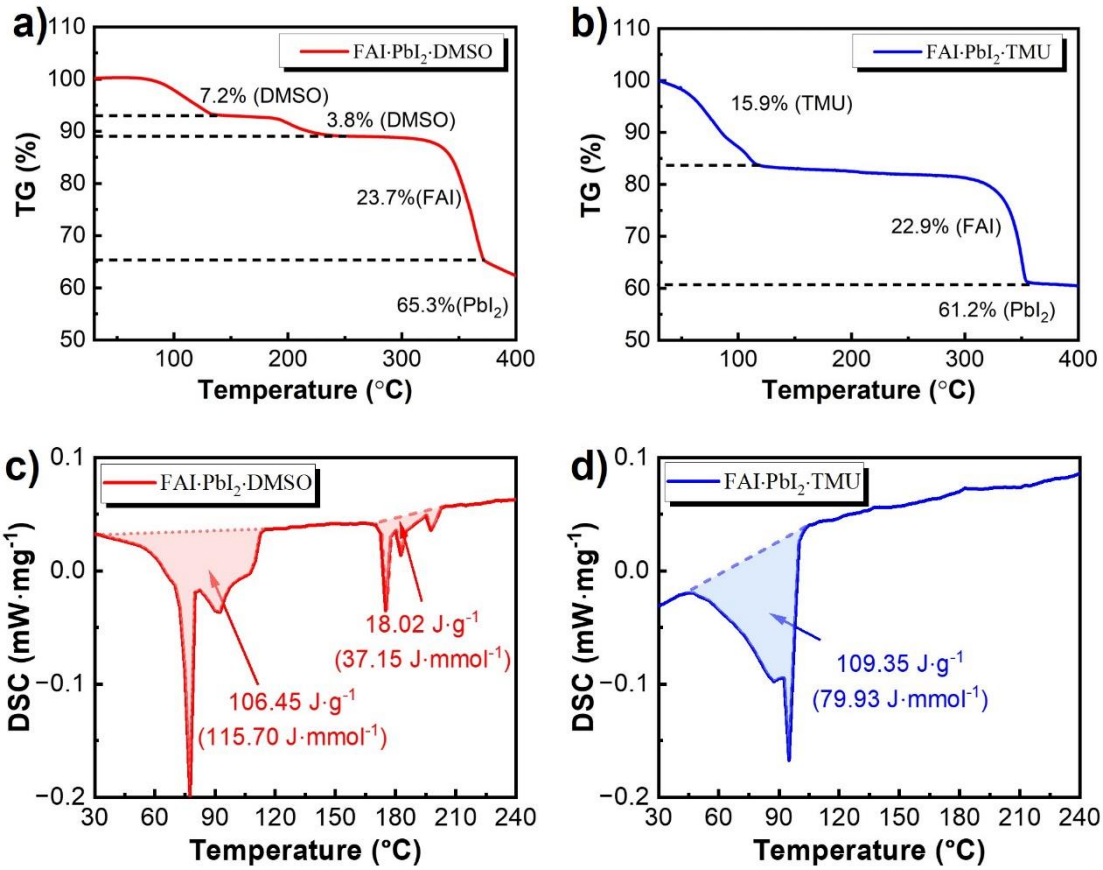

Figure 4.3. a, b) TG analysis of a) the FAI·PbI_2·DMSO and b) the FAI·PbI_2·TMU adducts. c, d) DSC study of c) the FAI·PbI_2·DMSO and d) the FAI·PbI_2·TMU adducts.

DMSO at the second stage, which is much higher than the annealing temperature, may cause difficulty in eliminating DMSO and thus result in residue in perovskite film. This is unquestionably detrimental to the quality and stability of perovskite film. The binding strength between the Lewis base and perovskite components were further verified by DSC, where the energy required for eliminating Lewis bases from their adducts was integrated from the differential heat absorbed. As shown in **Figure 4.3c**, the binding energy of DMSO with perovskite components in their adduct during the first weight-loss state was calculated to be 115.7 J·mmol^{-1}, while that of TMU was 79.9 J·mmol^{-1} (**Figure**

4.3d). Accordingly, I can draw a conclusion that the interaction of TMU with perovskite components in the adduct film is weaker than that of DMSO, which benefits the formation of α-$FAPbI_3$ crystal nuclei and their growth.[175-177]

4.4 Study of crystallization dynamic of perovskite films

Though a weaker coordination benefits the formation of α-$FAPbI_3$ crystal nuclei and their growth, too fast crystallization of the perovskite would result in low-quality films with voids and cracks throughout the perovskite films, which possibly cause current leakage and may even short-circuit the devices.[177, 178] Due to the low coordination of TMU with perovskite components, fast crystallization of perovskite films was inevitable if no further steps were taken. Perovskite films with TMU as a coordinator were therefore full of cracks and voids on surface (**Figure 4.4a**).

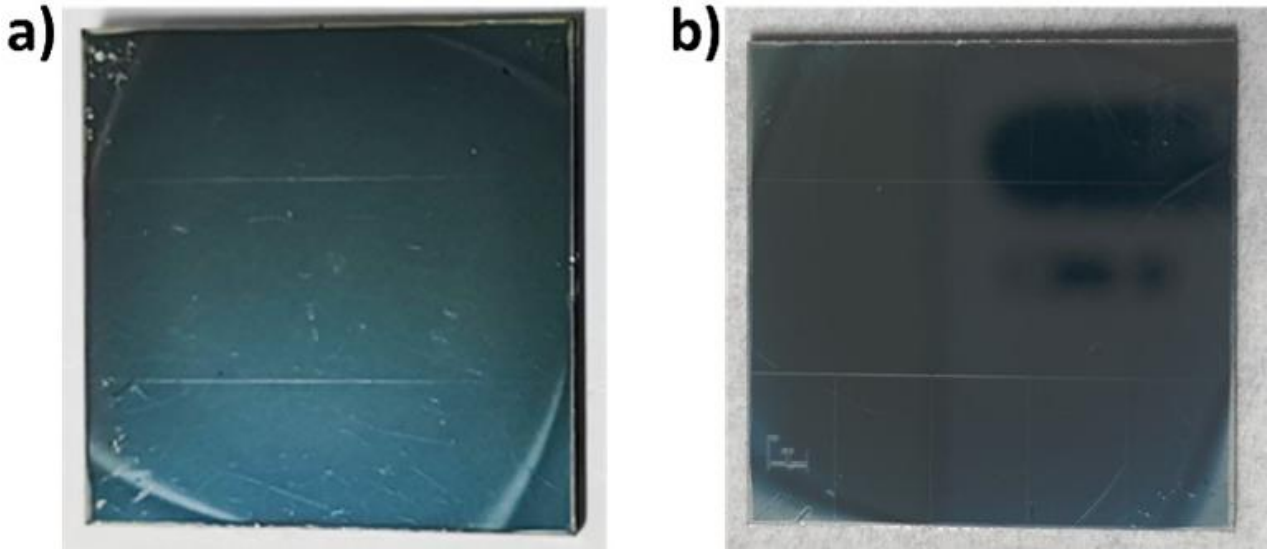

Figure 4.4. Photographs of perovskite films fabricated using a) regular anti-solvent processing and b) coordinator replenishment strategy, both fabricated from the precursor with TMU as coordinator.

To address this issue, we added 1 vol% of TMU into the anti-solvent to regulate the crystallization rate of α-$FAPbI_3$ films based on a TMU coordinator. The fabrication process for such an approach is illustrated in **Figure 4.5a**. The fabrication began with dripping appropriated amount of perovskite precursor on the substrate, followed by dripping anti-solvent onto the precursor liquid film during spin-coating process, nucleation at the end of spin-coating, and crystal-growth during the annealing process. At the stage of anti-solvent dripping, TMU in the perovskite liquid film was extracted rapidly by DE due to the weak coordination of TMU with perovskite components. By adding the polar solvent (TMU) into the nonpolar anti-solvent (DE), the polarity of the resulting mixed anti-solvent (TMU:DE=1:100) was increased and thus the extraction rate of TMU from the perovskite liquid films during the dripping process of anti-solvent was slowed down. In addition, a coordinator exchange

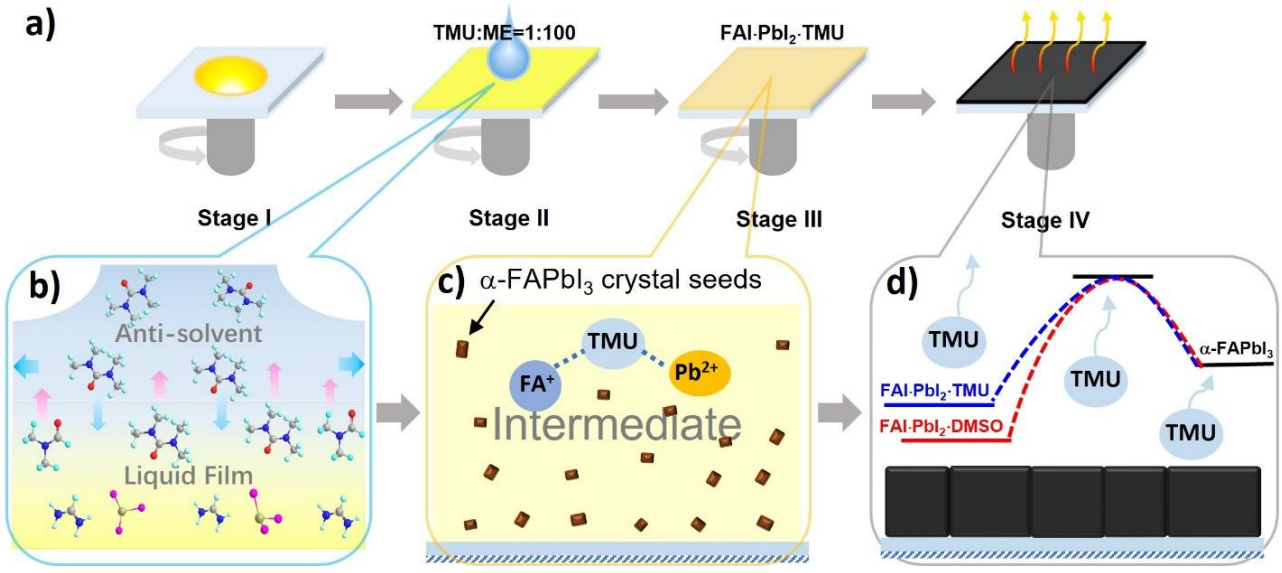

Figure 4.5. Study of crystallization dynamic of perovskite films based on different solvent coordinators. a) Schematics to illustrate the spin-coating process of perovskite films. b) Schematic of coordinator replenishment process. c) Schematic of the composition of adducts films. d) Schematic of the annealing process and energy barrier between adduct films and α-$FAPbI_3$.

process was supposed to exist at the interface of the perovskite wet film and the anti-solvent contacted with the precursor liquid film. While the TMU in the precursor film was extracted out, parts of the TMU in the anti-solvent enters the precursor liquid film and thus replenishes the coordinator vacancies as a result of the insufficiency of TMU (**Figure 4.5b**). I have called this process, therefore, a coordinator replenishment (CR) process.

The TMU-CR process conserved higher quantity of TMU coordinator in the film at the end of spin-coating, which also benefited the nucleation and crystallization of α-$FAPbI_3$ during annealing. As a result, the perovskite films fabricated from precursor with TMU as coordinator became smooth and compacted, without formation of voids and cracks (**Figure 4.4b**). Adding even a small amount of DMSO into the anti-solvent (DMSO:DE=1:5000) for deposition of perovskite films based on DMSO coordinator, however, would lead to unfavorable coverage loss due to the strong solubility of perovskite components in DMSO, while this would not happen for that based on TMU coordinator. (**Figure 4.6, Table 4.2**). This suggest that the CR approach was not suitable for fabrication of perovskite films based on DMSO coordinator. Therefore, if not further stated, the perovskite fabricated based on TMU coordinator was fabricated through the CR approach and was named as "TMU-CR", while that based on DMSO coordinator was fabricated through the regular approach with pure DE as anti-solvent, which was named as "control".

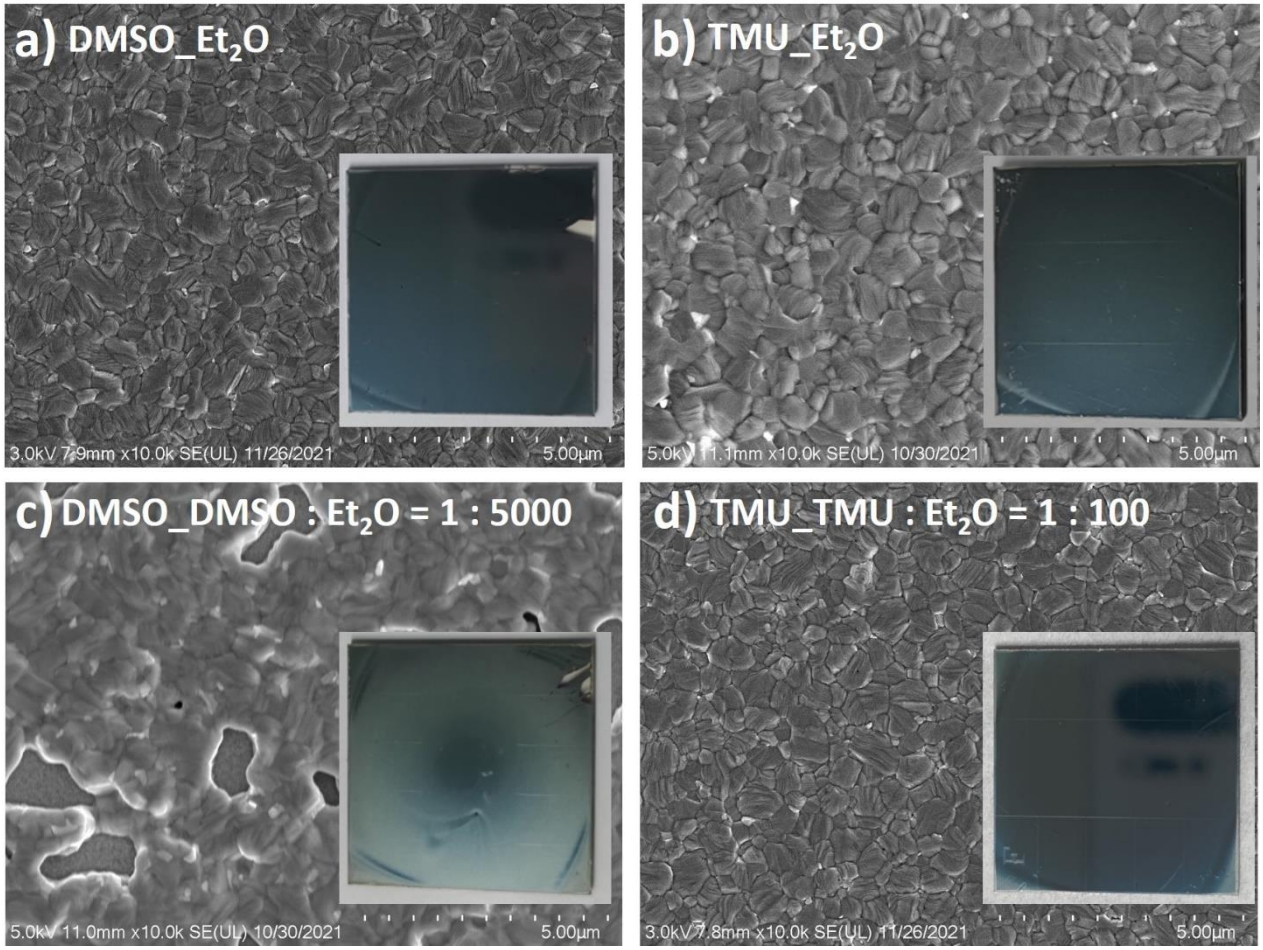

Figure 4.6. SEM surface scanning of the a, b) perovskite films fabricated from precursors with a) DMSO and b) TMU as coordinator using diethyl ether as anti-solvent, and c, d) the perovskite films fabricated from the same precursors but with a certain amount of Lewis base adding into the anti-solvent (fabrication conditions were listed in **Table 4.2**). Photographs of the relative films were embedded.

Table 4.2. Fabrication conditions of the perovskite films in **Figure 4.6**.

NO.	Solvent	Anti-solvent	Intermediate	**Figure 4.6**
1	DMF:DMSO=8:1	Et_2O	$FAI{\cdot}PbI_2{\cdot}DMSO$	a
2	DMF:DMSO=8:1	$DMSO:Et_2O$=1:5000	$FAI{\cdot}PbI_2{\cdot}DMSO$	c
3	DMF:TMU=8:1	Et_2O	$FAI{\cdot}PbI_2{\cdot}TMU$	b
4	DMF:TMU=8:1	$TMU:Et_2O$=1:100	$FAI{\cdot}PbI_2{\cdot}TMU$	d

4. Coordinator Replenishment Strategy Improving $FAPbI_3$-based PSCs

To demonstrate the superiority of TMU as an alternative coordinator for the fabrication of α-$FAPbI_3$ based perovskite, I first compared the crystallization dynamics of perovskite based on each coordinator. The as prepared perovskite films before annealing were aged for 1h at room temperature to monitor their nucleation. As shown in **Figure 4.7a**, the fresh adduct film fabricated based on DMSO coordinator is colorless translucent, while that based on TMU coordinator is pale yellow, probably due to the different absorption nature of their adduct species. As expected, both gradually transfer to brown during the aging period, attributing to the formation of MA-containing α-$FAPbI_3$ perovskite crystal seeds as portrayed in **Figure 4.5c**.[158] The chemical structure of the nuclei was confirmed by the comparison of its XRD pattern with $MAPbI_3$ and $FAPbI_3$ (**Figure 4.7b**). Nevertheless, the films exhibited a visible difference in color variance. For the control adduct film, it was not until the 15^{th} minute that an obvious color mutation was observed, while the change in TMU-CR adduct film is noticeable after aging for only 5 min. This suggested a larger number of black-phase nuclei existed in the TMU-CR adduct film. To prove my hypothesis, I further conducted XRD analysis for the films aged for 30 min. Comparing to the control adduct film, which shows mainly δ-phase perovskite nuclei (with peak at $2\theta \approx 11.7°$) and a bit of α-phase nuclei (with peak at $2\theta \approx 13.9°$), the TMU-CR film formed α-phase nuclei superior to the δ-phase counterpart (**Figure 4.7c**). This indicates that the $FAI{\cdot}PbI_2{\cdot}$TMU adduct preferably transfers into the α-phase instead of the δ-phase $FAPbI_3$ nuclei compared with $FAI{\cdot}PbI_2{\cdot}$DMSO adduct, probably benefiting from the lower activation energy that required for the transformation as illustrated in the energy bands diagram embedded in **Figure 4.5d**.[178]

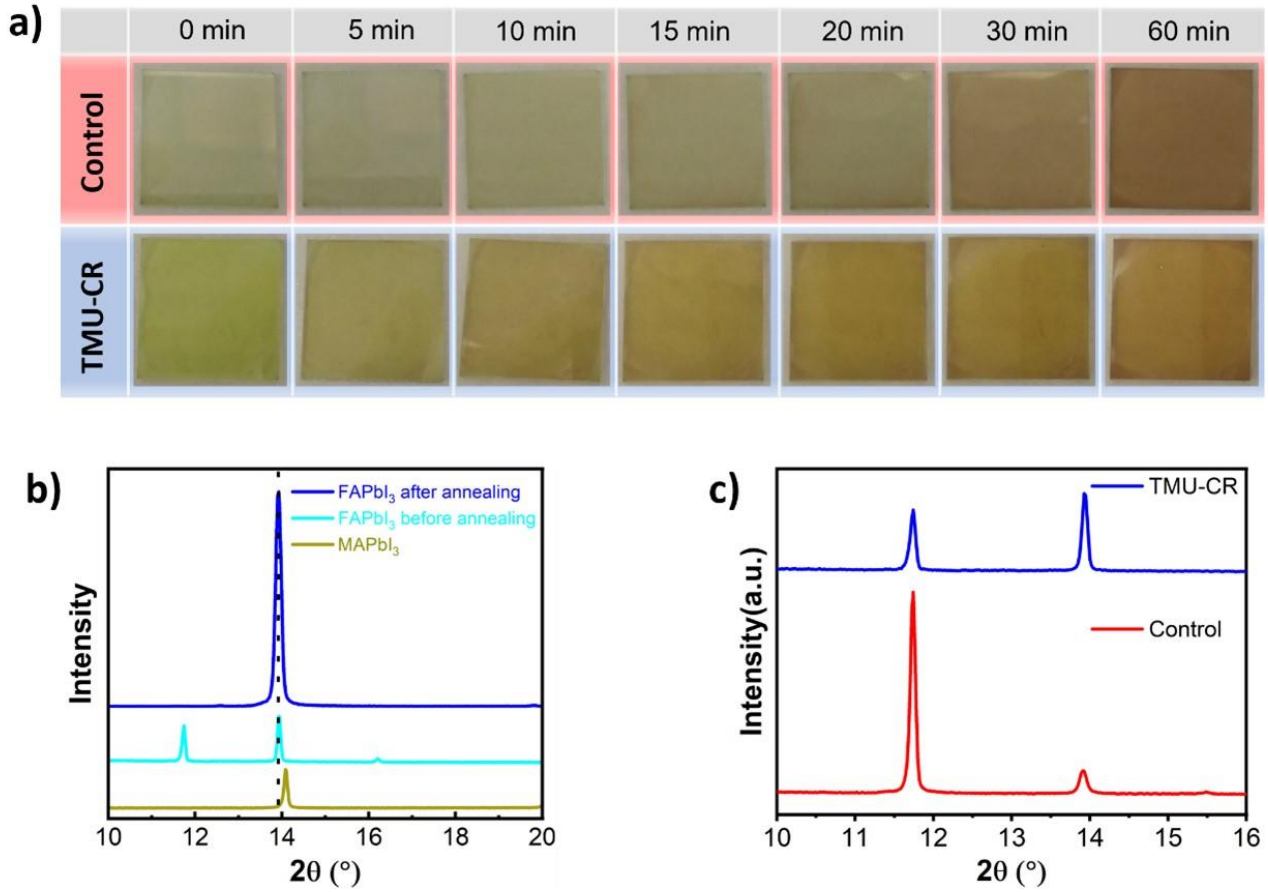

Figure 4.7. Study of crystallization dynamic of perovskite films based on different solvent coordinators. a) Photographs of the as prepared adduct films aging for various time at room temperature. b) XRD patterns of the perovskite films of $FAPbI_3$ before and after annealing, and $MAPbI_3$. c) XRD patterns of adduct films aging for 30 min at RT.

$FAI{\cdot}PbI_2{\cdot}TMU$ adducts also promoted direct formation of α-$FAPbI_3$ and inhibits the formation of δ-$FAPbI_3$ intermediate phase, which was demonstrated by the in-situ GIWAXS measurements during the annealing process (**Figure 4.8**). After spin-coating, both resulting perovskite wet films were placed on a heat plate at room temperature, which was then immediately heated to 150 °C with a rate of 60 $K{\cdot}min^{-1}$ and kept constant. 2D contour maps of time-dependent in-situ GIWAXS were obtained accordingly (**Figure 4.8a, b**). Representative 2D GIWAXS patterns are shown in **Figure 4.8c-h**. The peaks at $q{\approx}0.82$ $Å^{-1}$ and $q{\approx}1.00$ $Å^{-1}$ were assigned to (100) plane of δ-$FAPbI_3$ and α-$FAPbI_3$,

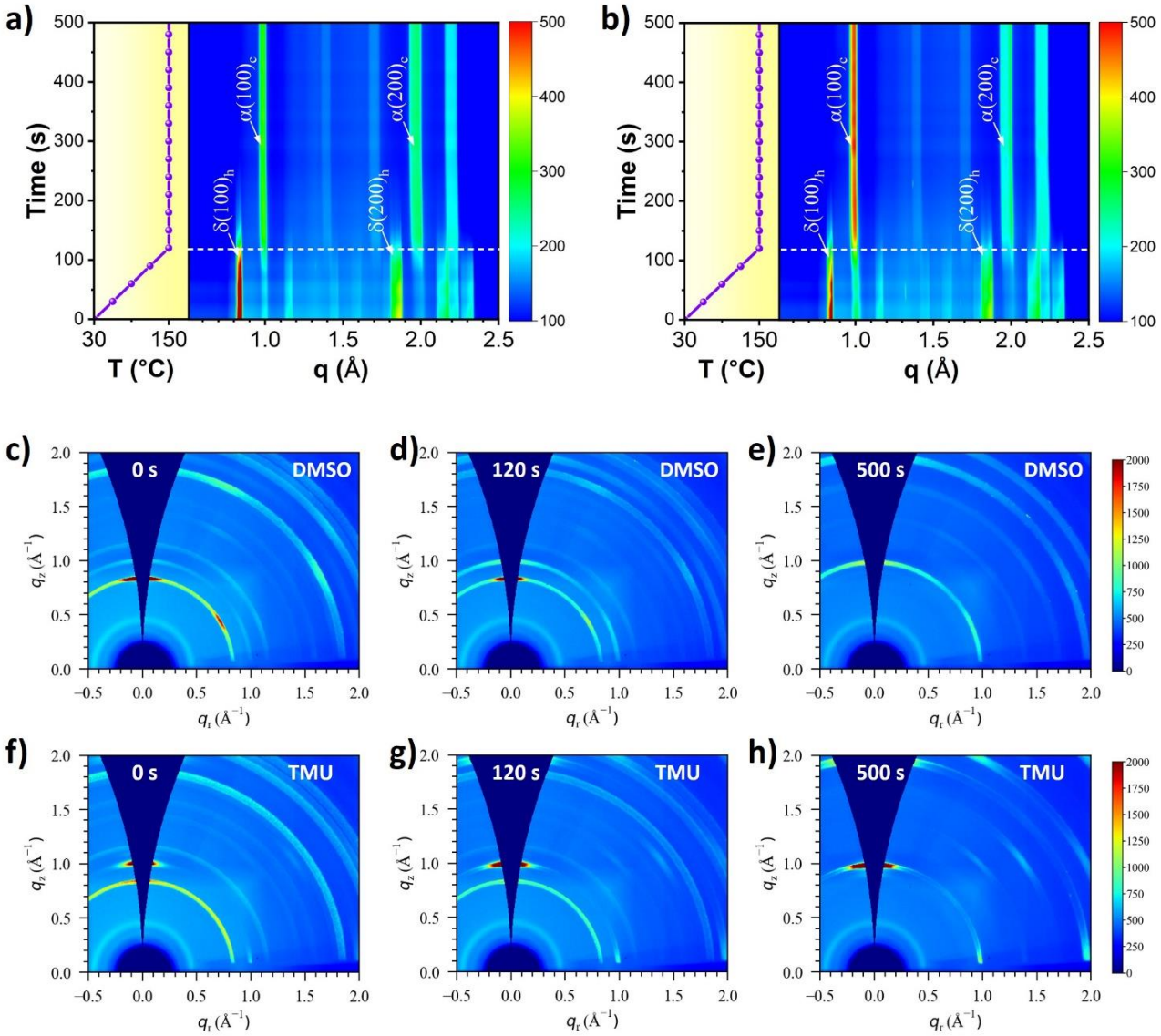

Figure 4.8. Study of crystallization dynamic of perovskite films based on different solvent coordinators. a, b) In-situ GIWAXS patterns of d) control and e) TMU-CR perovskites. c-h) Representative 2D GIWAXS patterns of c-e) control and f-h) TMU-CR perovskite films during the annealing process.

respectively (**Figure 4.8a, b**; **Figure 4.9**). Both δ-$FAPbI_3$ and α-$FAPbI_3$ were observed in both the control film and the TMU-CR film at the beginning of annealing, indicating that α-phase crystal nuclei formed immediately after spin-coating and δ-$FAPbI_3$ was formed due to the escape of Lewis base from the adduct films (**Figure 4.8a, b**). $FA_aPb_bI_c(coordinator)_d$ adduct intermediate can be

characterized structurally during the crystallization process through GIWAXS and XRD measurements, where the peaks will be at the regions of $q<0.8$ Å^{-1} and $2\theta<10°$, repectively.[37, 150, 179] However, peaks in the region of $q<0.8$ Å^{-1} were not observed in my GIWAXS patterns from the beginning to the end of annealing, suggesting that no other intermediate phases formed during the whole annealing process (**Figure 4.8a, b**; **Figure 4.9a, b**).

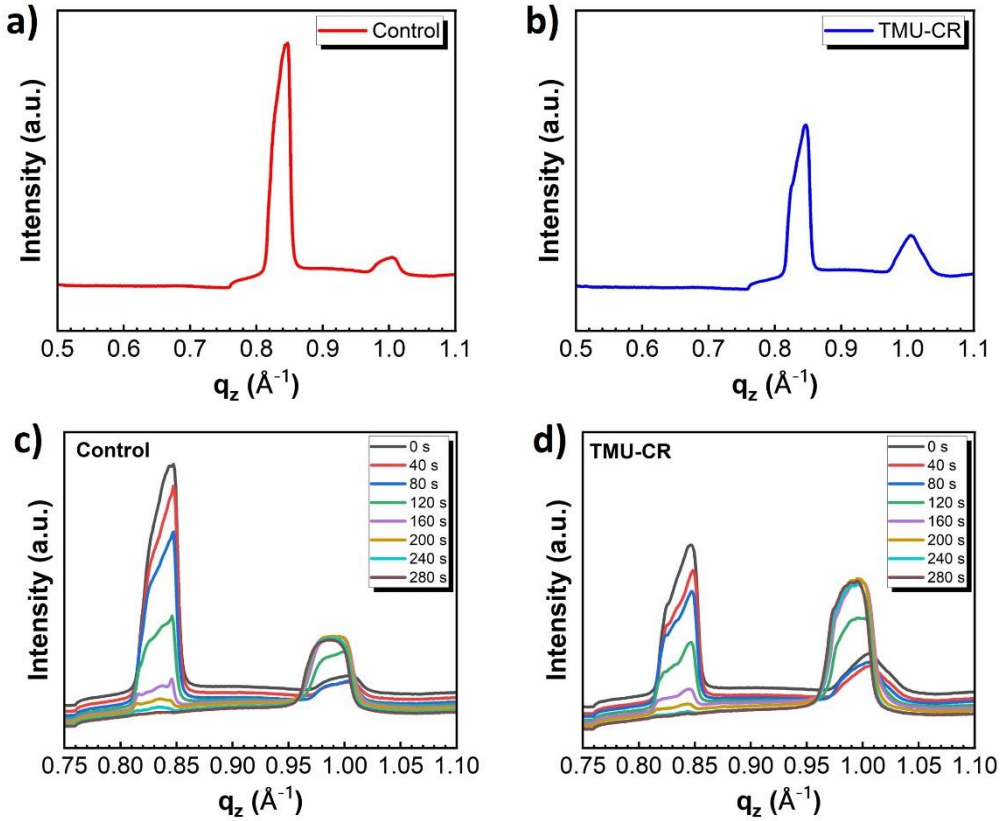

Figure 4.9. a, b) 1D GIWAXS patterns derived from 2D GIWAXS patterns of intermediate adduct films at the beginning of annealing. c, d) 1D GIWAXS patterns derived from 2D GIWAXS patterns of intermediate adduct films at various time of annealing.

As presented, the control film generates mainly δ-$FAPbI_3$ coordinated with a negligible amount of α-$FAPbI_3$ at the initial annealing (**Figure 4.8a, Figure 4.9a**). Yet the situation for TMU-CR film is

quite different, where the intensity of δ-$FAPbI_3$ signal significantly decreases and that of α-$FAPbI_3$ is tremendously enhanced (**Figure 4.8b; Figure 4.9b**). This indicates that the formation of δ-$FAPbI_3$ was inhibited, and the $FAI{\cdot}PbI_2{\cdot}$TMU adducts preferentially transformed into α-$FAPbI_3$, which is consistent with previous analysis of their XRD patterns. It is noteworthy that δ-$FAPbI_3$ in the control film is highly oriented to (100) out-of-plane direction, while that in the TMU-CR film is equally oriented to different direction. The orientation for α-$FAPbI_3$ nuclei, on the other hand, is just the reverse (**Figure 4.8c, f**). This suggests a higher potential for the TMU-CR film to form high-quality α-$FAPbI_3$ perovskite film, which is the key to obtaining high performance PSCs.

With temperature increased, the δ-$FAPbI_3$ gradually transform into α-$FAPbI_3$ in both the control film and the TMU-CR film. Meanwhile, the α-$FAPbI_3$ nuclei continually grows. When the annealing temperature reached 150 °C at the 120s, the phase transition from δ-phase to α-phase was accelerated, and α-$FAPbI_3$ rapidly grow to their highest level (**Figure 4.8d, g**). Phase transformation and growth rate of α-$FAPbI_3$ for both films were determined to be similar, as exhibited in 1D GIWAXS patterns derived from 2D GIWAXS patterns (**Figure 4.9c, d**). This means that the δ-$FAPbI_3$ disappearance and α-$FAPbI_3$ reaching a peak of both films happened at similar time. The resulting TMU-CR film exhibits much higher crystallinity with preferable (100) out-of-plane orientation, compared with the control (**Figure 4.8e, h**). This led to a conclusion that using TMU as a coordinator can readily promote the formation of (100) out-of-plane oriented α-$FAPbI_3$ but barely affect their growth rate, and this benefits both the orientation and the grain size of the resulting α-$FAPbI_3$ film.

4.5 Film quality investigation

Based on the above understanding of their crystallization dynamics, the TMU-CR film was expected to possess higher film quality with better physical and photoelectrical characteristics compared to the control. SEM was performed to estimate both the surface and cross-sectional morphologies of perovskite films. **Figure 4.10a, b** shows the top-view morphologies of both the control and the TMU-CR films. Both show grains in irregularly shaped with lateral grain size approaching 1 μm. This is consistent with their similar crystallization rate mentioned previously. Compared with the control film, which display tiny gaps at grain boundaries in part of the regions, the TMU-CR film is highly compact. This phenomenon was also observed in their cross-sectional SEM images (**Figure 4.10c, d**). In addition, bubbles were observed in the bulk of the control grains, which may be generated during the removal of DMSO residues due to the high evaporation temperature (~190 °C) of DMSO. This undesirable defect, however, is eliminated from the TMU-CR film, benefiting from the easy evaporation of TMU. These gaps and bubbles in the control films play as centers for carrier recombination, which, therefore reduces the performance of the as fabricated PSCs. The TMU-CR film, on the other hand, did not present such phenomena. Benefiting from the CR process, the TMU-CR film was “polished” to a decreased surface roughness of 11.7 nm compared to 16.9 nm for the control film (**Figure 4.10e, f**). This contributes to the tight contact with ETL, and thus benefits the electron transfer.

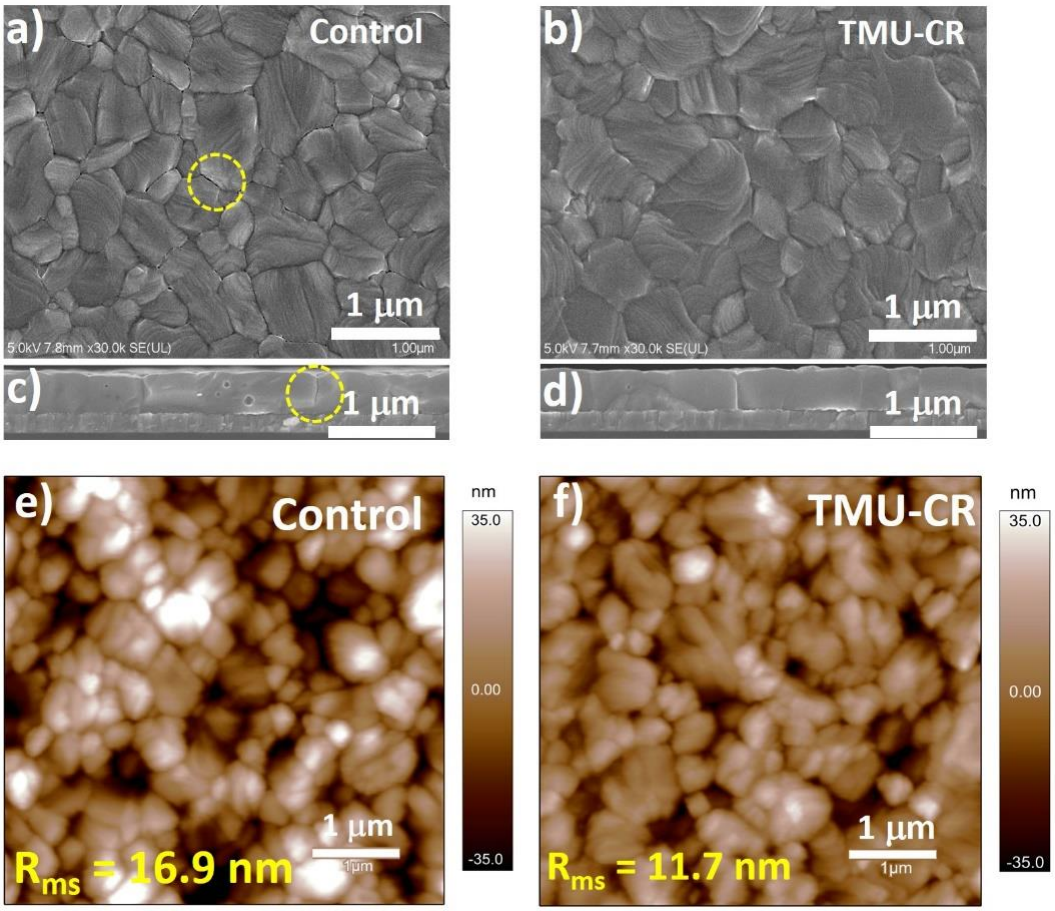

Figure 4.10. a, b) Top-view SEM images of the a) control and b) TMU-CR perovskite. c-d) Cross-sectional SEM images of the c) control and d) TMU-CR perovskite. AFM images of e) control and f) TMU-CR perovskite films.

The TMU-CR film also shows superior light absorption compared to the control according to the UV-vis absorption spectra (**Figure 4.11a**). This was ascribed to a higher crystallinity of the TMU-CR film. Furthermore, the PL and TRPL show improvement of film quality for TMU-CR perovskite. As shown in **Figure 4.11a**, both static-state PL spectra have peaks at 805 nm, which is close to the band edge of UV-vis absorption. However, the intensity of the TMU-CR pattern is nearly twice of the control, demonstrating a lower trap density in the TMU-CR film and thus the non-radiative recombination was inhibited. This is in support of the analysis of their SEM images. Similarly, the average carrier

lifetime of TMU-CR film evaluated through TRPL is calculated to be 776 ns, which is more than two times to 349 ns of the control (**Figure 4.11b**, **Table 4.3**). This further demonstrated the improvement of film quality prepared through TMU-CR approach.

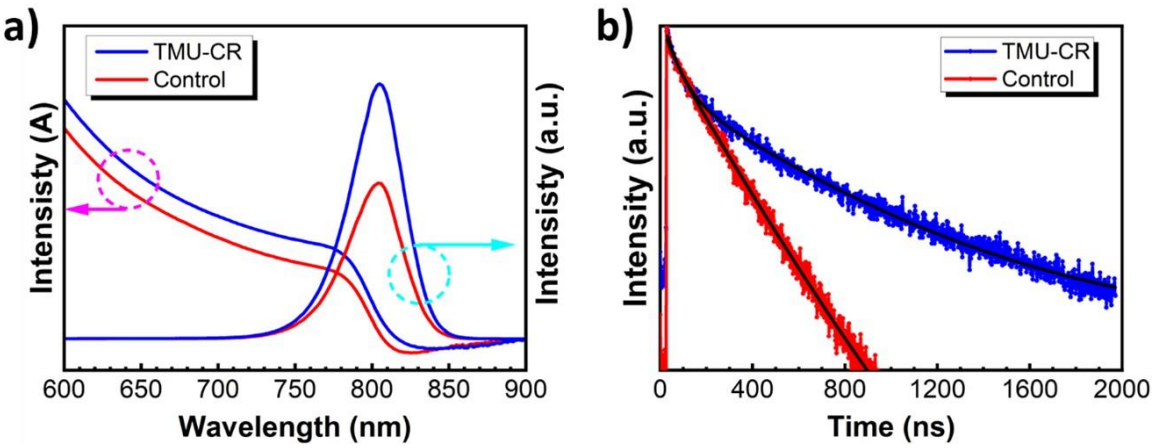

Figure 4.11. a) UV-vis absorption (left axis) and PL (right axis) patterns of as prepared perovskite films. b) TRPL patterns of perovskite films. The fitting of the spectra was based on **Equation 3.2** and the average lifetimes were calculated through **Equation 3.3** as depicted in **Section 3.4.3**.

Table 4.3. Fitting parameters of TRPL patterns of control and TMU-CR perovskite films. The TRPL spectra were fitted through **Equation 3.2** and the average lifetimes (τ_{ave}) of perovskite films were calculated via **Equation 3.3** based on the fitting fast-decay-time constant (τ_1) and slow-decay-time constant (τ_2).

	A_1	τ_1 (ns)	A_2 (%)	τ_2 (ns)	τ_{ave} (ns)
Control	31.12	14.39	52.72	357.31	349.34
TMU-CR	10.66	64.84	83.50	784.05	776.54

To get a deeper insight to the non-radiative recombination, photoelectric properties and carrier transfer dynamic in both the control and TMU-CR films were further investigated through ultra-fast TAS. Both films were deposited on quartz glass and illuminated on the top surface with a 400-nm

pump laser. 2D contour maps of TA spectra were shown in **Figure 4.12a, b**, and representative 1D transient TA spectra at various decay time were derived from the 2D TA spectra for better observation (**Figure 4.12c, d**). The Negative signals observed at around 785 nm are attributed to photobleaching (PB, $\Delta A < 0$), which are related to excited charges at the band edge, the relaxation of hot carriers from bimolecular recombination, and trap-assisted monomolecular recombination.[160, 180] The intensity of the PB negative signal of TMU-CR film exhibits a larger ΔA value compared to the control, indicating a higher light absorption and higher carrier density. This is consistent with the increased

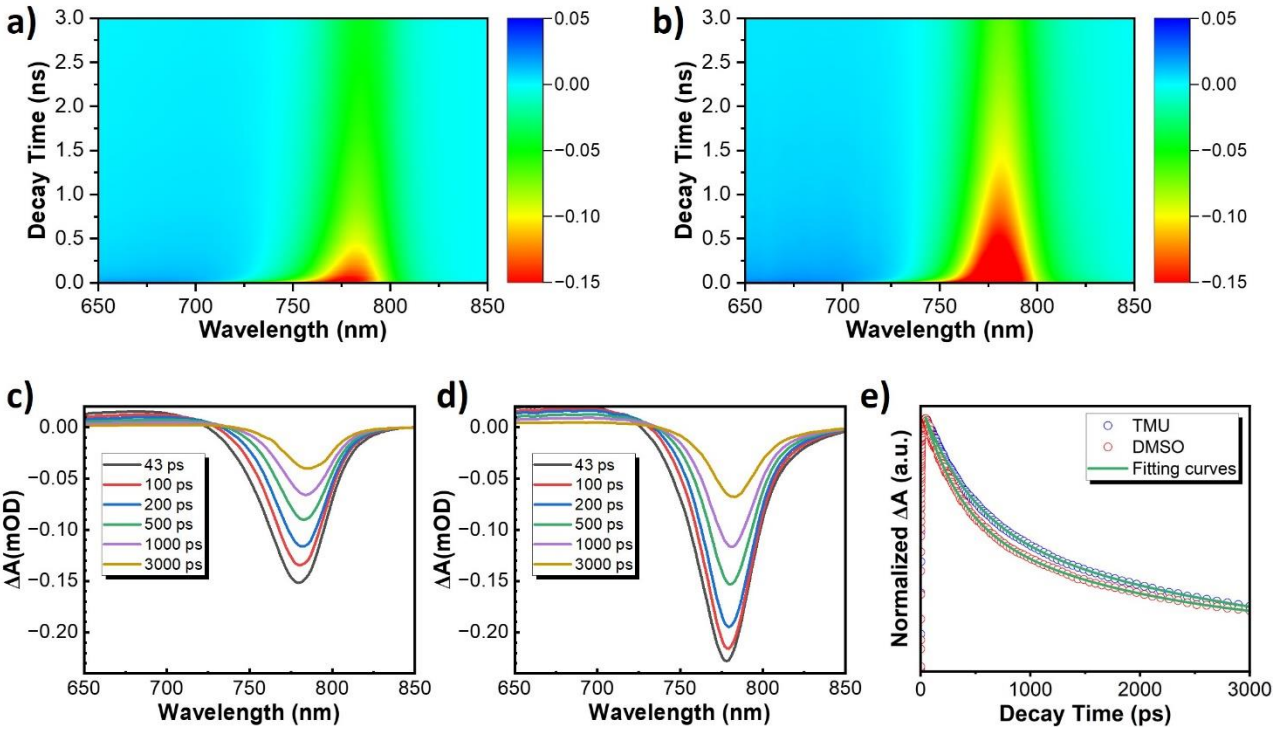

Figure 4.12. a, b) Ultra-fast TA analysis of the a) control and b) TMU-CR perovskite films deposited on quartz glass. The scale bar is the intensity of diffraction. c, d) 1D transient TA spectra at various decay time derived from the 2D Ultra-fast TA spectra of c) control and d) TMU-CR perovskite films. e) Normalized TA decays at 785 nm of 2D TA spectra, and their fitting curves. ΔA is the signal derectly obtained from the measurements, and it was the difference between the probe absorption $A(\lambda)$ obtained by irradiating the sample with the probe light minus the probe absorption $A_0(\lambda)$ obtained by directly exciting the sample with the probe light.

UV-vis absorption.[181, 182] Normalized PB decays at 785 nm were derived from 2D PB signals of both the control and TMU-CR films (**Figure 4.12e**)were fitted with a bi-exponential equation (**Equation 3.2**). The corresponding fitting parameters and the average lifetime calculated from **Equation 3.3** are listed in **Table 4.4**. Compared to 1630.4 ps of the control film, the ns-TAS decay lifetime of TMU-CR films significantly increased to 2701.1 ps, demonstrating a significantly suppressed defect-assisted non-radiative recombination.

Table 4.4. Fitting parameters of TA decays in **Figure 4.12e**. The TA spectra were fitted through **Equation 3.2** and the average lifetimes (τ_{ave}) of perovskite films were calculated via **Equation 3.3** based on the fitting fast-decay-time constant (τ_1) and slow-decay-time constant (τ_2).

	A_1	τ_1 (ps)	A_2	τ_2 (ps)	τ_{ave} (ps)
Control	0.444	334.2	0.476	1848.9	1630.4
TMU-CR	0.456	459.0	0.541	2991.1	2701.1

The enhanced film quality was further supported by XRD and GIWAXS analysis. As displayed in **Figure 4.13a**, both XRD patterns of the films confirm a well-crystalline α-phase perovskite with negligible PbI_2, but the peak intensity of the TMU-CR films is enhanced compared to that of the control, proving a significant gain in film crystallinity. Besides, a higher orientation in TMU-CR film can be also recognized from the XRD patterns. These are further confirmed by GIWAXS measurements. As shown in the 2D GIWAXS patterns, the diffraction rings assigned to the (100) plane of TMU-CR perovskite film is brighter than that of the control, suggesting a higher crystallinity (**Figure 4.13b, c**). In addition, the majority diffraction intensity of TMU-CR film concentrates to a

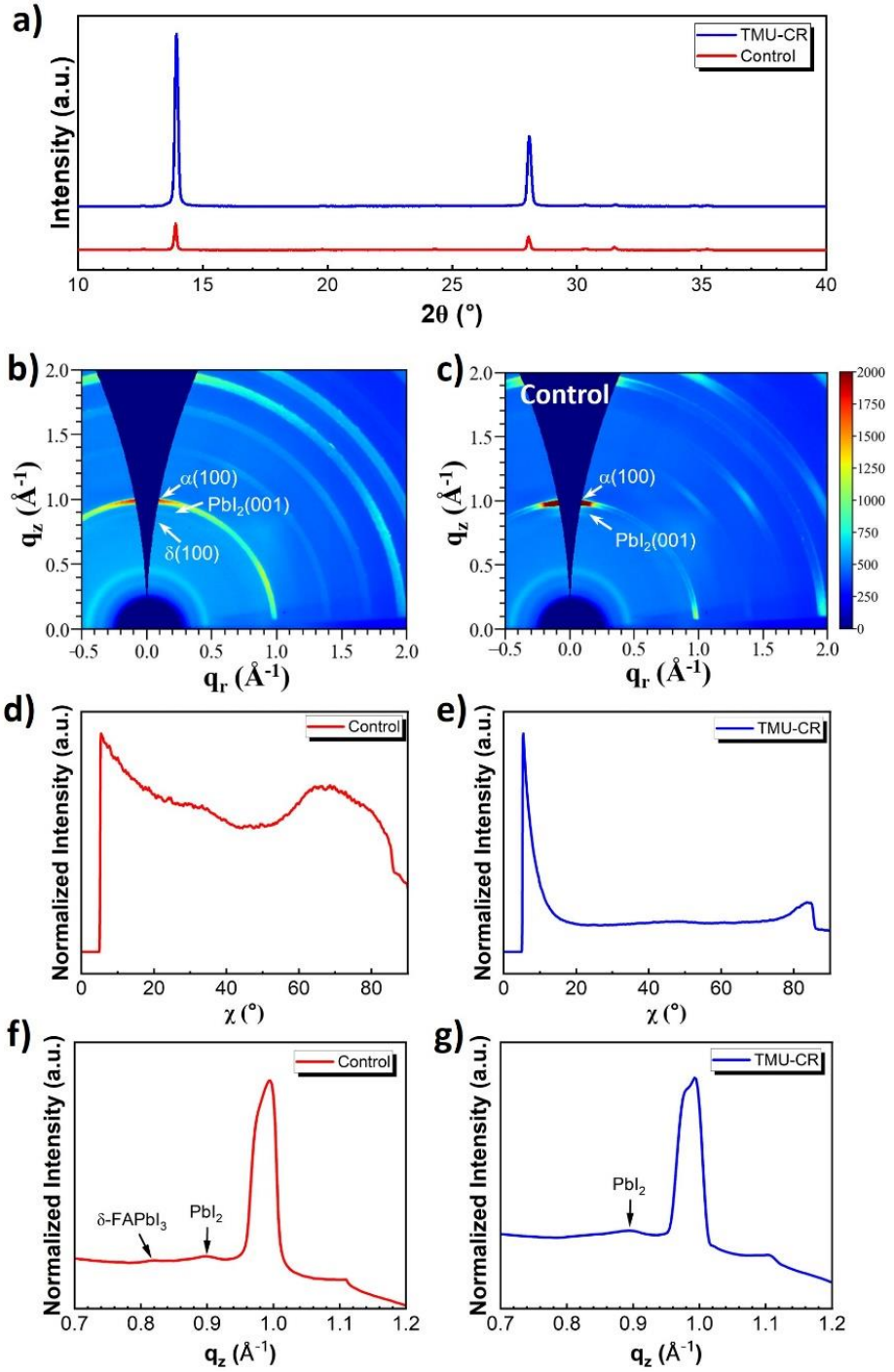

Figure 4.13. a) XRD patterns of as prepared perovskite films. b, c) 2D GIWAXS maps of the b) control and c) TMU-CR perovskite films. The scale bar is the intensity of diffraction. d, e) Azimuthal angular intensity of the (100) plane integrated from the 2D GIWAXS patterns of d) control and e) TMU-CR perovskite films. f, g) Integral patterns of 2D GIWAXS patterns of f) control and g) TMU-CR perovskite films.

narrow angle range, demonstrating a highly out-of-plane orientation (**Figure 4.13c**). The control, on the other hand, is more likely distributed to all direction evenly, though the intensity is relatively higher in out-of-plane direction (**Figure 4.13b**). Moreover, the azimuthal angular intensity of the (100) plane was also integrated from the GIWAXS patterns to illustrate their difference more clearly (**Figure 4.13d, e**).

For the control film, a broad distribution from 0-90° azimuthal angle (φ) was observed, suggesting that there is crystal growth evenly in all directions (**Figure 4.13d**). In contrast, the TMU-CR film exhibits only one sharp peak at the low azimuthal angle (φ), revealing that TMU-CR perovskite assemble in only one direction, that perpendicular to the substrate (**Figure 4.13e**). It is also noteworthy that besides PbI_2, a small quantity of δ-$FAPbI_3$ was observed in the 2D GIWAXS pattern of the control as well as its integral pattern (**Figure 4.13f**), whilst none is observed in that of the TMU-CR film (**Figure 4.13h**). The elimination of non-photoactive δ-$FAPbI_3$ certainly accounts for a lower trap density and enhanced stability of the film. In short, the above evidence all robustly support that α-$FAPbI_3$ perovskite film fabricated through the TMU-CR method is of high quality with much higher crystallinity and preferable (100) plane out-of-plane orientation.

Phase stability, another factor to evaluate the quality of a α-$FAPbI_3$ perovskite film, mainly determined by the residual lattice strain (ε) in the perovskite films. I first used Williamson–Hall (WH) method to evaluate their difference in out-of-plane lattice strain according to the XRD peaks

broadening in **Figure 4.13a**.[115] Lattice strains of the control and TMU-CR α-$FAPbI_3$ perovskite films, obtained from the slopes of the fitting curves, were estimated to be 4.42×10^{-4} and 1.09×10^{-4}, respectively (**Figure 4.14**). A positive value of the lattice strain suggests a tensile strain. Accordingly, both films exhibit a tensile lattice strain in the out-of-plane direction, and perovskite films fabricated from TMU-CR method show a notable relaxation of tensile strain. This suggests improved film quality and phase stability of the TMU-CR α-$FAPbI_3$ films, as internal tensile strain within the α-$FAPbI_3$ unit cell contributes to the formation of vacancies, and subsequently α-to-δ phase transition.[147]

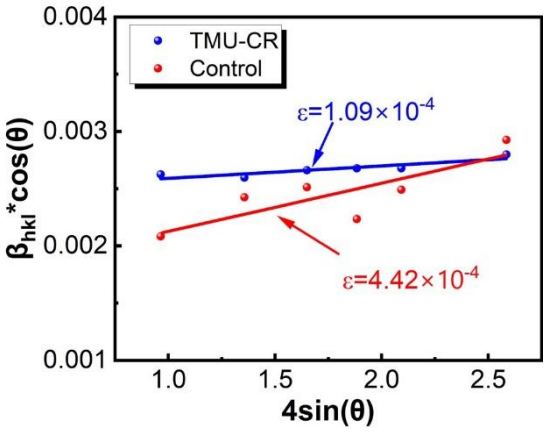

Figure 4.14. WH plots of the perovskite films. β_{hkl} is the value of FWHM of the relevant XRD peak.

To further support the above results and provide more details of the lattice strains inside the α-$FAPbI_3$ films, 1D GIWAXS patterns were obtained from the 2D patterns by plotting along out-of-plane (q_z) (**Figure 4.15a**) and in-plane (q_r) (**Figure 4.15b**) directions. The (100) out-of-plane peaks shown negligible shift, while the in-plane (100) peaks of TMU-CR film exhibits a noticeable shift of 0.003 $Å^{-1}$ to a lower q value, compared to the peak of the control. This indicates an increase in d-space of (100) plane, and thus a lattice expansion in the in-plane direction. This result is consistent with the

relaxation of lattice expansion perpendicular to substrate, determined by the WH method. This is related to the fact that when d-space decreases in the out-of-plane direction, that in the in-plane direction must increase to keep its lattice volume.[155] Therefore, the in-plane lattice expansion is attributed to the relaxation of in-plane compressive strain. This was also supported by the decrease of strain-induced band gap energy (E_g) as presented in **Figure 4.15c**. [155]

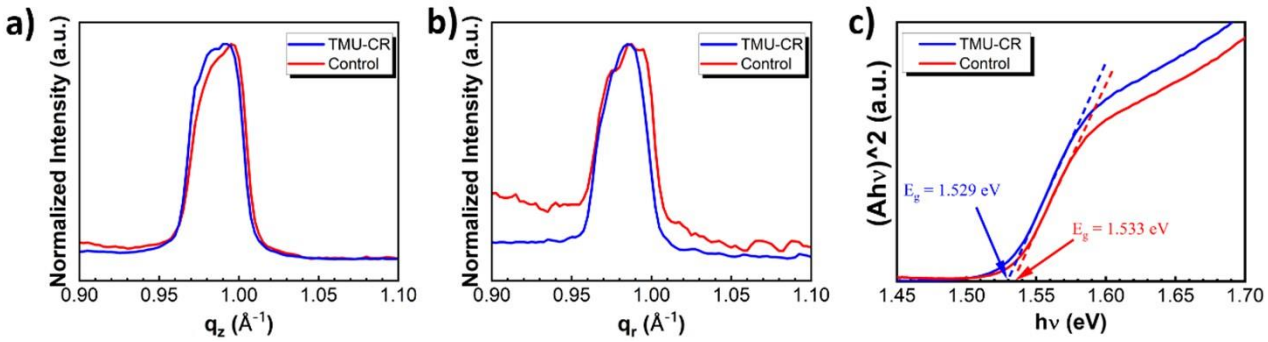

Figure 4.15. Normalized 1D GIWAX patterns of the control and TMU-CR perovskite films in a) out-of-plane and b) in-plane directions. c) Tauc-plots of perovskite films.

4.6 Amelioration of energy band alignment

Besides the improved quality of perovskite films, the semiconducting characteristic and energy band structure of the perovskite films as well as the energy band alignment inside the devices are also critical for achieving a high-performance PSC. To determine whether the optimized TMU-CR fabrication method alters the semiconducting feature and energy band structures of the α-$FAPbI_3$ perovskite film, I first performed UPS along with UV-vis measurements to estimate the VBM, WF, E_f, and CBM of perovskites. As shown in **Figure 4,16a**, WF of the control and TMU-CR perovskite films were obtained from the cut-off of the UPS patterns, which were determined to be 5.01 eV and

5.14 eV, respectively. Their Fermi level, therefore, are at -5.01 eV and -5.14 eV relative to the vacuum energy level. The VBMs with respect to Fermi level were evaluated to be 0.77 eV and 0.64 eV for the control and TMU-CR films, suggesting intrinsic and p-type semiconducting nature, respectively. Their VBMs were therefore calculated to have the same value, -5.78 eV. The bandgap (E_g) of the perovskite films determined by the Tauc-plots, derived from the UV-vis patterns, both give values of 1.53 eV (**Figure 4.15c**). CBMs calculated from E_g and VBM, therefore, are both -4.25 eV. This means that TMU-CR method does not change the VBM and CBM of the perovskite but leads to a 0.13 eV downshift of the Fermi level, and hence modifies the intrinsic nature of the perovskite to a p-type

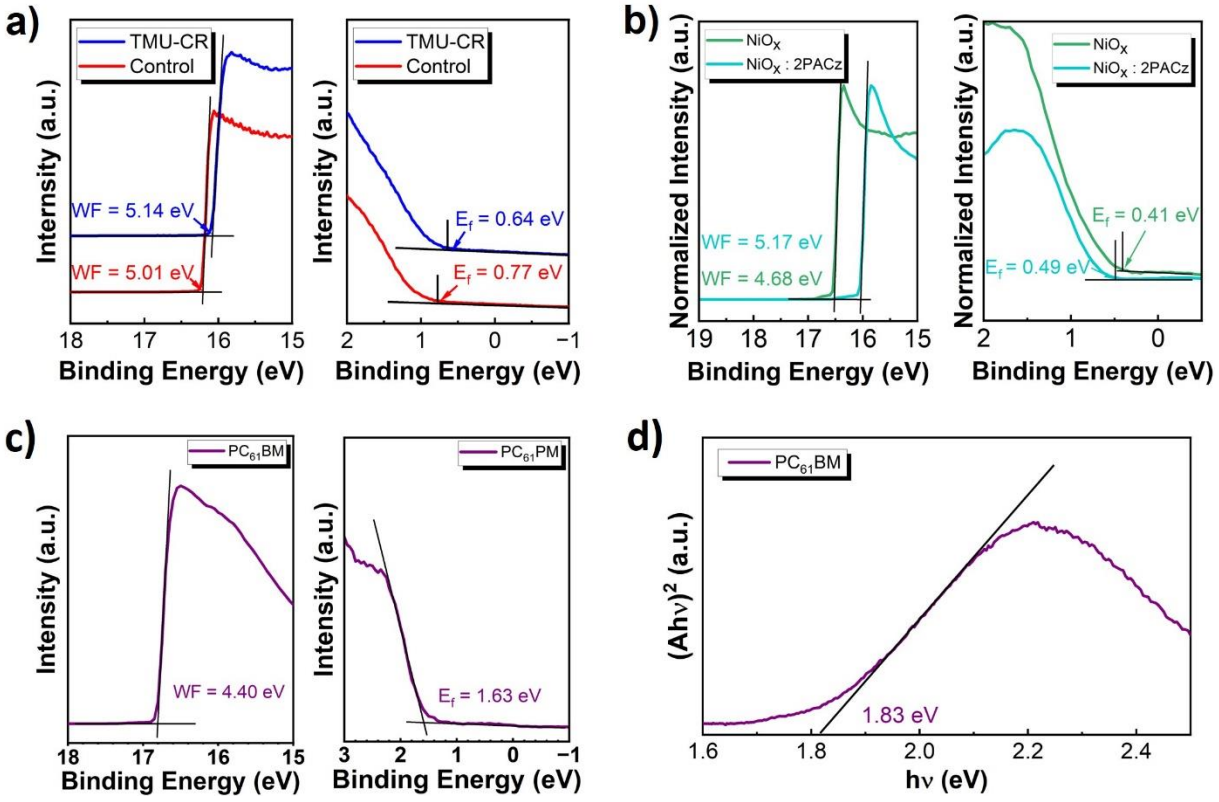

Figure 4.16. UPS spectra of the a) perovskite films. b) NiOx and NiOx:2PACz as well as c) PCBM. d) Tauc-plot of PCBM derived from UV-vis absorption.

semiconducting nature. What is noteworthy is that the change in semiconducting nature helps to account for the advanced performance of TMU-CR PSCs.

To elucidate the above clarification, the VBM of the HTL and CBM of the ETL were further acquired from their UPS patterns and Tauc-plots through the same calculation method (**Figure 4.16b-d**). Accordingly, the VBM of HTL and CBM of ETL were evaluated to be -5.66 eV and -4.20 eV, respectively. Band alignment of perovskite with HTL and ETL was thus summarized in **Figure 4.17** according to the results obtained above. Taking a look at the top-surface of the perovskite, the energy band offset (ΔE) between CBM of perovskite and CBM of PCBM is only 0.05 eV, which is believed to have negligible hindrance on the electron transport. The ΔE = 0.12 eV between the VBM of perovskite and VBM of NiOx/2PACz substrate, is much higher than that at the top interface. This more likely induces a great barrier for hole extraction. A p-type perovskite fabricated through the TMU-CR method can construct an internal electric field that points from the top to the bottom of

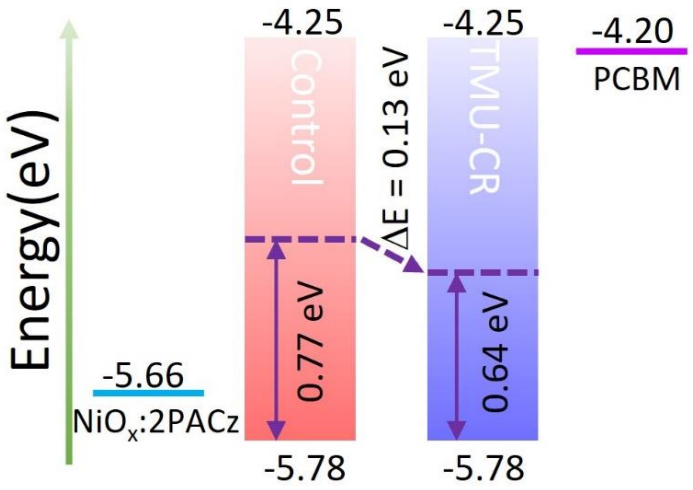

Figure 4.17. Energy band alignment at top and bottom interface of perovskite films in their PSCs.

perovskite. This therefore benefits the hole extraction at the bottom interface of perovskite and alleviates the obstacle caused by the considerable energy band offset between the perovskite and HTL.

The decrease in Fermi level of TMU-CR perovskite film is also affirmed by KPFM, which is measured accompanied with the surface morphology scanning as presented previously (**Figure 4.10**). As shown in **Figure 4.18a, b**, the surface potential of the control and TMU-CR perovskite films is distinct in a scope of 5μm × 5μm square. A lower surface potential of TMU-CR films points to a larger work function and thus a deeper Fermi level, which is in accordance with the results estimated from UPS measurements. KPFM line scans were derived from the KPFM maps (red lines in **Figure 4.18a, b**) to exhibit the change numerically, as shown in **Figure 4.18c**. The average surface potential for the control and the TMU-CR films are calculated to be 94.84 mV and -21.03 mV, respectively. Their potential difference is therefore around 0.12 V, which is consistent with their energy difference (0.13 eV) measured by the UPS technique. This demonstrated the reliability of the UPS results and supported the superiority of the semiconducting nature of the TMU-CR films.

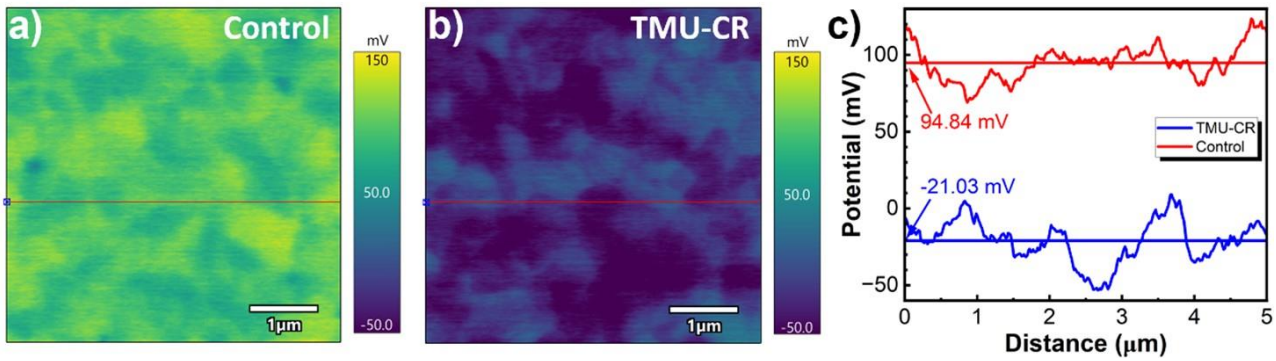

Figure 4.18. a, b) KPFM images of the a) control and b) TMU-CR perovskite films. c) Line scans derived from the KPFM images at the axis of y = 2.0 μm.

4.7 Performance of PSCs

Possessing the merits of high film quality and superior semiconducting properties, PSCs with TMU-CR α-$FAPbI_3$ perovskite films are expected to exhibit both enhanced power conversion performance and long-term stability. I therefore fabricated PSCs with an inverted planar structure to investigate their performance and long-term stability. The detailed device structure is ITO/NiOx/2PACz/Perovskite(α-$FAPbI_3$)/PEABr/PCBM/BCP/Ag, as shown in **Figure 4.19a**. J-V curves of both champion devices fabricated from the control and TMU-CR methods are presented in **Figure 4.19b**, with their detailed photovoltaic parameters embedded. Compared to the control device with a PCE (η in tables) of 21.28% in reverse scanning, the TMU-CR device shows a significantly increased PCE of 23.18%, with its V_{oc} increasing from 1.10 V to 1.13 V, J_{sc} increasing from 24.72 $mA{\cdot}cm^{-2}$ to 25.15 $mA{\cdot}cm^{-2}$, FF increasing from 78.24% to 81.58%. The increased J_{sc} in TMU-CR device is supported by the increased integral J_{sc} from 23.5 $mA{\cdot}cm^{-2}$ to 24.1 $mA{\cdot}cm^{-2}$ derived from their EQE, as shown in **Figure 4.19c**. Integral J_{sc} are both within 5% loss compared to those measured from their J-V curves, in support of the reliability of the high J_{sc}. Moreover, the performance of the control device in forward scanning is much inferior to that in reverse scanning, suggesting a noticeable hysteresis and thus abundant trap density presented in the perovskite film. Furthermore, negligible hysteresis is observed in the TMU-CR device, proving a significantly improved α-$FAPbI_3$ film quality with suppressed defects density.

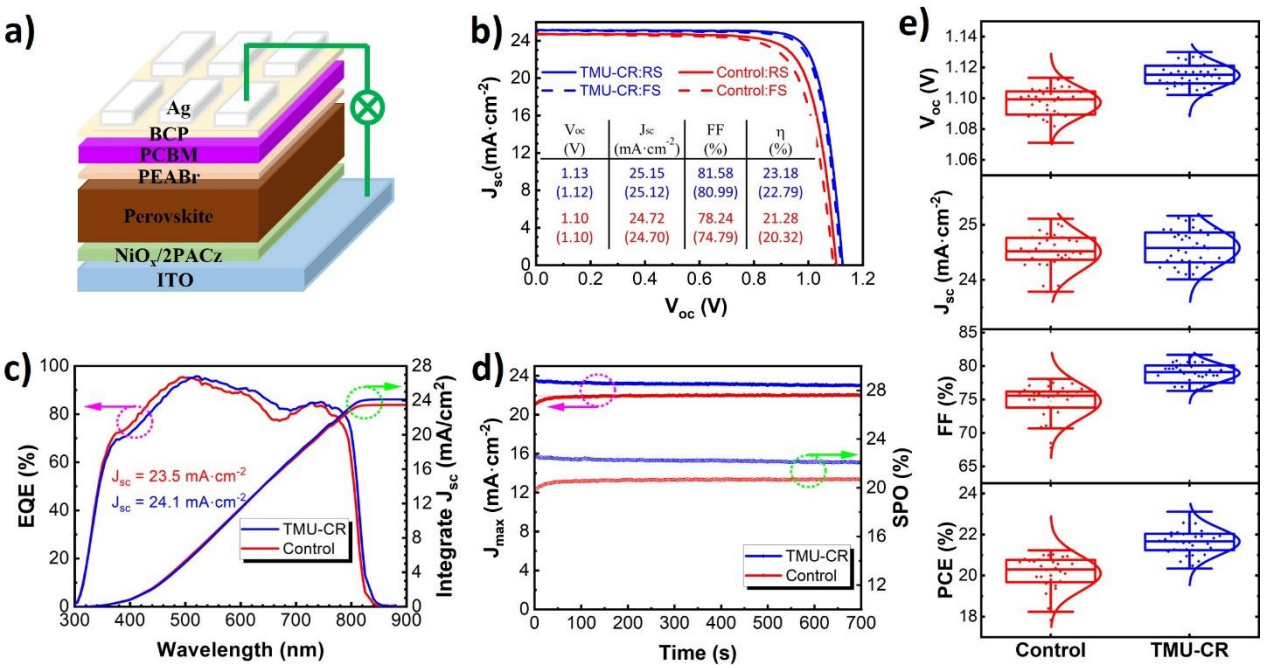

Figure 4.19. a) Schematic of the structure of as prepared PSCs. b) J-V curves in reverse (solid line) and forward (dashed line) scans of champion PSCs under illumination (AM 1.5 G, 100 $mW \cdot cm^{-2}$). c) EQE (left) and their integral J_{sc} (right) patterns of the champion PSCs. d) SPO current density (left) and PCE (right) of unencapsulated PSCs at the voltage of maximum power point (MPP). e) Performance distribution for 30 devices of each set of devices.

SPO is more reliable for estimating the PCE of a device. Hence, I performed SPO to track the current densities and efficiencies of both champion devices at voltages of their fixed maximum power point (MPP), which are 0.94 V for the control and 0.98V for TMU-CR PSCs. As shown in **Figure 4.19d,** after continuous exposure to 1-sun illumination for 700 s**,** the control device displays a stable current density of 21.93 $mA \cdot cm^{-2}$, while the TMU-CR one exhibits a higher current density of 23.13 $mA \cdot cm^{-2}$. The steady-state PCE can therefore be calculated from the current density and MPP voltages to be 20.61% and 22.67% respectively. This increase in the steady PCE is in agreement with the J-V results and thus demonstrates a remarkable improvement of device performance.

The performance distribution of a batch of 30 devices was also conducted to estimate their reproducibility (**Figure 4.19e**). Their detailed photovoltaic parameters are summarized in **Table 4.5**. As presented, the average efficiency of the control and the TMU-CR PSCs are 20.11±0.86% and 21.66±0.65%, respectively. The enhanced statistical efficiency and reduced statistical derivation in V_{oc}, FF, and PCE lead to my conclusion that the TMU-CR approach benefits both performance and reproducibility of PSCs.

Table 4.5. Average and standard derivation of photovoltaic parameters for 30 pieces of PSCs prepared from each method. The parameter η refers to PCE.

Samples	V_{oc}(V)	J_{sc}(mA·cm^{-2})	FF(%)	η(%)
Control	1.097±0.009	24.51±0.35	74.75±2.60	20.11±0.86
TMU-CR	1.115±0.008	24.59±0.33	78.97±1.39	21.66±0.65

4.8 Device physics

To understand the intrinsic mechnism of their improvement in photovoltaic performance, I then performed a series of characterization on the device physics of the PSCs. Firstly, the increase in build-in potential (V_{bi}) from 0.85 V to 1.00 V as shown in **Figure 4.20a** provides a solid validation in the improvement of V_{oc} as shown in the J-V curves and V_{oc} distribution (**Figure 4.19b, e**). Then, EIS of PSCs was performed to study their intrinsic resistance (**Figure 4.20b**). The parameters fitted from Nyquist plots using the equivalent circuit model embeded in **Figure 4.20b** are listed in **Table 4.6**. The TMU-CR PSC generates a remarkably increased recombination resistance (R_{rec}) of 3457.0 Ω

compared to 919.6 Ω of the control. Meanwhile, its charge transfer resistance (R_s) is slightly reduced from 15.34 Ω to 12.19 Ω. The increase in R_{rec} and decrease in R_s augments the barrier for charge recombination and remove the ostacle for charge extraction, which benefit the carrier transfer and therefore help to explain the enhancement of the perfermance.

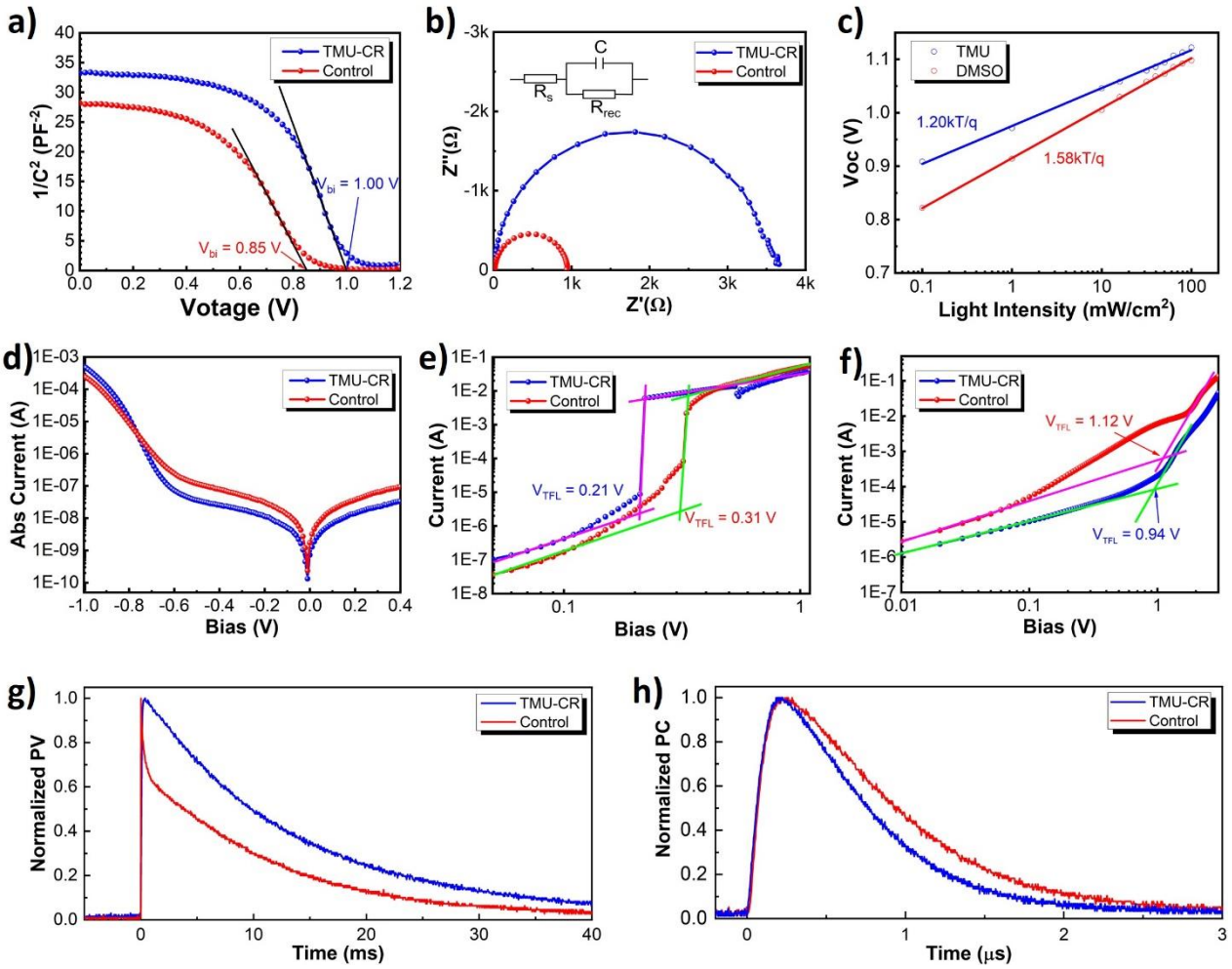

Figure 4.20. a) Mott-Schottky plots of as prepared PSCs. b) Nyquist plots of PSCs measured at a voltage of 0.95 V near their MPP voltage. The equivalent circuit model for fitting was embedded. c) Plots of V_{oc}-Light intensity and their fitting curves, measured by scanning J-V curves under various light intensity (100 $mW \cdot cm^{-2}$ - 0.1 $mW \cdot cm^{-2}$). d) Dark J-V curves PSCs. e, f) SCLC patterns of e) eletron-only device and f) hole-only devices. g, h) TPV (g) and TPC (h) of PSCs

Table 4.6. The fitting parameters of the Nyquist plots according to the equivalent circuit model employed in **Figure 4.20b**. R_s, R_{rec}, and C refer to series resistance, recombination resistance, and capacitance, respectively.

	R_s (Ω)	R_{rec} (Ω)	C (F)
Control	15.34	919.6	8.877×10^{-9}
TMU-CR	12.19	3457.0	8.373×10^{-9}

The charge recombination level can also be estimated by the ideality factor (n) and dark J–V measurements of PSCs. The ideality factor (n) can be calculated through the following diode equation: Incorperating the light intensity dependent V_{oc} obtained from J-V measurement under a range of light intensity (from 100 $mW\cdot cm^{-2}$ to 0.1 $mW\cdot cm^{-2}$), n (**Equation 3.4**) for the control and TMU-CR devices was calculated to be 1.58 and 1.20, respectively(**Figure 4.20c**). The decreasing n for TMU-CR PSC suggests a reduction of trap-assisted recombination. This was also supported by its smaller dark current density (J_0) derived from dark J-V scanning of perovskite devices (**Figure 4.20d**).

To further determine the trap-density reduction in the TMU-CR perovskite, the exact trap density was evaluated through SCLC measurements of both electron-only device and hole-only devices. The eletron-only devices were fabricated with a structure of ITO/SnO_2/Perovskite/PEABr/PCBM/BCP/Ag, while the hole-only devices were fabricated as ITO/NiOx/2PACz/Perovskite/PEABr/Spiro-OMeTAD/Au. For electron-only devices, V_{TFL} of control and TMU-CR PSCs were estimated to be 0.31 V and 0.21 V, respectively (**Figure 4.20e**). Their trap densities (**Equation 3.5,** section 3.5.5) were therefore calculated to be 1.87×10^{-15} cm^{-3} and $1.27\times10^{-}$

^{15} cm^{-3}, respectively. The reduction of V_{TFL} and their corresponding trap density strongly evidence that the TMU-CR approach effectively improved the crystallinity and minimized the trap density of α-$FAPbI_3$ perovskite film. This is also backed up by the same tendency in electron-only devices (**Figure 4.20f**).

Furthermore, TPV and TPC were conducted to study their time-resolved carrier dynamics (**Figure 4.20g, h**). Their fitting results are listed in **Table 4.7**. As expected, the TMU-CR device exhibited a longer carrier lifetime ($\tau_{TPV,\ TMU\text{-}CR}$=13.00 ms) as well as a shorter charge extraction time ($\tau_{TPC,\ TMU\text{-}CR}$=0.57 μs) compared with the control counterpart ($\tau_{TPV,\ Control}$=10.88 ms $\tau_{TPV,\ Control}$=0.80 μs). These are strong evidence in support of reduced charge combination and higher charge carrier mobility in devices, respectively, and agree with the smaller charge transfer resistence (R_{rec}) measured from EIS (**Figure 4.20b, Table 4.6**).

Table 4.7. Fitting lifetimes from TPV and TPC of PSCs. τ_{TPV} and τ_{TPC} refer to average TPV lifetime and TPC lifetime, respectively.

	τ_{TPV} (ms)	τ_{TPV} (μs)
Control	10.88	0.80
TMU-CR	13.00	0.57

4.9 Stability of PSCs

The improved crystallinity and inhibited trap density in perovskite film and device are reflected in

the long-term stability as well. As displayed in **Figure 4.21a**, the TMU-CR devices exhibit less decay rate and highly improved long-term stability. After storing in a dry box with humidity of around 20% for over 1500 h, the unencapsulated TMU-CR devices retained an average PCE of 19.64%, which is 85.6% of initial efficiency ($h_{initial}$=22.94%). The control devices, on the other hand, maintained 7.71%, which is only 37.2% of the highest point ($h_{initial}$=20.73%). Maximum power point tracking (MPPT) was further performed to assess their operative stability under continuous light illumination with encapsulated devices. The PCE was tracked for 1000 h under white LED light with intensity of 100 $mW \cdot cm^{-2}$, which was produced by a light-emitting diode (LED) solar simulator. The device exhibited superior operating stability, maintaining 81% of the initial efficiency after 1000 h, whereas the control died after 420 h, with only 49% of its initial efficiency retained (**Figure 4.21b**).

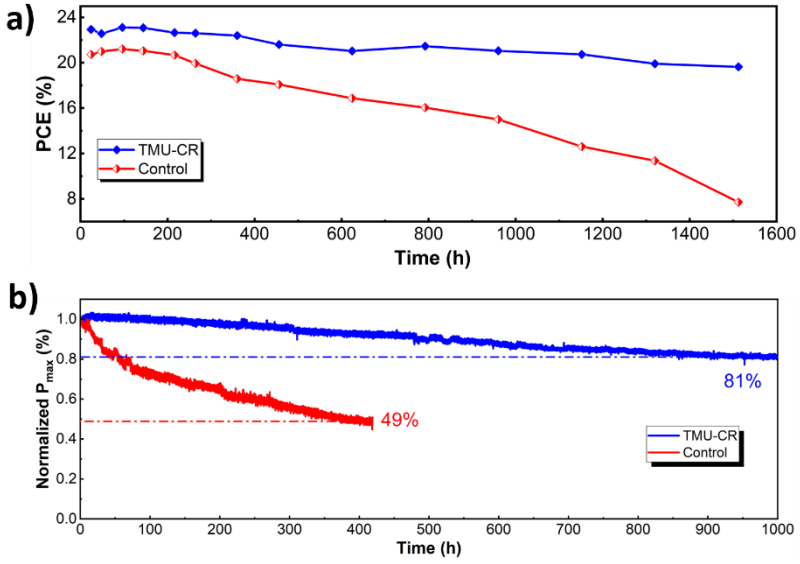

Figure 4.21. a) PCE tracking of PSCs. The devices were unencapuslted and stored in dry box with humidity of ~20%. b) Normalized MPPT of encapsulated PSCs under continuous white LED light illumination at room temperature with a humidity of around 50%. The PSCs were encapsulated with glass and UV curing adhesive.

4.10 Conclusions

In summary, I have introduced TMU as an alternative coordinator for replacing DMSO and proposed a TMU-CR strategy for controlling the air-processed crystallization dynamics through simply adding a small amount of TMU solvent into the anti-solvent. By studying the interaction properties of TMU's adduct with perovskite components, I found that TMU shows a slightly weaker coordination, which benefits the formation of α-$FAPbI_3$ crystal nuclei and their growth. This leads to a high-crystallinity α-$FAPbI_3$ perovskite film with reduced trap density, preferable crystal orientation, and favorable semiconducting nature. As a result, the as fabricated inverted-structure PSC fabricated through this TMU-CR strategy exhibit a significantly improved PCE of 23.18%, with a V_{oc} of 1.13 V and FF of 81.58%, accompanied by a highly enhanced operating stability of $T_{80} > 1000$ h tracking under continuous 1-sun standard illumination. In addition, the unencapsulated TMU-CR device retained 85.6% of its initial PCE after exposure in air for over 1500 h. This work introduces an innovative and effective strategy to regulate the crystallization dynamics of pure α-$FAPbI_3$ perovskite, and thus improve both the photovoltaic performance and long-term stability of α-$FAPbI_3$ based inverted PSCs.

Chapter 5

PREFERENTIAL COORDINATING SN IONS TO BALANCE THE CRYSTALLIZATION OF MIXED SN-PB PSCS

TLPs with a tunable and ideal bandgap exhibit great potential in approaching the S–Q limit of PCE. However, two critical issues need to be addressed, including the oxidation of Sn^{2+} and composition and phase segregation. The latter results from the unbalanced crystallization rate between Sn- and Pb-based perovskites. Here, I will report a strategy to solve these problems by introducing 3,4-dihydroxybenzylamine hydrobromide (DHBABr) in the TLP precursor solution to address the above critical issues. DHBABr was revealed comprehensively to form a steady amorphous FAI-DHBABr-SnI_2 complex to retard the crystallization rate of Sn-based perovskite and hence balance the crystallization rate between Sn- and Pb-based perovskites. As a result, the spatial distribution of Sn/Pb was greatly converged across the whole TLP film, which benefits the up scaling of the manufacturing process. Relying on this strategy, a champion-device PCE of 22.44% with a V_{oc} of 0.853 V and FF of 80.0% was achieved, along with enhanced long-term stability. With reducibility and strong coordination ability, DHBABr inhibits the iodide migration and the oxidation of Sn^{2+} and hence accounts for the enhanced device stability. A manuscript based on this work was submitted to *Advanced Materials* and is under review.

5. Preferential Coordinating Sn Ions to Balance the Crystallization of Mixed Sn-Pb PSCs

5.1 Introduction

Single-junction PSCs have experienced rapid progress for the past decade and achieved a recorded certified efficiency of 26.1%, approaching that of single crystalline silicon solar cells.[1] However, high-efficiency PSCs rely on Pb-based perovskites and their bandgaps are limited to be over 1.5 eV, and can't be further cut down, with their PCE reaching a bottleneck. Substituting Sn^{2+} into Pb-based perovskite can effectively reduce the band gap (E_g) to an ideal range of 1.1-1.4 eV, [14, 60, 183] which is promising to break that bottleneck. Moreover, the incorporation of Sn will alleviate the usage of toxic Pb, enhancing the future market share of PSCs by diminishing their influence on the ecosystem.

Considering the above concerns, TLPSCs have attracted increasing attention in recent years,[128, 139-141, 184] especially working as the bottom cells of tandem solar cells owing to their narrow bandgaps.[66, 81, 100, 185, 186] However, the study of the physical and chemical properties of TLP materials are rare and still in their infancy.[93, 187, 188] As we know, the mixing of Sn and Pb would inevitably cause composition and phase segregations due to their different crystallization rates and chemical environments, deriving interfacial defects, mismatch of band levels, and inhomogeneous bandgap in devices. In addition, the high oxidation inclination of Sn^{2+} to Sn^{4+} would lead to the formation of tin vacancy defects, p-type self-doping, as well as decomposition of the perovskite. These issues would undercut the photovoltaic performances and long-term stability of their resultant devices. [93, 183, 189, 190]

Incorporation of precursor additives, such as octylammonium tetrafluoroborate ($OABF_4$),

pyrrolidinium thiocyanate (PySCN), SnF_2 and its adducts, and natural SnO_x, etc. have been determined to be effective in improving crystal quality and reducing defect density on the surface and at grains interface.[139, 140, 191-193] Treatment at both the top surface[81, 100, 194] and the bottom interface[184] of TLP with designated molecules not only reduces interfacial defect density, but also improves energy band alignment, mitigating the energy barrier and facilitating the carrier extraction at the interface. In addition, replacing the generally used PEDOT:PSS with an alternative p-type semiconducting material would result in an energetically aligned interface between the perovskite absorber and transparent conductive oxide (TCO).[185, 195] Regarding the oxidation of Sn^{2+}, reductive metal powder has been used for eliminating Sn^{4+} from the chemical sources, [196-198] while organic additives with reductive groups,[66, 141, 199, 200] and 2D additive engineering strategy [186, 201-203] have been applied for suppressing oxidation during both the fabrication process and service. [204, 205]

These aforementioned efforts have partially addressed some of the above problems of TLPSCs. However, the more important issue is the unbalanced crystallization rate between Sn- and Pb-based perovskites which has received scarce attention. Composition and phase segregation result from the faster crystallization of Sn-based perovskite compared with the Pb-based counterpart. Incorporating PbS quantum dots and extra DMSO could adjust their crystallization rates to some degree and herein alleviate the Pb/Sn composition segregation,[206, 207] but this does not balance the crystallization rates. Iso-pentylammonium tetrafluoroborate ([PNA]BF_4) and MPA2FPh-BT-BA have been employed as the template to anchor Pb or Sn ions and further to modulate the interfacial crystallization rate of Pb-

or Sn-based perovskite,[182] obtaining some progress. Nevertheless, this interfacial anchoring effect is limited to the interface rather than the whole perovskite layer. Recently, Zhang et al. introduced hydrazine sulfate into the TLP precursor solution to slow down the crystallization speed of Sn-based perovskite by selectively coordinating Sn^{2+} ions.[128] Although the interaction mechanism deserves further exploration, it shows a promising direction to effectively slow down the crystallization rate of Sn-based perovskite, depending on the different coordination strength of functional groups with Sn/Pb ions in the TLP precursor solution. Certainly, this research direction has large possibilities and requires more investigation of functional molecules and working mechanisms behind any improvement.

Regarding the mechanism, it has been hardly reported so far any experiments to distinguish the strength difference of the molecule coordinating between Sn and Pb, which is nevertheless a vital issue in the study because it is almost impossible that the molecule coordinates with Sn only while leaving Pb alone. Another crucial but easily neglected issue is the spatial inhomogeneity of Sn/Pb ratio due to segregation, which predominates when up scaling for mass production.

To address the above critical issues, here I introduced 3,4-dihydroxybenzylamine hydrobromide (DHBABr) into TLP precursor solution to retard the release rate of Sn^{2+} from the preferentially coordinated DHBABr-Sn complex, and hence mediate the crystallization rate between Sn- and Pb-based perovskites. Depending on the effect of DHBABr, the spatial distribution of Sn/Pb ratio was

remarkably narrowed and unified across the whole film, which on average was measured around 47.6:52.4, showing a distinct improvement compared to the values of 46.7:53.3 of the control, albeit it is still lower than the 50:50 input ratio. Owing to the more uniform composition distribution and phase uniformity, a championPCE of 22.44% was achieved, along with an enhanced operational stability of T_{80} = 476 h under continuous light illumination. The relationship between structure, property, and device performance was investigated comprehensively by means of materials characterizations and device physics analysis. It is worthy to note that the chemical shifts in both infrared (IR) and NMR distinguish in the solid state the preference of DHBABr-SnI_2 coordination, along with XPS measurements.

5.2 Experimental details

5.2.1 Materials

Unless specified otherwise, all materials were used as received. Tin powder (Sn, 99.99%), tin fluoride (SnF_2, 99%), 3,4-dihydroxybenzylamine hydrobromide (DHBABr, 98%), and anhydrous solvents including N, N-dimethylformamide (DMF), dimethyl sulfoxide (DMSO), ethyl acetate (EA), and isopropanol (IPA) were purchased from Sigma-Aldrich. Lead iodide (PbI_2, 99.99%) and formamidinesulfinic acid (FSA, >92%) were purchased from TCI. Formamidinium iodide (FAI, 99.99%) and methylammonium iodide (MAI, 99.99%) were purchased from Great Cell Solar. Bathocuproine (BCP, >99%), phenyl-C61-butyric acid methyl ester (PCBM, >99%) and fullerene (C60, 99.5%) were purchased from Lumtec. Tin (II) iodide (SnI_2, 99.999%) was purchased from

5. Preferential Coordinating Sn Ions to Balance the Crystallization of Mixed Sn-Pb PSCs

Yingkou Shangneng Photoelectric Material Co., LTD. Poly(3,4-ethylenedioxythiophene):polystyrenesulfonate (PEDOT:PSS, AI 4083, 1.3 - 1.7 wt.% in water) was purchased from Ossila. Dimethyl sulfoxide-d6 (DMSO-d6) was purchased from J&K Scientific. ITO glass was purchased from Suzhou ShangYang Solar Technology Co. Ltd.

5.2.2 Preparation of the TLP precursors

Both the control and target precursors were prepared with a main composition of $MA_{0.3}FA_{0.7}Pb_{0.5}Sn_{0.5}I_3$ in a concentration of 1.8 M. For the control precursor, 14.0 mg of SnF_2 (10 mol% relative to SnI_2), 84.8 mg of MAI, 216.7 mg of FAI, 335.3 mg of SnI_2, and 414.9 mg of PbI_2 were weighed and added to a 4 ml vial successively, then a stirrer, 750 ml of DMF and 230 ml of DMSO were added to the vial. The mixture was shaken until all the components dissolved, then was further stirred for 2 h at RT. Sn powder (5 mg) was added into the solution, and the mixture was further stirred for 10 min at RT. Then 20 μl of FSA (15 $mg \cdot ml^{-1}$, 0.15 mol% relative to A-site cations) was added to the mixture and shaken for a while without further stirring. For the target precursor (DHBA-dop), DHBABr (1.0 mg, 0.3 mol% relative to A-site cations) was weighed and added to the 4 ml vial at the beginning, while the other steps are the same as the control one.

5.2.3 Fabrication of the TLPSCs

The ITO glasses were cleaned with detergent, deionized water, isopropanol, acetone, and isopropanol successively in an ultrasonic water bath (600 W, 40 kHz) with the temperature kept below 30 °C. The

ITO glasses were then dried under N_2 flow and treated with UV-ozone for 30 mins to ameliorate the infiltration performance of ITO substrate. 70 μl of aqueous PEDOT:PSS (1.3 - 1.7 wt.%) was spin-coated onto the substrate with a speed of 4000 rpm for 30 s, then was annealed for 10 min at 150 °C. The as prepared perovskite precursor solution was spin-coated onto the PEDOT:PSS substrate with speed of 1000 rpm for 10 s and then 4000 rpm for 60 s. After 18 s of the second step of spinning process, anti-solvent EA (500 μl) was dropped on to the film within 2 s. Afterward, the substrates were annealed for 10 min at 100 °C. For passivation of the perovskite, DHBABr with concentration of 0.075 $mg \cdot ml^{-1}$ in IPA was spin-coated on the top of the perovskite with a speed of 4000 rpm for 30 s without annealing. Then a layer of PCBM (5 $mg \cdot ml^{-1}$ in CB) spin-coated with a speed of 6000 rpm for 35 s and annealed at 100 °C, followed by deposition of C_{60} (20 nm), BCP (6 nm), and Ag (100 nm) via thermal evaporation. The thickness of each layer was monitored and controlled using a film thickness gauge within the thermal evaporator.

5.2.4 Performance and stability characterizations of TLPSCs

The performance and stability of the PSCs were characterized through J-V, dark J-V, light dependent V_{oc}, SCLC, SPO, EIS, MS, EQE, TPV, and MPPT measurements, which were performed according to the methods mentioned in Chapter 3. ,

5.2.5 Materials and films characterization

The characterizations relative to materials and film quality of the TLP were evaluated through the

SEM images, AFM-IR images, AFM spectra, XRD patterns, steady state PL spectra, TRPL spectra, UV-vis absorption spectra, FTIR spectra, NMR spectra, fine scanning of XPS spectra, UPS spectra, and ICP-MS data, which were measured according to the methods presented in Chapter 3. spectra,

5.2.6 Electrostatic potential calculation

The electrostatic potential of DHBABr was calculated with the Gaussian 09 revision D.01 suite. The ground state geometry was optimized through a DFT methodology using the B3LYP functional in combination with the 6-311G* basis set.

5.3 Film quality analysis

The chemical structure and electronegative potentials of DHBABr are shown in **Figure 5.1**, which indicates DHBABr is inclined to coordinate with both Sn^{2+}(Pb^{2+}) and I^- ions in the TLP precursor solution. Here, TLP has a formula of $MA_{0.3}FA_{0.7}Sn_{0.5}Pb_{0.5}I_3$, and its films were deposited by an modified method as previously reported.[66] Owing to its bifunctional groups, DHBABr can be employed as both dopant and surface modifier for TLP films. The perovskite with DHBABr as the dopant in the TLP precursor solution is marked as “DHBA-dop” and the “DHBA-dop” perovskite further surface-passivated by the molecule is denoted as “DHBA-dop+pas” in the text while the pristine perovskite is denoted as “Control”.

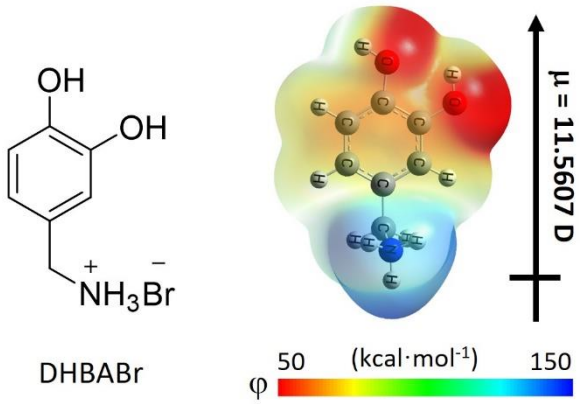

Figure 5.1. Chemical structure of DHBABr and its electrostatic potential.

To investigate the effect of DHBABr on the morphology of the TLP films, SEM and AFM measurements were conducted. The TLP films for examination were deposited on ITO/PEDOT:PSS. **Figure 5.2a-c** shows the top-view SEM images of the TLP films with a scale bar of 1 μm. The films all have a similar morphology without any pinholes. The grains are of similar size and shape. However, the amount of irregular white particles appearing on the surface of the films decreased after DHBABr doping (**Figure 5.2a, b**). Surface passivation with DHBABr further reduced the number of white particles, resulting in a smooth surface without any non-perovskite substance (**Figure 5.2c**). This demonstrates a polishing effect on the surface of the perovskites.[208] The white particles were proposed to be related to SnF_2, which might hinder the charge transfer between the perovskite layer and ETL when an excessive amount exists at the interface.[209-212]

To support my hypothesis, XPS measurements were conducted to analyze the quantity of F element on the surface of these TLP films (**Figure 5.3**). The integrated area of the F1s peak of the control was

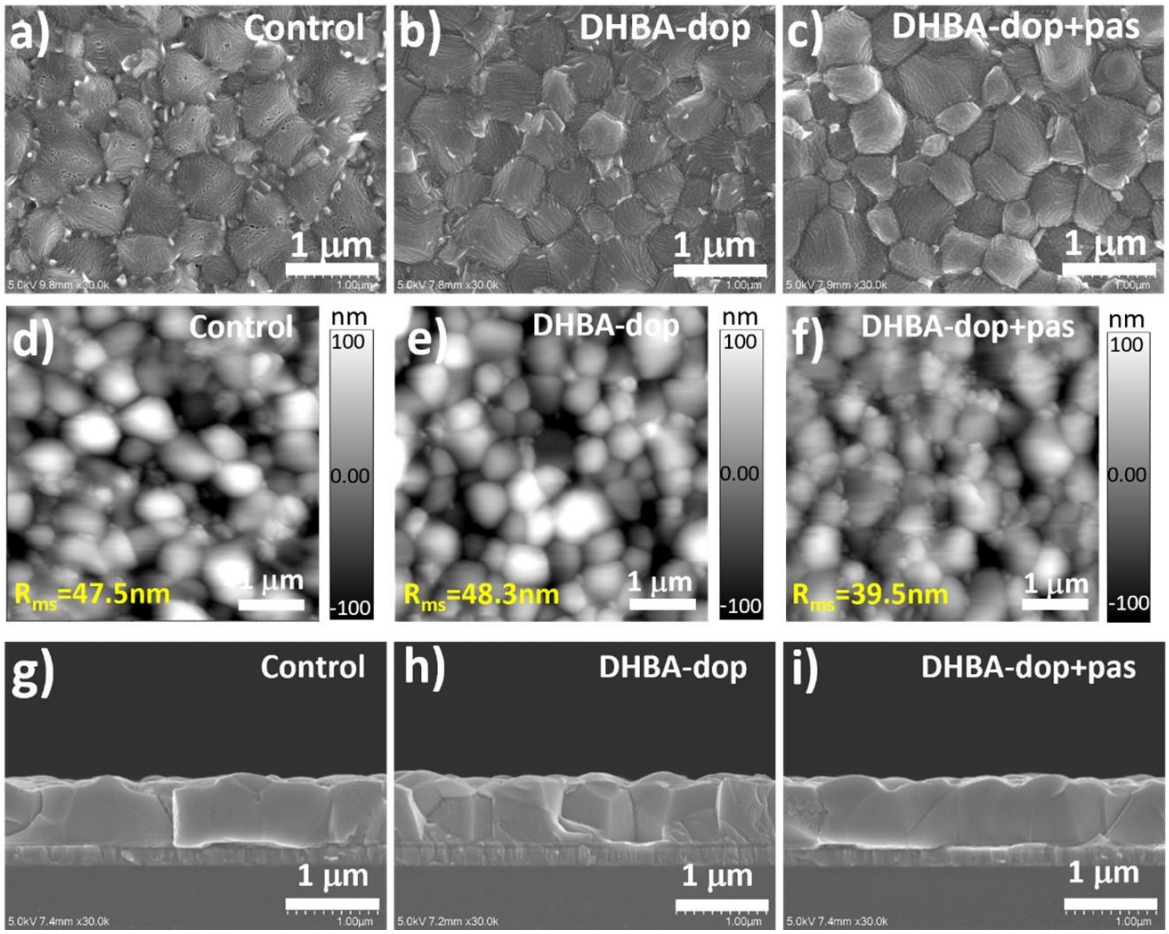

Figure 5.2. b-d) Top-view SEM images and e-g) surface AFM images, and g-i) cross-sectional SEM images of as prepared TLP films.

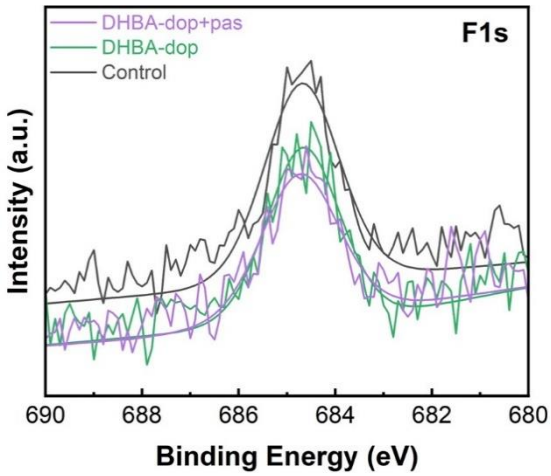

Figure 5.3. XPS F1s spectra of as prepared TLP films.

much higher than that of DHBA-dop, while the pattern of DHBA-dop+pas shows slightly less area than that without surface passivation. The result was further confirmed by the ratios of F element to Sn, Pb, and I element, which were calculated according to their XPS F1s, Sn3d, Pb4f, and I5d spectra (**Table 5.1**). This agrees with the results of SEM, indicating that both DHBABr doping and surface passivation can reduce the formation of SnF_2 on the perovskite surface, and thus prevent the charge extraction hindrance.[209-212] DHBABr doping does not noticeably change the surface roughness ($R_{ms,control}$=47.5 nm (**Figure 5.2d**); $R_{ms, DHBABr}$=48.3 nm (**Figure 5.2e**)) of the perovskite as illustrated via AFM morphology scanning measurements. After surface passivation, however, the surface roughness decreased around 20% to 39.5 nm (**Figure 5.2f**), suggesting that a surface reconstruction occurs during the passivation process,[208, 213] which results in a better contact with ETL and benefits the carrier extraction.[209, 211] The cross-sectional images of the TLP films show similar morphology and thickness (**Figure 5.2g-i**).

Table 5.1. The ratios of F element on surface of TLP films comparing to Pb, Sn, and I elements integrated via XPS spectra of as prepared TLP films.

	F:Pb	F:Sn	F:I
Control	47.90:52.10	21.88:78.12	13.35:86.65
DHBA-dop	42.25:57.75	17.83:82.17	10.21:89.79
DHBA-dop+pas	40.75:60.25	16.44:83.56	9.270:90.83

The XRD patterns of the three TLP films show a well crystalline 3D perovskite phase without any impurity-phase peaks like PbI_2, SnI_2, non-perovskite phase, and 2D phases (**Figure 5.4a**). They also

show similar absorption character, except for a little red shift of absorption edges after doping DHBABr (DHBA-dop) and further passivation (DHBA-dop+pas) (**Figure 5.4b, c**). However, their PL and TRPL reveal an improvement in film quality after doping and further surface passivation of DHBABr (**Figure 5.4d-f**). When excited at the upper side of films, the extracted exciton lifetime (τ_{ave}) is enhanced from 0.797 μs to 1.316 μs after the doping of DHBABr (**Figure 5.4e** and **Table 5.2**). This demonstrates that the bulk quality of TLP films is obviously improved. After further surface passivation, the lifetime increases further to 1.443 μs, which indicates the front-surface traps of DHBA-dop TLP films still exist and can be passivated by the molecule. When excited at the bottom side adjacent to ITO glass, the extracted exciton lifetime increases significantly from 1.093 μs to

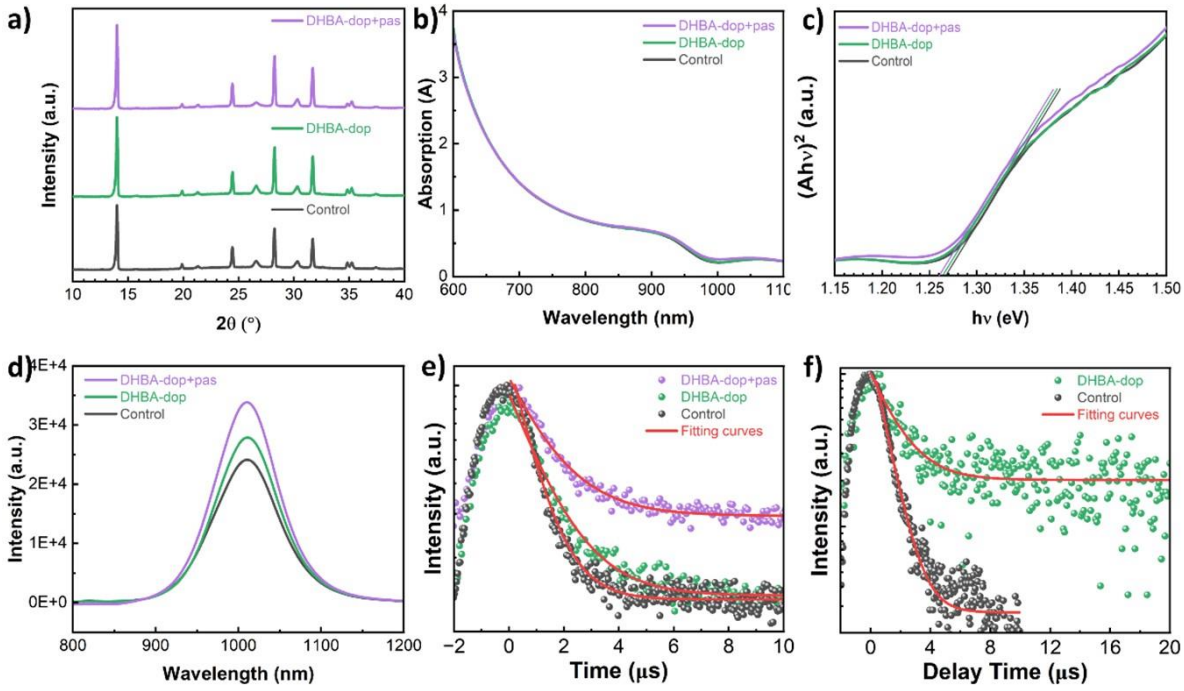

Figure 5.4. a) XRD patterns, b) UV–vis absorption spectra and c) Tauc-plot of the three TLP films. d) Steady-state and time-resolved PL (e) of the three TLP films exited from the top side. f) TRPL of control and DHBA-dop TLP films exited from the bottom side. The fitting of the spectra was based on **Equation 3.2** and the average lifetimes were calculated through **Equation 3.3** as depicted in Section 3.4.3.

1.639 μs after the doping of DHBABr (**Figure 5.4f** and **Table 5.33**). This manifests that the DHBA-dop bottom interface is functionalized by DHBABr and hence non-irradiative recombination at the interface was suppressed.

Table 5.2. Fitting parameters of TRPL that were stimulated from the front side. The TRPL spectra were fitted through **Equation 3.2** and the average lifetimes (τ_{ave}) of perovskite films were calculated via **Equation 3.3** based on the fitting fast-decay-time constant (τ_1) and slow-decay-time constant (τ_2).

	A_1	τ_1 (μs)	A_2	τ_2 (μs)	τ_{ave} (μs)
Control	441.02	0.7976	393.85	0.7966	0.797
DHBA-dop	363.11	1.3162	424.54	1.3163	1.316
DHBA-dop+pas	305.55	1.4435	472.40	1.4434	1.443

Table 5.3. Fitting parameters of TRPL that were stimulated from the back side. The TRPL spectra were fitted through **Equation 3.2** and the average lifetimes (τ_{ave}) of perovskite films were calculated via **Equation 3.3** based on the fitting fast-decay-time constant (τ_1) and slow-decay-time constant (τ_2).

	A_1	τ_1 (μs)	A_2	τ_2 (μs)	τ_{ave} (μs)
Control	20.46	1.0932	52.03	1.0933	1.093
DHBA-dop	15.42	1.6389	65.90	1.6395	1.639

5.4 Schottky contact at the top and bottom interface of TLP films

Bulk doping as well as surface passivation would change the electronic structure, which significantly affects carrier transport at the interfaces. To investigate electron transport at the upper interface of TLP films with the PCBM:C60 ETL, UPS was utilized to reveal the band structures of the three kinds

of TLP films (**Figure 5.5a**), along with HTL (**Figure 5.5b**) and ETL (**Figure 4.16c**). Work functions of the three TLP films change slightly within 0.1 eV, but the gap between Fermi level and VBM increases gradually from 0.6 to 0.8 eV at the surface layer of the TLP films. According to the Tauc plots of TLP films shown in **Figure 5.4c**, their E_g can be determined at ca. 1.26 eV. Then, I can conclude that the DHBABr doping leads to a weak n-type feature from the neutral for TLP films, which is also examined by performing negative Hall coefficients tests. Interestingly, the surface treatment of DHBABr can further lift the electron density in the treated surface layer without altering the VBM and CBM. These phenomena indicate DHBABr has a strong interaction with TLP and exists at the grain boundaries and surfaces of TLP films.[40] Based on the above collected data, the measured VBM of PEDOT:PSS (**Figure 5.5b**), and CBM of PCBM calculated in **Chapter 4** (**Figure 4.17**), the band alignment of the whole device is shown schematically in **Figure 5.6**.

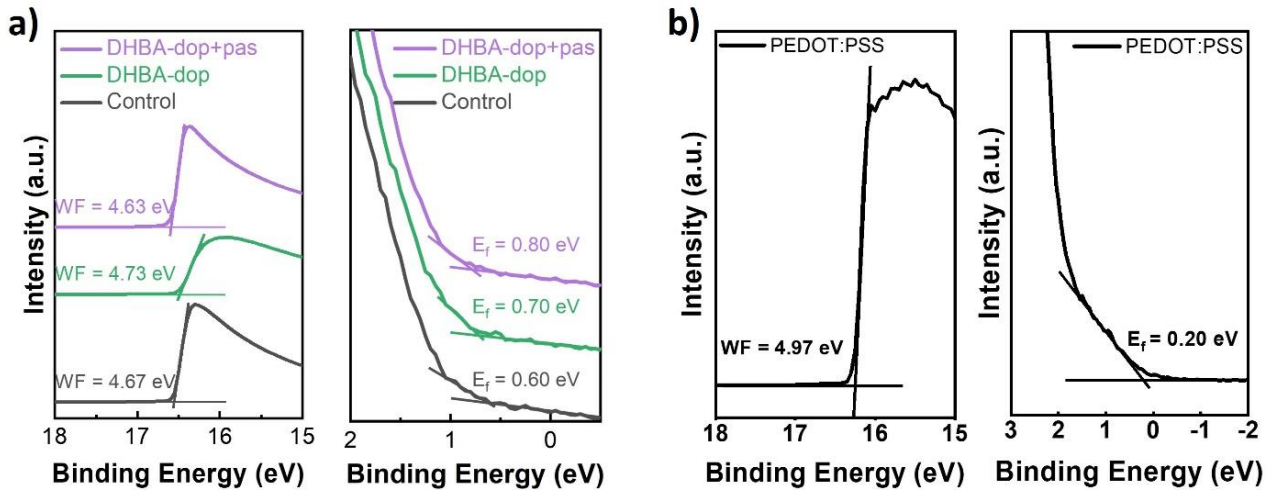

Figure 5.5. UPS spectra of a) perovskites and b) PEDOT:PSS measured under a bias of -10V.

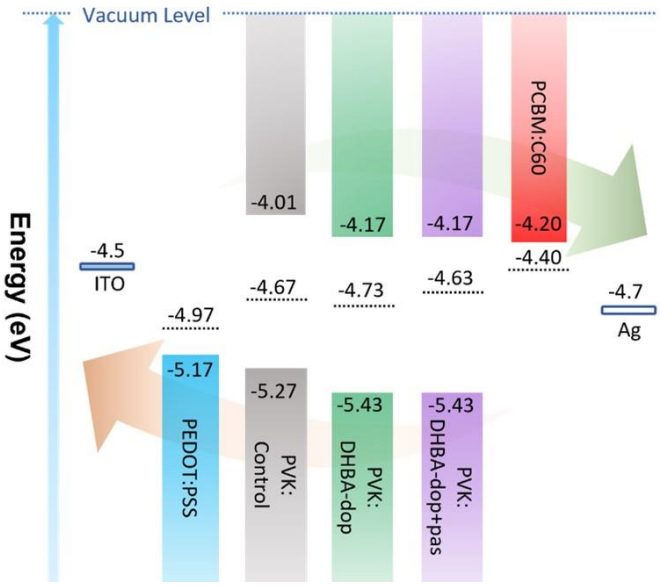

Figure 5.6. Device energy level diagram for the three TLPs.

Firstly, for DHBA-dop and DHBA-dop+pas, their CBMs move downward from -4.01 eV to -4.17 eV while their VBMs move from -5.27 eV to -5.43 eV compared with the Control, respectively (**Figure 5.6**). The downshift of CBM and VBM of TLP films can augment the electron escape energy and inhibit the oxidation of Sn^{2+},[188] enhancing the device photovoltaic performance. Secondly, referring to the band bending at the interface, we can observe the changes of two critical values, band bending and offset. After the doping of DHBABr, the band bending is enlarged positively from 0.27 eV to 0.33 eV while the offset (ΔE) decreases effectively from 0.19 eV to 0.03 eV (**Figure 5.7a, b**). Both can enhance the transport rate of electron at the interface of TLP/PCBM:C60.[32] Further surface passivation would reconstruct a new TLP layer with higher doping concentration of the molecule,[156] which bridges the mismatched Fermi levels from bulk DHBA-dop to PCBM, and hence further facilitates the electron transport (**Figure 5.7c**).

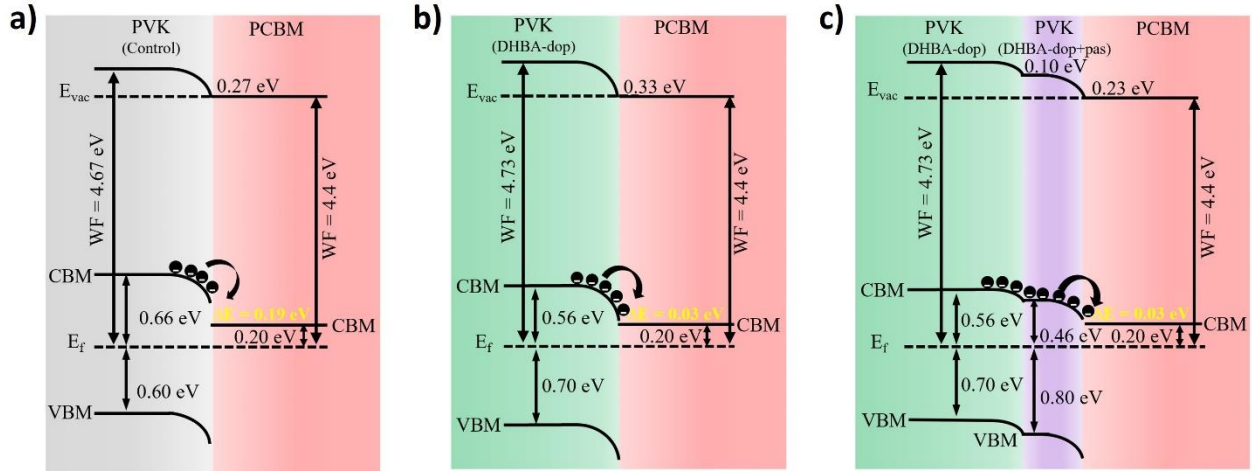

Figure 5.7. Schematics of energy band bending at interfaces between ETL and c) Control, d) DHBA-dop and e) DHBA-dop+pas. All TLP films were fabricated on ITO/PEDOT:PSS substrates.

At the buried bottom surface of the TLP films, the band levels of the Control and DHBA-dop were investigated, which were prepared by peeling off the TLP films from the substrate.[40] The work function of the Control and DHBA-dop at the bottom surface is slightly reduced to 4.66 eV and 4.71 eV (**Figure 5.8a**), respectively. In contrast to the front surface, the gap between Fermi level and VBM for DHBA-dop shrinks to 0.61 eV and hence maintains neutral character while the Control remains almost the same. This demonstrates both DHBA-dop and Control have the same composition of the buried bottom interfaces at the same PEDOT:PSS substrate. Accordingly, the offset between TLP and PEDOT was deduced to be 0.11 eV for Control and 0.15 eV for the DHBA-dop (**Figure 5.8b, c**). This suggests DHBA-dop has a hole-transport rate inferior to that of the Control.

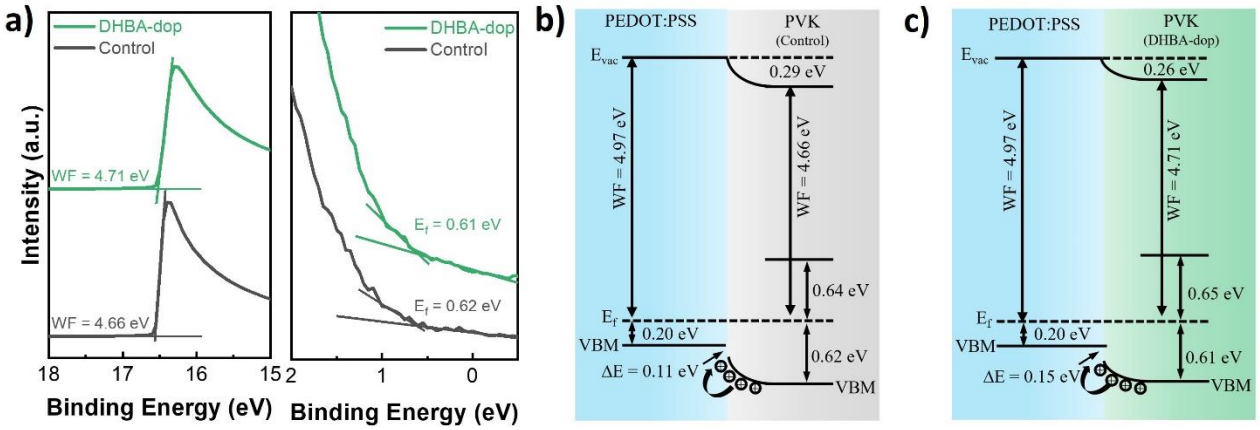

Figure 5.8. a) UPS spectra of the bottom surface of perovskite measured under a bias of -10 V. b-c) Schematics of energy band bending at interfaces between HTL and a) control perovskite and b) DHBA-dop perovskite.

5.5 Performance and stability of PSCs

With understanding of DHBABr's impact on film quality and interface, and the optimized energy band alignment, I then fabricated PSCs to evaluate the enhancement of the photovoltaic performance and long-term stability. The PSCs were fabricated with an inverted planar structure of ITO/PEDOT:PSS/TLP/DHBABr (with/without)/PCBM/C60/BCP/Ag (**Figure 5.9**), where BCP stand for Bathocuproine.

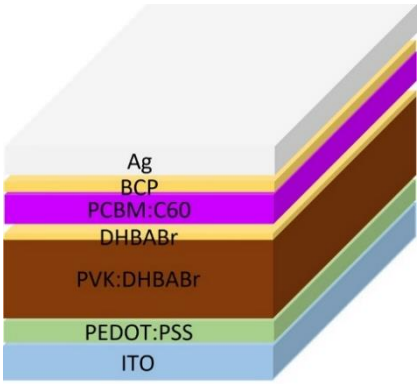

Figure 5.9. Inverted planar structure of as prepared TLPSCs with DHBABr passivation.

5. Preferential Coordinating Sn Ions to Balance the Crystallization of Mixed Sn-Pb PSCs

Figure 5.10a presents the reverse-scan J–V curves of the champion devices of the above three kinds of TLP films, with a table of photovoltaic parameters inserted. Compared to the Control, the PCE of DHBA-dop was improved from 20.22% to 21.62%, with the V_{oc} and FF enhanced from 0.799 V to 0.831V and from 77.1% to 79.0%, respectively. This can be attributed to the improved film quality and the reduced offset at the interface of TLP/PCBM discussed above. Further passivating the surface of TLP film with DHBABr can decrease the surface trap density and hence inhibit the interfacial non-

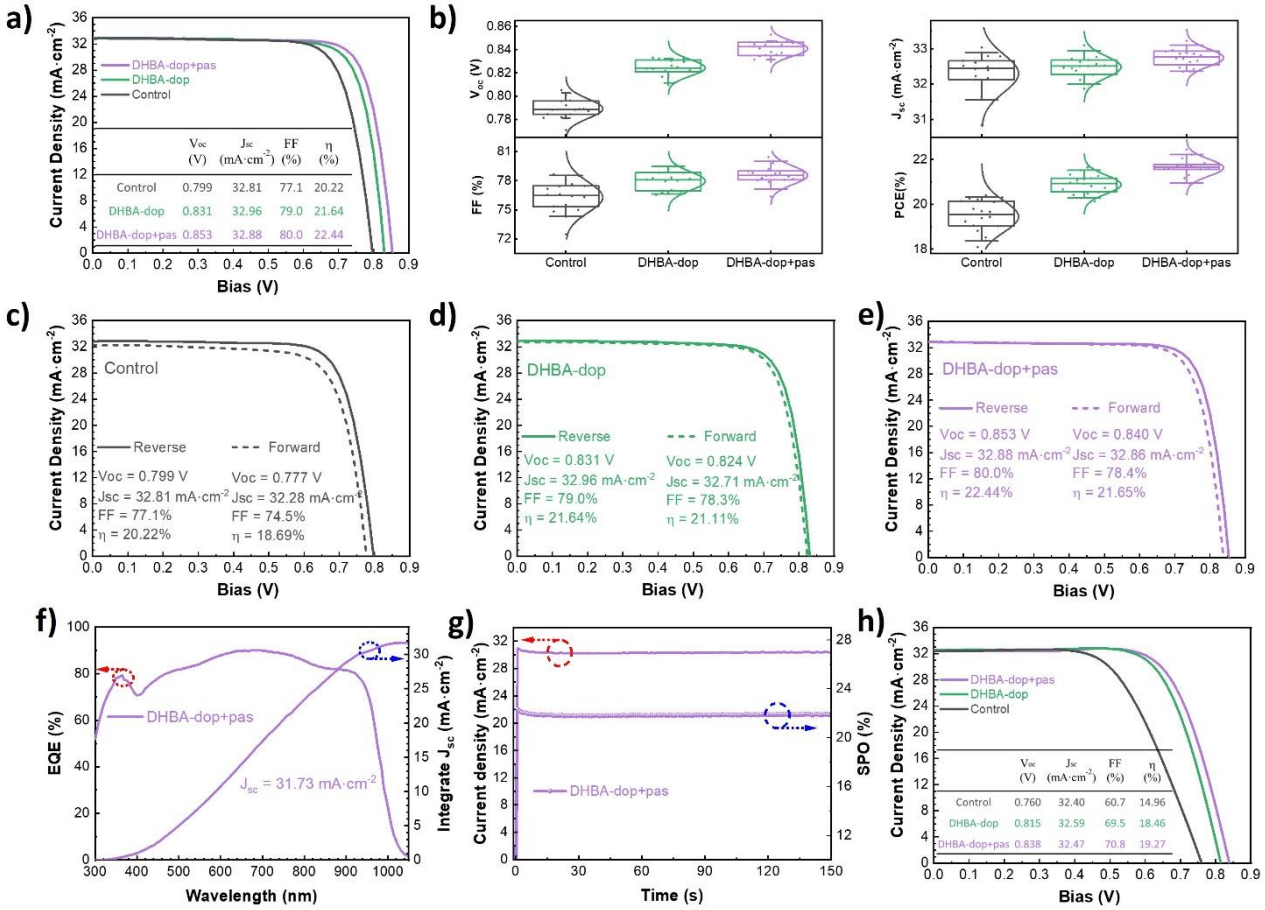

Figure 5.10. Photovoltaic performance and long-term stability of as prepared PSCs. a) J–V curves in reverse scans of champion PSCs under AM 1.5 G illumination (100 $mW \cdot cm^{-2}$). b) Performance distribution for 18 devices of each set of devices. c-e). J-V curves of thec) control, d) DHBA-dop, and e) DHBA-dop+pas devices in both forward (dashed line) and reverse (solid line) scaning. f) External quantum efficiency (EQE) of the champion device. g) SPO of an unencapsulated DHBA-dop+pas device at the voltage of maximum power point (MPP). h) Reverse-scan J–V curves of champion devices with active area of 1 cm^2, table of detailed parameters was embedded.

radiative recombination, which boosts V_{oc} and *FF* and results in a champion efficiency of 22.44% in reverse scan, with 0.853 V in V_{oc}, 32.88 mA·cm^{-2} in J_{sc}, and FF in 80.0%. The improvement, in my opinion, is attributed to the inhibition of interface non-radiative recombination after passivation with DHBABr.

Table 5.4. Average and standard derivation of photovoltaic parameters. The parameter η refers to PCE.

	V_{oc} (V)	J_{sc} (mA·cm^{-2})	FF (%)	η (%)
Control	0.789±0.008	32.31±0.53	76.3±1.6	19.47±0.69
DHBA-dop	0.824±0.007	32.49±0.31	78.0±1.0	20.89±0.41
DHBA-dop+pas	0.841±0.006	32.75±0.25	78.6±0.9	21.64±0.38

The performance distribution of a batch of 18 devices for each group exhibits similar trend in each photovoltaic parameters as those shown in J-V curves (**Figure 5.10b**). The statistical data show an average efficiency of 21.64±0.38%, 20.89±0.41, and 19.47±0.70 for the DHBA-dop+pas, the DHBA-dop, and the Control respectively. Detailed photovoltaic parameters are listed in **Table 5.4**. DHBA-dop and DHBA-dop+pas TLPSCs show reduced statistical standard deviation in each photovoltaic parameter, indicating improved reproducibility and uniformity obtained with DHBABr doping and passivation. All the three TLP films based devices show a hysteresis in *J-V* curves with a differentia in V_{oc} (**Figure 5.10c-e**), which may be attributed to the ion migration induced by the ion vacancies on PEDOT:PSS substrate.[185, 214] Integrated J_{sc} of the champion device was measured by EQE

instrument. The integrated J_{sc}=31.73 mA·cm^{-2} fell within 5% loss of that measured in J-V curve (32.88 mA·cm^{-2}), which supports the high value of current density (**Figure 5.10f**). **Figure 5.10g** presents the SPO of DHBA-dop+pas device. The unencapsulated device displayed an initial current density of 30.90 mA·cm^{-2}, and a PCE of 22.25% at the voltage of maximum power point at V_{max}=0.72 V. I then assess the continuing power output ability of the PSCs through SPO in a scale of 150 seconds, which is a more reliable method to evaluate the PCE of solar cells as well. The current density stabilized at around 30.1 mA·cm^{-2} under continuing illumination with 1-sun standard light intensity (AM 1.5G, 100 mW·cm^{-2}) at room temperature, resulting in a steady powder output of 21.7% (**Figure 5.10h**). The decrease in efficiency compared with its initial output was attributed to the hysteresis,[215] which is consistent with the *J-V* curve shown in **Figure 5.10e**. Large-scale devices with an active area of 1 cm^2 were also compared to study the potential for upscaling production. The DHBA-dop and DHBA-dop+pas devices exhibit significantly improved PCE of 18.46% and 19.27%, compared to 14.96% of the control (**Figure 5.10h**). This confirmed the enhancement of film uniformity even for this larger scale device.

The stability of the PSCs was then evaluated. I first monitored the PCE decay over time. The DHBA-dop and DHBA-dop+pas devices exhibit reduced decay rate and highly improved long-term stability (**Figure 5.11a**). After storing in a glove box with inert atmosphere for around 2000 h, the DHBA-dop and DHBA-dop+pas devices retained an average PCE of 18.09±0.61% and 20.35±0.38% respectively, which are 86.1% and 92.4% of their highest efficiency respectively. The control devices, on the other

hand, maintained 13.42±2.24%, which is only 68.8% of the highest point. In addition, to further study the operating stability of these TLP devices, I conducted MPPT with encapsulated devices. The PCE was tracked for 500 h under continuous illumination of white light with intensity of 100 mW·cm^{-2}, which was produced by light-emitting diode (LED) solar simulator. DHBA-dop and DHBA-dop+pas devices exhibit a good light-soaking stability under a standard sun irradiation intensity of 100 mW·cm^{-2}, maintaining 80% of its initial PCE after 418 h and 476 h, which is comparable to the previous reported values,[184, 196] whist the Control decreased to 80% of its initial PCE after 275 h (**Figure 5.11b**).

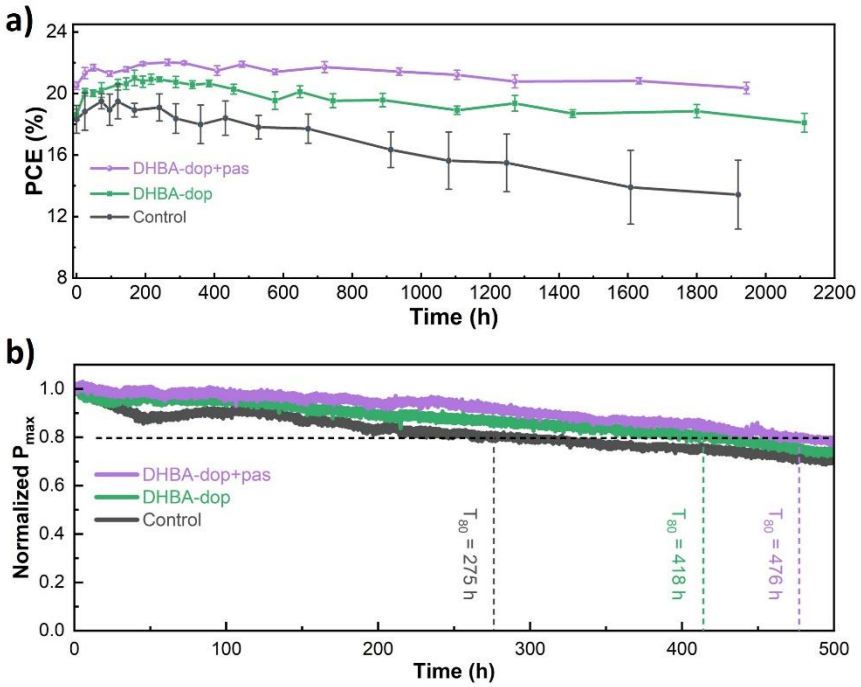

Figure 5.11. a). Average PCE tracking of six devices in each condition. The devices were unencapuslted, stored in glowbox with N_2 atmosphere, and scaned J-V curves in air atmorsphere. The error bars are sample standard deviations (n = 6). b) Normalized MPPT of devices (encapsulated) under continuous white LED light illumination at room temperature with a humidity of around 50%. The PSCs were encapsulated with glass and UV curing adhesive. The device was tracked after approaching its highest efficiency.

5.6 Device physics

Then I investigated the performance improvement in terms of device physics. As the dark J-V scans in **Figure 5.12a** show, the dark current density (J_D) was reduced from 42.4 nA to 4.57 nA by one order of magnitude after the DHBABr doping, which declined further to 1.42 nA after DHBABr passivation (**Figure 5.12a**). The decrease of both bulk and interfacial defect density contributes to the obvious enhancements of V_{oc} and FF discussed above. Light intensity dependent V_{oc} testing data also prove the decline of defect density in device, with the ideal factor (n) diminishing from 1.24 to 1.12 and 1.08 (**Figure 5.12b**). Furthermore, TPV measurements were conducted to study their time-resolved carrier dynamics (**Figure 5.12c**). The carrier lifetime of the Control, DHBA-dop and DHBA-dop+pas

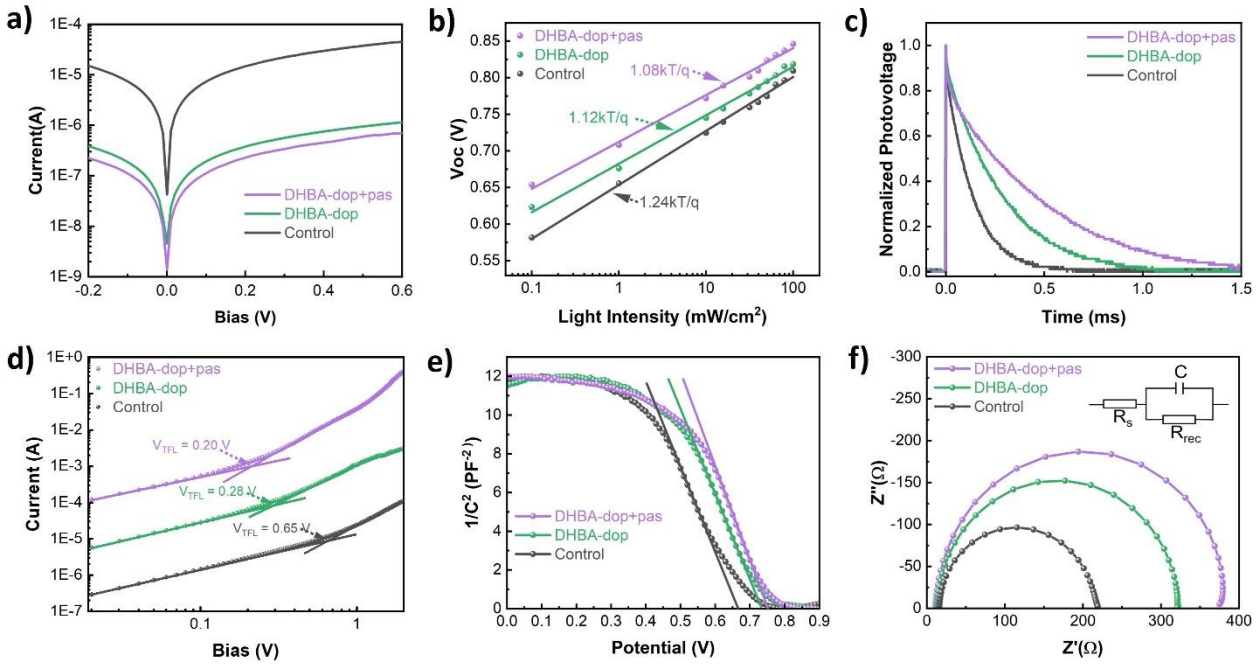

Figure 5.12. **Study of device physics**. a) Dark J-V curves of devices with an active area of ~0.15 cm^2. b) Plots of Light intensity dependent V_{oc} and their fitting curves. c) TPV of devices. d) SCLC of hole-only devices with a structure of ITO/PEDOT:PSS/TLP/Spiro-OMeTAD/Au, tested in dark. e) Mott-Schottky plots of devices. f) Nyquist plots of devices, with the equivalent circuit model inset.

are determined to be 0.131 ms, 0.283 ms, and 0.512 ms, repectively (**Table 5.5**). This result confirms the reduced charge combination both in bulk and at the interface.

Table 5.5. Fitting lifetimes from TPV of TLPSCs. τ_{TPV} refers to average TPV lifetime.

	τ_{TPV} (ms)
Control	0.131
DHBA-dop	0.283
DHBA-dop+pas	0.512

To determine the trap-density, the SCLC of hole-only devices were measured. The devices were fabricated with a structure of ITO/PEDOT:PSS/TLP/DHBABr (with/without)/Spiro-OMeTAD/Au. V_{TFL} of the Control, DHBA-dop, and DHBA-dop+pas devices were estimated to be 0.65 V, 0.28 V, and 0.20 V, respectively (**Figure 5.12d**). Their trap densities were therefore calculated to be 3.93×10^{-15} cm^{-3}, 1.69×10^{-15} cm^{-3}, and 1.21×10^{-15} cm^{-3}, respectively, according to **Equation 3.5** in section 3.5.5. The reduction of V_{TFL} and their corresponding trap density comfirmed that additive doping notably minimized the trap density in the bulk TLP films, while the post-treatment further decreased the defect density at the film surface, with both contributing to the enhancement of V_{oc}. The increase of the build-in potential (V_{bi}), from 0.66 V to 0.73 V and 0.75 V for DHBA-dop and DHBA-dop+pas (**Figure 5.12e**), confirmed the enhancement of V_{oc}, in agreement with the improved V_{oc} as shown in their J-V curves (**Figure 5.12a**). **Figure 5.12f** showed the Nyquist plots of the three devices with the equivalent circuit model inserted, with the fitting parameters listed in **Table 5.6**. The recombination

resistance (R_{rec}) increased from 194.3 Ω to 306.1 Ω after the DHBABr doping, and it further increased to 372.7 Ω by the surface passivation. Meanwhile, the charge transfer resistance (R_s) decreased from 16.61 Ω to 14.17 Ω with the DHBABr doping, and further declined to 11.95 Ω after the surface passivation. This shows once again that doping and passivation of DHBABr improves the film quality and reduces the bulk and interfacial trap states remarkably.

Table 5.6. The fitting parameters of the EIS plots according to the equivalent circuit model employed in **Figure 5.12f**. R_s, R_{rec}, and C refer to series resistance, recombination resistance, and capacitance, respectively.

	R_s (Ω)	R_{rec} (Ω)	C (F)
Control	16.61	194.3	2.429×10^{-8}
DHBA-dop	14.17	306.1	2.913×10^{-8}
DHBA-dop+pas	11.95	372.7	2.776×10^{-8}

5.7 Mechanism study of the suppression of the composition segregation

Chemical coordination and hydrogen bonding can be probed as a chemical shift of vibrational absorption peaks. In FTIR Spectroscopy mode, the absorption peaks for pure DHBABr at 1517 cm^{-1}, 1289 cm^{-1}, 1272 cm^{-1}, and 1202 cm^{-1} can be asigned to stretching vibration (ν) of C=C bond, C-O+C=C bond, C-O bond, and formation vibration (δ) of O-H bond, respectively (**Figure 5.13**).[216-219] TLP films with DHBABr doping show evident peaks of $DHBA^+$ while the Control does not. The red-shift of $\nu_{C-O+C=C}$, ν_{C-O}, and δ_{O-H}, and blue-shifted of $\nu_{C=C}$ confirmed the strong interaction between DHBABr and TLP (**Figure 5.13**).

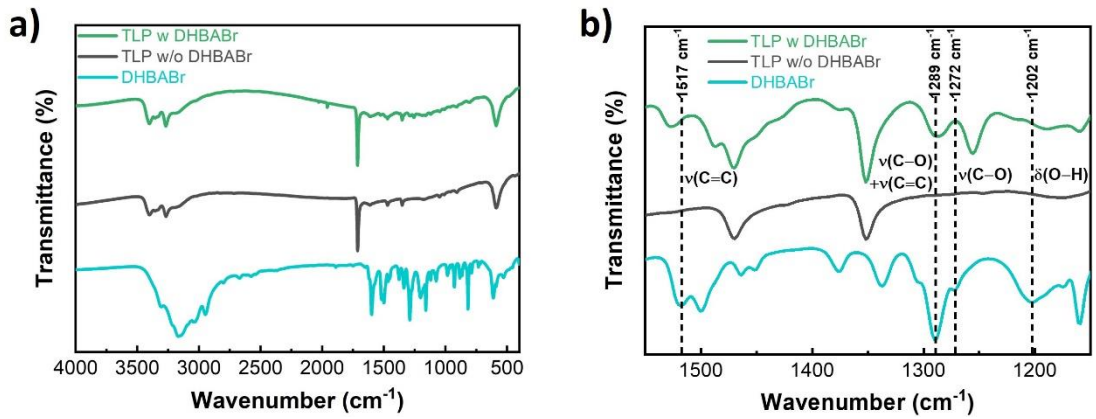

Figure 5.13. a) Full-range and b) magnified FTIR spectra of DHBABr and TLP films with and without DHBABr deposited on KBr wafer. Content of DHBABr in perovskite was increased to 10% relative to A-site cation to pronounce the shift of peaks.

To differentiate the interactions between DHBABr and each component of TLP, FAI, PbI_2, and SnI_2 were mixed with DHBABr separatively for characterization. For the mixture of DHBABr and FAI, the peaks of $\nu_{C-O+C=C}$, ν_{C-O}, and δ_{O-H} red-shifted to 1286 cm^{-1}, 1264 cm^{-1}, and 1195 cm^{-1}, respectively, while the peaks of $\nu_{C=N}$ in FA^+ blue-shifted from 1698 cm^{-1} to 1701 cm^{-1}, indicating a hydrogen bond formed between FA^+ and the phenolic hydroxyl groups in $DHBA^+$ (**Figure 5.14a**). This is because formation of hydrogen bonds weaken the C-O bond and O-H bond in $DHBA^+$, as well as N-H bond in FA^+. The elongation of the N-H bond will also strengthen the C=N bond in FA^+ (**Figure 5.14b**), resulting in a blue-shift of $\nu_{C=N}$. Vibrational shifts of chemical bonds in the mixture of DHBABr and PbI_2, and mixture of DHBABr and SnI_2 also confirmed strong coordination between DHBABr and PbI_2 /SnI_2 (**Figure 5.14c**). Similar to that in the mixture of DHBABr and FAI, red-shifts of $\nu_{C-O+C=C}$, ν_{C-O}, and δ_{O-H} suggest a coordination between oxygen atoms and metal atoms of PbI_2 and SnI_2. Hydrogen bonding between active hydrogen atom in $DHBA^+$ and I^- may also exist. Blue-shift of $\nu_{C=C}$ in benzene rings may be due to the disruption of conjugation between the benzene ring and lone pair

electrons in oxygen atoms. Interestingly, compared with the vibrational shifts of the peaks in the mixture of DHBABr and PbI_2 ($\Delta\nu_{C-O+C=C}$=0 cm^{-1}, $\Delta\nu_{C-O}$=-7 cm^{-1}, $\Delta\delta_{O-H}$=-2 cm^{-1}, and $\Delta\nu_{C=C}$=5 cm^{-1}), that in the mixutre of DHBABr and SnI_2 was much more remarkable ($\Delta\nu_{C-O+C=C}$=1 cm^{-1}, $\Delta\nu_{C-O}$=-16 cm^{-1}, $\Delta\delta_{O-H}$=-6 cm^{-1}, and $\Delta\nu_{C=C}$=11 cm^{-1}). These enlarged vibrational shifts indicate that DHBABr exhibits a stronger interaction with SnI_2 and, thus prefers to coordinate SnI_2 more than PbI_2.

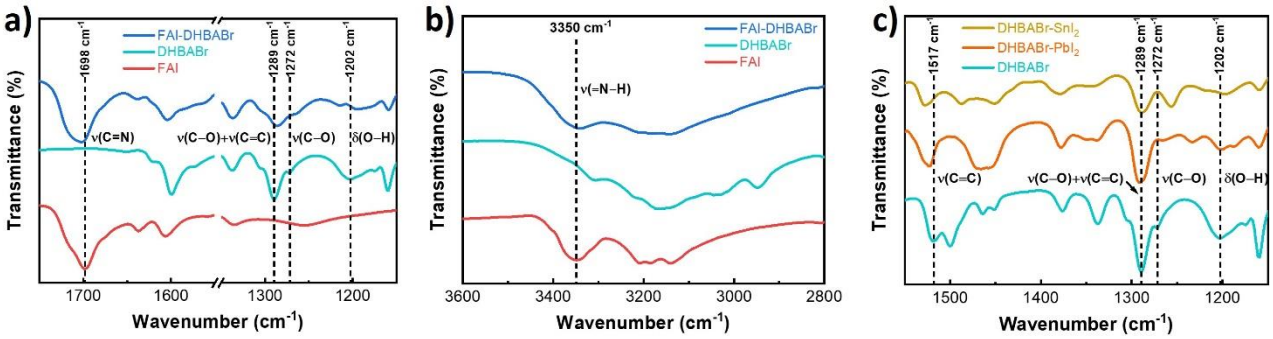

Figure 5.14. Study of the interactions between DHBABr and TLP components through a FTIR technique. a) magnified FTIR spectra of FAI, DHBABr and their mixture, deposited on KBr wafer. b) Magnified FTIR spectra of FAI, DHBABr, and their mixture in a molar ratio of 1:1, deposited on KBr wafer.c) magnified FTIR spectra of DHBABr, and its mixture with PbI_2 and SnI_2 in a molar ratio of 1:1, deposited on KBr wafer.

On the basis of this discovery, I further conducted ^{1}H NMR and ^{13}C NMR to confirm this. **Figure 5.15a** shows the ^{1}H NMR spectra of DHBABr and its mixtures with FAI, PbI_2, and SnI_2, respectively. The chemical structure of $DHBA^+$ with atom-positions labled as number is embedded. Two peaks at around 9 ppm were assigned to reactive hydrogen in position 8 and 9, a peak at around 8 ppm was assigned to hydrogen in NH_3^+, and peaks between 6.5-7 ppm were assigned to hydrogen in benzene ring. The hydrogen in position 7 displayed a signal at 3.82 ppm, which exhibits negligible shift and

thus was eliminated for discussion here (**Figure 5.15a**). The range with peaks of hydrogen in hydroxyl group and hydrogen in benzene ring was magnified as shown below **Figure 5.15a**. The peaks between 8.6 ppm and 9.4 ppm were normallized in order to display the position of the broadened peak in the pattern of the mixture of DHBABr and SnI_2. The broadened peak was also fitted to two peaks in a area-ratio of 1:1, referring to hydrogen in position 8 and 9, respectively. As expected, all peaks exhibit a chemical shift to various degree, supporting the interaction between DHBABr and TLP components, consistent with the result in FTIR. Active protons are expected to escape from hydroxyl groups and are probably solvated by forming $H^+[DMSO]_xI$, which result in a up-field shift of the peaks of active hydrogen in hydroxyl group.[40] The strength of coordination from electron lone pair in oxygen to PbI_2 and SnI_2 alters the ionization of DHBABr. As shown in the normalized and magnified patterns (pink area), the peak referred to active protons at position 8 of $DHBA^+$ in the mixture of DHBABr and PbI_2 are up-shifted from 9.10 ppm to 9.09 ppm, while that in the mixture of DHBABr and SnI_2 are both up-shifted to 9.03 ppm. The larger shift demonstrates a higher degree in ionization of DHBABr, and thus confirms stronger interaction between DHBABr and SnI_2 compared with that between DHBABr and PbI_2. This conclusion was also supported by the change of peak shape from sharp to broad and overlapped for the mixtures of DHBABr and SnI_2, which was attributed to the increased activity and faster ion exhange of the proton. Similar trends were exhibited in the up-field shift of the peaks assigned to hydrogen in benzene ring, which is consistent with the different red-shift of FTIR peaks due to the elimination of conjugation between the benzene ring and lone pair electrons in oxygen atom as discussed before. In short, the larger chemical shifts of the peaks referred to hydrogen in the

Ph-OH groups and the change of their shapes further supports my statement that DHBABr has a stronger interaction with SnI_2, compared to PbI_2.

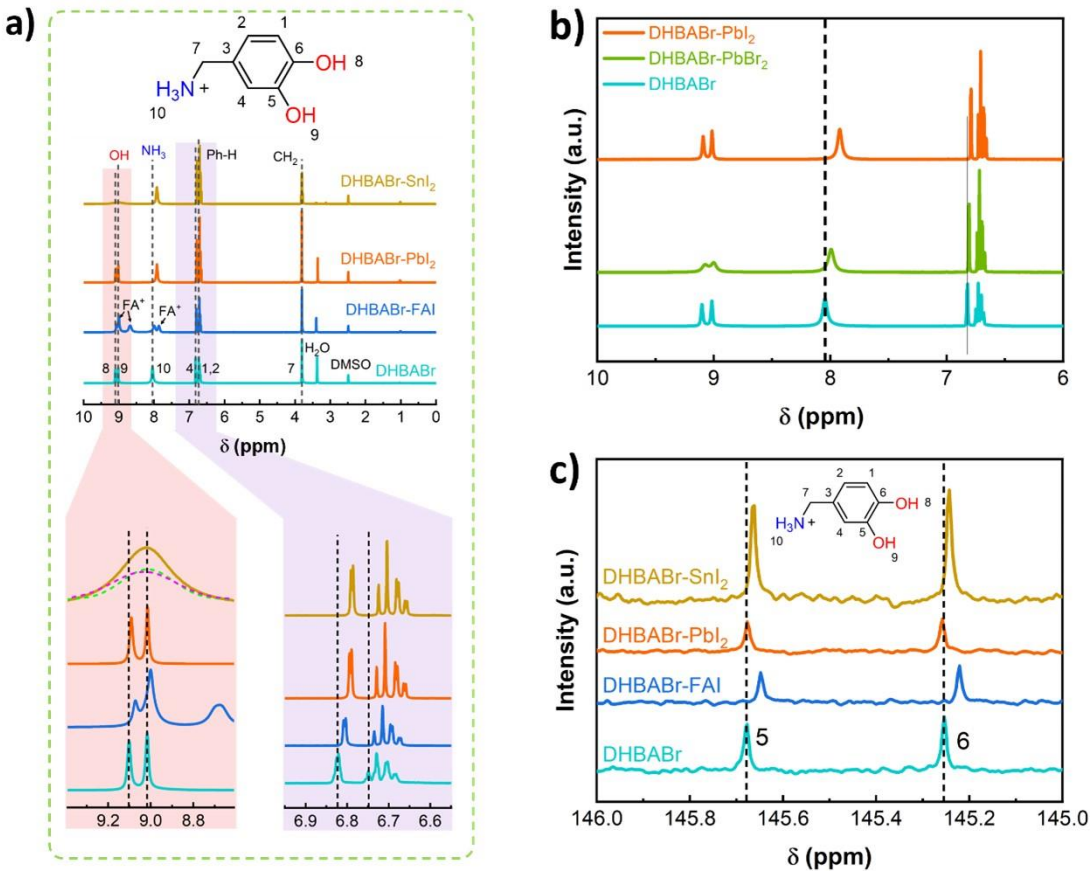

Figure 5.15. Study of the Interactions between DHBABr and TLP components through NMR techniques. a)^{1}H NMR spectra of DHBABr and its mixture with FAI, PbI_2, and SnI_2 in a molar ratio of 1:1, dissoved in DMSO d6. b) ^{1}H NMR spectra of DHBABr and its mixture with $PbBr_2$ and PbI_2 in a molar ratio of 1:1, dissolved in DMSO d6. c) ^{13}C NMR spectra of DHBABr and its mixture with FAI, PbI_2, and SnI_2 in a molar ratio of 1:1, dissolved in DMSO d6.

The shift in the up-field direction of the peaks at around 8 ppm referring to hydrogen in NH_3^+ group was mainly attributed to the different electron-withdrawing abilities of Br^- and I^- ions, leading to different electrostatic interactions in the ionic bond, which is confirmed by an alleviated degree of

shift when replacing PbI_2 with $PbBr_2$ in the mixture (**Figure 5.15b**). Higher concentration of Br^- in the solution are responsible for the slight shift in mixture of DHBABr-$PbBr_2$ compared with pure DHBABr.[40] The distance of shift is the same in both the mixture of DHBABr-PbI_2 and the mixture of DHBABr-SnI_2, indicating negligible interation exists between NH_3^+ group and metal ions. The chemical shift discussed above is consistent with the up-shift of ^{13}C NMR signals (**Figure 5.15c**).

In terms of the high-resolution XPS spectra, two peaks at 143.07 eV and 138.22 eV (referred to Pb $4f_{5/2}$ and Pb $4f_{7/2}$) of the pristine TLP film are down shifted to 142.87 eV and 138.02 eV after the DHBABr doping, while two peaks at 495.01 eV and 486.55 eV (referred to Sn $3d_{3/2}$ and Sn $3d_{5/2}$) are down shifted to 494.78 eV and 486.31 eV, respectively. Furthermore, the peaks of I 3d also move by 0.08 eV in red shift (**Figure 5.16**). This further supports the interaction of DHBABr with both Sn and Pb.

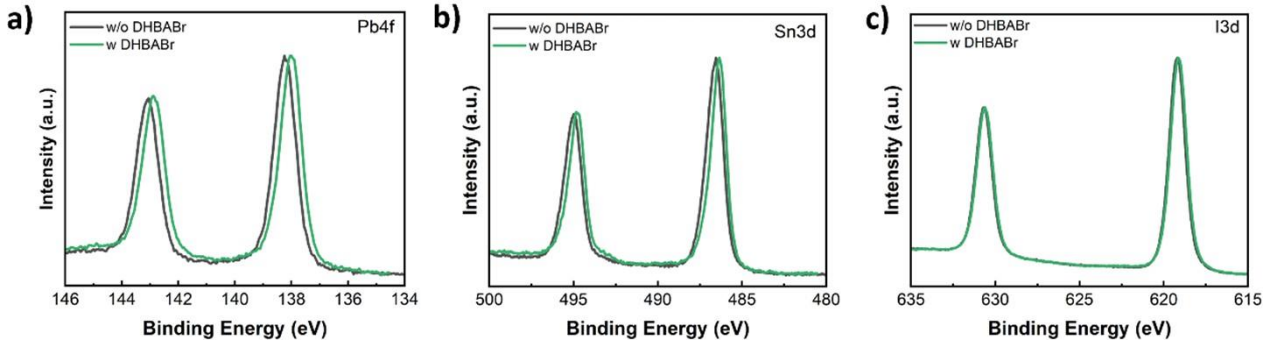

Figure 5.16. XPS spectra of a) Pb4f, b) Sn3d, and c) I3d of TLP films with and without DHBABr doping.

5. Preferential Coordinating Sn Ions to Balance the Crystallization of Mixed Sn-Pb PSCs

The function of DHBABr on the crystallization speed of Pb- and Sn-based perovskites was investigated in the thermal annealing process (**Figure 5.17**). α-$FAPbI_3$ perovskite without DHBABr doping shows slow crystallization and didn't reach the ultimate state until annealing for 40 s (**Figure 5.17a**). After doping with DHBABr, the film became well crystallized immediately after annealing for 20 s. In the XRD pattern of the wet film without DHBABr doping (**Figure 5.17c**), there are several small-angle peaks related to intermediates of DMSO-FA-Pb-I complexes,[220, 221] In contrast, with the doping, the small-angle peaks of intermediates disappear and only the peak of δ-phase $FAPbI_3$ perovskite exists around 12° with an augmented intensity. Correlating the above FTIR, NMR and XRD evidence shown in **Figure 5.17a** and **c**, I can conclude that $DHBA^+$ ions can grasp DMSO from the DMSO-FA-Pb-I complexes by the strong hydrogen bond between –OH and –S=O in the antisolvent quenching process, facilitating the formation of room-temperature stable δ-phase $FAPbI_3$ perovskite and promoting its crystallization speed, which results in the crystallization difference shown in **Figure 5.17a**. Regarding α-$FASnI_3$ perovskite, FTIR and NMR data have proven that Sn^{2+} has stronger interaction with DHBA than Pb^{2+}. As a result, an amorphous DHBA-FA-Sn-I complex probably forms in the anti-solvent quenching process, which retards the crystallization of the α-$FASnI_3$ perovskite. This assumption is verified by both the annealing-time dependent (001) peak intensity evolution of the $FASnI_3$ perovskite films (**Figure 5.17b**) and their corresponding unannealed wet films (**Figure 5.17d**). The more stable amorphous DHBA-FA-Sn-I complexes suppresses the formation of the DMSO-FA-Pb-I intermediates and reduce the crystallization rate of α-$FASnI_3$ perovskite at room temperature (**Figure 5.17d**). This contributes to the subsequent increase of

crystallization in the thermal annealing process (**Figure 5.17b**). The XRD patterns prove that DHBA effectively promotes the crystallization of $FAPbI_3$ perovskite while retarding that of $FASnI_3$, which help to balance the crystallization rate between the Sn- and Pb-based perovskites. This allows the formation of TLP film with improved uniformity of both composition and phase. This point was proved by the following composition tests, especially across the whole film, which is an important parameter that has been rarely reported by the previous literature.[128, 182, 185]

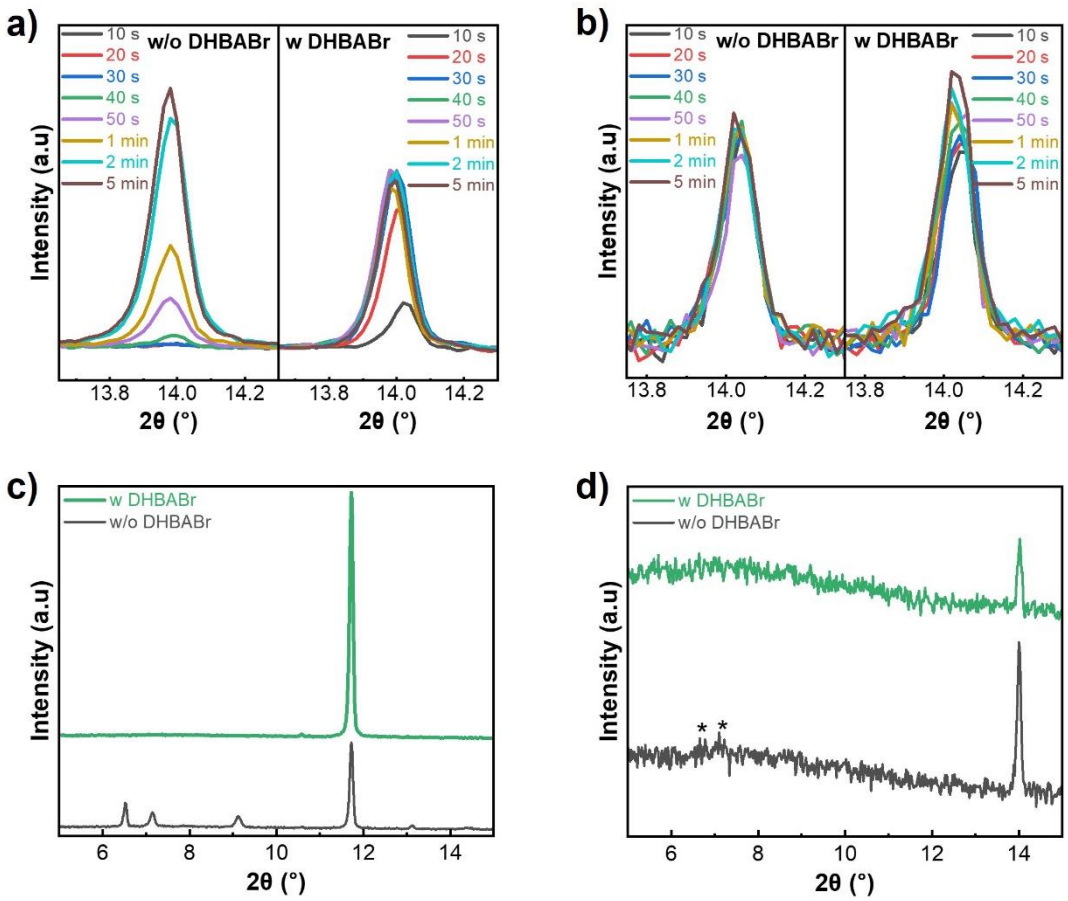

Figure 5.17. XRD patterns of a) $FAPbI_3$ without and with DHBABr doping and b) $FASnI_3$ without and with DHBABr doping, annealed for various time. c, d) XRD patterns of c) $FAPbI_3$ without and with DHBABr doping and d) $FASnI_3$ without and with DHBABr doping, eliminated from anti-solvent treatment and annealing. DHBABr doping was enlarged to 2% to magnify the phenomena.

This assumption was first proven by the slightly increased Sn content in the TLP films (**Figure 5.18**). The increased Sn content was assumed to be captured and kept by DHBABr anchoring.

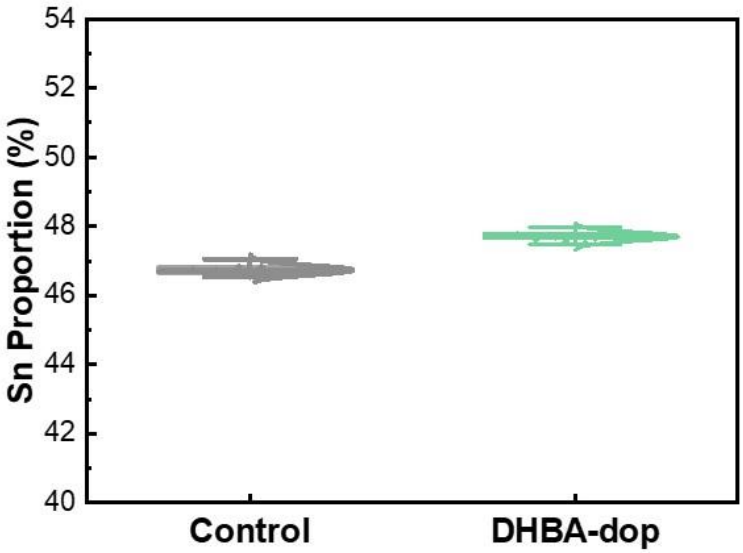

Figure 5.18. Sn atomic proportion of B-site metal in 10 pieces of the control and DHBA-dop TLP films, measured using ICP-MS.

Furthermore, to prove the improved spatial homogeneity, I performed ICP-MS measurements for analyzing the Sn/Pb distribution at various position of both the control and DHBA-dop TLP films. I divided each film into 12 regions (**Figure 5.19a**) and scraped the TLP powder in each region off. Three pieces of each kind of TLP films (control and DHBA-dop) were scraped according to the abovementioned method and consequently, 36 points of each kind of TLPs films were collected for measurements of Sn/Pb distribution. Obviously, the statistical distribution of Sn proportion is narrowed with DHBABr doping (**Figure 5.19b**), which is consistent with the smaller calculated full width at half maximum (FWHM) of steady-state PL of DHBABr doped TLP films (**Table 5.7**).

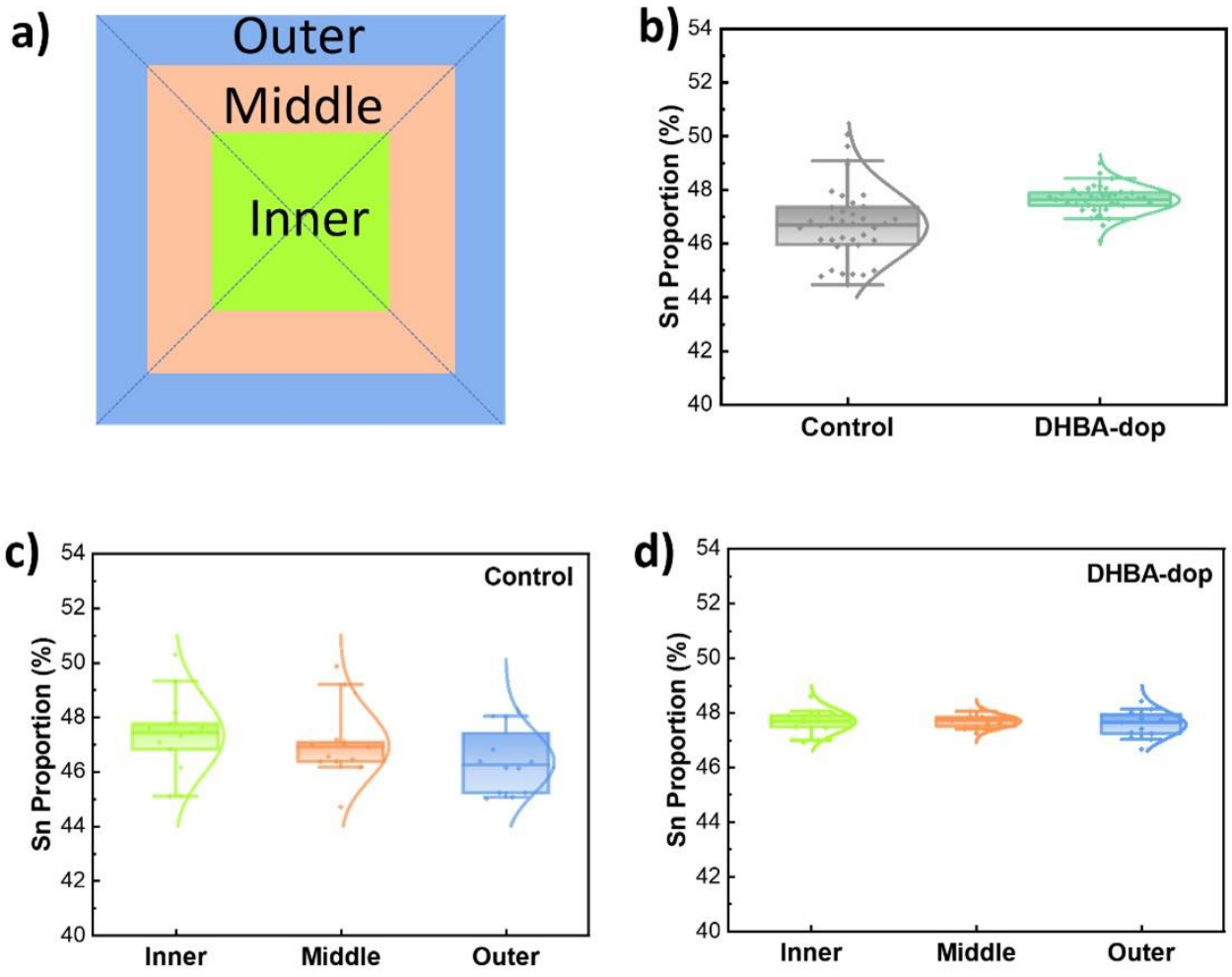

Figure 5.19. a) Schematic of 12 regions divided for ICP-MS measurement. b) Distribution of Sn proportion in 36 areas in the Control and DHBA-dop films, tested witha ICP-MS instrument. c, d) Distribution of Sn proportion in the center, middle, and outer areas of c) Control and d) DHBABr-dop films, respectively. These data were measuredwith a ICP-MS instrument.

Table 5.7. FWHM of static-state PL obtained by Gaussian fitting from patterns of **Figure 5.4d**.

	FWHM (nm)
Control	96.2457
DHBA-dop	92.7671
DHBA-dop+pas	92.6919

Moreover, I founnd the average Sn proportion of DHBA-dop reached 47.6%, larger than 46.7% of the control, which is closer to the 50% value of the designed ratio. This demonstrates that Sn is prone to be lost in the TLP film forming process and DHBABr can suppress this by the strong coordination to SnI_2 discussed above. I assembled such 36 points into 3 groups in a radial sequnce from center to border. Regarding the Control, the Sn proportion distribution is enlarged if away from the inner and its average value decreases successively from inner to outer (**Figure 5.19c**). In sharp contrast, for DHBA-dop, the Sn proportion average value remains statistical unchanged and its distribution maintains a narrow range from inner to outer (**Figure 5.19d**).

Besides the uniformity in the horizontal direction, I further performed XPS depth profile at device position to compare depth dependent Sn/Pb ratio of the three TLP films. As presented in **Figure 5.20**, both the control and DHBA-dop TLP films show gradient Sn/Pb ratio in the vertical direction, with the surface and bottom of the TLP films having higher Sn ratio than the middle. Overall, the average Sn proportion in DHBA-dop perovskite is slightly higher than that in the control perovskite, consistent with the results measured by ICP-MS. However, fluctuations of Sn/Pb ratio in the bulk of the control perovskite was observed (**Figure 5.20a**), while the line for the Sn/Pb ratio at DHBA-dop was smoother, without obvious fluctuations at a small range of depth (**Figure 5.20b**). This unambiguously demonstrates the DHBABr doping also led to an improved vertical uniformity in the bulk film.

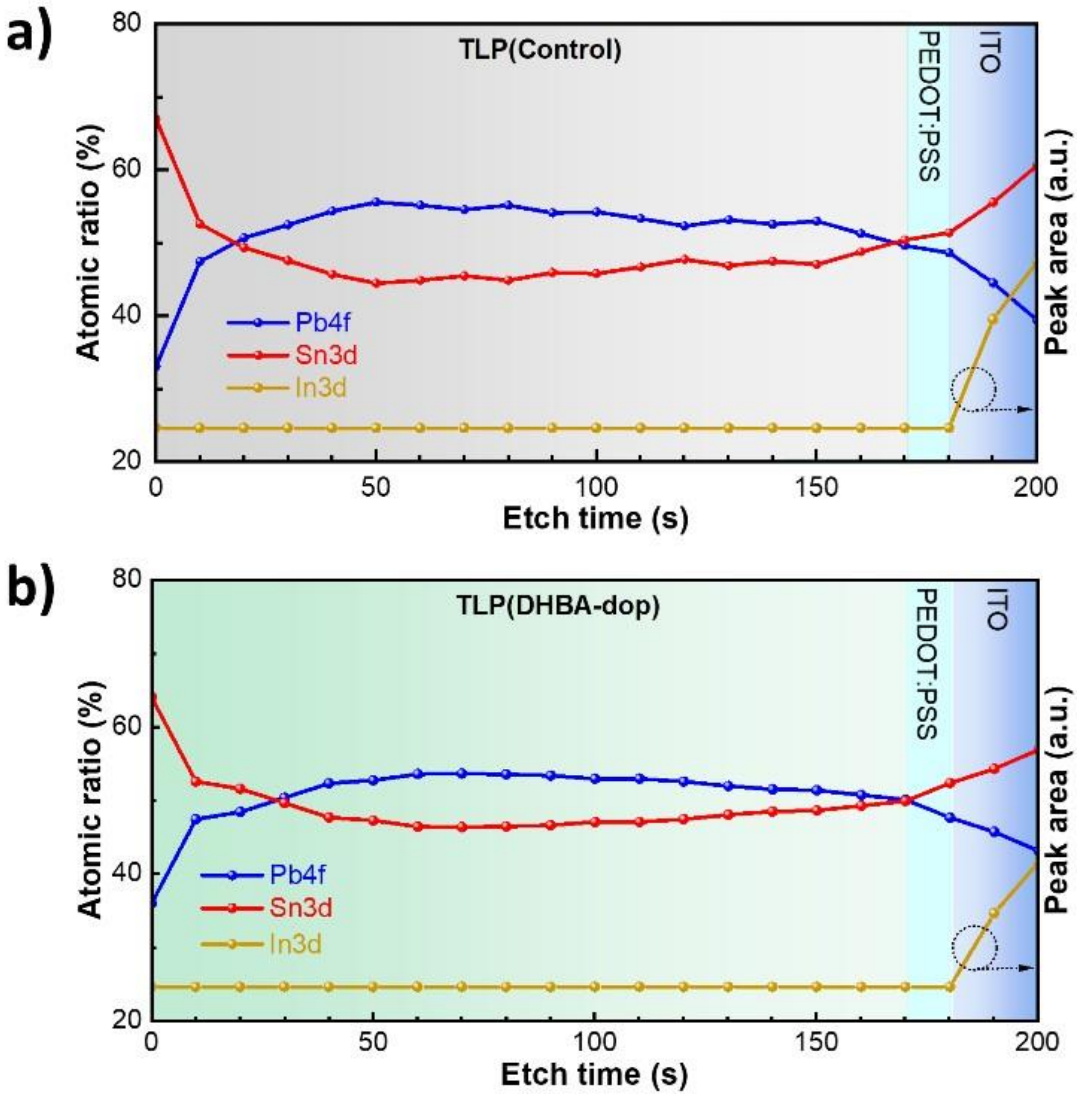

Figure 5.20. Depth dependent Sn/Pb ratio obtained from XPS depth profiles of a) the control and b) the DHBA-dop TLP films. Both were performed at a 500 μm spot within the position for device fabrication (Ag electrode deposition).The right y-axis refer to peak areas of In3d. The appearance of In3d signals means it was etched into the bottom of the TLP films.

Moreover, I performed TEM-EDS measurement on 10 individual perovskite particles to reveal the distribution of Sn/Pb at a microscopic level. The perovskite particles for TEM-EDS test were collected by scraping perovskite powder from TLP films and dispersing them into Chlorobenzene

(CB). Though obvious heterogeneity was not observed in the Sn/Pb element distribution in such microscope level (**Figure 5.21**), the Sn/Pb proportion is diverse in each particle. The Sn proportion of each particle assessed with TEM-EDS was listed in **Table 5.8**. Average Sn proportions in these control particles and DHBA-dop particles were calculated to be 48.44% and 52.55% respectively. This Sn proportion in DHBA-dop perovskite tested by EDS measurement is higher than that in the control perovskite, which is consistent with the ICP-MS results. Regarding the different values compared to those measured by ICP-MS technique, it is because EDS technique has less precision. Moreover, these EDS data have also demonstrated that DHBABr doping leads to convergent distribution of Sn proportion, suggesting a more homogeneous Sn/Pb distribution in microscale. As presented in **Table 5.8**, Sn proportion in the control particles fluctuated significantly from 34.01% to 59.8%, with a standard deviation of 8.8, while Sn proportion in DHBA-dop particles fluctuated from 44.44% to 59.25%, with a much narrower standard deviation of 4.5%. This forcefully and convincingly demonstrated that DHBA-dop perovskite exhibited significantly enhanced homogeneity in microscope level.

Table 5.8. The Sn proportion (%) in 10 individual perovskite particles of the Control and DHBA-dop TLP films.

Samples	1	2	3	4	5	6	7	8	9	10	Avg.	SD
Control	39.35	46.81	59.8	38.03	58.58	56.87	42.59	34.01	49.12	59.27	48.4	8.8
DHBA-dop	56.91	59.25	55.93	52.43	54.44	56.09	47.66	44.44	52.05	46.26	52.6	4.5

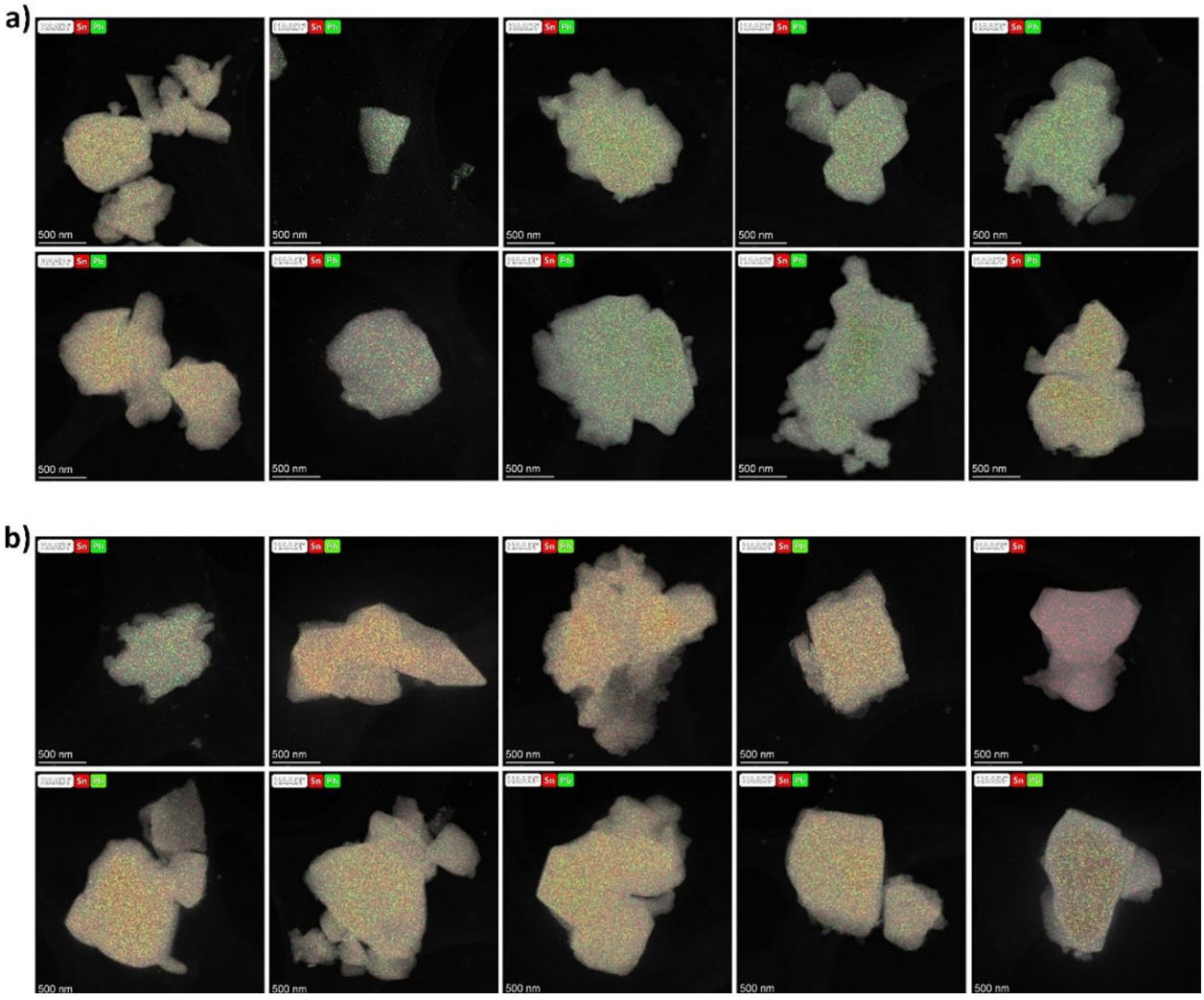

Figure 5.21. TEM-EDS images of dispersed perovskite particles scraped from a) control and b) DHBA-dop TLP films. The particles are randomly selected.

5.8 The primary reasons behind the improved stability

The above study and previous findings of reduced charge recombination suggest a passivation function of DHBABr in the TLP films as well. To reveal the passivation mode in the perovskite, I first verified the distribution of DHBABr in the perovskite through AFM-IR measurements. The surface of the perovskite was probed based on the characteristic peak of $\nu_{C=C}$ at 1525 cm^{-1} (**Figure 5.13b**), which consists of the benzene ring of DHBABr but not in all other components in perovskite.

As presented in **Figure 5.22**, the surface of the control displays no signal for $\nu_{C=C}$, while distinctive molecule signals appear at parts of the boundaries and surface of crystalline grain in DHBA-dop TLP film, suggesting that $DHBA^+$ was extruded to the GBs and surface of perovskite. After post-treatment with DHBABr, the signal of $\nu_{C=C}$ is dispersed all over the surface of perovskite, meaning a full coverage on the surface of perovskite.

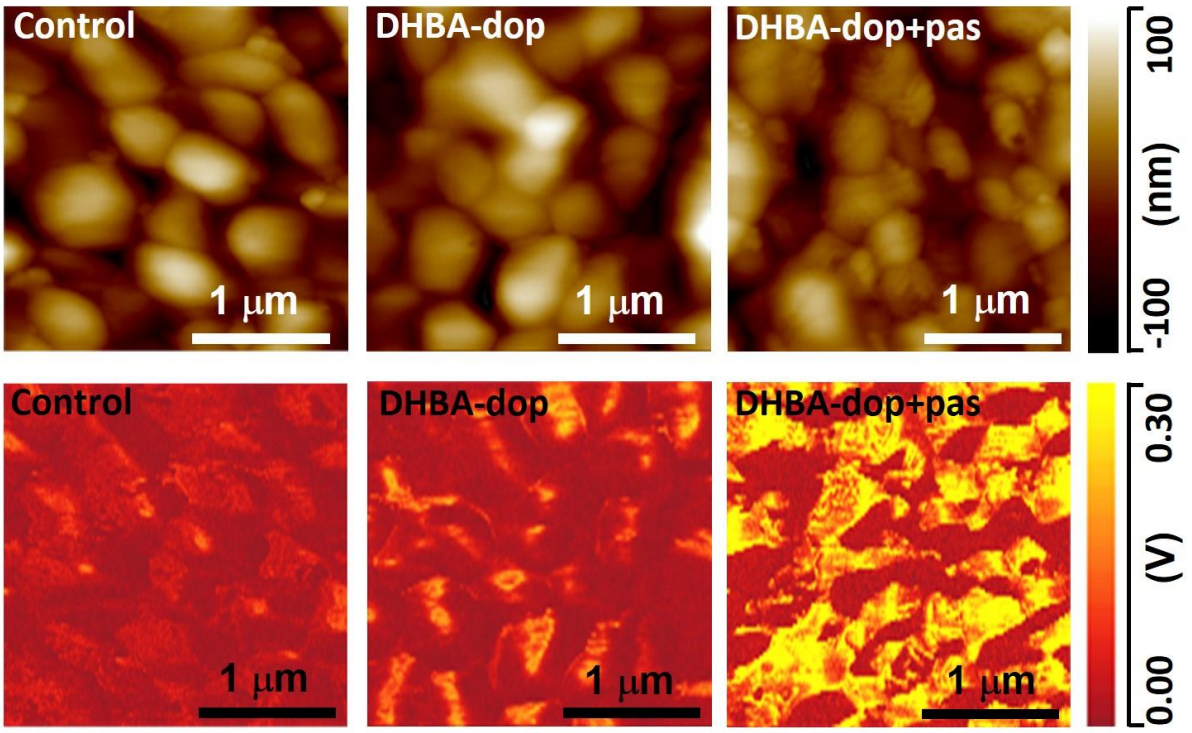

Figure 5.22. AFM-IR images of the three TLP films surfaces, recorded with a feature absorption peak of DHBABr.

According to the distribution of $DHBA^+$ and the proposed interaction mechanism, I can confidently infer the passivation mode as follows (**Figure 5.23**): First, interaction between the terminal NH_3^+ group and I^- allow $DHBA^+$ partially to replace MA^+ and FA^+ during the crystallization process and

passivate their vacancies on the surface and at GBs of the TLP films. Secondly, the electron-rich nature of the phenolic hydroxyl groups in $DHBA^+$ allow it to occupy the vacancy of I^- and anchor with the under-coordinated Pb^{2+} and especially Sn^{2+}, and therefore eliminate the recombination sites.

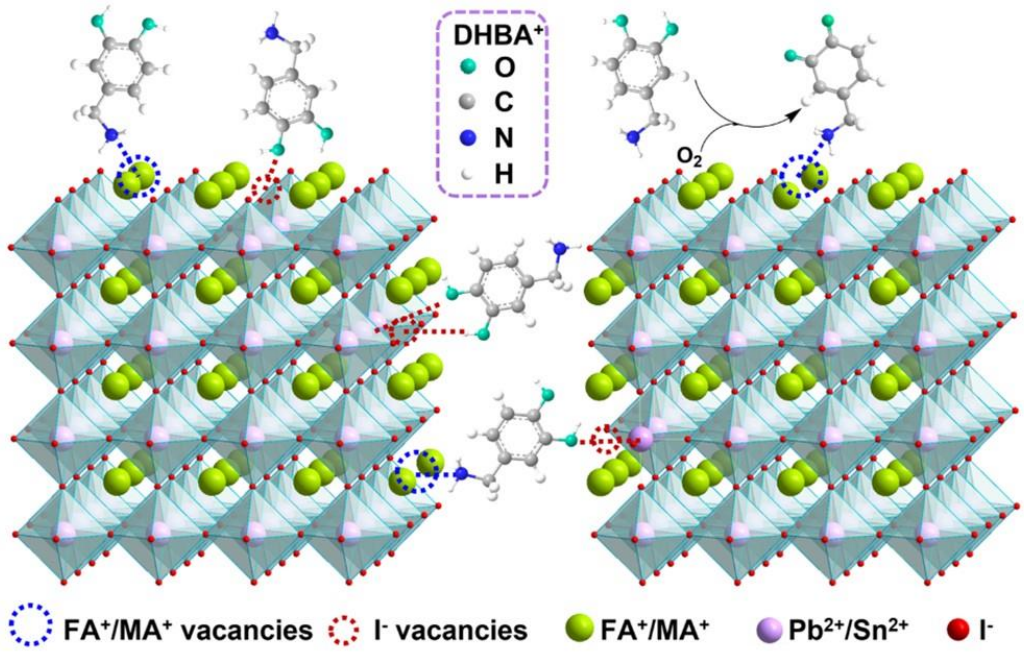

Figure 5.23. Schematic illustration of the distribution of $DHBA^+$ and its coordination with perovskite.

With regards to the increased long-term stability of PSCs, I would attribute this to the inhibition of iodide migration and oxidation retardant in the TLP films and the devices. Iodide can diffuse in perovskite devices and is corrosive to the Ag electrode, due to the existence of I^- vacancies and the high reactivity between iodide and silver, which leads to the damage of the electrode and degradation of perovskite. Through filling vacancies of I^- at GBs and the surface of perovskite, DHBABr closes the channels of iodide diffusion, and thus inhibits the migration out from the perovskite (**Figure 5.23**). Besides, formation of hydrogen bonds between -OH and I^-, and between $-NH_3^+$ and I^-, which was

supported by the chemical shifts of protons in -OH and $-NH_3^+$ of $DHBA^+$ in its mixture with perovskite composites (**Figure 5.15a**), traps the volatile iodide near $DHBA^+$ in the perovskite and therefore suppresses the silver electrode from corrosion. The corrosion rate of Ag electrodes in PSCs placed in air at room temperature with humidity of around 20% further confirmed my assumption (**Figure 5.24**). Electrodes for fresh control, DHBA-dop and DHBA-dop+pas TLPSCs are the same and are all in white color. After aging in air, electrodes for all devices suffer from corrosion. However, corrosion of electrodes in the DHBA-dop and the DHBA-dop+pas devices is much milder than that in the control devices. This was further backed up by the XPS spectra of I3d scanned on the surface of electrode in devices after 10-days aging in air, where the quantity of I on the electrode surface of DHBABr doping and passivation devices is lower than that in the control device (**Figure 5.24b**). This strongly supports the inhibition of iodide migration and electrode corrosion in PSCs after DHBABr doping and post-treatment. The lifetime for PSCs, in this way, were prolonged.

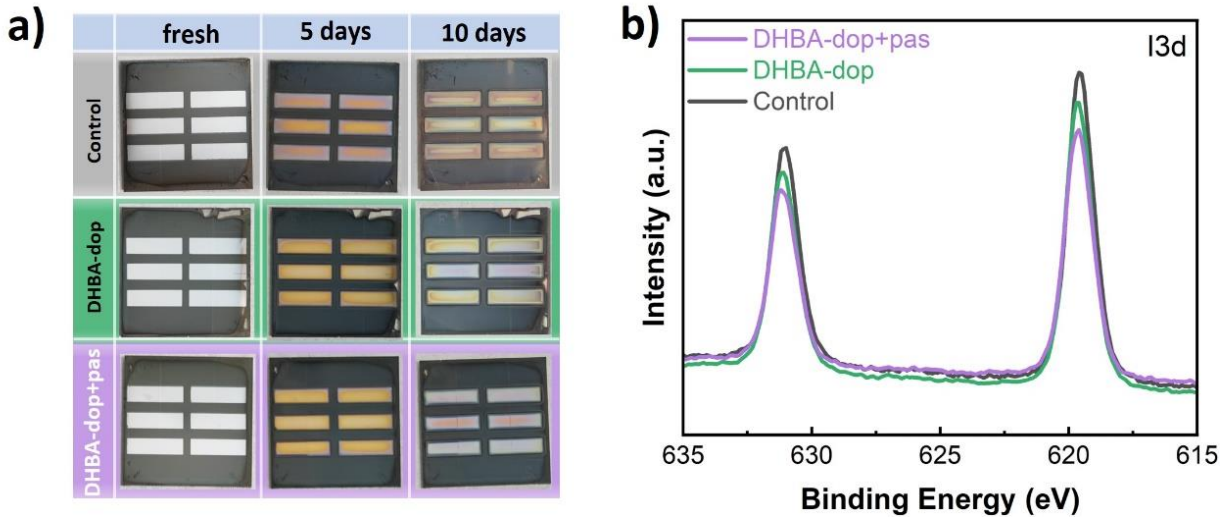

Figure 5.24. a) Photographs of PSCs aged in air in various time. b) XPS spectra of I3d scanned on the surface of electrodes in PSCs aging for 10 days.

5. Preferential Coordinating Sn Ions to Balance the Crystallization of Mixed Sn-Pb PSCs

Degradation of perovskite induced by Sn^{2+} oxidation causes a challenge in long-term stability of PSCs as well. The phenolic hydroxyl group was previously demonstrated to be reductive and thus can hinder the oxidation of Sn^{2+} to Sn^{4+} and I^- to I_2.[59, 200, 222] Therefore, DHBABr with phenolic hydroxyl group was believed to be reductive and was able to capture the O_2 permeated into the interface and GBs of perovskite as shown in **Figure 5.23**, and therefore to retard the oxidation of perovskite. To verify the contribution of DHBABr in inhibiting the oxidation of TLP films, I placed the three TLP films in a dry box at RT with humidity lower than 20% to evaluate the oxygen tolerance of the films. The color on the surface of the TLP films changes gradually after aging in air due to the oxidation of Sn^{2+} (**Figure 5.25**). The color of the control TLP film turned darker black with a slight red tint after 48h, indicating a serious oxidation of Sn^{2+} in the films. The color change in DHBA-dop TLP films was suppressed, which was attributed to the oxidation hinderance of DHBABr at GBs and on the surface of TLP. The variation in the passivation TLP films is negligible, due to the full coverage of DHBABr on the surface.

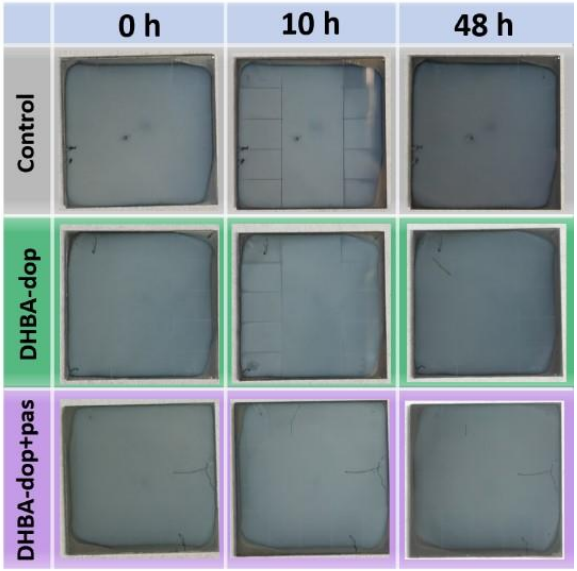

Figure 5.25. Photographs of TLP films aged in air for various time.

The change in film morphologies of both surface and cross-section after aging for 3 days was then estimated to further support the stability improvement. The control perovskite shows a rough surface with dense holes distributed mainly in GBs, indicating grain decomposition initiated from the boundaries (**Figure 5.26a**). This is consistent with the cross-sectional morphology, which displayed fragmentary grains boundaries. The DHBA-dop and DHBA-dop+pas TLPs, on the other hand, exhibits intact surface morphology, demonstrating negligible degradation caused by Sn^{2+} oxidation and I^- migration. Compared to DHBA-dop perovskite, which displayed slightly damaged cross-sectional morphology, the DHBA-dop+pas TLP film show negligible change compared to the fresh one (**Figure 5.2g-i**), indicating a better film protection from oxygen. The degradation of these films is consistent with the decrease in degradation of their UV-vis absorption (**Figure 5.26b**).

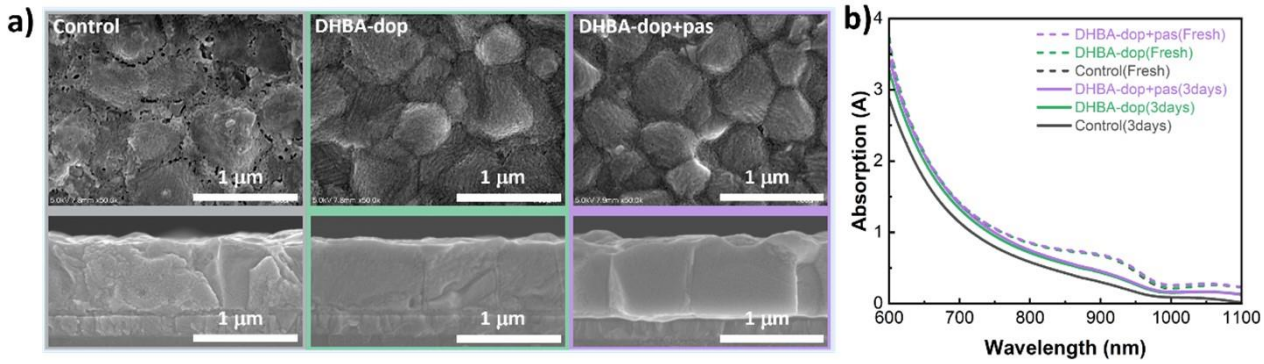

Figure 5.26. a) Surface and cross-sectional SEM images of TLP films aged in air for 3days, with humidity at ~20%. b) UV-vis absorption spectra of fresh TLP films (dashed lines) and those aged for 3 days (solid lines).

XPS of Sn 3d spectra of TLP films exposed to air for 2 h was conducted to further confirm the oxidation inhibition effect in TLP films. The atomic ratio of Sn^{4+} in the total Sn element was

calculated to be 70.98% for the control (**Figure 5.27a**), 55.25% for DHBA-dop (**Figure 5.27b**), and 37.33% for the DHBA-dop+pas (**Figure 5.27c**) TLP films according to the integrated areas of fitted curves. The decreasing Sn^{4+} strongly confirmed DHBABr's retarding effect on Sn^{2+} oxidation, agreeing with the decreasing degradation rate of the TLP films (**Figure 5.26**) and increasing long-term stability of the corresponding devices (**Figure 5.11**).

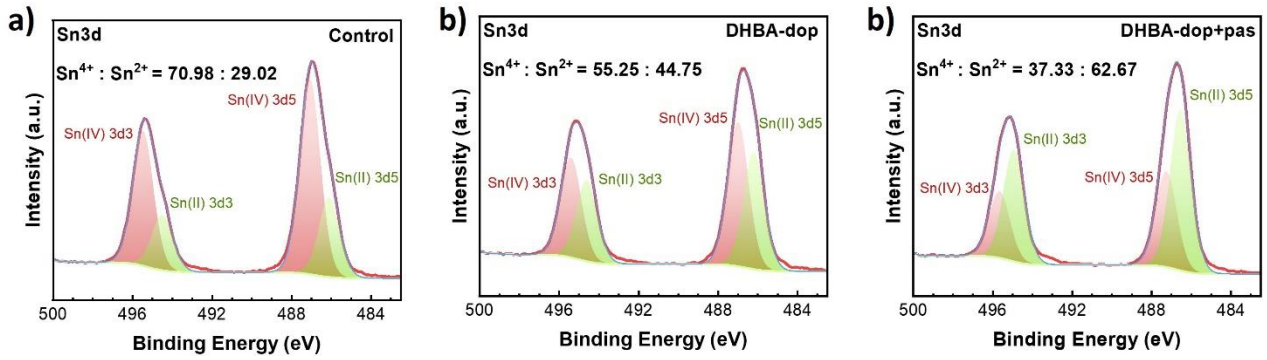

Figure 5.27. XPS spectra of Sn 3d of a) Control, b) DHBA-dop, and c) DHBA-dop+pas films exposed to air for 2 h, respectively.

5.9 Conclusions

In summary, I successfully addressed the composition-segregation issue of TLPs through balancing the crystallization rate between Sn- and Pb-based perovskites via preferentially coordinating Sn^{2+} ions with DHBABr. This coordinate preference was confirmed by the chemical shifts in both FTIR, NMR and XPS. The coordination preference between Sn^{2+} and DHBABr leads to the formation of an amorphous FAI-DHBABr-SnI_2 complex and thus to a reduction in the crystallization rate of the Sn-based perovskite which helps to balances the Sn/Pb perovskite crystallization rates. As a result, the spatial distribution of Sn/Pb was similar across the whole TLP film, with the average Sn/Pb ratio

reaching 47.6:52.4 compared to 46.7:53.3 for the divergent control film. This improved result is crucial to the up-scaling of manufacturing process for TLP films. Relying on this strategy, a champion-device PCE of 22.44% with a V_{oc} of 0.853V and FF of 80.0% was achieved, along with enhanced long-term stability. With reducibility and strong coordination ability, DHBABr inhibits the iodide migration and the oxidation of Sn^{2+} and hence accounts for the enhanced device stability. Moreover, the structure-performance relationship for the improvement was comprehensively examined. This work improves my understanding of mediating the critical crystallization rates of Sn- and Pb-based perovskites and affords an effective and general strategy to balance them.

Chapter 6

TEMPLATED-GROWTH PROCESS OF MIXED SN-PB PEROVSKITE INDUCED BY SNF_2-2PEA ADDUCT

Templated anchoring is one of the efficient strategies to prepare high-quality TLP films. However, the traditional templated-growth process is limited to happening on the surface of the substrate. In this chapter, I have proposed a more reasonable templated anchoring method that controls the crystallization in the whole film. This was achieved by using 2-phosphonoethan-1-aminium iodide (2PEAI) as an additive in the TLP precursor. It was demonstrated that the 2PEAI additive preferentially interacts with SnF_2 and forms SnF_2-2PEA adducts, which optimizes the crystallization process by anchoring the perovskite components in the precursor through the amine and phosphate groups. Consequently, I have prepared TLP films with high crystallinity, better morphology, suitable energy band alignment, and suppressed defect density. The PSCs fabricated from such a templated-growth process achieved the highest PCE of 21.95%, with V_{oc} of 0.84V, J_{sc} of 33.18 $mA \cdot cm^{-2}$, and FF of 78.8%.

6. Templated-Growth Process of Mixed Sn-Pb Perovskite Induced by SnF_2-2PEA Adduct

6.1 Introduction

As mentioned in Chapter 5, TLPs have ideal bandgap at the range of 1.1-1.4 eV and thus become one of the most promising candidates to achieve power conversion efficiency approaching the S-Q efficiency limit (32.7%).[13, 14] In addition, TLPs are suitable for fabrication of all-perovskite tandem solar cells by combining with wide-bandgap perovskite solar cells.[100] Moreover, TLPs reduce the utilization of toxic Pb elements, which decreases the risk of Pb leakage and environmental contamination. Nevertheless, TLPs faced a series of problems derived from the unbalanced crystallization rate of Sn- and Pb-based perovskites and the easily oxidizable nature of Sn(II). Consequently, TLPs suffer from significant interfacial defects, mismatch of band levels, inhomogeneous bandgaps, and easy degradation derived from high oxidation inclination of Sn^{2+}.[183] These problems undoubtedly bring negative influence to the performance and long-term stability of the PSCs, and limits the further development of mixed Sn-Pb perovskite.[93, 183, 190, 223]

Optimizing the crystallization process of the TLP films is one of the most efficient strategies to overcome these issues. As mentioned in Chapter 5, balancing the crystallization of Sn- and Pb-based perovskite can improve the homogeneity of the TLP films accompanied with lower defect density. Following these routes, Chen et al. have demonstrated balanced crystallization in the vertical direction by introducing a layer of iso-pentylammonium tetrafluoroborate ([PNA]BF_4) on the top of PEDOT:PSS, which facilitates the growth of Pb-based perovskite.[182] Fang et al. clarified a TLP film with homogeneous component and energy distribution via introducing hydrazine sulfate (HS), which

selectively coordinates with Sn^{2+} during crystallization.[128] In Chapter 5, I have introduced DHBABr as an additive that preferentially coordinates with Sn^{2+} and thus, improved the Sn/Pb distribution in the radial and vertical direction of the TLP films.

Besides balancing the crystallization rate of Sn- and Pb-based perovskites, it is also reasonable to improve the crystallinity of TLP by controlling their crystallization dynamics through templated anchoring. Zhao and co-workers employed MPA2FPh-BT-BA as a template to anchor Pb or Sn ions and modulate the interfacial crystallization rate of Pb- or Sn-based perovskite.[185] However, this templated anchoring is limited to the buried interface rather than the whole TLP film. So, it is more reasonable to explore the templated anchoring method that controls the crystallization in the whole film. SnF_2 is a widely used additive in tin-based perovskites and TLPs.[224, 225] Previous research have demonstrated that SnF_2 regulates the crystallization of TLP films, resulting in highly oriented topological growth and enhanced crystallinity.[192] However, SnF_2 would preferentially accumulate at GBs and perovskite interfaces after the crystallization process, which may induce more defects and phase separation at GBs and interfaces.[192, 209] To address these problems, Seok's group has utilized SnF_2–pyrazine complex to regulate the crystal growth and prepare $FASnI_3$ films without any phase segregation caused by SnF_2.[209] Similarly, Zong et al. have employed $SnF_2 \cdot 3FACl$ adducts to prepare high-quality TLP films, forming a stable SnF_2 phase at GBs.[226] These SnF_2 adducts have the benefits of leading oriented topological growth and stabilizing the SnF_2 phase and, therefore, suppressing phase degradation initializing at GBs to a certain degree. However, the organic species of the adducts

will either diffuse into the perovskite or evaporate after annealing and, therefore, cannot functionalize in the long term. Thus, it is crucial to select a stable organic species that can both anchor SnF_2 to form an adduct with SnF_2 and anchor perovskite components to regulate the templated growth of TLP films.

Long-chain organic phosphonic acid is a kind of organic acid, which is a non-volatile molecule containing P-O groups that can strongly bind with metal cations like Pb^{2+} and Sn^{2+}.[227-229] It was reported that long-chain organic phosphonic acid can be extruded to the GBs of perovskite after crystallization, similar to SnF_2.[40] Defects at GBs and interfaces, therefore, can be passivated due to their strong coordination between P-O groups and metal cations.[40] In this chapter, I proposed a templated-growth strategy using a derivative of the long-chain organic phosphonic acid, 2-phosphonoethan-1-aminium iodide (2PEAI), as an additive in TLP precursor. It was demonstrated that 2PEAI shows strong coordination with SnF_2, forming a SnF_2-2PEA adduct. By anchoring PbI_2 and SnI_2 in the precursor, this adduct regulates the crystal growth of the perovskite, resulting in TLP films with high crystallinity, better morphology, and suitable band energy for carrier transportation. In addition, the SnF_2-2PEA adduct preferentially accumulates at GBs and interfaces, passivating the vacancies and thus suppressing the defect-induced non-radiative recombination. Consequently, the PSCs fabricated from such a templated-growth process achieved the highest PCE of 21.95%. A range of characterization methods were employed to study the crystallinity and morphology of TLP films, the band alignment and performance of the relative PSCs, and the mechanism of the templated anchoring process. However, this research work could not be fully completed during the PhD

experimental time. Therefore, more characterization methods should be employed to study the quality of the TLP films, the performance and long-term stability of PSCs, and, more importantly, the mechanism behind the improvement of the TLP film crystallinity.

6.2 Experimental details

6.2.1 Materials

Unless specified otherwise, all materials were used as received. Tin powder (Sn, 99.99%), tin floride (SnF_2, 99%), and anhydrous solvents including N, N-dimethylformamide (DMF), dimethyl sulfoxide (DMSO), ethyl acetate (EA), and isopropanol (IPA) were purchased from Sigma-Aldrich. Lead iodide (PbI_2, 99.99%) and formamidinesulfinic acid (FSA, >92%) were purchased from TCI. Hydroiodic Acid (55%) was purchased from Aladdin. (2-Aminoethyl)phosphonic acid (2AEPA) was purchased from Leyan. Formamidinium iodide (FAI, 99.99%) and methylammonium iodide (MAI, 99.99%) were purchased from Great Cell Solar. Bathocuproine (BCP, >99%), phenyl-C61-butyric acid methyl ester (PCBM, >99%) and fullerene (C60, 99.5%) were purchased from Lumtec. Tin (II) iodide (SnI_2, 99.999%) was purchased from Yingkou Shangneng Photoelectric Material Co., LTD. Poly(3,4-ethylenedioxythiophene):polystyrenesulfonate (PEDOT:PSS, AI 4083, 1.3-1.7 wt.%) was purchased from Ossila. Dimethyl sulfoxide-d6 was purchased from the J&K Scientific. ITO glass was purchased from Suzhou ShangYang Solar Technology Co. Ltd. All materials mentioned above were used as received.

6.2.2 Synthesis of 2-phosphonoethan-1-aminium iodide (2PEAI)

200 mg of (2-aminoethyl)phosphonic acid (2AEPA) was weighed and added into a 4 ml vial. Then, 1 ml of deionized water was added to the vial. The resulting mixture was shaken until the powder completely dissolved. After that, 1 ml of hydroiodic acid was added to the vial, and the vial was shaken for a while to complete the reaction. Lastly, the obtained solution was dried in a freeze dryer for 48 hours to remove the excess hydroiodic acid and water. The final product was collected and stored in a glove box filled with N_2 gas. The chemical equation is shown in **Figure 6.1**.

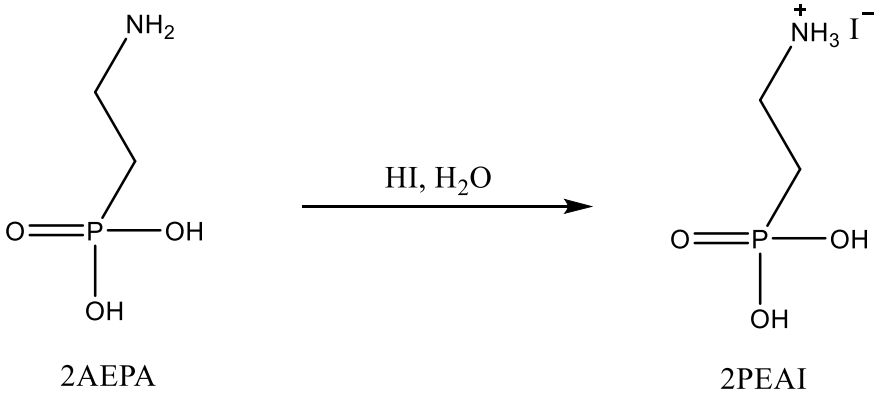

Figure 6.1. Chemical equation of the synthesis of 2PEAI.

6.2.3 Preparation of the TLP precursor

Both the control and target precursors were prepared with a main composition of $MA_{0.3}FA_{0.7}Pb_{0.5}Sn_{0.5}I_3$ in a concentration of 1.8 M. For the control precursor, 14.0 mg of SnF_2 (10 mol% relative to SnI_2), 84.8 mg of MAI, 216.7 mg of FAI, 335.3 mg of SnI_2, and 414.9 mg of PbI_2 were weighed and added to a 4 ml vial successively, then a stirrer, 750 ml of DMF and 230 ml of

DMSO were added to the vial. The mixture was shaken until all the components dissolved, then was further stirred for 2 h at RT. Sn powder (5 mg) was added to the solution, then the mixture was further stirred for 10 min at RT. Then 20 μl of FSA (15 $mg \cdot ml^{-1}$ in DMSO, 0.15 mol% relative to A-site cations) was added to the mixture and shaken for a while without further stirring. For the target precursor (with SnF_2-2PEA adduct), 2PEAI (1.4 mg, 0.3 mol% relative to A-site cations) was weighed and added to the 4 ml vial at the beginning, while the other steps were the same as the control one.

6.2.4 Fabrication of TLPSCs

The ITO glasses were cleaned with detergent, deionized water, isopropanol, acetone, and isopropanol successively in an ultrasonic water bath (600 W, 40 kHz) with the temperature kept below 30 °C. The ITO glasses were then dried under N_2 flow and treated with UV-ozone for 30 mins to ameliorate the infiltration performance of ITO substrate. 70 μl of aqueous PEDOT:PSS (1.3-1.7 wt.%) was spin-coated onto the substrate with a speed of 4000 rpm for 30 s, then was annealed for 10 min at 150 °C. The as prepared perovskite precursor solution was spin-coated onto the PEDOT:PSS substrate with speed of 1000 rpm for 10 s and then 4000 rpm for 60 s. After 18 s of the second step of spinning process, anti-solvent EA (500 μl) was dropped on to the film within 2 s. Afterward, the substrates were annealed for 10 min at 100 °C. Then a layer of PCBM (5 $mg \cdot ml^{-1}$ in CB) was spin-coated with a speed of 6000 rpm for 35 s and annealed for 1 min at 100 °C, followed by deposition of C_{60} (20 nm), BCP (6 nm), and Ag (100 nm) via thermal evaporation. The thickness of each layer was monitored and controlled using a film thickness gauge within the thermal evaporator.

6.2.5 Performance and stability characterizations of TLPSCs

The performance and stability of the PSCs were evaluated through J-V, dark J-V, SCLC, SPO, EIS, MS, TPC, and TPV measurements, which were performed according to the methods mentioned in Chapter 3.

6.2.6 Materials and films characterization

The characterizations relative to materials and film quality of TLP were evaluated through SEM images, AFM images, XRD patterns, static-state PL spectra, UV-vis absorption spectra, Fine scanning of XPS spectra, UPS spectra, FTIR spectra, NMR spectra, which were measured according to the methods presented in Chapter 3.

6.3 Mechanism study: interaction modes and templated anchoring

To study how 2PEAI regulates the crystallization of the TLP films in the fabrication process and its role in the resulting TLP films, I first investigated the interaction behavior between 2PEAI and perovskite components. As shown in the chemical structure (**Figure 6.1**), 2PEAI contains an amine group and a phosphate group at each side of the chain. The terminal amine allows 2PEAI to partially replace MA^+ and FA^+ cations during the crystallization process and passivate MA and FA vacancies on the surface and at GBs of the TLP films.[81, 201, 230] The phosphate group, on the other hand, is a strong electron donor that can coordinate with electron acceptors like Pb^{2+} and Sn^{2+} metal cations.[40]

6. Templated-Growth Process of Mixed Sn-Pb Perovskite Induced by SnF_2-2PEA Adduct

NMR measurements were first performed to reveal the interaction modes. **Figure 6.2a** presents the ^1H NMR spectra of 2PEAI and its mixture with FAI, PbI_2, SnI_2, and SnF_2. In the spectrum of 2PEAI, the peak at 2.5 ppm refers to the solvent (DMSO), the peaks at 1.9 ppm and 2.9 ppm refer to hydrogens in the chain, while the peaks at 8.2 ppm refer to hydrogens of the amine group. The active hydrogens of the phosphate group were not detected. After mixing with FAI, PbI_2, SnI_2, and SnF_2, the peak due to the amine group up-field shifts to around 7.9 ppm, 7.7 ppm, 7.7 ppm, and 7.7 ppm respectively, suggesting strong interaction between the amine group and perovskite components. It is noteworthy that the chemical shifts are attributed to the increased quantity of ionic interaction between I^- and NH_3^+ because the distance of the chemical shifts grows with increasing concentration of I^- ions in the solution.

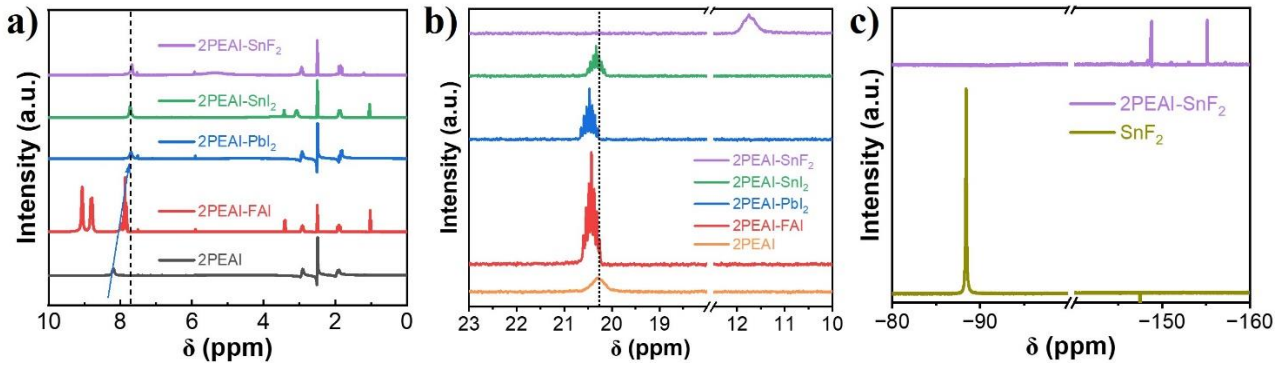

Figure 6.2. Study of chemical interaction between 2PEAI and perovskite components using NMR techniques. a) ^1H NMR spectra of 2PEAI and its mixture with FAI, PbI_2, SnI_2, and SnF_2. b) ^{31}P NMR spectra of 2PEAI and its mixture with FAI, PbI_2, SnI_2, and SnF_2. c) ^{19}F NMR spectra of 2PEAI and its mixture with SnF_2. The mixtures were all prepared by dissolving 2PEAI and each perovskite component in a molar ratio of 1:1, with DMSO-d6 as solvent and its chemical shift as reference.

6. Templated-Growth Process of Mixed Sn-Pb Perovskite Induced by SnF_2-2PEA Adduct

As hydrogen signals referred to the phosphate group were not presented in the ^1H NMR spectra, I further conducted ^{31}P NMR measurement to analyze the interaction between phosphate groups and perovskite components. As shown in **Figure 6.2b**, the peaks due to the P atom in the mixtures of 2PEAI-FAI, 2PEAI-PbI_2, and 2PEAI-SnI_2 slightly shifts in the down-field direction, while the peak of the 2PEAI-SnF_2 mixture remarkably shifts in up-field direction, compared to that in the pure 2PEAI solution. This indicates that the interaction modes between 2PEAI and FAI, PbI_2, and SnI_2 are different from that between 2PEAI and SnF_2. In addition, the interaction of 2PEAI with SnF_2 is much stronger than that with other perovskite components. The down-field shift means that electron cloud density in the P atom decreases, suggesting a transfer of electrons from the P atom to its adjacent atom or the interaction objects, and vice versa. Accordingly, I proposed that in the mixtures of 2PEAI-FAI, 2PEAI-PbI_2, and 2PEAI-SnI_2, 2PEAI acts as an electron donor, while FAI, PbI_2, and SnI_2 act as an electron acceptor. The proposed modes are shown in **Figure 6.3a, b**. For the mixtures of 2PEAI-FAI, 2PEAI interacts with FAI through the hydrogen bonds between hydrogen atoms in FA^+ and O atoms in P-OH/P=O (**Figure 6.3a**). Regarding the mixtures of 2PEAI-PbI_2 and 2PEAI-SnI_2, 2PEAI interacts with PbI_2 and SnI_2 through donor-acceptor coordination between O atoms in P-OH/P=O and the metal cations (**Figure 6.3b**). In this model, electrons transfer from the P atom in 2PEAI to FA^+ and metal atoms in PbI_2 and SnI_2 (**Figure 6.3a, b**), which leads to decreased electron cloud density around P atom and thus results in a down-field shift of peaks in their ^{31}P NMR spectra (**Figure 6.2b**).

6. Templated-Growth Process of Mixed Sn-Pb Perovskite Induced by SnF_2-2PEA Adduct

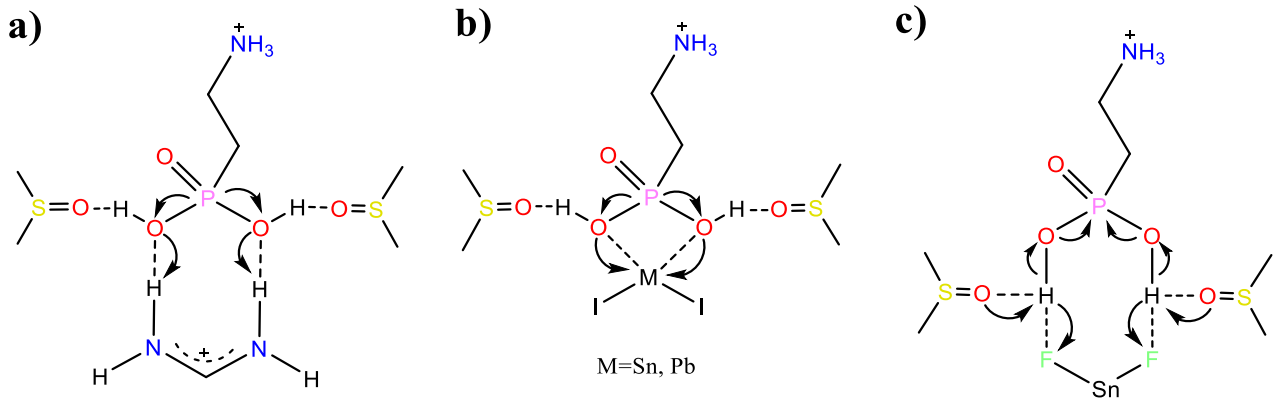

Figure 6.3. The proposed interaction modes between 2PEAI and perovskite components.

In terms of the mixtures of 2PEAI-SnF_2, their interaction is totally different. 2PEAI interacts with SnF_2 through the hydrogen bonds between hydrogen atoms in P-OH and the F atoms in SnF_2 instead of forming metal-ligand coordination (**Figure 6.3c**). This interaction mode may not directly increase the electron cloud density of the P atom in 2PEAI. Instead, it may be because the formation of H···F hydrogen bonds will weaken the O-H bonds of the phosphate group, leading to the withdrawal of electron cloud around from oxygen atoms to the P atom (**Figure 6.3c**). This explains the up-field shift of peak referred P atom after mixing with SnF_2. This proposed interaction mode was further supported by the ^{19}F NMR spectra of SnF_2 and its mixture with 2PEAI, where the peak due to the F atom remarkably shifts to the up-field position (**Figure 6.2c**). The up-field shift may be relevant to the DMSO solvent. Besides SnF_2, 2PEAI also forms H···O hydrogen bonds with DMSO. Thus, additional electrons flow from S=O groups in DMSO to the strong-electronegativity F atoms in SnF_2 (**Figure 6.3c**), accounting for the up-field shift of the peak referred to F atom (**Figure 6.2c**).

The different interaction modes may be attributed to the different electronegativity of I and F elements.

6. Templated-Growth Process of Mixed Sn-Pb Perovskite Induced by SnF_2-2PEA Adduct

I atoms have relatively low electronegativity, and thus, the mixtures of 2PEAI-PbI_2 and 2PEAI-SnI_2 prefer to interact through the stronger O···M(Pb/Sn) coordination mode. In contrast, F atoms have strong electronegativity and, therefore, H···F hydrogen bonds prove superior to the O···M(Pb/Sn) coordination in the mixture of 2PEAI-SnF_2.

XPS measurements of the mixture was then further performed to confirm my hypothesis. As shown in **Figure 6.4**, both the Pb4f peaks of PbI_2 (**Figure 6.4a**) and Sn3d peaks of SnI_2 (**Figure 6.4b**) shift to lower binding energy, suggesting increased electron density in the metal atom. This is consistent with the NMR data and my hypothesis that O···M(Pb/Sn) coordination dominates in the mixtures of 2PEAI-PbI_2 and 2PEAI-SnI_2. As for the mixture of 2PEAI-SnF_2, the Sn3d peaks exhibit negligible shift, indicating barely any interaction between O atoms in the phosphate group and the Sn atom in SnF_2 (**Figure 6.4c**). Furthermore, the strong H···F hydrogen bonds were verified by the evident blue shift of the F1s peak of SnF_2 (**Figure 6.4d**). It is worth noting that the chemical shift of F1s peak is opposite to that in the ^{19}F spectra, but I can firmly attribute it to the lack of DMSO in this XPS measurement. F atoms, therefore, cannot attract additional electrons from S=O group of DMSO. Instead, it has to share its electron with H atoms in 2PEAI, which results in the decrease of electron cloud density around it, accounting for its chemical shift to a higher binding energy.

6. Templated-Growth Process of Mixed Sn-Pb Perovskite Induced by SnF_2-2PEA Adduct

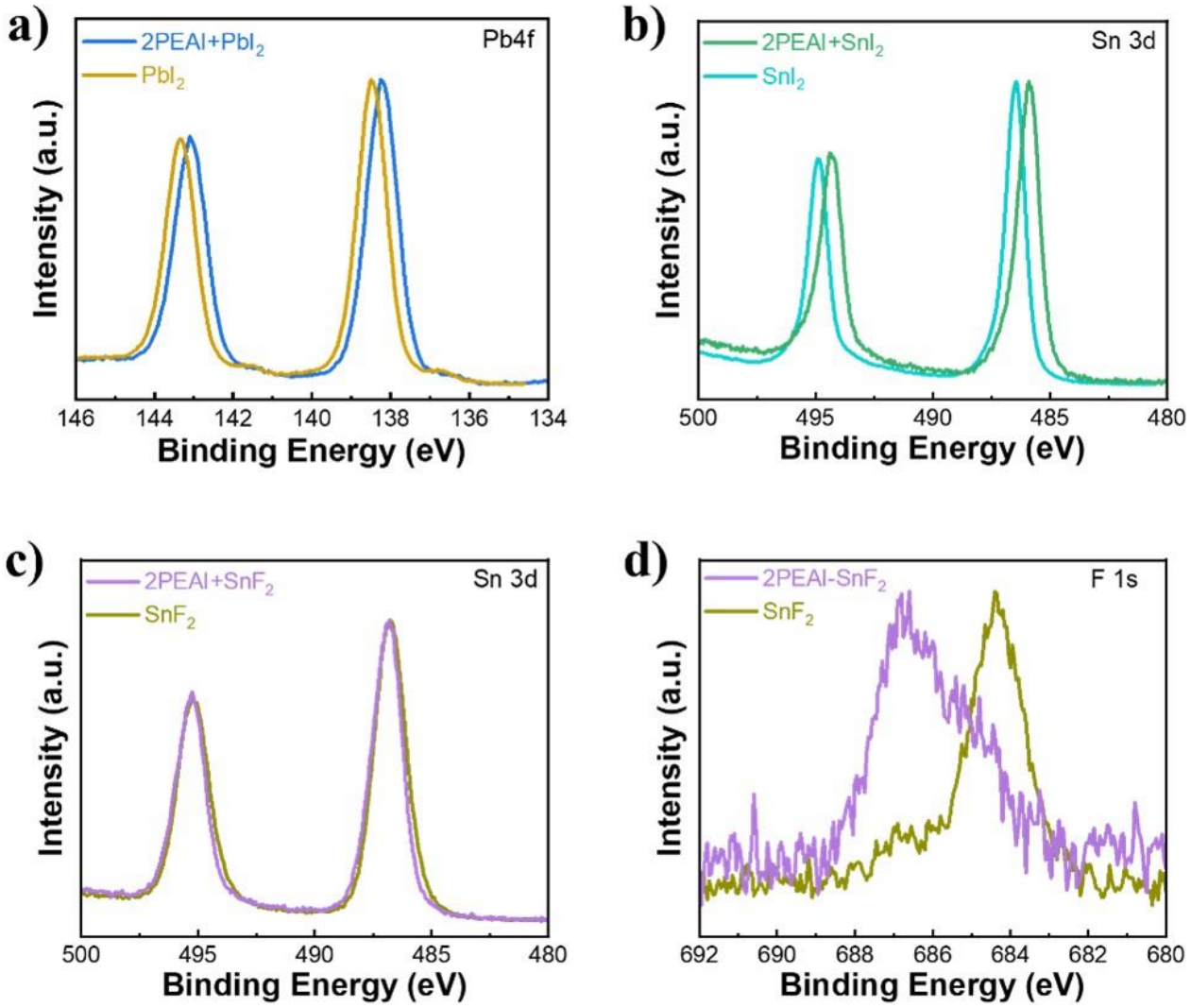

Figure 6.4. Study of chemical interaction between 2PEAI and perovskite components using XPS techniques. a) Pb4f XPS spectra of PbI_2 and its mixture with 2PEAI. b) Sn3d XPS spectra of SnI_2 and its mixture with 2PEAI. c) Sn3d XPS spectra of SnF_2 and its mixture with 2PEAI. d) F1s XPS spectra of SnF_2 and its mixture with 2PEAI.

According to the above analysis, I proposed a hypothesis of 2PEAI's role in regulating the crystal growth process of TLP films: Firstly, in the perovskite precursor, 2PEAI preferentially coordinates with SnF_2 and immediately formed SnF_2-2PEAI adducts in the precursor. The fast formation of adducts was observed by the fast color change from white to orange after adding 2PEAI powder to

the incompletely dissolved SnF_2 solution (**Figure 6.5**). Secondly, the SnF_2-2PEA adducts anchor the other perovskite components through the NH, P-O, and P=O groups in 2PEAI. Thirdly, during the anti-solvent treatment and annealing process, the adducts act as templates to facilitate the pre-nucleation of the perovskite crystal, which benefits the formation of high-quality TLP films.[176] Lastly, the adducts were extruded to the GBs and interface and passivate the defects at the GBs and interface. This was demonstrated by the SEM images discussed in the next section.

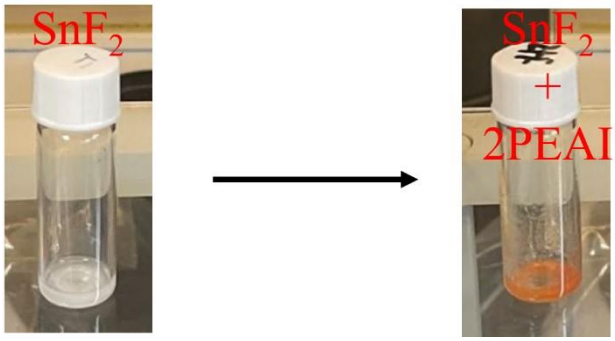

Figure 6.5. Photographs recording the immediate color change from white to orange after adding 2PEAI powder to the incompletely dissolved SnF_2 solution.

6.4 Study of the film quality

Morphology is one of the most important factors that determines the quality of TLP films. SEM characterization was employed to investigate the effect of the templated growth strategy on the morphology of the resulting TLP films. **Figure 6.6a-f** shows the top-view SEM images of TLP films in various magnifications. The control film showed a terrace-like surface texture with pinholes as a result of the accumulation of SnF_2 on the surface (**Figure 6.6a, c, e**).[225] In addition, the control film contains a small amount of tiny bright particles on the surface (**Figure 6.6c**), which are relative to

6. Templated-Growth Process of Mixed Sn-Pb Perovskite Induced by SnF_2-2PEA Adduct

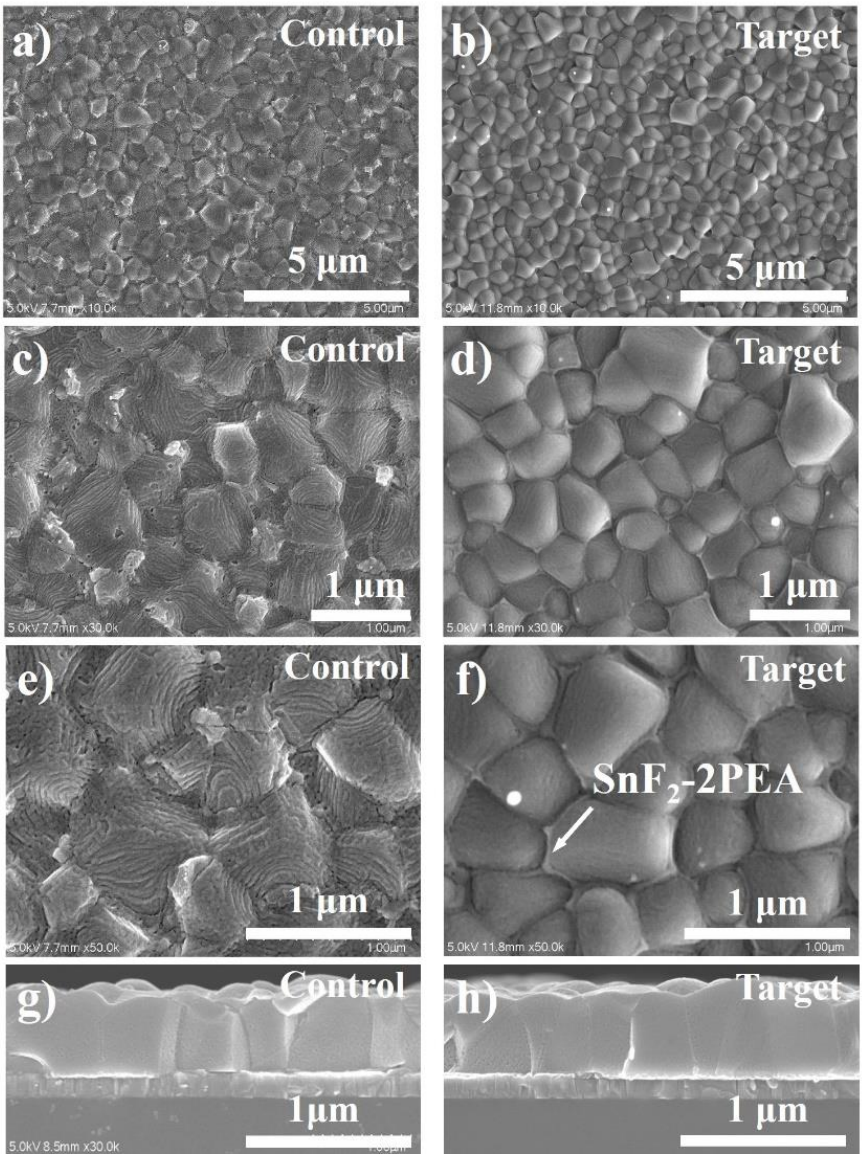

Figure 6.6. a-f) Top-view SEM images of the a, c, e) control and b, d, f) target TLP films in various scales. g, h) Cross-sectional SEM images of the g) control and h) target TLP films in various scales.

SnF_2 and probably are SnF_2-rich perovskite grains, as demonstrated in Chapter 5. Both the terrace-like structure and bright particles on the surface would lead to an uneven surface and poor contact between the TLP films and ETL and, thus hinder the charge transporting.[209, 225] In contrast, the target film presented a smooth surface without textured feature and extra bright particles on the surface (**Figure 6.6b, d, f**), leading to a compact contact of the TLP film and ETL which benefits the carrier

transfer at the interface. It is noteworthy that the GBs of the target film are filled with something different to the perovskite crystal, which may well be the amorphous SnF_2-PEA adducts. These cross-link amorphous SnF_2-PEA adducts will play a key role in passivating defects at GBs and thus suppressing defect-induced charge recombination. In terms of the cross-sectional morphology, the control and target films show similar thicknesses and morphologies, except that the target film presents lower surface roughness (**Figure 6.6g, h**). The improved surface roughness of the target film was further supported by the AFM measurements. As shown in **Figure 6.7**, the target film exhibits an evidently smoother surface with a significantly decreased surface roughness of R_{ms}=19.2 nm, compared to R_{ms}=44.2 nm of the control film.

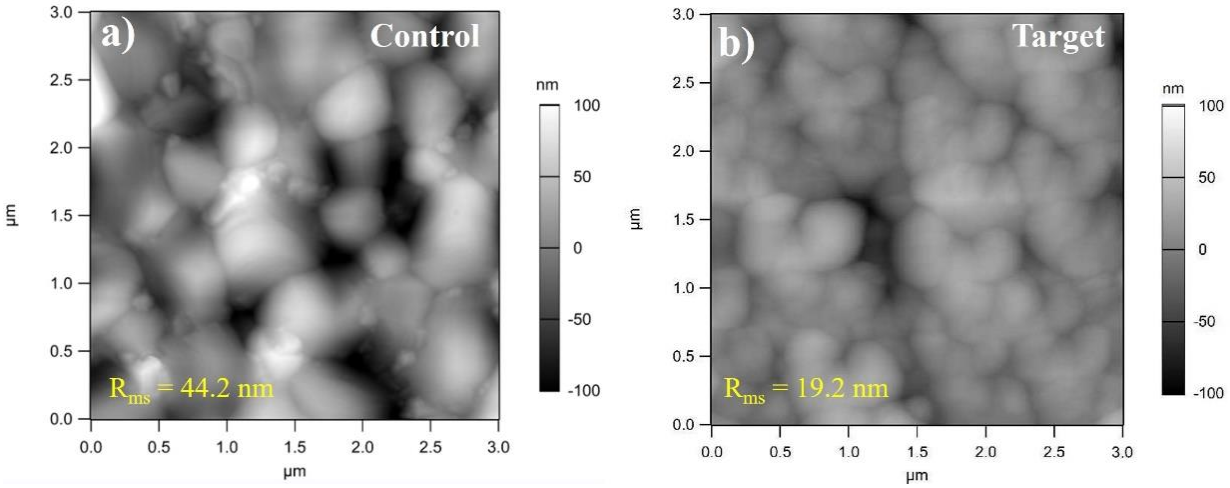

Figure 6.7. AFM images of the control and the target TLP films.

Besides the improvement of surface morphology, this templated-growth strategy also leads to improved crystallinity and suppressed defect density, as demonstrated by the XRD and static-state PL measurements. As shown in **Figure 6.8a**, both the control and target TLP films present a pure α-phase

perovskite without any impurities like PbI_2 and non-perovskite phases. However, the peak intensity of the target film is much stronger than that of the control, indicating a significant increase in crystallinity due to the templated anchoring crystallization process (**Figure 6.8a**). The PL intensity of the target film was noticeably increased, around ten times that of the control (**Figure 6.8b**). This points out that the defect density in perovskite was effectually decreased and, therefore, the non-radiative recombination in the TLP films was suppressed, profiting from the improved crystallinity and the defects passivation on the surface and especially at GBs by the SnF_2-2PEA adducts. Moreover, the target TLP film also exhibits slightly improved absorption of the low-wavelength light owing to the improved crystallinity (**Figure 6.8c**).

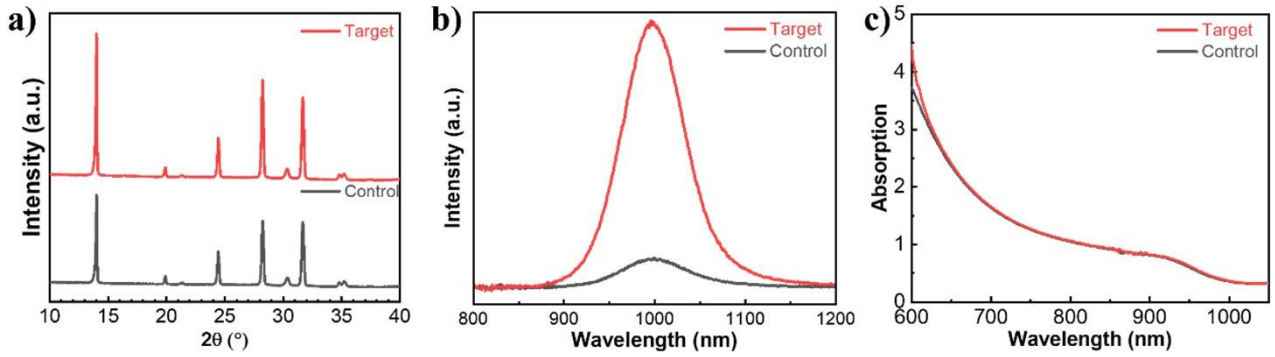

Figure 6.8. a) XRD patterns, steady-state PL, and UV-vis absorption spectra of the control and target TLP films.

6.5 Schottky contact

Chemical doping and surface passivation of perovskites, along with the change of their electrical properties, significantly affect the photovoltaic performance of PSCs.[40, 184, 230] We first performed KPFM measurements to investigate the distribution of surface potential (relative to the probe) on the

surface of the TLP films in a scope of 3 μm × 3 μm. As shown in **Figure 6.9a, b**, the target TLP film presents a more uniform surface potential in the measured scanned area, reflecting an improved homogeneity of composition and surface roughness. Moreover, the target film shows a higher surface potential compared to the control one. The average surface potential of the target film obtained from the KPFM line scan is -168 mV, which is higher than -253 mV of the control film (**Figure 6.9c**). This higher surface potential means a shallower Fermi level, indicating suppressed p-type self-doping in the target TLP film.[188]

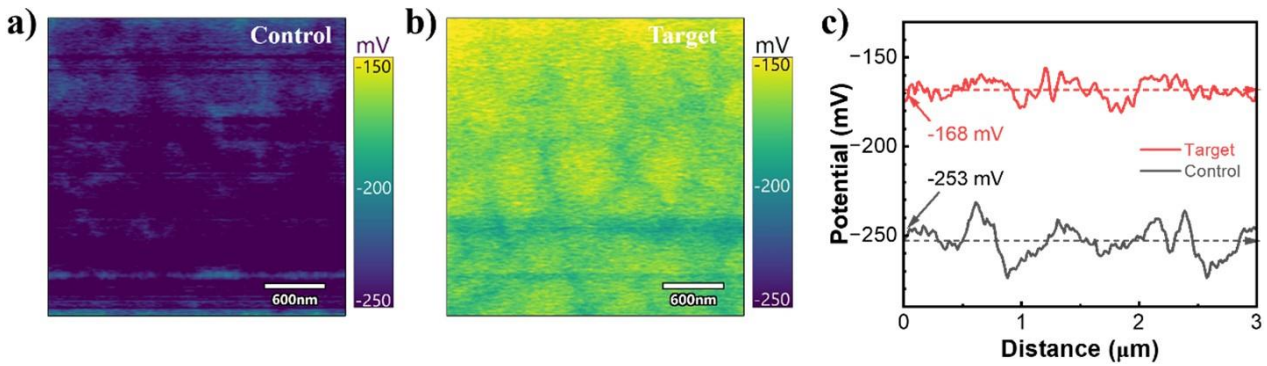

Figure 6.9. KPFM images of the a) control and b) target TLP films. c) Line scans derived from the KPFM images at the axis of y=1.5 μm.

To further investigate the semiconducting characteristic of the TLP films and the charge transfer dynamic at the interface of the TLP films, I employed UPS measurements to evaluate the energy band level of the TLP films as well as the energy band alignment inside the devices. The UPS spectra of the TLP films are shown in Figure **6.10a**. The work function of the control and target films derived from the cut-off edge were estimated to be 4.66 eV and 4.58 eV, respectively. The VBMs with respect to Fermi level were directly obtained from the tail of the spectra, which are 0.61 eV and 0.84 eV for

the control and target films, respectively. According to the bandgap (1.26 eV) of perovskite, the CBMs with respect to Femi level were then evaluated to be -4.01 eV and -4.16 eV for the control and target film, respectively. Combining with the VBM of PEDOT:PSS (-5.17 eV, **Figure 5.6** in Chapter 5) and CBM of PCBM (-4.20 eV, **Figure 5.6** in Chapter 5), the band alignment at the top and bottom interface of the TLP films can be summarized in **Figure 6.10b.**

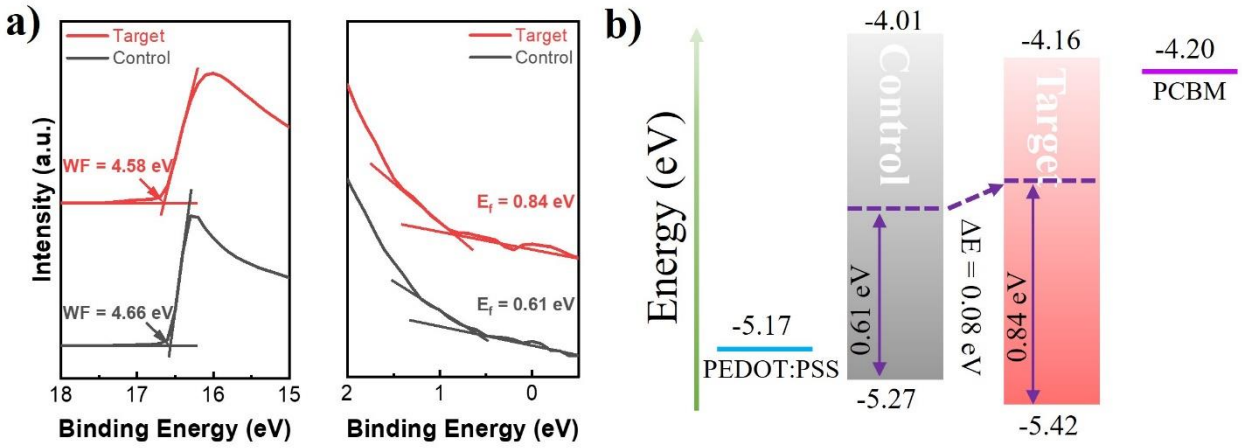

Figure 6.10. a) UPS spectra of the TLP films. b) Energy band alignment at top and bottom interface of TLP films in their TLPSCs.

As presented, the Fermi level with respect to the VBM of the control (0.61 eV) is close to the intrinsic value (0.63 eV), suggesting an intrinsic or weak p-type semiconducting nature. In contrast, the value of 0.84 eV for the target film is far beyond the intrinsic value, pointing out an n-type semiconducting nature, which is beneficial for charge extraction at the top interface because an internal electric field that points from the top to the bottom of perovskite will be constructed at the interface, thus facilitating the transfer of electrons. The Fermi level of the target film upshifts 0.08 eV compared to

that of the control, which is consistent with the value evaluated from the KPFM results (85 mV, **Figure 6.9c**), demonstrating the reliability of the data. In addition, the CBM and VBM of the target film downshift 0.15 eV compared to that of the control. The up-shift of the Fermi level and downshift of CBM and VBM leads to a weaker potential for the tin composition to be oxidized and suggests a suppression of the p-type self-doping, which is harmful to the photovoltaic performance.[188] This agrees with my previous statement made in the analysis of KPFM data.

Furthermore, the downshift of CBM results in a better band alignment and thus decreases the electron extraction barrier at the interface of the TLP layer and the ETL. When contacting PCBM, there appears to be an energy gap of 0.19 eV between the surface of the control TLP films and PCBM. This large energy offset results in a great barrier for charge extraction and V_{oc} loss. The offset between the target perovskite and PCBM decreases to 0.04 eV. Consequently, the energy band between the surface of the target TLP film is well matched with that of PCBM, resulting in an optimized band alignment at the top interface and, therefore, benefiting the electron extraction on the top surface of the target TLP film.

6.6 Performance of PSCs

Based on the improvement in film quality and the energy band alignment, the photovoltaic performance of the PSCs should be significantly enhanced. Therefore, PSCs with an inverted planar structure of ITO/PEDOT:PSS/Perovskite/PCBM/C60/BCP/Ag were fabricated to estimate the enhancement of PCE. The reverse-scanning J–V curves were measured and shown in **Figure 6.11**.

The detailed parameters are summarized in **Table 6.1**. As presented, the PCE of the champion device of the target PSCs was significantly enhanced from 19.88% to 21.95%, with a V_{oc} enhanced from 0.80 V to 0.84 V, a J_{sc} enhanced from 32.30 mA·cm^{-2} to 33.18 mA·cm^{-2}, and an FF enhanced from 76.9% to 78.8%. The improvement is attributed to the improvement of film quality, the inhibition of non-radiative recombination at GBs and interface by SnF2-2PEA adducts, and the optimization of band alignment at TLP film interface. The PCE achieved in this work is slower than that achieved in the work presented in Chapter 5 because this work is not a continue work based on that presented in Chapter 5. Instead, it is a parallel work. In addition, the perovskite in this work lacks surface passivation due to the ineffective of DHBABr (used in the work presented in Chapter 5) as a passivator on this perovskite. An effective passivator should be explored and use for post-treatment of this perovskite in the future.

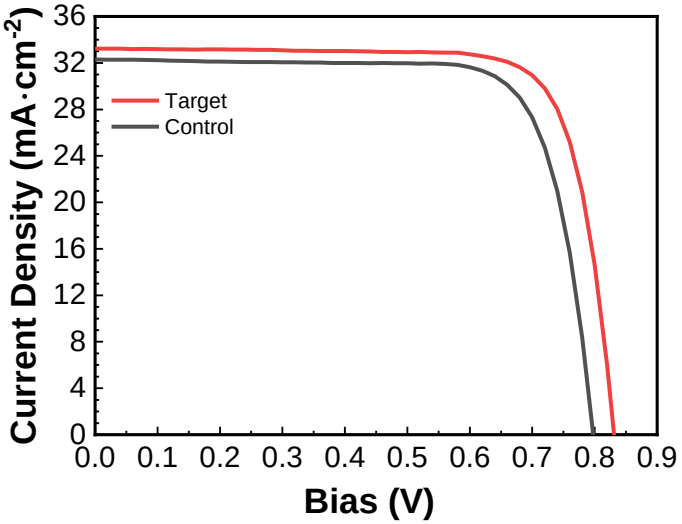

Figure 6.11. J-V curves of the control and target TLPSCs.

Table 6.1. Detailed parameters of J-V curves in **Figure 6.11**. The parameter η refers to PCE.

	V_{oc} (V)	J_{sc} (mA·cm^{-2})	FF (%)	η (%)
Control	0.80	32.30	76.9	19.88
Target	0.84	33.18	78.8	21.95

6.7 Device physics

The improvement of the photovoltaic performance was also reflected in the device physics of the TLPSCs. First, Mott-Schottky measurements were performed to obtain the build-in potential (V_{bi}) of the devices, which reflects the trap density in the TLP films. The rise of V_{bi} from 0.72 V to 0.75 V, as depicted in **Figure 6.12a**, suggests a suppression of trap density in the target TLP film and thus serves as strong evidence supporting the enhancement of V_{oc} (**Figure 6.11**). Subsequently, resistance in the PSCs was studied through the Nyquist plots derived from EIS measurements (**Figure 6.12b**). The parameters obtained by fitting the Nyquist plots with the equivalent circuit model embedded in **Figure 6.12b** are detailed in **Table 6.2**. Notably, the target device demonstrates a significant increase in recombination resistance (R_{rec}) at 13453 Ω, in contrast to the control's value of 5475 Ω. Concurrently, its charge transfer resistance (R_s) experiences a slight reduction from 26.58 Ω to 11.51 Ω. This increase in R_{rec} and decrease in R_s contribute to an enhanced barrier against charge recombination and a reduction in the impediment to charge extraction. As a result, these changes facilitate carrier transfer and can be attributed to the observed improvement in performance.

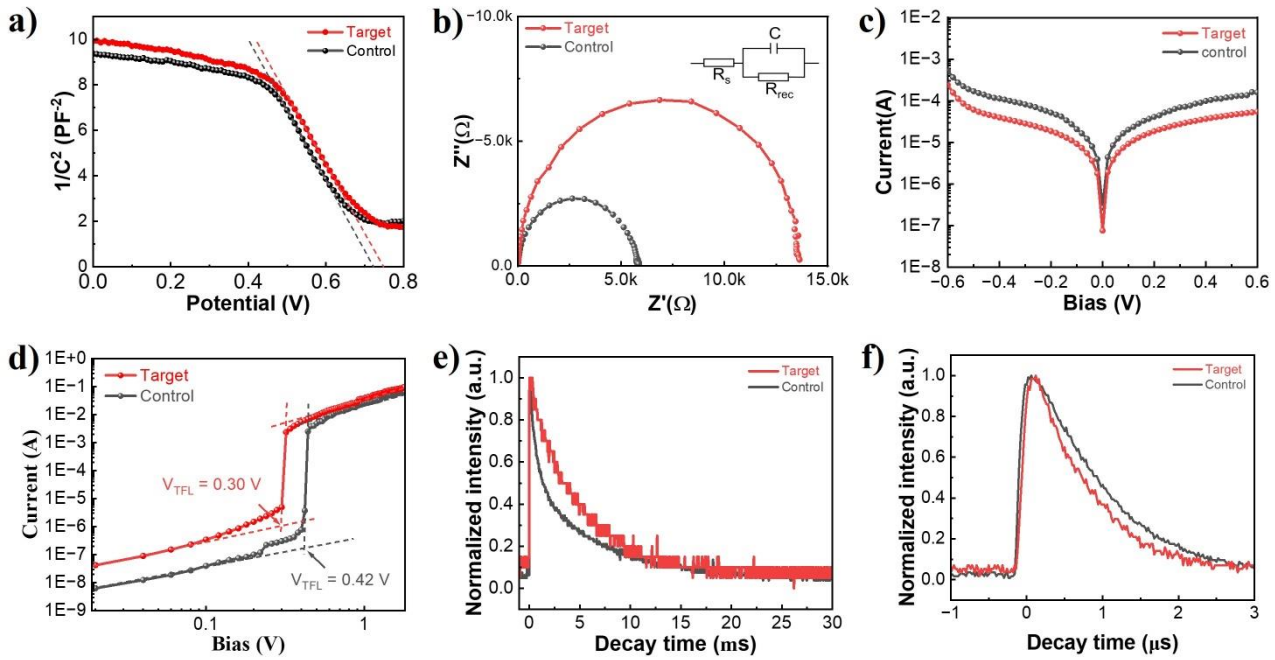

Figure 6.12. **Study of device physics**. a) Dark J-V curves of devices with an active area of ~0.15 cm^2. b) Mott-Schottky plots of devices, recorded from 0V to 0.8 V, with a step size of 0.01 V. c) Nyquist plots of devices, measured in a bias of 0.5 V, with a frequency range of 1 Hz - 1×10^6 Hz. The equivalent circuit model was embedded. d) SCLC of electron-only devices with a structure of ITO/SnO_2/perovskite/PCBM:C_{60}/Ag, tested in a dark enviroment. e) TPV of devices. f) TPC of devices.

Table 6.2. The fitting parameters of the EIS plots according to the equivalent circuit model employed in **Figure 6.12b**. R_s, R_{rec}, and C refer to series resistance, recombination resistance, and capacitance, respectively.

	R_s (Ω)	R_{rec} (Ω)	C (F)
Control	26.58	5475	1.14×10^{-8}
Target	11.51	13453	1.05×10^{-8}

Furthermore, dark J-V measurements were conducted to obtain the saturation dark current density of the TLP devices. The absolute dark current (J_0) for the control was evaluated to be 2.67×10^{-7} A, while that for the target was 7.57×10^{-8} A (**Figure 6.12c**). The decrease in J_0 indicated a suppressed charge

recombination and thus reflected a lower trap density in the target TLP film. However, exact values of defect density remain to be measured. Consequently, SCLC measurements of electron-only devices with a structure of ITO/SnO_2/perovskite/PCBM:C_{60}/Ag were performed. V_{TFL} for the control and target electron-only devices were estimated at 0.42V and 0.30V, respectively, as shown in **Figure 6.12d**. Consequently, their trap densities were calculated to be 2.54×10^{-15} cm^{-3} and 1.81×10^{-15} cm^{-3}, respectively, according to **Equation 3.5** in section 3.5.5. This reduction in V_{TFL} and the corresponding decrease in trap density provide strong evidence that the templated-growth crystallization process effectively enhances the crystallinity of the target TLP film while minimizing trap density.

Finally, TPV and TPC techniques were utilized to investigate the dynamics of carriers at the interface, as depicted in **Figure 6.12e and f**, respectively. The fitting results for these measurements are provided in **Table 6.3**. The target device demonstrated a prolonged carrier lifetime ($\tau_{TPV,\ Target}$ = 4.87 ms) and a shorter charge extraction time ($\tau_{TPC,\ Target}$ = 0.80 μs) when compared to the control device ($\tau_{TPV,\ Control}$ = 2.98 ms $\tau_{TPC,\ Control}$ = 1.10 μs). These findings indicate that the templated-growth method and the resulting SnF_2-2PEA adducts at GBs and the interface have beneficial impacts in improving the film quality and passivating vacancies at GBs and the interface, leading to reduced charge recombination and enhanced charge extraction in the target perovskite device.

In summary, the above MS, EIS, dark J-V, SCLC, TPV, and TPC studies have shown a decrease in trap density in the devices, in support of the positive impact of templated-growth strategy in

regulating the crystallization and growth of TLP films.

Table 6.3. Fitting lifetimes from TPV and TPC of the TLPSCs. τ_{TPV} and τ_{TPC} refer to average TPV lifetime and TPC lifetime, respectively.

	τ_{TPV} (ms)	τ_{TPC} (μs)
Control	2.98	1.10
Target	4.87	0.80

6.8 Conclusions

In this chapter, I have proposed a templated-growth strategy to prepare high-quality TLP films. In this strategy, 2PEAI was used as an additive to form SnF_2-2PEA adducts in the precursor, which results in a templated-growth crystallization process by anchoring PbI_2 and SnI_2 in the precursor during the anti-solvent treatment and annealing process. The mechanism of the templated growth process has been investigated through NMR and XPS technologies. As a result, I have fabricated high-quality TLP films with improved crystallinity, better morphology, and suitable energy band alignment for carrier extraction. Moreover, the SnF_2-2PEA adducts accumulated at GBs and the perovskite interface serve as passivators to passivate the vacancies, resulting in significantly decreased defect density in the TLP films and devices. This was supported by a series of electrochemical studies of the devices. Consequently, I have achieved a remarkably enhanced PCE of 21.95% in the champion target PSC, compared to 19.88% of the control.

Chapter 7

CONCLUSIONS AND FUTURE PROSPECTIVES

This chapter will encapsulate my research discoveries from Chapters 4 to 6 and suggest potential avenues for future research based on my findings.

7. Conclusions and Future Prospectives

7.1 Conclusions

The utilization of renewable energy is a hot topic in this century. PSCs as a photovoltaic technology have attracted increasing interest since they were first discovered in 2009,[9] due to their high potential to convert solar energy into electricity energy with high-efficiency, along with their low-cost production process.[28] Among all kinds of PSCs, narrow-bandgap perovskite solar cells are theoretically able to convert solar energy with an efficiency approaching the S-Q limit (32.7%).[13, 14] That is why I choose to study narrow-bandgap PSCs, including pure $FAPbI_3$ PSCs and TLPSCs. In this thesis, I focused on regulating the crystallization dynamics of perovskite films to improve their film quality, which is one of the most important factors that affect the photovoltaic performance of PSCs. These were achieved by solvent engineering and additive engineering.

Chapter 4 introduces a coordinator replenishment strategy to enhance the crystallization process of α-$FAPbI_3$ perovskite in an air atmosphere. This includes the replacement of widely used DMSO solvent additive with TMU. It was demonstrated that TMU exhibits a weaker coordination with the perovskite components. This is the key factor that enables this approach to reduce the energy barrier for the formation of pure α-$FAPbI_3$ perovskite and facilitate the prenucleation of the perovskite films, which is beneficial to the quality of pure α-$FAPbI_3$ perovskite films, including higher crystallinity, better orientation, lower defects density, and relaxed lattice strains. Consequently, a significantly increased PCE of 23.2% was achieved in $FAPbI_3$-based inverted planar PSCs. Furthermore, the long-term stability of the as prepared $FAPbI_3$-based PSCs was enhanced due to the relaxation of lattice

strain in the perovskite films. This advancement represents a significant stride towards achieving more efficient and stable inverted PSCs based on pure α-$FAPbI_3$.

Chapter 5 aimed to achieve a balanced crystallization rate of both Sn and Pb-based components in TLPs during their anti-solvent treatment and annealing processes. It is worth noting that the unbalanced crystallization rate of Sn- and Pb-based components is the primary reason accounting for the poor quality of TLP films, which is mainly reflected in the abundant defects in the TLP film and component segregation across the whole film. This chapter presents a novel approach in which DHBABr was introduced into the precursor solution as an additive. DHBABr is shown to have stronger coordination with SnI_2 compared to PbI_2 and, thus preferentially forms a stable intermediate complex with SnI_2 to slow down the crystallization rate of Sn-based perovskite. This, thereby, leads to a balanced crystallization rate between Sn- and Pb-based perovskites. Consequently, TLP films were realized with more uniform Sn/Pb distribution across the entire film and suppressed defect density at GBs and at the interface. This led to achieving an exceptional power conversion efficiency of 22.44% and enhanced long-term stability in the champion device.

Chapter 6 introduces a more systematic templated anchoring approach to control crystallization throughout the entire film. This approach incorporates 2-phosphonoethan-1-aminium iodide (2PEAI) as an additive in a TLP precursor. The interaction between the 2PEAI additive and each perovskite component has been widely investigated, which led to a conclusion that 2PEAI selectively interacts

with SnF_2, forming a SnF_2-2PEA adduct in the precursor. This SnF_2-2PEA adduct acted as a template to regulate the crystallization dynamics of the TLP films by securely anchoring the perovskite components through amine and phosphate groups. Consequently, TLP films with significantly improved crystallinity, enhanced morphology, appropriate energy band alignment, and reduced defect density were obtained. TLPSCs fabricated using this templated-growth process achieve an impressive highest PCE of 21.95%. Due to the absence of surface passivation for the perovskite, this PCE is lower than that achieved in the work presented in Chapter 5. An effective surface passivator should be explored for this perovskite in the future works.

As a whole, this thesis focuses on narrow-bandgap PSCs, including α-$FAPbI_3$-based PSCs and TLPSCs. Chapter 4 has introduced a coordinator replenishment approach to enhance the crystallization of α-$FAPbI_3$ perovskite. Chapter 5 focuses on achieving balanced crystallization of Sn and Pb in TLPs, addressing composition segregation issues. Chapter 6 presents a templated anchoring approach to control crystallization in TLP films. Through these innovative approaches, the research endeavors to improve the efficiency and stability of TLPSCs, contributing to the advancement of renewable energy technology.

7.2 Future perspectives

Chapter 6 has demonstrated the potential of the templated-growth process using 2PEAI to achieve highly efficient PSCs. Though I have explored the interaction between 2PEAI and perovskite

components and proposed a mechanism for the crystallization process, 2PEAI's role in crystallization process was not evidently understood. This necessitates a deeper study of the crystallization process, such as in-situ GIWAXS and PL characterizations. In addition, evidence for determining the improvement of photovoltaic performance, such as EQE and SPO, should be further explored. Moreover, the effects of this strategy on the stability of the PSCs need to be studied. Therefore, in the future, I will continue to focus on this project, aiming to confirm the mechanism of the crystallization process and assess the long-term stability of the devices.

To further improve the performance and stability of the PSCs, here, I would also like to propose some area that could be engineered. These include the areas of surface passivation, tandem device, hole transporting layer optimization and oxidation hinderance.

First, surface passivation of the perovskite films is one of the most effective ways to inhibit non-radiative recombination in PSCs. This was widely explored in Pb-based perovskite, and a great deal of passivators have been discovered to be effective in enhancing the photovoltaic performance of Pb-based PSCs. However, these passivators are found to be ineffective and even detrimental in TLPs. This may be because formation of 2D/3D heterostructures can occur on the surface of TLP films when using the commonly used passivators like phenethylammonium iodide (PEAI), which will hinder charge transport at the TLP films with large thicknesses.[231-233] I have found that DHBABr can suppress the defect density on the surface of the TLP films and, thus improve the V_{oc} and FF of the

PSCs. However, it is found to be not universally applicable. When the TLP was doped with 2PEAI in Chapter 6, passivating the perovskite surface with DHBABr could not achieve a similar improvement to that achieved in Chapter 5. Therefore, exploring a universally applicable and effective passivator for TLP is feasible to further improve the performance of TLPSCs in future work.

Second, my present research is based on single-junction PSCs. But TLPSCs with a bandgap of 1.26 eV are suitable for fabricating all-perovskite tandem solar cells, which have shown great potential to achieve higher PCEs over 30% and can theoretically overcome the S-Q limit.[100, 185] Therefore, it is feasible to fabricate all-perovskite tandem solar cells based on my single-junction TLPSCs and thus further improve the PCE of the devices in the future.

Regarding to the stability, it could be further improved by suppressing the degradation of the perovskite layer. PEDOT:PSS is a commonly used hole-transporting material for TLPSCs, but its hygroscopic and acidic nature would facilitate the degradation of perovskite films and, therefore, lead to inferior long-term stability.[195] Other researchers have developed some alternatives such as MPA2FPh-BT-BA, bilayer 2PACz/MPA, and P3CT-Cs.[128, 185, 195] However, these materials seem to be not universally applicable. Hence, searching for a non-hygroscopic and neutral HTM that is effective for hole-transporting is an area feasible to both further improve the performance and long-term stability of the TLPSCs.

Moreover, oxidation of Sn(II) in the TLPs is the most key factor that has limit the long-term stability of TLPSCs. Though surface passivation and producing 2D/3D heterojunction perovskite can hinder the H_2O and O_2 intrusion in a certain degree, the heterojunction interface would also suppress the charge transfer at the interface and thus limit the performance of the devices as well.[231-233] Suppressing oxidation of Sn(II) through reductive additives is another effective strategy that would significantly improve the oxidation hindrance of the TLP and, therefore, further improve the long-term stability of the solar cells. In Chapter 5, we have introduced a reductive DHBABr to improve both the performance and stability of TLPSCs. However, the DHBABr molecule may produce an unfavorable H_2O molecule under oxidation, which is also harmful to the TLP. Therefore, investigating a more suitable reductive agent for suppressing the oxidation of Sn(II) is another area that could be further explored to improve the stability of the devices.

In summary, the areas of surface passivation, tandem device, alternative HTM, and oxidation hinderance could be further engineered to improve the performance and long-term stability of PSCs.

LIST OF REFERENCES

1. Best Research-Cell Efficiency Chart, https://www.nrel.gov/pv/cell-efficiency.html, (accessed 22 May, 2024).
2. *Net Zero by 2050*, International Energy Agency (IEA), 2021. https://www.iea.org/reports/net-zero-by-2050
3. *Distribution of electricity generation worldwide in 2022*, 2023. https://www.statista.com/statistics/269811/world-electricity-production-by-energy-source/
4. N. Li, X. Niu, Q. Chen and H. Zhou, *Chem. Soc. Rev.*, 2020, **49**, 8235-8286.
5. M. A. Green, *Prog Photovolt*, 2009, **17**, 183-189.
6. C. Ballif, F.-J. Haug, M. Boccard, P. J. Verlinden and G. Hahn, *Nat. Rev. Mater*, 2022, **7**, 597-616.
7. J. Ramanujam, D. M. Bishop, T. K. Todorov, O. Gunawan, J. Rath, R. Nekovei, E. Artegiani and A. Romeo, *Prog. Mater Sci.*, 2020, **110**, 100619.
8. I. Massiot, A. Cattoni and S. Collin, *Nat. Energy*, 2020, **5**, 959-972.
9. A. Kojima, K. Teshima, Y. Shirai and T. Miyasaka, *J. Am. Chem. Soc.*, 2009, **131**, 6050-6051.
10. G. Nazir, S. Y. Lee, J. H. Lee, A. Rehman, J. K. Lee, S. Il Seok and S. J. Park, *Adv. Mater.*, 2022, **34**, 2204380.
11. Z. Saki, M. M. Byranvand, N. Taghavinia, M. Kedia and M. Saliba, *Energy Environ. Sci.*, 2021, **14**, 5690-5722.
12. R. Prasanna, A. Gold-Parker, T. Leijtens, B. Conings, A. Babayigit, H. G. Boyen, M. F. Toney and M. D. McGehee, *J. Am. Chem. Soc.*, 2017, **139**, 11117-11124.
13. A. Polman, M. Knight, E. C. Garnett, B. Ehrler and W. C. Sinke, *Science*, 2016, **352**, aad4424.
14. W. Shockley and H. J. Queisser, *J. Appl. Phys.*, 1961, **32**, 510-519.
15. J. Park, J. Kim, H.-S. Yun, M. J. Paik, E. Noh, H. J. Mun, M. G. Kim, T. J. Shin and S. I. Seok, *Nature*, 2023, **616**, 724-730.
16. G. E. Eperon, S. D. Stranks, C. Menelaou, M. B. Johnston, L. M. Herz and H. J. Snaith, *Energy Environ. Sci.*, 2014, **7**, 982–988.
17. *Global Electricity Review 2023*, Ember, 2023.
18. A.-E. Becquerel, *CR Acad. Sci*, 1839, **9**, 1.
19. H. Wang, J. S. He, H. M. Xiang, R. Ran, W. Zhou, W. Wang and Z. P. Shao, *ENERGY & FUELS*, 2023, **37**, 6401-6423.
20. K. Fukuda, K. Yu and T. Someya, *Adv. Energy Mater.*, 2020, **10**, 2000765.
21. L. Liu, A. Najar, K. Wang, M. Y. Du and S. Z. Liu, *Adv. Sci*, 2022, **9**, 2104577.
22. G. Richhariya, A. Kumar, P. Tekasakul and B. Gupta, *RENEWABLE & SUSTAINABLE ENERGY REVIEWS*, 2017, **69**, 705-718.
23. H. Chen, S. Xiang, W. Li, H. Liu, L. Zhu and S. Yang, *Solar RRL*, 2018, **2**, 1700188.
24. J. H. Im, C. R. Lee, J. W. Lee, S. W. Park and N. G. Park, *Nanoscale*, 2011, **3**, 4088-4093.
25. H. S. Kim, C. R. Lee, J. H. Im, K. B. Lee, T. Moehl, A. Marchioro, S. J. Moon, R. Humphry-

Baker, J. H. Yum, J. E. Moser, M. Gratzel and N. G. Park, *Sci Rep*, 2012, **2**, 591.
26. A. Mallick and I. Visoly-Fisher, *MATERIALS ADVANCES*, 2021, **2**, 6125-6135.
27. J. Y. Jeng, Y. F. Chiang, M. H. Lee, S. R. Peng, T. F. Guo, P. Chen and T. C. Wen, *Adv. Mater.*, 2013, **25**, 3727-3732.
28. J. Seo, T. H. Song, S. Rasool, S. Park and J. Y. Kim, *ADVANCED ENERGY AND SUSTAINABILITY RESEARCH*, 2023, **4**, 2200160.
29. R. Sharif, A. Khalid, S. W. Ahmad, A. Rehman, H. G. Qutab, H. H. Akhtar, K. Mahmood, S. Afzal and F. Saleem, *NANOSCALE ADVANCES*, 2023, **5**, 3803-3833.
30. M. Kim, G.-H. Kim, T. K. Lee, I. W. Choi, H. W. Choi, Y. Jo, Y. J. Yoon, J. W. Kim, J. Lee, D. Huh, H. Lee, S. K. Kwak, J. Y. Kim and D. S. Kim, *Joule*, 2019, **3**, 2179-2192.
31. E. Edri, S. Kirmayer, A. Henning, S. Mukhopadhyay, K. Gartsman, Y. Rosenwaks, G. Hodes and D. Cahen, *Nano Lett.*, 2014, **14**, 1000-1004.
32. B. Tu, Y. Shao, W. Chen, Y. Wu, X. Li, Y. He, J. Li, F. Liu, Z. Zhang, Y. Lin, X. Lan, L. Xu, X. Shi, A. M. C. Ng, H. Li, L. W. Chung, A. B. Djurišić and Z. He, *Adv. Mater.*, 2019, **31**, 1805944.
33. H. Min, D. Y. Lee, J. Kim, G. Kim, K. S. Lee, J. Kim, M. J. Paik, Y. K. Kim, K. S. Kim, M. G. Kim, T. J. Shin and S. Il Seok, *Nature*, 2021, **598**, 444-450.
34. Z. Huang, Y. Bai, X. Huang, J. Li, Y. Wu, Y. Chen, K. Li, X. Niu, N. Li, G. Liu, Y. Zhang, H. Zai, Q. Chen, T. Lei, L. Wang and H. Zhou, *Nature*, 2023, **623**, 531-537.
35. H. Guo, W. Xiang, Y. Fang, J. Li and Y. Lin, *Angew. Chem. Int. Ed. Engl.*, 2023, **62**, e202304568.
36. D. X. Yuan, A. Gorka, M. F. Xu, Z. K. Wang and L. S. Liao, *Phys. Chem. Chem. Phys.*, 2015, **17**, 19745-19750.
37. B.-w. Park, H. W. Kwon, Y. Lee, D. Y. Lee, M. G. Kim, G. Kim, K.-j. Kim, Y. K. Kim, J. Im, T. J. Shin and S. I. Seok, *Nat. Energy*, 2021, **6**, 419-428.
38. J. Jeong, M. Kim, J. Seo, H. Lu, P. Ahlawat, A. Mishra, Y. Yang, M. A. Hope, F. T. Eickemeyer, M. Kim, Y. J. Yoon, I. W. Choi, B. P. Darwich, S. J. Choi, Y. Jo, J. H. Lee, B. Walker, S. M. Zakeeruddin, L. Emsley, U. Rothlisberger, A. Hagfeldt, D. S. Kim, M. Grätzel and J. Y. Kim, *Nature*, 2021, **592**, 381-385.
39. W. Hui, L. Chao, H. Lu, F. Xia, Q. Wei, Z. Su, T. Niu, L. Tao, B. Du, D. Li, Y. Wang, H. Dong, S. Zuo, B. Li, W. Shi, X. Ran, P. Li, H. Zhang, Z. Wu, C. Ran, L. Song, G. Xing, X. Gao, J. Zhang, Y. Xia, Y. Chen and W. Huang, *Science*, 2021, **371**, 1359.
40. Q. Tan, Z. Li, G. Luo, X. Zhang, B. Che, G. Chen, H. Gao, D. He, G. Ma, J. Wang, J. Xiu, H. Yi, T. Chen and Z. He, *Nature*, 2023, **620**, 545–551.
41. Z. Liang, Y. Zhang, H. Xu, W. Chen, B. Liu, J. Zhang, H. Zhang, Z. Wang, D. H. Kang, J. Zeng, X. Gao, Q. Wang, H. Hu, H. Zhou, X. Cai, X. Tian, P. Reiss, B. Xu, T. Kirchartz, Z. Xiao, S. Dai, N. G. Park, J. Ye and X. Pan, *Nature*, 2023, **624**, 557-563.
42. J. Frenkel, *Phys. Rev.*, 1931, **37**, 17-44.
43. R. S. Knox, *Theory of Excitons, Solid state physics*, New York: Academic, New York, vol.5 1963.
44. G. L. Miessler, G. L. Miessler and D. A. Tarr, *Inorganic Chemistry*, Pearson Education, Inc., Fifth Edition, 2012. 230-234
45. N. Marinova, S. Valero and J. L. Delgado, *J. Colloid Interface Sci.*, 2017, **488**, 373-389.

46. M. A. Green, A. Ho-Baillie and H. J. Snaith, *Nature Photonics*, 2014, **8**, 506-514.
47. M. T. Weller, O. J. Weber, J. M. Frost and A. Walsh, *The Journal of Physical Chemistry Letters*, 2015, **6**, 3209-3212.
48. V. M. Goldschmidt, *Naturwissenschaften*, 1926, **14**, 477-485.
49. A. Amat, E. Mosconi, E. Ronca, C. Quarti, P. Umari, M. K. Nazeeruddin, M. Grätzel and F. De Angelis, *Nano Lett*, 2014, **14**, 3608-3616.
50. M. Saliba, T. Matsui, K. Domanski, J.-Y. Seo, A. Ummadisingu, S. M. Zakeeruddin, J.-P. Correa-Baena, W. R. Tress, A. Abate, A. Hagfeldt and M. Grätzel, *Science*, 2016, **354**, 206.
51. A. Binek, F. C. Hanusch, P. Docampo and T. Bein, *The Journal of Physical Chemistry Letters*, 2015, **6**, 1249-1253.
52. T. A. S. Doherty, S. Nagane, D. J. Kubicki, Y.-K. Jung, D. N. Johnstone, A. N. Iqbal, D. Guo, K. Frohna, M. Danaie, E. M. Tennyson, S. Macpherson, A. Abfalterer, M. Anaya, Y.-H. Chiang, P. Crout, F. S. Ruggeri, S. Collins, C. P. Grey, A. Walsh, P. A. Midgley and S. D. Stranks, *Science*, 2021, **374**, 1598-1605.
53. Q. Jiang, J. Tong, Y. Xian, R. A. Kerner, S. P. Dunfield, C. Xiao, R. A. Scheidt, D. Kuciauskas, X. Wang, M. P. Hautzinger, R. Tirawat, M. C. Beard, D. P. Fenning, J. J. Berry, B. W. Larson, Y. Yan and K. Zhu, *Nature*, 2022, **611**, 278-283.
54. C. Yi, J. Luo, S. Meloni, A. Boziki, N. Ashari-Astani, C. Grätzel, S. M. Zakeeruddin, U. Röthlisberger and M. Grätzel, *Energy Environ. Sci.*, 2016, **9**, 656-662.
55. F. Xie, C.-C. Chen, Y. Wu, X. Li, M. Cai, X. Liu, X. Yang and L. Han, *Energy Environ. Sci.*, 2017, **10**, 1942-1949.
56. S.-H. Turren-Cruz, A. Hagfeldt and M. Saliba, *Science*, 2018, **362**, 449.
57. S. D. Stranks, G. E. Eperon, G. Grancini, C. Menelaou, M. J. P. Alcocer, T. Leijtens, L. M. Herz, A. Petrozza and H. J. Snaith, *Science*, 2013, **342**, 341-344.
58. D. K. Lee, K. S. Lim, J. W. Lee and N. G. Park, *J. Mater. Chem. A*, 2021, **9**, 3018-3028.
59. W. Jia, Z. Wei, B. Liu, D. Yan, Y. Huang, M. Li, Y. Tao, R. Chen and L. Xu, *Acs Applied Materials & Interfaces*, 2022, **14**, 46801-46808.
60. Y. Ogomi, A. Morita, S. Tsukamoto, T. Saitho, N. Fujikawa, Q. Shen, T. Toyoda, K. Yoshino, S. S. Pandey, T. Ma and S. Hayase, *J. Phys. Chem. Lett.*, 2014, **5**, 1004-1011.
61. D. Liu, B. B. Yu, M. Liao, Z. Jin, L. Zhou, X. Zhang, F. Wang, H. He, T. Gatti and Z. He, *ACS Appl Mater Interfaces*, 2020, **12**, 30530-30537.
62. G. E. Eperon, G. M. Paternò, R. J. Sutton, A. Zampetti, A. A. Haghighirad, F. Cacialli and H. J. Snaith, *J. Mater. Chem. A*, 2015, **3**, 19688-19695.
63. R. Sheng, A. W. Ho-Baillie, S. Huang, M. Keevers, X. Hao, L. Jiang, Y. B. Cheng and M. A. Green, *J Phys Chem Lett*, 2015, **6**, 3931-3934.
64. B. Walker, G. H. Kim and J. Y. Kim, *Adv. Mater.*, 2019, **31**, e1807029.
65. B. B. Yu, Z. Chen, Y. Zhu, Y. Wang, B. Han, G. Chen, X. Zhang, Z. Du and Z. He, *Adv. Mater.*, 2021, **33**, e2102055.
66. K. Xiao, R. Lin, Q. Han, Y. Hou, Z. Qin, H. T. Nguyen, J. Wen, M. Wei, V. Yeddu, M. I. Saidaminov, Y. Gao, X. Luo, Y. Wang, H. Gao, C. Zhang, J. Xu, J. Zhu, E. H. Sargent and H. Tan, *Nat. Energy*, 2020, **5**, 870-880.

67. J. Even, L. Pedesseau, J.-M. Jancu and C. Katan, *The Journal of Physical Chemistry Letters*, 2013, **4**, 2999-3005.
68. S. Tao, I. Schmidt, G. Brocks, J. Jiang, I. Tranca, K. Meerholz and S. Olthof, *Nat Commun*, 2019, **10**, 2560.
69. J. Im, C. C. Stoumpos, H. Jin, A. J. Freeman and M. G. Kanatzidis, *J. Phys. Chem. Lett.*, 2015, **6**, 3503-3509.
70. A. Goyal, S. McKechnie, D. Pashov, W. Tumas, M. van Schilfgaarde and V. Stevanović, *Chem. Mater.*, 2018, **30**, 3920-3928.
71. Y. Lei, Y. Xu, M. Wang, G. Zhu and Z. Jin, *Small*, 2021, **17**, e2005495.
72. H. Jin, E. Debroye, M. Keshavarz, I. G. Scheblykin, M. B. J. Roeffaers, J. Hofkens and J. A. Steele, *Materials Horizons*, 2020, **7**, 397-410.
73. W. J. Yin, T. Shi and Y. Yan, *Adv. Mater.*, 2014, **26**, 4653-4658.
74. J. S. Yun, A. Ho-Baillie, S. Huang, S. H. Woo, Y. Heo, J. Seidel, F. Huang, Y. B. Cheng and M. A. Green, *J Phys Chem Lett*, 2015, **6**, 875-880.
75. D. W. de Quilettes, S. M. Vorpahl, S. D. Stranks, H. Nagaoka, G. E. Eperon, M. E. Ziffer, H. J. Snaith and D. S. Ginger, *Science*, 2015, **348**, 683-686.
76. Z. Ni, C. Bao, Y. Liu, Q. Jiang, W.-Q. Wu, S. Chen, X. Dai, B. Chen, B. Hartweg, Z. Yu, Z. Holman and J. Huang, *Science*, 2020, **367**, 1352-1358.
77. Y. Yang, M. J. Yang, D. T. Moore, Y. Yan, E. M. Miller, K. Zhu and M. C. Beard, *Nat. Energy*, 2017, **2**, 16207.
78. L. Zhang, M. G. Ju and W. Liang, *Phys. Chem. Chem. Phys.*, 2016, **18**, 23174-23183.
79. L. M. Herz, *ACS Energy Lett.*, 2017, **2**, 1539-1548.
80. P. Shi, Y. Ding, B. Ding, Q. Xing, T. Kodalle, C. M. Sutter-Fella, I. Yavuz, C. Yao, W. Fan, J. Xu, Y. Tian, D. Gu, K. Zhao, S. Tan, X. Zhang, L. Yao, P. J. Dyson, J. L. Slack, D. Yang, J. Xue, M. K. Nazeeruddin, Y. Yang and R. Wang, *Nature*, 2023, **620**, 323-327.
81. R. Lin, J. Xu, M. Wei, Y. Wang, Z. Qin, Z. Liu, J. Wu, K. Xiao, B. Chen, S. M. Park, G. Chen, H. R. Atapattu, K. R. Graham, J. Xu, J. Zhu, L. Li, C. Zhang, E. H. Sargent and H. Tan, *Nature*, 2022, **603**, 73-78.
82. M. M. Lee, J. Teuscher, T. Miyasaka, T. N. Murakami and H. J. Snaith, *Science*, 2012, **338**, 643-647.
83. J. Burschka, N. Pellet, S. J. Moon, R. Humphry-Baker, P. Gao, M. K. Nazeeruddin and M. Gratzel, *Nature*, 2013, **499**, 316-319.
84. M. Liu, M. B. Johnston and H. J. Snaith, *Nature*, 2013, **501**, 395-398.
85. B. Philippe, B.-W. Park, R. Lindblad, J. Oscarsson, S. Ahmadi, E. M. J. Johansson and H. Rensmo, *Chem. Mater.*, 2015, **27**, 1720-1731.
86. J. Liu, Y. Wu, C. Qin, X. Yang, T. Yasuda, A. Islam, K. Zhang, W. Peng, W. Chen and L. Han, *Energ Environ Sci*, 2014, **7**, 2963-2967.
87. N. P. Gallop, O. Selig, G. Giubertoni, H. J. Bakker, Y. L. A. Rezus, J. M. Frost, T. L. C. Jansen, R. Lovrincic and A. A. Bakulin, *The Journal of Physical Chemistry Letters*, 2018, **9**, 5987-5997.
88. B. Brunetti, C. Cavallo, A. Ciccioli, G. Gigli and A. Latini, *Sci Rep*, 2016, **6**, 31896.
89. E. J. Juarez-Perez, Z. Hawash, S. R. Raga, L. K. Ono and Y. Qi, *Energy Environ. Sci.*, 2016, **9**,

3406-3410.
90. N. Aristidou, I. Sanchez-Molina, T. Chotchuangchutchaval, M. Brown, L. Martinez, T. Rath and S. A. Haque, *Angewandte Chemie International Edition*, 2015, **54**, 8208-8212.
91. J. W. Lee and N. G. Park, *Adv Energy Mater*, 2019, DOI: 10.1002/aenm.201903249, 1903249.
92. N. H. Nickel, F. Lang, V. V. Brus, O. Shargaieva and J. Rappich, *Adv Electron Mater*, 2017, **3**, 1700158.
93. L. Lanzetta, T. Webb, N. Zibouche, X. Liang, D. Ding, G. Min, R. J. E. Westbrook, B. Gaggio, T. J. Macdonald, M. S. Islam and S. A. Haque, *Nat. Commun.*, 2021, **12**, 2853.
94. C. H. Chen, S. N. Cheng, L. Cheng, Z. K. Wang and L. S. Liao, *Adv. Energy Mater.*, 2023, **13**, 2204144.
95. H. Sato, C. Ishii, S. M. M. Nakayama, T. Ichise, K. Saito, Y. Watanabe, K. Ogasawara, R. Torimoto, A. Kobayashi, T. Kimura, Y. Nakamura, J. Yamagishi, Y. Ikenaka and M. Ishizuka, *Environ. Pollut.*, 2022, **308**, 119580.
96. M. E. Markowitz, P. E. Bijur, H. A. Ruff, K. Balbi and J. F. Rosen, *Environ. Health Perspect.*, 1996, **104**, 968-972.
97. I. R. Benmessaoud, A. L. Mahul-Mellier, E. Horvath, B. Maco, M. Spina, H. A. Lashuel and L. Forro, *Toxicol Res (Camb)*, 2016, **5**, 407-419.
98. I. Chung, B. Lee, J. He, R. P. Chang and M. G. Kanatzidis, *Nature*, 2012, **485**, 486-489.
99. F. Hao, C. C. Stoumpos, D. H. Cao, R. P. H. Chang and M. G. Kanatzidis, *Nature Photonics*, 2014, **8**, 489-494.
100. R. Lin, Y. Wang, Q. Lu, B. Tang, J. Li, H. Gao, Y. Gao, H. Li, C. Ding, J. Wen, P. Wu, C. Liu, S. Zhao, K. Xiao, Z. Liu, C. Ma, Y. Deng, L. Li, F. Fan and H. Tan, *Nature*, 2023, **620**, 994–1000.
101. Y. Jiang, L. Qiu, E. J. Juarez-Perez, L. K. Ono, Z. Hu, Z. Liu, Z. Wu, L. Meng, Q. Wang and Y. Qi, *Nat. Energy*, 2019, **4**, 585-593.
102. Z. Li, X. Wu, B. Li, S. Zhang, D. Gao, Y. Liu, X. Li, N. Zhang, X. Hu, C. Zhi, A. K. Y. Jen and Z. Zhu, *Adv. Energy Mater.*, 2021, **12**, 2103236.
103. Z. Li, X. Wu, S. Wu, D. Gao, H. Dong, F. Huang, X. Hu, A. K. Y. Jen and Z. Zhu, *Nano Energy*, 2022, **93**, 106853.
104. X. Li, F. Zhang, H. He, J. J. Berry, K. Zhu and T. Xu, *Nature*, 2020, **578**, 555-558.
105. S. Chen, Y. Deng, X. Xiao, S. Xu, P. N. Rudd and J. Huang, *Nature Sustainability*, 2021, **4**, 636-643.
106. W. Chen, Y. D. Zhu, J. W. Xiu, G. C. Chen, H. M. Liang, S. C. Liu, H. S. Xue, E. Birgersson, J. W. Ho, X. S. Qin, J. Y. Lin, R. J. Ma, T. Liu, Y. L. He, A. M. C. Ng, X. G. Guo, Z. B. He, H. Yan, A. B. Djurisic and Y. Hou, *Nat. Energy*, 2022, **7**, 229-237.
107. D. McMullan, *Scanning*, 1995, **17**, 175-185.
108. G. Binnig, C. F. Quate and C. Gerber, *Phys. Rev. Lett.*, 1986, **56**, 930-933.
109. M. Fujihira, *Annu. Rev. Mater. Sci.*, 1999, **29**, 353-380.
110. A. Hammiche, H. M. Pollock, M. Reading, M. Claybourn, P. H. Turner and K. Jewkes, *Applied Spectroscopy*, 1999, **53**, 810-815.
111. A. Dazzi, R. Prazeres, F. Glotin and J. M. Ortega, *Opt. Lett.*, 2005, **30**, 2388-2390.

112. J. Goldstein, *Scanning Electron Microscopy and X-Ray Microanalysis: Third Edition*, Springer US, 2003.
113. S. Guo, X. Z. Zhang, M. W. Hao, T. W. Duan, W. Z. Wang, Z. M. Li, G. W. Liu, S. H. Cai and Y. Y. Zhou, *Advanced Optical Materials*, 2024, **12**, 2301255.
114. W. H. Bragg and W. L. Bragg, *Proceedings of the Royal Society of London. Series A, Containing Papers of a Mathematical and Physical Character*, 1997, **88**, 428-438.
115. G. K. Williamson and W. H. Hall, *Acta Metall.*, 1953, **1**, 22-31.
116. J. A. Steele, E. Solano, D. Hardy, D. Dayton, D. Ladd, K. White, P. Chen, J. Hou, H. Huang, R. A. Saha, L. Wang, F. Gao, J. Hofkens, M. B. J. Roeffaers, D. Chernyshov and M. F. Toney, *Adv. Energy Mater.*, 2023, **13**, 2300760.
117. P. R. Griffiths, J. A. De Haseth and J. D. Winefordner, *Fourier Transform Infrared Spectrometry*, Wiley, 2007.
118. I. I. Rabi, J. R. Zacharias, S. Millman and P. Kusch, *Phys. Rev.*, 1938, **53**, 318-318.
119. A. W. Coats and J. P. Redfern, *Analyst*, 1963, **88**, 906-924.
120. J. Mahoney, C. Monroe, A. M. Swartley, M. G. Ucak-Astarlioglu and C. A. Zoto, *Spectrosc. Lett.*, 2020, **53**, 726-736.
121. C. Li, N. Zhang and P. Gao, *Materials Chemistry Frontiers*, 2023, **7**, 3797-3802.
122. W. C. Price, in *Advances in Atomic and Molecular Physics*, eds. D. R. Bates and B. Bederson, Academic Press, 1974, vol. 10, pp. 131-171.
123. D. W. Koppenaal, C. J. Barinaga and M. R. Smith, *J. Anal. At. Spectrom.*, 1994, **9**, 1053-1058.
124. P. B. Nagy, *AIP Conf. Proc.*, 2013, **1511**, 1482-1489.
125. A. A. Edwards and B. D. Alexander, in *Encyclopedia of Spectroscopy and Spectrometry (Third Edition)*, eds. J. C. Lindon, G. E. Tranter and D. W. Koppenaal, Academic Press, Oxford, 2017, pp. 511-519.
126. J. Tauc, *Mater. Res. Bull.*, 1968, **3**, 37-46.
127. M. Tebyetekerwa, J. Zhang, Z. Xu, T. N. Truong, Z. Yin, Y. Lu, S. Ramakrishna, D. Macdonald and H. T. Nguyen, *ACS Nano*, 2020, **14**, 14579-14604.
128. W. Zhang, H. Yuan, X. Li, X. Guo, C. Lu, A. Liu, H. Yang, L. Xu, X. Shi, Z. Fang, H. Yang, Y. Cheng and J. Fang, *Adv. Mater.*, 2023, **35**, 2303674.
129. K. Grodecki, K. Murawski, J. Rutkowski, A. Kowalewski and J. Sobieski, *Opto-Electronics Review*, 2021, **29**, 91-96.
130. J. Xiu, B. Han, H. Gao, X. Chen, Z. Chen, S. Gong, X. Yan, W. Tian, X. Zhang, T. Chen, X. Feng, G. Chen, D. He, Y. Deng, S. Jin, P. R. Slater and Z. He, *Adv. Energy Mater.*, 2023, **13**.
131. O. J. Sandberg, C. Kaiser, S. Zeiske, N. Zarrabi, S. Gielen, W. Maes, K. Vandewal, P. Meredith and A. Armin, *Nature Photonics*, 2023, **17**, 368-374.
132. S. Zeiske, O. J. Sandberg, N. Zarrabi, W. Li, P. Meredith and A. Armin, *Nat. Commun.*, 2021, **12**, 3603.
133. Z. Zhang, J. Liang, J. Wang, Y. Zheng, X. Wu, C. Tian, A. Sun, Y. Huang, Z. Zhou, Y. Yang, Y. Liu, C. Tang and C. C. Chen, *Adv. Energy Mater.*, 2023, **13**, 2300181.
134. A. Guerrero, J. Bisquert and G. Garcia-Belmonte, *Chem. Rev.*, 2021, **121**, 14430-14484.
135. A. Lasia, in *Electrochemical Impedance Spectroscopy and its Applications*, ed. A. Lasia,

Springer New York, New York, NY, 2014, DOI: 10.1007/978-1-4614-8933-7_10, pp. 251-255.
136. O. Almora, C. Aranda, E. Mas-Marzá and G. Garcia-Belmonte, *Appl. Phys. Lett.*, 2016, **109**, 173903.
137. E. A. Duijnstee, J. M. Ball, V. M. Le Corre, L. J. A. Koster, H. J. Snaith and J. Lim, *ACS Energy Lett.*, 2020, **5**, 376-384.
138. W. Chen, D. Li, X. Chen, H. Chen, S. Liu, H. Yang, X. Li, Y. Shen, X. Ou, Y. Yang, L. Jiang, Y. Li and Y. Li, *Adv. Funct. Mater.*, 2021, **32**, 2109321.
139. J. Wang, M. A. Uddin, B. Chen, X. Ying, Z. Ni, Y. Zhou, M. Li, M. Wang, Z. Yu and J. Huang, *Adv. Energy Mater.*, 2023, **13**, 2204115.
140. L. Huang, H. Cui, W. Zhang, D. Pu, G. Zeng, Y. Liu, S. Zhou, C. Wang, J. Zhou, C. Wang, H. Guan, W. Shen, G. Li, T. Wang, W. Zheng, G. Fang and W. Ke, *Adv. Mater.*, 2023, **35**, e2301125.
141. J. Cao, H. L. Loi, Y. Xu, X. Guo, N. Wang, C. K. Liu, T. Wang, H. Cheng, Y. Zhu, M. G. Li, W. Y. Wong and F. Yan, *Adv. Mater.*, 2021, DOI: 10.1002/adma.202107729, e2107729.
142. M. Jeong, I. W. Choi, E. M. Go, Y. Cho, M. Kim, B. Lee, S. Jeong, Y. Jo, H. W. Choi, J. Lee, J.-H. Bae, S. K. Kwak, D. S. Kim and C. Yang, *Science*, 2020, **369**, 1615.
143. T. Zhang, Q. Xu, F. Xu, Y. Fu, Y. Wang, Y. Yan, L. Zhang and Y. Zhao, *Sci. Bull.*, 2019, **64**, 1608-1616.
144. Y. Huang, X. Lei, T. He, Y. Jiang and M. Yuan, *Adv. Energy Mater.*, 2021, **12**, 2100690.
145. P. Raval, R. M. Kennard, E. S. Vasileiadou, C. J. Dahlman, I. Spanopoulos, M. L. Chabinyc, M. Kanatzidis and G. N. Manjunatha Reddy, *ACS Energy Lett.*, 2022, **7**, 1534-1543.
146. Z.-A. Nan, L. Chen, Q. Liu, S.-H. Wang, Z.-X. Chen, S.-Y. Kang, J.-B. Ji, Y.-Y. Tan, Y. Hui, J.-W. Yan, Z.-X. Xie, W.-Z. Liang, B.-W. Mao and Z.-Q. Tian, *Chem*, 2021, **7**, 2513-2526.
147. Y. Chen, Y. Lei, Y. Li, Y. Yu, J. Cai, M.-H. Chiu, R. Rao, Y. Gu, C. Wang, W. Choi, H. Hu, C. Wang, Y. Li, J. Song, J. Zhang, B. Qi, M. Lin, Z. Zhang, A. E. Islam, B. Maruyama, S. Dayeh, L.-J. Li, K. Yang, Y.-H. Lo and S. Xu, *Nature*, 2020, **577**, 209-215.
148. H. Zhang and N. G. Park, *Angew. Chem. Int. Ed.*, 2022, **61**, e202212268
149. M. Saliba, T. Matsui, K. Domanski, J.-Y. Seo, A. Ummadisingu, S. M. Zakeeruddin, J.-P. Correa-Baena, W. R. Tress, A. Abate, A. Hagfeldt and M. Grätzel, *Science*, 2016, **354**, 206-209.
150. X. Sun, D. Li, L. Zhao, Y. Zhang, Q. Hu, T. P. Russell, F. Liu, J. Wei and H. Li, *Adv. Mater.*, 2023, **35**, e2301115.
151. H. Min, M. Kim, S.-U. Lee, H. Kim, G. Kim, K. Choi, J. H. Lee and S. I. Seok, *Science*, 2019, **366**, 749.
152. D.-H. Kang, S.-U. Lee and N.-G. Park, *ACS Energy Lett.*, 2023, **8**, 2122-2129.
153. Y. Zhang, Y. Li, L. Zhang, H. Hu, Z. Tang, B. Xu and N. G. Park, *Adv. Energy Mater.*, 2021, **11**, 2102538.
154. H. Lu, Y. Liu, P. Ahlawat, A. Mishra, W. R. Tress, F. T. Eickemeyer, Y. Yang, F. Fu, Z. Wang, C. E. Avalos, B. I. Carlsen, A. Agarwalla, X. Zhang, X. Li, Y. Zhan, S. M. Zakeeruddin, L. Emsley, U. Rothlisberger, L. Zheng, A. Hagfeldt and M. Grätzel, *Science*, 2020, **370**, eabb8985.
155. T. Du, T. J. Macdonald, R. X. Yang, M. Li, Z. Jiang, L. Mohan, W. Xu, Z. Su, X. Gao, R. Whiteley, C. T. Lin, G. Min, S. A. Haque, J. R. Durrant, K. A. Persson, M. A. McLachlan and J. Briscoe, *Adv. Mater.*, 2022, **34**, 2107850.

156. W. Chen, B. Han, Q. Hu, M. Gu, Y. Zhu, W. Yang, Y. Zhou, D. Luo, F.-Z. Liu, R. Cheng, R. Zhu, S.-P. Feng, A. B. Djurišić, T. P. Russell and Z. He, *Sci. Bull.*, 2021, **66**, 991-1002.
157. H. Hu, D. B. Ritzer, A. Diercks, Y. Li, R. Singh, P. Fassl, Q. H. Jin, F. Schackmar, U. W. Paetzold and B. A. Nejand, *Joule*, 2023, **7**, 1574-1592.
158. L. Bi, Q. Fu, Z. Zeng, Y. Wang, F. R. Lin, Y. Cheng, H. L. Yip, S. W. Tsang and A. K. Jen, *J. Am. Chem. Soc.*, 2023, **145**, 5920-5929.
159. Y. L. Huang, B. Z. Wang, T. H. Liu, D. Y. Li, Y. J. Zhang, T. Q. Zhang, X. Y. Yao, Y. Wang, A. Amini, Y. Q. Cai, B. M. Xu, Z. K. Tang, G. C. Xing and C. Cheng, *Adv. Funct. Mater.*, 2023, **33**, 2302375.
160. X. F. Jiang, X. Wang, X. Wu, S. F. Zhang, B. Z. Liu, D. Zhang, B. Li, P. Xiao, F. Xu, H. P. Lu, T. Chen, A. K. Y. Jen, S. F. Yang and Z. L. Zhu, *Adv. Energy Mater.*, 2023, **13**, 2300700.
161. W. He, J. Hu, C. Chen, Y. Chen, L. Zeng, X. Zhang, B. Cai, Y. Mai and F. Guo, *ACS Applied Materials & Interfaces*, 2020, **12**, 55830-55837.
162. Y. Zhang, J. Wang, J. Xu, W. Chen, D. Zhu, W. Zheng and X. Bao, *RSC Advances*, 2016, **6**, 79952-79957.
163. J. Xi, Z. Wu, K. Xi, H. Dong, B. Xia, T. Lei, F. Yuan, W. Wu, B. Jiao and X. Hou, *Nano Energy*, 2016, **26**, 438-445.
164. T. N. Mandal, J. H. Heo, S. H. Im and W. S. Kim, *Small*, 2023, **19**, e2305246.
165. D. Zhang, H. Zhang, H. Guo, F. Ye, S. Liu and Y. Wu, *Adv. Funct. Mater.*, 2022, **32**, 2200174.
166. Z. Xu, L. Zeng, J. Hu, Z. Wang, P. Zhang, C. J. Brabec, K. Forberich, Y. Mai and F. Guo, *Nano Energy*, 2022, **91**, 106658.
167. Y. Xu, H. Li, S. Ramakrishnan, D. Song, Y. Zhang, M. Cotlet and Q. Yu, *ACS Applied Energy Materials*, 2022, **5**, 9858-9869.
168. A. Al-Ashouri, E. Köhnen, B. Li, A. Magomedov, H. Hempel, P. Caprioglio, J. A. Márquez, A. B. Morales Vilches, E. Kasparavicius, J. A. Smith, N. Phung, D. Menzel, M. Grischek, L. Kegelmann, D. Skroblin, C. Gollwitzer, T. Malinauskas, M. Jošt, G. Matič, B. Rech, R. Schlatmann, M. Topič, L. Korte, A. Abate, B. Stannowski, D. Neher, M. Stolterfoht, T. Unold, V. Getautis and S. Albrecht, *Science*, 2020, **370**, 1300-1309.
169. J.-W. Lee, Z. Dai, C. Lee, H. M. Lee, T.-H. Han, N. De Marco, O. Lin, C. S. Choi, B. Dunn, J. Koh, D. Di Carlo, J. H. Ko, H. D. Maynard and Y. Yang, *J. Am. Chem. Soc.*, 2018, **140**, 6317-6324.
170. E. A. Alharbi, A. Y. Alyamani, D. J. Kubicki, A. R. Uhl, B. J. Walder, A. Q. Alanazi, J. Luo, A. Burgos-Caminal, A. Albadri, H. Albrithen, M. H. Alotaibi, J. E. Moser, S. M. Zakeeruddin, F. Giordano, L. Emsley and M. Gratzel, *Nat Commun*, 2019, **10**, 3008.
171. Q. He, M. Worku, L. Xu, C. Zhou, H. Lin, A. J. Robb, K. Hanson, Y. Xin and B. Ma, *ACS Appl Mater Interfaces*, 2020, **12**, 1159-1168.
172. Q. Jiang, Y. Zhao, X. Zhang, X. Yang, Y. Chen, Z. Chu, Q. Ye, X. Li, Z. Yin and J. You, *Nature Photonics*, 2019, **13**, 460-466.
173. Y. Q. Zhang, Y. Z. Zhang, B. F. Niu, Y. C. Huang, H. T. Wu, W. F. Fu and H. Z. Chen, *Adv. Funct. Mater.*, 2023, **33**, 2307949.
174. Y. Marcus, *Chem. Soc. Rev.*, 1993, **22**, 409-416.

175. Q. Cao, S. Yang, Q. Gao, L. Lei, Y. Yu, J. Shao and Y. Liu, *ACS Appl Mater Interfaces*, 2016, **8**, 7854-7861.
176. Y. Wang, L. Li, Z. Wu, R. Zhang, J. Hong, J. Zhang, H. Rao, Z. Pan and X. Zhong, *Angew. Chem. Int. Ed. Engl.*, 2023, **62**, e202302342.
177. W. Zuo, M. M. Byranvand, T. Kodalle, M. Zohdi, J. Lim, B. Carlsen, T. Magorian Friedlmeier, M. Kot, C. Das, J. I. Flege, W. Zong, A. Abate, C. M. Sutter-Fella, M. Li and M. Saliba, *Adv. Mater.*, 2023, **35**, e2302889.
178. S. Sanchez, L. Pfeifer, N. Vlachopoulos and A. Hagfeldt, *Chem. Soc. Rev.*, 2021, **50**, 7108-7131.
179. Y. Wang, Z. Shi, Y. Wang, Q. U. Khan, X. Li, L. Deng, Y. Pan, X. Zhang, Y. Yang, X. Yue, T. Hu, F. Liu, H. Wang, C. Li, K. Liu, W. Yuan, C. Cong, A. Yu and Y. Zhan, *Adv. Mater.*, 2023, **35**, e2302298.
180. X. Li, X. Wu, B. Li, Z. Cen, Y. Shang, W. Lian, R. Cao, L. Jia, Z. Li, D. Gao, X. Jiang, T. Chen, Y. Lu, Z. Zhu and S. Yang, *Energy Environ. Sci.*, 2022, **15**, 4813-4822.
181. S. Ravishankar, S. Gharibzadeh, C. Roldán-Carmona, G. Grancini, Y. Lee, M. Ralaiarisoa, A. M. Asiri, N. Koch, J. Bisquert and M. K. Nazeeruddin, *Joule*, 2018, **2**, 788-798.
182. Z. Zhang, J. Liang, Y. Zheng, X. Wu, J. Wang, Y. Huang, Y. Yang, Z. Zhou, L. Wang, L. Kong, K. M. Reddy, C. Qin and C.-C. Chen, *J. Mater. Chem. A*, 2021, **9**, 17830-17840.
183. E. L. Lim, A. Hagfeldt and D. Bi, *Energy Environ. Sci.*, 2021, **14**, 3256-3300.
184. S. Hu, K. Otsuka, R. Murdey, T. Nakamura, T. Minh Anh, T. Yamada, T. Handa, K. Matsuda, K. Nakano, A. Sato, K. Marumoto, K. Tajima, Y. Kanemitsu and A. Wakamiya, *Energy Environ. Sci.*, 2022, **15**, 2096-2107.
185. J. Zhu, Y. Luo, R. He, C. Chen, Y. Wang, J. Luo, Z. Yi, J. Thiesbrummel, C. Wang, F. Lang, H. Lai, Y. Xu, J. Wang, Z. Zhang, W. Liang, G. Cui, S. Ren, X. Hao, H. Huang, Y. Wang, F. Yao, Q. Lin, L. Wu, J. Zhang, M. Stolterfoht, F. Fu and D. Zhao, *Nat. Energy*, 2023, **8**, 714–724.
186. J. Tong, Q. Jiang, A. J. Ferguson, A. F. Palmstrom, X. Wang, J. Hao, S. P. Dunfield, A. E. Louks, S. P. Harvey, C. Li, H. Lu, R. M. France, S. A. Johnson, F. Zhang, M. Yang, J. F. Geisz, M. D. McGehee, M. C. Beard, Y. Yan, D. Kuciauskas, J. J. Berry and K. Zhu, *Nat. Energy*, 2022, **7**, 642–651.
187. D. Ricciarelli, D. Meggiolaro, F. Ambrosio and F. De Angelis, *ACS Energy Lett.*, 2020, **5**, 2787-2795.
188. D. Meggiolaro, D. Ricciarelli, A. A. Alasmari, F. A. S. Alasmary and F. De Angelis, *J. Phys. Chem. Lett.*, 2020, **11**, 3546-3556.
189. S. Gu, R. Lin, Q. Han, Y. Gao, H. Tan and J. Zhu, *Adv. Mater.*, 2020, **32**, e1907392.
190. C. Wang, Z. Song, C. Li, D. Zhao and Y. Yan, *Advanced Functional Materials*, 2019, **29**.
191. C. Li, Z. Song, C. Chen, C. Xiao, B. Subedi, S. P. Harvey, N. Shrestha, K. K. Subedi, L. Chen, D. Liu, Y. Li, Y.-W. Kim, C.-s. Jiang, M. J. Heben, D. Zhao, R. J. Ellingson, N. J. Podraza, M. Al-Jassim and Y. Yan, *Nat. Energy*, 2020, **5**, 768-776.
192. Q. Chen, J. Luo, R. He, H. Lai, S. Ren, Y. Jiang, Z. Wan, W. Wang, X. Hao, Y. Wang, J. Zhang, I. Constantinou, C. Wang, L. Wu, F. Fu and D. Zhao, *Adv. Energy Mater.*, 2021, **11**, 2101045.
193. K. J. Savill, A. M. Ulatowski, M. D. Farrar, M. B. Johnston, H. J. Snaith and L. M. Herz, *Adv. Funct. Mater.*, 2020, **30**, 2005594.

194. J. Luo, R. He, H. Lai, C. Chen, J. Zhu, Y. Xu, F. Yao, T. Ma, Y. Luo, Z. Yi, Y. Jiang, Z. Gao, J. Wang, W. Wang, H. Huang, Y. Wang, S. Ren, Q. Lin, C. Wang, F. Fu and D. Zhao, *Adv. Mater.*, 2023, **35**, e2300352.
195. G. Kapil, T. Bessho, Y. Sanehira, S. R. Sahamir, M. Chen, A. K. Baranwal, D. Liu, Y. Sono, D. Hirotani, D. Nomura, K. Nishimura, M. A. Kamarudin, Q. Shen, H. Segawa and S. Hayase, *ACS Energy Lett.*, 2022, **7**, 966-974.
196. R. Lin, K. Xiao, Z. Qin, Q. Han, C. Zhang, M. Wei, M. I. Saidaminov, Y. Gao, J. Xu, M. Xiao, A. Li, J. Zhu, E. H. Sargent and H. Tan, *Nat. Energy*, 2019, **4**, 864-873.
197. T. Nakamura, S. Yakumaru, M. A. Truong, K. Kim, J. Liu, S. Hu, K. Otsuka, R. Hashimoto, R. Murdey, T. Sasamori, H. D. Kim, H. Ohkita, T. Handa, Y. Kanemitsu and A. Wakamiya, *Nat. Commun.*, 2020, **11**, 3008.
198. W. Zhang, X. Li, S. Fu, X. Zhao, X. Feng and J. Fang, *Joule*, 2021, **5**, 2904-2914.
199. J. Sanchez-Diaz, R. S. Sánchez, S. Masi, M. Krecmarová, A. O. Alvarez, E. M. Barea, J. Rodriguez-Romero, V. S. Chirvony, J. F. Sánchez-Royo, J. P. Martinez-Pastor and I. Mora-Seró, *Joule*, 2022, **6**, 861-883.
200. Y. Xing, Z. Deng, T. Guo, Z. Zhang, Q. Tai, R. Zhao, J. Xiong, Q. Wang, L. Huang, X. Liu, Z. Hu, Y. Zhu and J. Zhang, *Chem. Eng. J.*, 2023, **462**, 142122.
201. W. Ke, C. Chen, I. Spanopoulos, L. Mao, I. Hadar, X. Li, J. M. Hoffman, Z. Song, Y. Yan and M. G. Kanatzidis, *J. Am. Chem. Soc.*, 2020, **142**, 15049-15057.
202. J. Tong, Z. Song, H. Kim Dong, X. Chen, C. Chen, F. Palmstrom Axel, F. Ndione Paul, O. Reese Matthew, P. Dunfield Sean, G. Reid Obadiah, J. Liu, F. Zhang, P. Harvey Steven, Z. Li, T. Christensen Steven, G. Teeter, D. Zhao, M. Al-Jassim Mowafak, F. A. M. van Hest Maikel, C. Beard Matthew, E. Shaheen Sean, J. Berry Joseph, Y. Yan and K. Zhu, *Science*, 2019, **364**, 475-479.
203. D. Yu, Q. Wei, H. Li, J. Xie, X. Jiang, T. Pan, H. Wang, M. Pan, W. Zhou, W. Liu, P. C. Y. Chow and Z. Ning, *Angew. Chem. Int. Ed.*, 2022, **61**, e202202346.
204. M. I. Saidaminov, I. Spanopoulos, J. Abed, W. Ke, J. Wicks, M. G. Kanatzidis and E. H. Sargent, *ACS Energy Lett.*, 2020, **5**, 1153-1155.
205. J. Pascual, G. Nasti, M. H. Aldamasy, J. A. Smith, M. Flatken, N. Phung, D. Di Girolamo, S.-H. Turren-Cruz, M. Li, A. Dallmann, R. Avolio and A. Abate, *Materials Advances*, 2020, **1**, 1066-1070.
206. T. Zhang, H. Ban, Q. Sun, H. Pan, H. Yu, Z. Zhang, X. Zhang, Y. Shen and M. Wang, *J. Energy Chem.*, 2022, **65**, 179-185.
207. H. L. Zhu, J. Xiao, J. Mao, H. Zhang, Y. Zhao and W. C. H. Choy, *Adv. Funct. Mater.*, 2017, **27**, 1605469.
208. L. Zhao, Q. Li, C. H. Hou, S. Li, X. Yang, J. Wu, S. Zhang, Q. Hu, Y. Wang, Y. Zhang, Y. Jiang, S. Jia, J. J. Shyue, T. P. Russell, Q. Gong, X. Hu and R. Zhu, *J. Am. Chem. Soc.*, 2022, **144**, 1700-1708.
209. S. J. Lee, S. S. Shin, Y. C. Kim, D. Kim, T. K. Ahn, J. H. Noh, J. Seo and S. I. Seok, *J. Am. Chem. Soc.*, 2016, **138**, 3974-3977.
210. M. Liao, B. B. Yu, Z. Jin, W. Chen, Y. Zhu, X. Zhang, W. Yao, T. Duan, I. Djerdj and Z. He,

ChemSusChem, 2019, **12**, 5007-5014.
211. B. B. Yu, M. Liao, Y. Zhu, X. Zhang, Z. Du, Z. Jin, D. Liu, Y. Wang, T. Gatti, O. Ageev and Z. He, *Adv. Funct. Mater.*, 2020, **30**, 2002230.
212. B. B. Yu, L. Xu, M. Liao, Y. Wu, F. Liu, Z. He, J. Ding, W. Chen, B. Tu, Y. Lin, Y. Zhu, X. Zhang, W. Yao, A. B. Djurišić, J. S. Hu and Z. He, *Solar RRL*, 2019, **3**, 1800290.
213. S. Hu, P. Zhao, K. Nakano, R. D. J. Oliver, J. Pascual, J. A. Smith, T. Yamada, M. A. Truong, R. Murdey, N. Shioya, T. Hasegawa, M. Ehara, M. B. Johnston, K. Tajima, Y. Kanemitsu, H. J. Snaith and A. Wakamiya, *Adv. Mater.*, 2023, **35**, e2208320.
214. Y. Yuan and J. Huang, *Acc. Chem. Res.*, 2016, **49**, 286-293.
215. S. N. Habisreutinger, N. K. Noel and H. J. Snaith, *ACS Energy Lett.*, 2018, **3**, 2472-2476.
216. S. J. Greaves and W. P. Griffith, *Spectrochimica Acta Part A: Molecular Spectroscopy*, 1991, **47**, 133-140.
217. T. Lana-Villarreal, A. Rodes, J. M. Pérez and R. Gómez, *J. Am. Chem. Soc.*, 2005, **127**, 12601-12611.
218. S. T. Martin, J. M. Kesselman, D. S. Park, N. S. Lewis and M. R. Hoffmann, *Environ. Sci. Technol.*, 1996, **30**, 2535-2542.
219. L. Öhrström and I. Michaud-Soret, *J. Phys. Chem. A*, 1999, **103**, 256-264.
220. A. A. Petrov, I. P. Sokolova, N. A. Belich, G. S. Peters, P. V. Dorovatovskii, Y. V. Zubavichus, V. N. Khrustalev, A. V. Petrov, M. Grätzel, E. A. Goodilin and A. B. Tarasov, *J. Phys. Chem. C*, 2017, **121**, 20739-20743.
221. J. Cao, X. Jing, J. Yan, C. Hu, R. Chen, J. Yin, J. Li and N. Zheng, *J. Am. Chem. Soc.*, 2016, **138**, 9919-9926.
222. T. Wang, Q. Tai, X. Guo, J. Cao, C.-K. Liu, N. Wang, D. Shen, Y. Zhu, C.-S. Lee and F. Yan, *ACS Energy Lett.*, 2020, **5**, 1741-1749.
223. S. Gu, R. Lin, Q. Han, Y. Gao, H. Tan and J. Zhu, *Adv Mater*, 2020, **32**, e1907392.
224. J. Pascual, M. Flatken, R. Felix, G. Li, S. H. Turren-Cruz, M. H. Aldamasy, C. Hartmann, M. Li, D. Di Girolamo, G. Nasti, E. Husam, R. G. Wilks, A. Dallmann, M. Bar, A. Hoell and A. Abate, *Angew. Chem. Int. Ed. Engl.*, 2021, **60**, 21583-21591.
225. J. Kurisinkal Pious, Y. Zwirner, H. Lai, S. Olthof, Q. Jeangros, E. Gilshtein, R. K. Kothandaraman, K. Artuk, P. Wechsler, C. Chen, C. M. Wolff, D. Zhao, A. N. Tiwari and F. Fu, *ACS Appl Mater Interfaces*, 2023, **15**, 10150−10157.
226. Y. Zong, Z. Zhou, M. Chen, N. P. Padture and Y. Zhou, *Adv. Energy Mater.*, 2018, **8**.
227. E. Akman, A. E. Shalan, F. Sadegh and S. Akin, *ChemSusChem*, 2021, **14**, 1176-1183.
228. Y. Zhao, P. Zhu, S. Huang, S. Tan, M. Wang, R. Wang, J. Xue, T. H. Han, S. J. Lee, A. Zhang, T. Huang, P. Cheng, D. Meng, J. W. Lee, J. Marian, J. Zhu and Y. Yang, *J. Am. Chem. Soc.*, 2020, **142**, 20071-20079.
229. X. Li, M. I. Dar, C. Yi, J. Luo, M. Tschumi, S. M. Zakeeruddin, M. K. Nazeeruddin, H. Han and M. Gratzel, *Nat Chem*, 2015, **7**, 703-711.
230. G. Kapil, T. Bessho, T. Maekawa, A. K. Baranwal, Y. Zhang, M. A. Kamarudin, D. Hirotani, Q. Shen, H. Segawa and S. Hayase, *Adv. Energy Mater.*, 2021, **11**, 2101069.
231. E. Ruggeri, M. Anaya, K. Galkowski, G. Delport, F. U. Kosasih, A. Abfalterer, S. Mackowski,

C. Ducati and S. D. Stranks, *Adv. Mater.*, 2019, **31**, e1905247.
232. L. Wen, Y. Deng, G. Zeng, G. Liu and X. Li, *Chem. Eng. J.*, 2023, **468**, 143446.
233. Z. Chen, M. Liu, Z. Li, T. Shi, Y. Yang, H. L. Yip and Y. Cao, *iScience*, 2018, **9**, 337-346.